WWU
MÜNSTER

First observation of double electron capture of Xe-124 and detection prospects for underlying nuclear interaction mechanisms in direct dark matter search

Alexander Fieguth, Dissertation 2018

wissen.leben
WWU Münster

Institut für Kernphysik
Westfälische Wilhelms-Universität Münster

Experimentelle Physik

Dissertationsthema

First observation of double electron capture of Xe-124 and detection prospects for underlying nuclear interaction mechanisms in direct dark matter search

Inaugural-Dissertation
zur Erlangung des Doktorgrades der Naturwissenschaften
im Fachbereich Physik
der Mathematisch-Naturwissenschaftlichen Fakultät
der Westfälischen Wilhelms-Universität Münster

vorgelegt von
Alexander Fieguth
aus Aschibulak, Kasachstan

— 2018 —

Dekan:	Prof. Dr. Michael Klasen
Erster Gutachter:	Prof. Dr. Christian Weinheimer
Zweiter Gutachter:	Prof. Dr. Dieter Frekers
Tag der mündlichen Prüfung:	__.__.____
Tag der Promotion:	__.__.____

Für Papa

Zwei Dinge erfüllen das Gemüt mit immer neuer und zunehmender Bewunderung und Ehrfurcht, je öfter und anhaltender sich das Nachdenken damit beschäftigt: der bestirnte Himmel über mir und das moralische Gesetz in mir.

— Kritik der praktischen Vernunft, *Immanuel Kant*

Abstract

The search for open tasks within and questions beyond the Standard Model of particle physics is in the focus of modern research. One of the main puzzles not explained is the dark matter component of the universe. The particle class of Weakly Interacting Massive Particles (WIMPs) fulfills all criteria from the Standard Model of Cosmology (ΛCDM) to explain dark matter and candidates for it are motivated by various theories, e.g., supersymmetric theories.
The XENON1T experiment is a detector searching for the direct detection of such WIMPs. It utilizes liquid xenon in a dual-phase time projection chamber. The result of a one tonne $\times$ year exposure set the most stringent limits of WIMP-nucleon interaction above $6\,\mathrm{GeV/c^2}$ with a minimum at $4.1 \cdot 10^{-47}\,\mathrm{cm^2}$ for a WIMP of $30\,\mathrm{GeV/c^2}$ with $90\,\%$ C.L.
The assumption of an isoscalar spin-independent interaction is motivated for such a limit, but is not verified yet. If a suppression is realized in nature, other interaction channels become interesting. A Monte Carlo study within this work sheds light on eight different interaction channels and reveals the potential in future detectors to measure the nature of the nuclear interaction mechanism once dark matter is detected.
For the particular interaction between a WIMP and the exchange pions within the nucleus the first limit is derived in this thesis using the full XENON1T exposure. This limit is at $6.4 \cdot 10^{-46}\,\mathrm{cm^2}$ for a $30\,\mathrm{GeV/c^2}$ WIMP with $90\,\%$ C.L.
An open task within the Standard Model is the direct observation of the double electron capture. For the isotope $^{124}\mathrm{Xe}$ the search was pursued in XENON100 superseding an existing external publication. In a study within this thesis on data of XENON1T, the decay mode of two-neutrino double K-shell electron capture was observed with a significance of 4.7σ. The resulting half-life of

$$T_{1/2}^{2\nu\mathrm{KK}} = 1.80^{+0.40(\mathrm{stat.})+0.07(\mathrm{sys.})}_{-0.39(\mathrm{stat.})-0.07(\mathrm{sys.})}\,10^{22}\,\mathrm{yr}$$

makes it the isotope with the longest half-life directly observed so far.

Zusammenfassung

Offene Fragen und Aufgaben innerhalb des Standardmodells der Teilchenphysik und darüber hinaus zu bearbeiten ist ein aktiver Teil der aktuellen Forschung. Eines der größten Rätsels außerhalb des Standardmodells ist die Dunkle Materie.
Die Teilchenklasse der WIMPs erfüllt alle Kriterien, die das Standardmodell der Kosmologie an Anforderungen für Teilchenkandidaten der Dunklen Materie stellt. Die Kandidaten für WIMPs entstammen diversen Theorien, aber vor allem in Theorien der Supersymmetrie gibt es vielversprechende Kandidaten.
Der XENON1T-Detektor versucht diese Teilchen der Dunklen Materie direkt nachzuweisen und arbeitet dabei mit einer Zwei-Phasen-Zeitprojektionskammer gefüllt mit flüssigem Xenon. Das Ergebnis der Suche in einem Tonnenjahr an Daten setzt die bisher strengste Grenze für den Wirkungsquerschnitt der isoskalaren spin-unabhänigen Streuung eines WIMPs an Nukleonen. Diese Grenze hat ihr Minimum bei $4.1 \cdot 10^{-47}\,\mathrm{cm}^2$ mit $90\,\%$ Konfidenz im Falle eines $30\,\mathrm{GeV/c}^2$ WIMPs.
Die Annahme, dass WIMPs über den isoskalaren Kanal interagieren, die für diese Grenze notwendig ist, ist in diversen Theorien unterdrückt. In diesem Fall kommen Interaktionskanäle zum Tragen, die sonst nur als untergeordnete Korrekturen auftauchen. Die Möglichkeit diese Interaktionskanäle von der Standardannahme zu unterscheiden, wurde in dieser Arbeit mit einer Monte-Carlo-Simulation für acht verschiedene Kanäle getestet und es wurde gezeigt, dass zukünftige Detektoren die Kanäle unterscheiden können.
Für die spezielle Wechselwirkung zwischen WIMPs und den Austauschpionen im Atomkern wurde hier die erste Grenze auf den Wechselwirkungsquerschnitt ermittelt. Diese liegt bei $6.4 \cdot 10^{-46}\,\mathrm{cm}^2$ für ein $30\,\mathrm{GeV/c}^2$ WIMP mit $90\,\%$ Konfidenz.
Eine offene Aufgabe innerhalb des Standardmodells ist der direkte Nachweis des vorrausgesagten doppelten Elektroneneinfangs. Für die Halbwertszeit dieses Prozesses im Isotop $^{124}\mathrm{Xe}$ wurde eine erste Grenze mit Hilfe des XENON100-Detektors ermittelt. Diese korrigiert einen Wert, den externe Wissenschaftler aus publizierten Daten ermittelt haben. Mit Daten von XENON1T wurde in Rahmen dieser Arbeit der Zerfall nachgewiesen. Dabei wurde der doppelte Elektroneneinfang aus der K-Schale mit einer Signifkanz von $4{,}7\sigma$ beobachtet. Die zugehörige Halbwertszeit wurde zu

$$\mathrm{T}_{1/2}^{2\nu\mathrm{KK}} = 1.80^{+0.40(\mathrm{stat.})+0.07(\mathrm{sys.})}_{-0.39(\mathrm{stat.})-0.07(\mathrm{sys.})}\,10^{22}\,\mathrm{yr}$$

bestimmt. Dies stellt den langlebigsten Zerfall eines Isotops dar, der bisher direkt beobachtet wurde.

Contents

Chapter 1

Introduction

The Standard Model of particle physics is a well motivated and successful theoretical framework build within the last century. In modern physics various open questions beyond the explanation horizon of the model make an extension of it necessary [1]. One striking evidence for physics beyond is the elusive dark matter, which is accountable for $26.8\,\%$ of the universe's energy content [2]. Although there is overwhelming evidence for its existence (e.g. [3, 4]) and the strong hint towards its particle nature [5], no detection has been achieved up to today. The gathered knowledge has been implemented into the standard model of cosmology (ΛCDM). This model, which describes a large part of the evolution of the universe with only a few parameters, incorporates the cosmological constant Λ, referred to as dark energy, and assumes that dark matter consists of particles at non-relativistic velocities (cold). Among a variety of possible dark matter candidates, the major prospect in the spotlight of the current research activities are weakly interacting massive particles (WIMPs). Particles of this class are heavy ($\mathcal{O}(\geq \mathrm{GeV/c^2})$), thermally produced in the beginning of the universe and interact only on a scale comparable with the weak interaction with each other. Furthermore, any interaction via the electromagenetic or strong force is heavily suppressed with WIMPs involved. Candidates belonging to this class arise from different theories, but are often motivated by supersymmetric theories (SUSY) [6]. For about three decades the search for these particles is ongoing with direct searches using earthbound detectors [7] or accelerators [8] as well as indirect searches looking for signatures from dark matter annihilation in the universe [9].
So far only exclusion limits on its cross section with baryonic matter could be established. The most stringent of those limits on the WIMP-nucleon interaction cross section are set by direct detection searches utilizing dual-phase liquid xenon time projections chambers (TPCs) [7]. Commonly, this experimental results rely heavily on various assumptions regarding the astrophysical inputs but also on assumptions on the underlying nuclear physics. In the light of lacking direct evidence of dark matter more and more of the assumptions of its search are scrutinized in order to extend the view on detection possibilities. This does not only address the astrophysical

assumptions but also concerns the underlying interaction mechanism between dark and baryonic matter [10, 11, 12].
Besides implications from non-standard particles, also constituents of the Standard Model of particle physics give rise to open quests. Here, the neutrinos play a major role, as they have been observed oscillating [13, 14], and thus, possess mass in contrary to the prediction in the Standard Model. The mass scale of the neutrinos, but also the mystery behind the particle-anti-particle asymmetry would be addressed, if a hypothetical neutrinoless double beta decay would be observed [15]. Therefore, experimental efforts are increasing with various isotopes being tested for this process [16] since an unambiguous positive result would reveal a Majorana nature of the neutrino [17]. Furthermore, it would be the first lepton number violating process observed, providing a link for Leptogenesis models, which target to explain the mentioned asymmetry between matter and anti-matter [18, 19].
Finally, there are also still observations to be made predicted by the Standard Model. One of these, is the double electron capture process with the emission of two neutrinos [20]. This decay has been only observed so far indirectly by geochemical experiments [21] and indicatively in $^{78}\mathrm{Kr}$ [22, 23]. A variety of theoretical predictions exists for the half-life of this decay and they differ depending on the chosen many-body method used to calculate the nuclear matrix elements [24, 25, 26, 27]. These large uncertainties are present since decades and need experimental input in order to resolved. This is the case for the two-neutrino emission modes of any double beta decay but especially the hypothetical neutrinoless emission branches suffer from unambiguous predictions [28]. An experimental observation of the decay mode would improve the situation to solve the contradictory predictions and give rise to comparison possibilities among different many-body theories.
The aim of this thesis is to shed light on these open tasks within the Standard Model and beyond. After introducing the theoretical considerations for the detector technology of dual-phase time projection chambers and the signal generation in xenon, a lead-in to direct dark matter search as well as two-neutrino double electron capture will be given. In the second chapter the XENON100 and XENON1T direct dark matter detectors will be described. The results on the WIMP-nucleon cross section for a one tonne$\times$year exposure of the latter will be presented in the third chapter. There, special emphasize will be set to non-standard nuclear interaction mechanisms. Further results on a particular unexplored coupling between WIMPs and the exchange pions within the xenon nucleus will be derived for the first time. Chapter 4 is dedicated to the two-neutrino double electron capture search with XENON100 and XENON1T. Afterwards, the final chapter will give a summary of the results as well as an outlook for further work.

1.1 The dual-phase time projection chamber (TPC)

The technology of time projection chambers (TPC) dates back to the 1970s and was introduced by D.R. Nygren [29]. Early adoptions already included liquid noble gases as sensitive target volumes and highlighted the advantages of this type of material [30]. Nowadays liquid noble gas TPCs are widely used within particle physics [31]; especially in the rare event searches at low energies, e.g. in the field of direct dark matter detection [7] and the search for neutrino-less double β-decays [32], liquid noble gas TPCs filled with xenon are a cutting-edge technology. The detector principle with a focus on in its special realization of a dual-phase TPC will be explained in this section with the spotlight on xenon as a detector medium in the follow-up section. Thereafter, two different applications will be presented: The search for direct interactions of dark matter particles and the search for rare double β-decays of the isotope $^{124}\mathrm{Xe}$.
Although there are different types of liquid noble gas TPCs, the basic principle is shared among them. A particle interaction within the liquid medium generates a two-fold signal simultaneously: prompt scintillation photons from excited dimer relaxation and free electrons from ionization. The first signal (often referred to as $S1$) can be detected with photo-sensitive detectors at the detector edges, as noble gases are transparent for their own scintillation light. The second signal ($S2$) requires the application of an external electric field. This way the electrons, which would otherwise recombine with the ions and contribute further to the scintillation signal, are guided away from interaction site towards the detector edges. There they are either registered directly via wire electrodes or amplified in order to enhance the signal. If the drift path of the electrons is known, e.g. through field simulations, the position in the detector can be determined from the charge signal. If the drift velocity v_d of the electrons is known, additional positional information can be obtained from the time difference between the $S1$ and the $S2$ signal.
The direct measurement of the ionization channel requires a certain amount of charge carrier and thus, has an energy threshold. This makes it more suitable for applications with larger signals, e.g the search for neutrino-less double β-decay ($\sim\mathrm{MeV}$). For smaller energy depositions of a few keV, as required at the search of direct dark matter interactions section 1.3, a modification of the liquid noble gas TPC is necessary. In addition to the liquid detector medium, a gaseous layer is maintained on top, making it a dual-phase TPC. Here, the electrons are removed from interaction site by an external electric field as well, but this time drifted towards the liquid-gas interface. In the gas phase they are accelerated by a second stronger electric field, leading to photons produced via proportional scintillation (electroluminescence). These photons are registered by the same photo-detectors as the scintillation signal. This method allows for the detection of photons produced by a single electron and effectively reduces the energy threshold. The principle is illustrated in fig. 1.1.

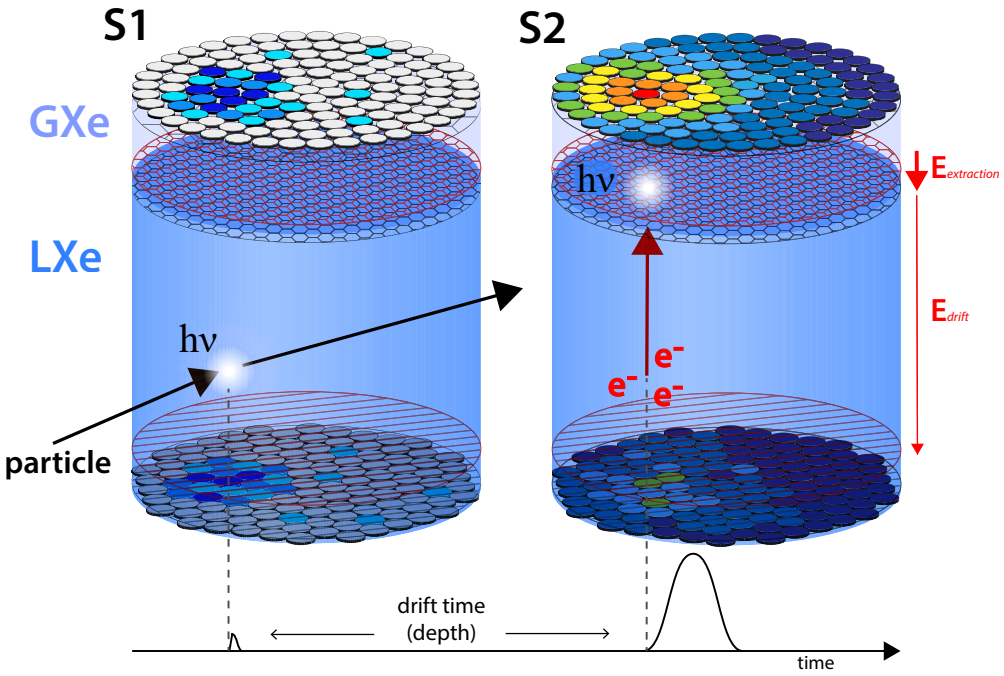

Figure 1.1.: Working principle of a dual-phase TPC. An energy deposition within the liquid volume generates scintillation photons (left) and charge carriers (right) at the same time. The scintillation photons are detected at the top and the bottom of the TPC by arrays of photomultiplier tubes (PMTs). As this happens right after the interaction it acts as a start signal. The electrons of the ionization process are drifted by an external drift field E_{drift} ($\mathcal{O}(100\,\text{V}\,\text{cm}^{-1})$) towards the top of the TPC. There, another electric field is applied, which is called the extraction field $E_{\text{extraction}}$. This stronger field ($\mathcal{O}(\text{kV}\,\text{cm}^{-1})$) accelerates the electrons within the gas phase, leading to proportional scintillation. Since this signal is localized beneath the upper PMT array, the amount of photons in each PMT (indicated by color code) points towards the interaction point in the x,y-plane. Additionally, the ionization signal acts as the stop signal and the time difference between both signals is used to derive the z-position for a given drift velocity v_d of the electrons ($\mathcal{O}(\text{mm}\,\mu\text{s}^{-1})$).

1.1.1 Particle identification

Liquid noble gas time projection chambers offer the possibility of particle identification. This is an important feature in order to discriminate background from signal interactions. Lighter particles, namely γ and β-particles, interact mainly with the electrons of the atomic shell (electronic recoils, ER), while heavier particles, as neutrons or WIMPs, interact directly with the nucleus (nuclear recoils, NR). The distinction of these two processes is achieved in two ways. Firstly, by investigation of the $S1$ signal and its pulse shape. Since the scintillation signal can be produced either by a short-lived singlet state or by a long-lived triplet state, its width is correlated to the contribution of each state to the total signal. This fraction points back to the aforementioned type of interaction. In experiments using the lighter noble gases,

e.g., argon, this is already used successfully to discriminate ER from NR with a discrimination power larger than 10^6 [33, 34]. For xenon this becomes more difficult since the relaxation time difference between the two states is reduced from a few orders of magnitude to only a few ns [35]. Nonetheless, especially in single-phase TPCs this approach is tested and pursued [36].
A second way of particle identification is achieved by comparing the ratio of the $S1$ to the $S2$ signal. This is owed to the fact that the underlying microscopic processes to create charge and light carrier (see section 1.2) differ between incident particles. This in turn, causes changes in the recombination fraction [37, 38]. For NR a smaller $S2$ size is expected for a given $S1$ signal as for ER. This is illustrated in fig. 1.2, where calibration sources inducing NR and ER in liquid xenon are used to investigate the discrimination space with a discrimination power of 10^3 [39].

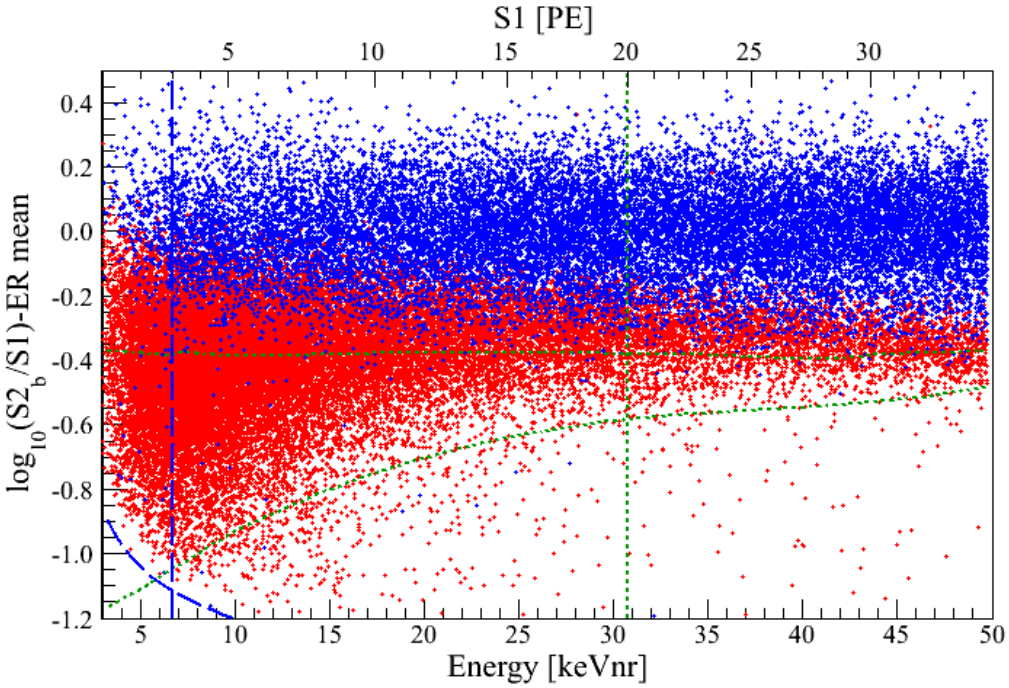

Figure 1.2.: Exemplary particle discrimination in a xenon dual-phase TPC. Nuclear recoils (red) and electronic recoils (blue) produced by calibration sources in XENON100 (see section 2.1) are indicated. The energy dependent separation parameter is the ratio of $S2$-over-$S1$. A separation of the two populations is visible. Figure from the XENON100 collaboration.

1.1.2 Signal corrections

Each dual-phase TPC's characteristic properties have to be taken into account in order to reconstruct the physical attributes of an initial particle interaction. Therefore several corrections have to be applied. A first correction arises from the geometrical dependence of the light collection, which leads to inhomogeneous illumination within

the cylindrical detector. This is not easily avoidable as the demand of a homogeneous electric field makes it impractical to mount photo sensors on the walls. This way any photon reaching the wall has to be reflected at least once in order to be detected by the photo sensors at the top or the bottom of the TPC. Although, usually a material with a reflectivity >$90\,\%$ [40] for the vacuum ultra violet (VUV)-photons ($\lambda \sim \mathcal{O}(100\,\mathrm{nm})$) is used, absorption losses occur, enhanced for multiple reflections. An additional influence on the light propagation is given by the total reflection at the interface between the liquid and gas. This is a pronounced effect for xenon due to its higher refractive index $n = 1.69$ in comparison to argon ($n = 1.45$) [41]. These geometric

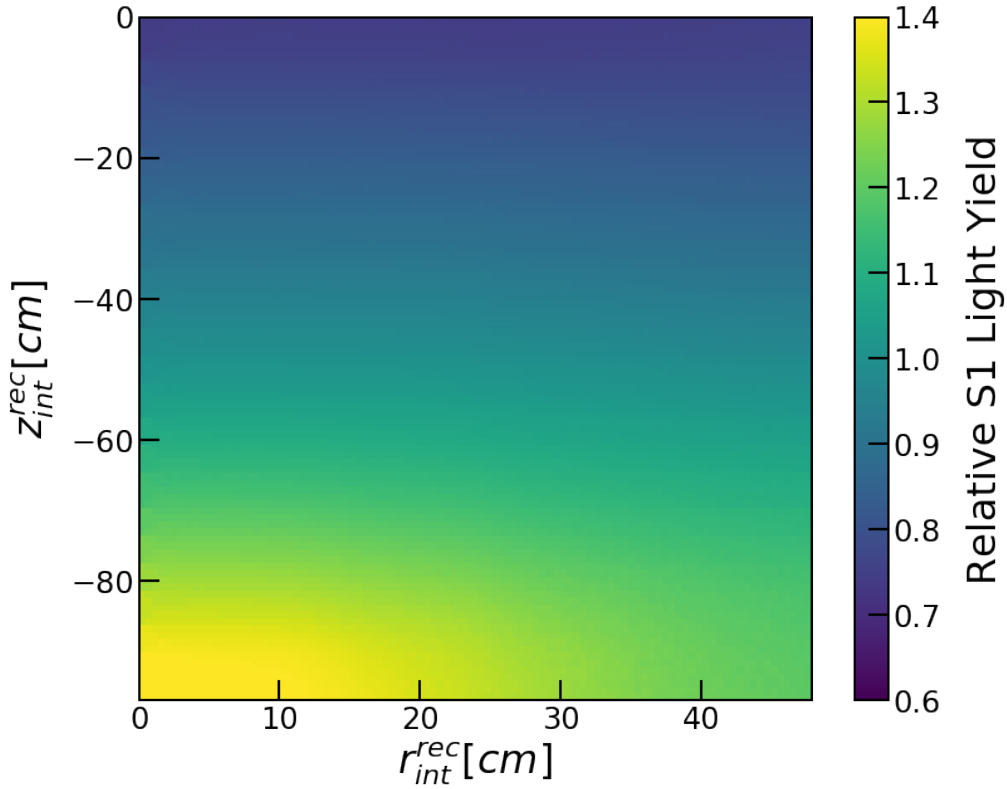

Figure 1.3.: Light collection efficiency (LCE) map for the $S1$ signal. Shown is the relative light yield normalized to the average as a function of the corrected position (see fig. 1.5). Depending on their position, $S1$s are corrected multiplicatively. This accounts for the effective solid angle of $S1$ light subtended by PMTs (including reflections), attenuation of light within the detector medium, and the PMT efficiencies themselves. The map was generated using the uniform source ^{83m}Kr. The LCE map is taken from XENON1T dual-phase TPC (see chapter 2). This figure was provided by Ted Berger.

considerations can be accounted for with a dedicated Monte Carlo (MC) simulation. As a few properties are not known to the desired precision (e.g., reflectivity of each material), the so called light collection efficiency (LCE) maps are derived from data of the operating detector and then compared to the MC simulation. An example for an entire detector mapping is shown for a dual-phase xenon TPC in fig. 1.3. The data for

the this is acquired by a uniform light source within the detector. This correction map affects predominately the $S1$ signal, which can originate from any point in the TPC. For the $S2$ signals they play a minor role due to their localized generation at the top. However, other effects lead to the need of correction maps for $S2$ signals as well. The main driver behind this, besides geometrical effects at the very edges of the TPC, are blind spots due to inactive photo sensors. This is of importance for the size correction as well as an input for the position reconstruction algorithms.
An example for corrections on signal registered at the top and the bottom array is shown in fig. 1.4. When comparing the two arrays in terms of uniformity, the proximity of the $S2$ signal to the top array is reflected. Here a non-functional photo sensor has an increased influence.

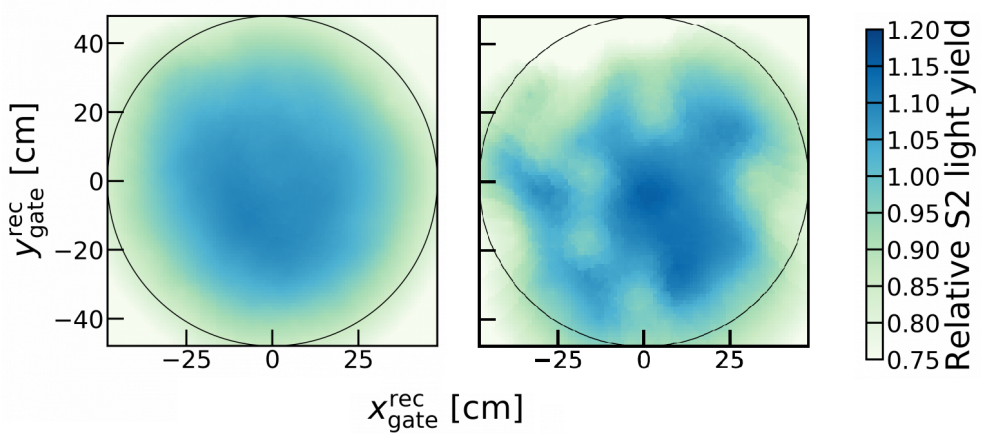

Figure 1.4.: Efficiency correction maps for the $S2$-signal. Exemplary maps from the XENON1T experiment (see chapter 2) for the light collection of the $S2$ signals: bottom PMT array (left) and top PMT array (right). This multiplicative correction is applied to all $S2$s based on their observed position (without field correction), since it is the true position of the $S2$ in the gaseous phase. The radial dependence is mainly caused by warping of the anode and cathode. Additionally, blind spots due to to turned off PMTS induce the pattern in the top map. The data for the correction was obtained using the uniform radioactive source ^{83m}Kr. This figure is based on Adam Brown´s work.

Although xenon is transparent to its own scintillation light and also has no electron affinity, both signals still suffer from absorption by impurities within the xenon. For the $S1$ signal water absorbs the VUV photons mainly. If effective continuous purification techniques are used, the mean free path of these photons becomes much larger than the effective path traveled within the detector. Impurities which attach the electrons, namely highly electronegative materials such as oxygen, have a strong impact on the size of the charge signal, despite of purification efforts. The so called electron lifetime τ_{e} represents the mean time until a free electron is attached within the detector. If a uniform distribution of electronegative impurities is assumed, the survival fraction of electrons N_e as a function of the initial interaction depth z is represented by

$$N_e(z) = N_0 \cdot e^{\frac{-z}{v_d \tau_e}}, \tag{1.1}$$

with an electric field dependent drift velocity v_d and an initial created amount of electrons N_0. The charge loss can be corrected using a monoenergetic source with a uniformly distributed N_0. Then τ_e is determined and eq. (1.1) all signals are corrected such that $N_e = N_0$ for all depths z. In the simplest approximation the drift path is assumed to be straight towards the gas-phase. However, this is not guaranteed for any electric field configuration. In fact the use of homogeneously distributed radioactive sources in the detector as well as detailed electric field simulations often reveal that the electric field lines deviate from straight lines the closer the interaction occurs towards the wall. This leads to longer drift paths for electrons as well as falsely reconstructed interaction positions in the (x,y)-plane of the detector, when not taken into account. As the effects causing this field distortion are often unforeseen, sometimes unpredictable and also time-dependent, they are corrected using data from aforementioned homogeneous radioactive calibration sources (e.g., ^{83m}Kr) as illustrated in fig. 1.5. The most common way of detecting the created photons in a

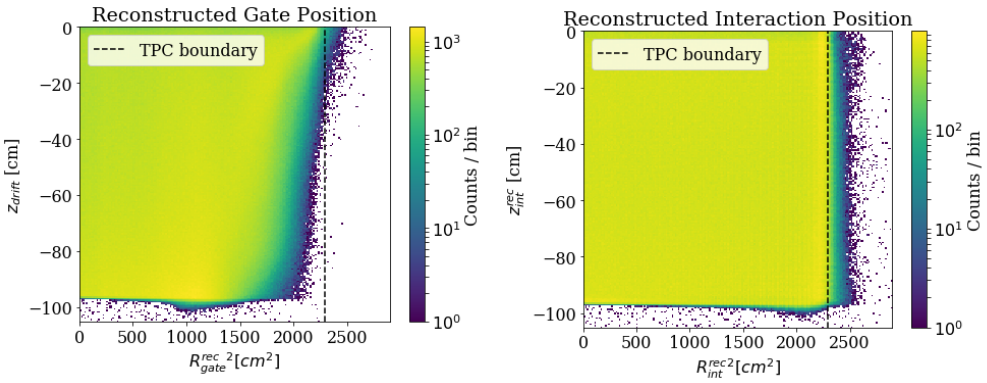

Figure 1.5.: Adjustment of the reconstructed position due to non-homogenous field lines. Left: Exemplary reconstructed event distribution (^{83m}Kr) in the XENON1T detector (see chapter 2). Due to a non-homogeneous field the shape of the detector is not reconstructed properly. Especially at high radii and low depths no events are reconstructed. As this is the position with the assumption of straight move of trajectories electrons this is called the reconstructed gate position. Right: Using the uniform source a three-dimensional correction from the reconstructed gate position to the true interaction position can be performed. Data and figure provided by Jinqiang Ye [42].

dual-phase TPC is the use of photomultiplier tubes (PMTs). These units utilize the photo effect to transform incident photons to electrons. The probability of creating such a photo electron (PE) per incident photon is called quantum efficiency (QE) and is depending on the wavelength of the respective photons. Once a photo electron is produced it is accelerated by an electric field towards a first amplification stage, a so-called dynode. The fraction of electrons reaching this stage is described by the collection efficiency (CE). At the first dynode a single photo electron produces multiple secondary electrons, which are further accelerated towards subsequent dynodes, increasing the number of electrons exponentially. The total amount of electrons produced per initially created photo electron is referred to as the gain

σ_g and determines the measurable signal. These gains are evaluated for each PMT using a light source with a well-defined output. This way, a measured current can be transformed back into the initial amount of photo electrons, and thus, photons. Details on PMTs can be found in [43] and the exact procedure of gain calibration is shown in [44].
Once all these corrections are applied, the signals are referred to as $cS1$ and $cS2$ and are usually measured in units of photo electrons (PE). Using these corrected values, a reconstruction of the nature of the initial energy deposition is possible, making dual-phase TPCs to a powerful tool searching for so far undetected interactions.

1.2 Signal generation in xenon

Xenon is advantageous as a detector material from a practical point of view since it offers the scintillation light with the largest wavelength ($\lambda = 178\,\mathrm{nm}$) among the usable noble gases, removing the need of a wavelength-shift before detection. Additionally, its boiling point at ambient pressure ($T_b = 165.05\,\mathrm{K}$) is the highest in comparison with the other considerable noble gases. From the detector physics point of view it has a high self-shielding capability for penetrating radiation, due to its atomic number ($Z = 54$) and its high density ($\rho_{LXe} \sim 3\,\mathrm{g\,cm^{-3}}$). Moreover, xenon provides the highest yield for scintillation and ionization of all noble gases, which is important for pushing energy thresholds to lower limits. This section focuses on the generation of the signal carriers in liquid xenon and the reconstruction of the initially deposited energy.
For a valid reconstruction of a given energy deposition in the detector, the micro-physical processes of signal generation in xenon have to be understood. Any energy deposition starts the production of excited xenon atoms[1] n_{ex} contributing to the $S1$-signal [45]:

$$\begin{aligned} \mathrm{Xe}^{*} + \mathrm{Xe} + \mathrm{Xe} &\rightarrow \mathrm{Xe}_2^{*} + \mathrm{Xe} \\ \mathrm{Xe}_2^{*} &\rightarrow 2\mathrm{Xe} + h\nu \end{aligned} \tag{1.2}$$

and the creation of xenon ion-electron pairs n_{i}:

$$\begin{aligned} \mathrm{Xe}^{+} + \mathrm{Xe} &\rightarrow \mathrm{Xe}_2^{+} \\ \mathrm{Xe}_2^{+} + \mathrm{e}^{-} &\rightarrow \mathrm{Xe}^{**} + \mathrm{Xe} \\ \mathrm{Xe}^{**} &\rightarrow \mathrm{Xe}^{*} + \mathrm{heat} \\ \mathrm{Xe}^{*} + \mathrm{Xe} + \mathrm{Xe} &\rightarrow \mathrm{Xe}_2^{*} + \mathrm{Xe} \\ \mathrm{Xe}_2^{*} &\rightarrow 2\mathrm{Xe} + h\nu. \end{aligned} \tag{1.3}$$

A third part of the energy is deposited in the form of atomic motion (heat), but as it is experimentally not easily accessible, it only reduces the amount of measurable signal carrier (so-called quenching). Consequently, an initial energy deposition distributed between the two processes of interest can be described by:

$$E_R = f \cdot W \cdot (n_{\mathrm{ex}} + n_{\mathrm{i}}), \tag{1.4}$$

where f is a quenching factor depending on the type of interaction and W is the average energy necessary to produce a single excited or ionized xenon atom. It is effectively found to be $(13.7 \pm 0.2)\,\mathrm{eV}$ per quantum[2] [46, 47]. The initially created quanta can be translated to the total number of signal carriers for the scintillation signal n_γ and the ionization signal n_{e} by:

[1] Sometimes in literature the term *excitons* is used for the excited xenon atoms
[2] Although, the value is different whether an ion or an exciton is produced, the effective value is close enough to describe both.

$$n_\gamma = n_{\mathrm{ex}} + r \cdot n_{\mathrm{i}} \tag{1.5}$$
$$n_{\mathrm{e}} = (1 - r) \cdot n_{\mathrm{i}}, \tag{1.6}$$

where r is the fraction of electrons recombining with ions. If no electric field is applied, the electrons recombine with the surrounding ions and enhance the $S1$ signal[3]. But, if an external field is applied, the electrons are removed from interaction site and can form the $S2$ signal. This recombination fraction contains information on the physical properties. Firstly, it is directly a function of the field strength as shown in fig. 1.6. An increase in the electric field strength translates to a rise in charge yield and a decrease in light yield. This anti-correlation itself, as seen in eq. (1.5), is an important feature for the energy reconstruction and is used for an enhanced energy resolution compared to the individual signal channels (see section 1.2.1). Furthermore, the

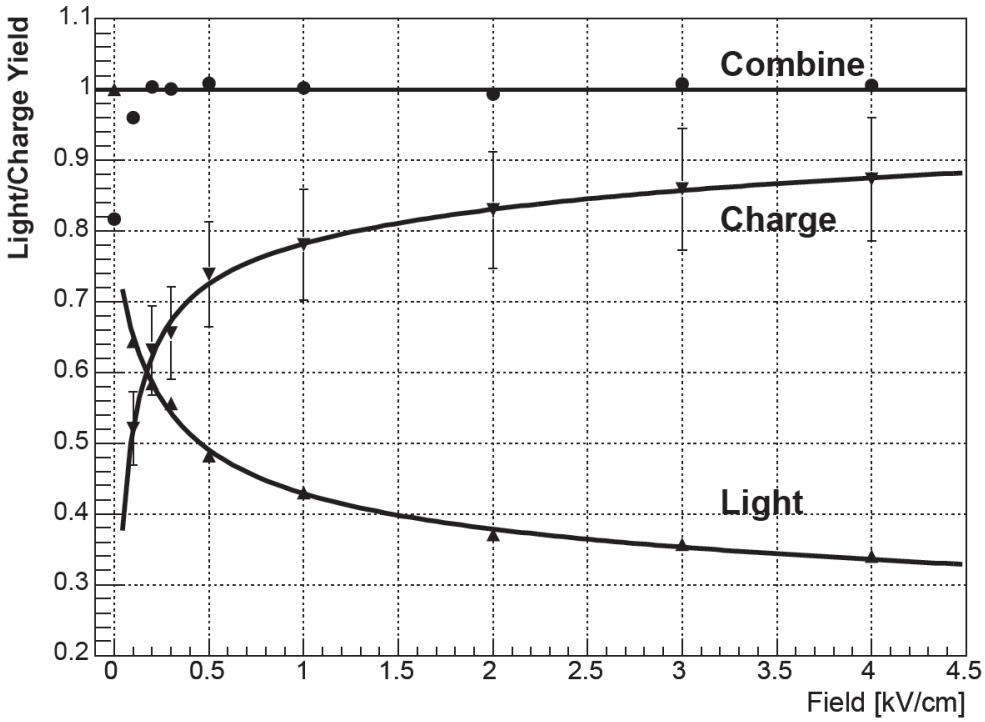

Figure 1.6.: Charge and light yields as a function of the electric drift field strength. A $662\,\mathrm{keV}$ γ-ray source has been used to investigate the signal yield in the two different channels. Figure taken from [48].

recombination probability depends on the density and total number of ions as well as on the track length of the energy depositions [37, 38]. These parameters are a function of the recoil energy and the type of interaction. Another process coupled directly to the track density is the reduction of the scintillation signal via biexcitonic quenching.

[3] This is not a complete process for low energy transfers, as even without field application a fraction of electrons can escape from the interaction site [45].

This occurs, if a collision of two excited xenon atoms produces an electron-ion-pair and a xenon atom in the ground state. Even if the electron and the ion recombine, only one photon results from two excitations [49, 50].
As mentioned in the previous section the possible types of interaction are a direct interaction with the nucleus (NR) or an interaction with the electrons from the atomic shell (ER).

1.2.1 Electronic recoils (ER)

ER produce a fixed ratio of $\frac{n_{\mathrm{ex}}}{n_{\mathrm{i}}} \sim 0.20$, which explains its relatively larger $S2$ signal in comparison to NR. In addition, ER have a relatively long track within the liquid xenon (e.g. $0.1\,\mathrm{mm}$ at $100\,\mathrm{keV}$). The reduction of the ion density along the track allows for easier extraction of electrons before recombination.
Due to the negligible mass of a single shell electron in comparison with the xenon nucleus, the fraction of energy lost in elastic collisions can be neglected. This allows to set the quenching factor f in eq. (1.4) to 1, and thus skip it for further considerations. Then eq. (1.4) can be rewritten in terms of the measurable quanta n_γ and n_e to

$$E_R = W \cdot (n_\gamma + n_e). \tag{1.7}$$

Energy reconstruction

As described in section 1.1 these quanta are not directly transformed into measured signals $cS1$ and $cS2$ due to detector effects. For the translation of n_e and n_γ into ($cS1$,$cS2$)-signals measured in photo electrons (PE) one can transform eq. (1.7) using the detector specific constants $g_1 = \frac{cS1}{n_\gamma}$ for the scintillation signal and $g_2 = \frac{cS2}{n_e}$ for the ionization signal. While g_1 incorporates the photon detection efficiency after spatial corrections, g_2 includes mainly the gas amplification of a single electron as well as the extraction efficiency of the electrons reaching the gas phase. The energy reconstruction can then be rewritten as:

$$E_R = W \cdot \left(\frac{cS1}{g1} + \frac{cS2b}{g2}\right). \tag{1.8}$$

While W is known from external measurements, g_1 and g_2 have to be determined from calibration data for the specific detector.
The straightforward way to obtain these for ER is the usage of several calibration sources with known energy, preferably deposited in a single interaction [44]. The sources are either introduced artificially or the radioactive background contaminations from the detector materials can be used. In xenon dual-phase TPCs calibration points from $5.2\,\mathrm{keV}$ [51] to $2615\,\mathrm{keV}$ [52] have been used for this purpose. If both signal channels ($cS1$ and $cS2$) are used for energy reconstruction it will be referred to as *combined energy scale* (CES) throughout this work.
An example for a mono-energetic line at $80.2\,\mathrm{keV}$ from an inelastic scattering of

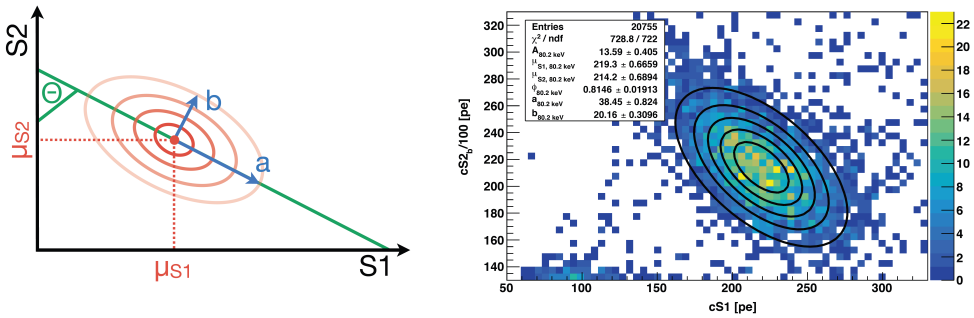

Figure 1.7.: Exemplary illustration of the two-dimensional elliptical Gaussian fits to a mono-energetic calibration source. Left: Scheme of the tilted ellipse with an indicated anti-correlation angle θ. The long axis is denoted by a while the short axis is denoted by b. Means for both signals are given as well. Fading intensity of the elliptical lines denotes a decrease in the amplitude. Right: Application to a inelastic γ after neutron scattering ($80.2\,\mathrm{keV}$). The contours denote the significance and the means are extracted by the fit. Notably, the y-axis is divided by 100 in order to support the fitting routine. Figures adapted from [53].

neutrons with $^{131}\mathrm{Xe}$ is shown in fig. 1.7 in the ($cS1$,$cS2b$)-space. One clearly sees the elliptical shape of the signals, which proofs a correlation, and its tilt, which exploits the degree of anti-correlation. The full description is given by a two-dimensional elliptic Gaussian of the form and is illustrated in fig. 1.7:

$$f = A \cdot e^{\frac{-((x-\mu_x)\cdot cos\theta-(y-\mu_y)\cdot sin\theta)^2}{2a^2}-\frac{((x-\mu_x)\cdot sin\theta+(y-\mu_y)\cdot cos\theta)^2}{2b^2}}. \tag{1.9}$$

A describes the amplitude in the center, μ_x,μ_y are the means on the respective axis, and θ the counter clockwise rotation angle representing the degree of anti-correlation. The two scaling constants of the major axis a and the minor axis b incorporate the fluctuations on the respective axis σ_x and σ_y. In principle a projection along the major axis would represent an energy calibration yielding the optimal resolution and would provide values for g_1 and g_2 [54], but due to the energy dependency of the anti-correlation, a different approach is pursued as suggested in [55]. Here, the mean signals[4] $\overline{cS1}$ and $\overline{cS2}$ are determined for more than one calibration source and analyzed together. The simple approach would be a projection on the respective signal axis ($cS1$ or $cS2$) for the signal of each calibration source. In this case the means $\overline{cS1}$ and $\overline{cS2}$ are given by a one-dimensional Gaussian fit. However, the use of (μ_x,μ_y) from the two-dimensional fit function (eq. (1.9)) increases the precision as it explores the anti-correlation. Figure 1.8 shows the relation of the two signal channels for different sources. By rearranging eq. (1.8) to

$$\frac{\overline{cS2}}{E} = \frac{g_2}{W} - \frac{g_1}{g_2}\frac{\overline{cS1}}{E} \tag{1.10}$$

[4] Often only the bottom part of the $cS2$ signal is used in order to avoid influence by saturation of the closest PMTs in the top array and is then denoted as $cS2b$.

the linear dependency between the two signal channels and the deposited energy can be explored by a fit to the data points from different calibration sources. This directly provides values for g_1 and g_2 (see fit function in fig. 1.8).

Any energy deposited by an ER in a detector will follow this linear description since

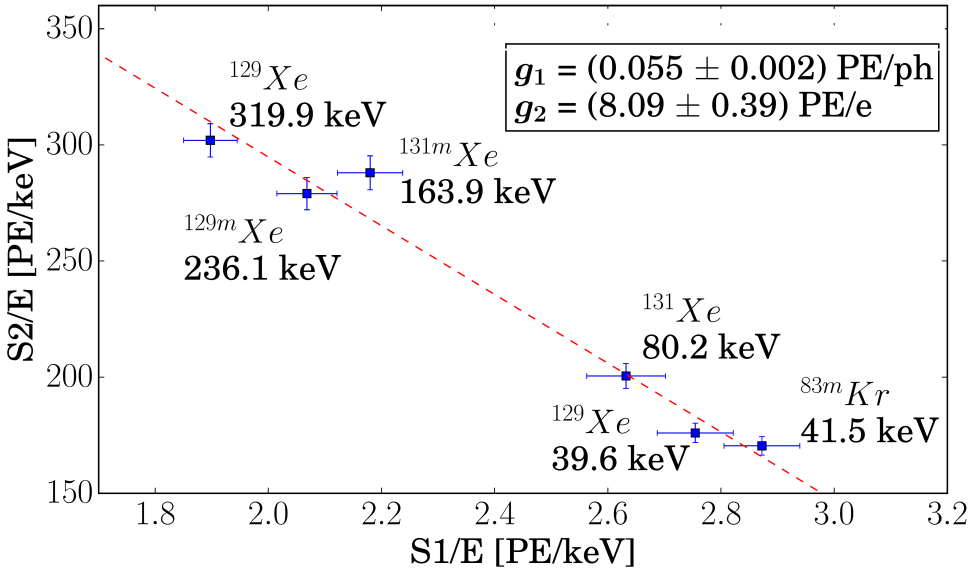

Figure 1.8.: Exemplary energy dependence of light and charge yield in a combined analysis. Light and charge yield are shown as function of deposited energy. Markers denote the mean charge and light yield from measurements of mono-energetic peaks. The red dashed line is a fit function of the form described in eq. (1.10) and can be used to reconstruct the energy for any given pair of $cS1$ and $cS2$ in an ER. The linear alignment of ER along this line indicates that the sum of charge yield and light yield is constant per unit energy. This plot is sometimes referred to as *Doke plot*. Taken from the tritium analysis run of XENON100 [56].

the sum of charge and light yield is always constant [44, 48]. Nevertheless, while it can be used to reconstruct the deposited energy, it can not be used to predict the light and charge yield separately of a specific source, since energy depositions within a dual-phase can be a multi-step process of unresolved single interactions. Thus, a total measured energy deposition could be a superposition of smaller energy depositions, including the charge and light yield at their respective energies. The energy reconstructed from ER is often denoted as keV_{ee}.

Energy resolution

The energy resolution R_E of a dual-phase xenon TPC is commonly referred to as

$$R_E[\%] = \frac{\sigma_E}{E} \cdot 100, \tag{1.11}$$

where σ_E is the standard deviation of a mono-energetic Gaussian line with the mean energy E. It depends on the intrinsic fluctuations of the ionization and scintillation processes, the gain variations of the PMTs as well as on the fluctuations in the number of detected photo electrons N_{pe} per produced signal quantum (n_γ,n_e). The influence of the latter decreases with the increasing amount of signal carriers, which leads to an improved resolution with increasing energy. As shown by [54] the fluctuations of the intrinsic processes are anti-correlated, and thus, the above mentioned combined energy scale (CES) improves the energy resolution significantly. The comparison of the single channels and their combination is shown in fig. 1.9. The energy dependence can be described by two constants a and b with the empirical formula:

$$R_E = \frac{a}{\sqrt{E}} + b. \tag{1.12}$$

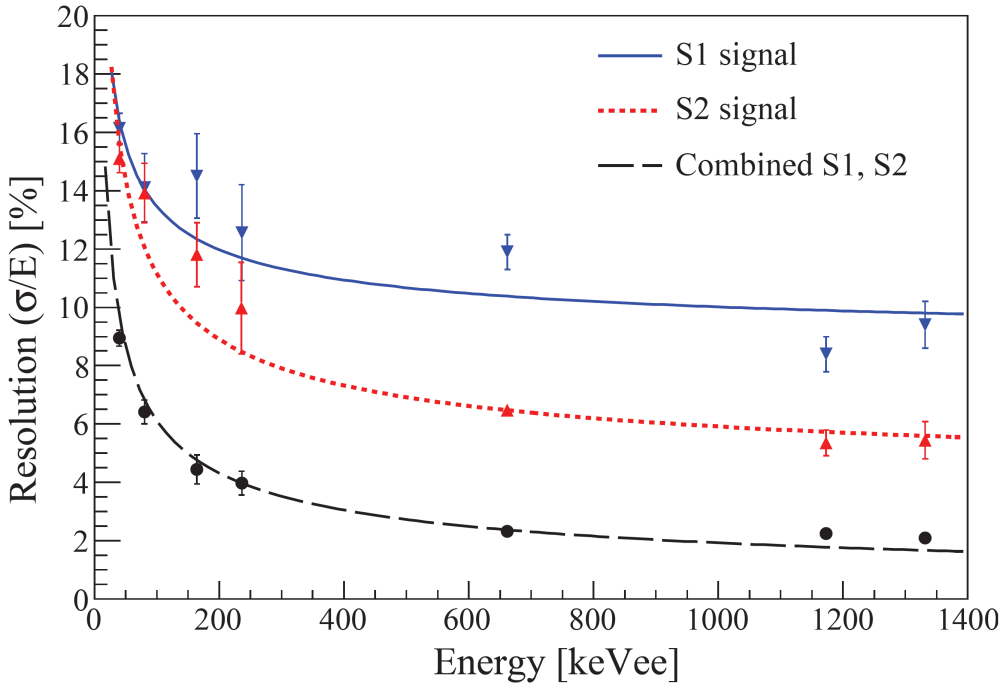

Figure 1.9.: Energy resolution in XENON100 using the single channels and their combination. The resolution is given as a function of energy using several ER calibration sources. The scintillation channel alone shows the worst resolution (blue), followed-up by the ionization signal (red). A combination of both provides the best result at any given energy (black). Figure from XENON100 [57].

1.2.2 Nuclear recoils (NR)

Since the track of an NR is short (e.g. $\sim 10^{-7}\,\mathrm{m}$ at $100\,\mathrm{keV}$), the ion density along the track is high. Therefore, recombination can take place rapidly and diminishes the ionization signal while enhancing the scintillation signal. Furthermore, the loss of energy to atomic motion from elastic scattering is not negligible. For this reason a so called quenching is present, which decreases the factor f in eq. (1.4) to a value smaller than 1.

Energy reconstruction

Due to the lack of experimentally accessible mono-energetic neutron sources, and the large angular dependence on energy transfer, the method used for ER is not applicable. The energy translation from $cS1$ to deposited energy E_{nr} for NR can be estimated using the scintillation channel and ER calibration data in the following way [58]:

$$E_{\mathrm{nr}} = \frac{cS1}{L_y} \frac{1}{L_{\mathrm{eff}}(E_{\mathrm{nr}})} \frac{S_{\mathrm{ee}}}{S_{\mathrm{nr}}}, \tag{1.13}$$

where L_y is the measured average light yield of the specific detector for a γ-particle at $122\,\mathrm{keV}$. In order to account for the quenching in NR compared to ER the L_{eff} parameter is used. It describes the energy-dependent relative scintillation efficiency of an NR compared to a γ of $122\,\mathrm{keV}$ at zero field strength and is based on several dedicated measurements (see [58] and references within). The ratio $\frac{S_{\mathrm{ee}}}{S_{\mathrm{nr}}}$ represents the different quenching of scintillation light for NR (S_{nr}) and for ER (S_{ee}) at given electric field. For the charge yield a similar description is possible. The reconstructed energy can be described as a function of the $cS2$ signal by:

$$E_{\mathrm{nr}} = \frac{cS2}{Y} \frac{1}{\mathcal{Q}_y(E_{\mathrm{nr}})}. \tag{1.14}$$

Here $\mathcal{Q}_y$ describes the charge yield parameterization for a given energy and electric field. Different dedicated measurements have been pursued to determine this parameter [58]. In addition to this Y is the secondary electron yield, which describes the amplification of a single electron. The two parameter L_{eff} and $\mathcal{Q}_y$ are shown as a function of energy from various measurements in fig. 1.10 together with a model from the *Noble Element Simulation Technique* (NEST) framework fitted to the data [59]. Hereby, both channels have been used to constrain free fit parameters, which correspond to physical properties of LXe. More details on the framework are given in [60]. Any energy reconstructed for NR is denoted as $\mathrm{keV_{NR}}$.

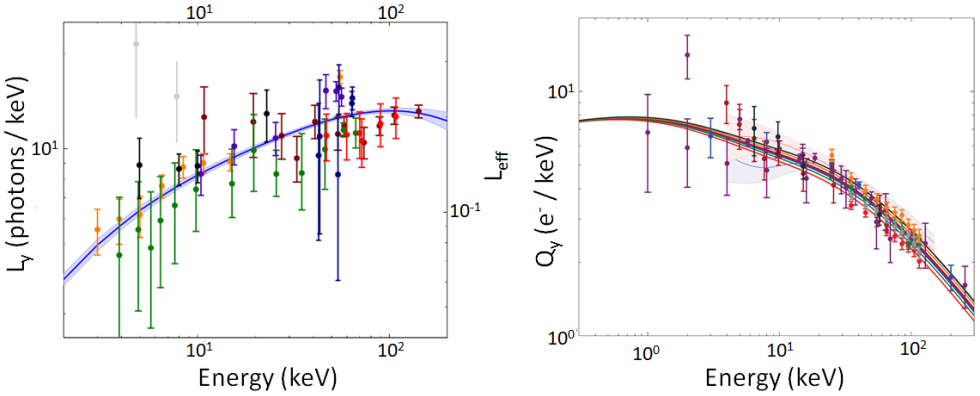

Figure 1.10.: Measurements for L_{eff} and $\mathcal{Q}_y$ fitted with a global model. Left: Light yield and L_{eff} as a function of energy from seven different measurements. The model fitted to the data points was also constrained by the ratio of the two signal channels. Right: Charge yield $\mathcal{Q}_y$ as measured by twelve different experiments. Both figures taken from [59].

1.3 Direct dark matter detection

The hypothesis that dark matter consists of **w**eakly **i**nteracting **m**assive **p**articles (WIMPs) opens up the possibility of its direct detection using earth-bound detectors. Any interpretation of experimental results from these detectors are based on specific assumptions which are shared among different experiments to ensure comparability. These assumptions are usually well motivated but have to be questioned as long as there is no actual detection. Within this section the derivation from the WIMP-hypothesis to the experimental signal is summarized with a focus on the standard nuclear physics assumptions about the underlying interaction of dark matter with baryonic matter.
The number of interactions per unit time $\frac{\mathrm{d}N}{\mathrm{d}t}$ can be derived from first principles as following:

$$\frac{\mathrm{d}N}{\mathrm{d}t} = N_T \mathbf{j} \sigma_{\chi N} \quad \text{with } \mathbf{j} = n_\chi \mathbf{v}. \tag{1.15}$$

Here N_T is the number of target nuclei. The cross section of the interaction $\sigma_{\chi N}$ is defined by the underlying particle and nuclear physics. The last term $\mathbf{j}$ represents the particle flux. It is composed of the incoming WIMP density n_χ, which is the ratio of the mass density ρ_0 and the WIMP mass m_χ, and of the velocities $\mathbf{v}$ of these WIMPs. This quantity is based on astrophysical observations and assumptions derived from these.

1.3.1 Velocity distribution and local density

A first crucial assumption has to be made on the local dark matter mass density ρ_0 at our position within the milky way. Commonly, a value of $0.3\,\mathrm{GeV\,cm^{-3}}$ is derived from direct measurements of the rotation curves in combination with N-body simulations as well as assuming a spherical halo density profile (with $\rho_0 \sim 1/r^2$) [61]. There are large uncertainties on the assumptions, which can alter the interpretation of a direct dark matter detection result [62]. If following the standard assumption of the halo model it implies a three-axial-symmetric Maxwell-Boltzmann velocity distribution $f_g(\mathbf{v})$ for the dark matter particles in the galactic rest frame. It can be described by:

$$f_g(\mathbf{v}) = k\left(\frac{1}{\sqrt{\pi} v_0}\right)^3 e^{-\left(\frac{v}{v_0}\right)^2}, \tag{1.16}$$

with

$$v_0 = \sqrt{\frac{2 k_B T}{m_\chi}} \tag{1.17}$$

being the most probable velocity, including the Boltzmann constant k_B, the temperature T and the dark matter particle mass m_χ. The velocity distribution has to be truncated since WIMPs with a sufficient velocity, the so-called escape velocity v_{esc}, overcome the gravitational bound and leave the gravitational potential of the galaxy.

This is approximated by a cut-off in eq. (1.16) leading to $f_g(\mathbf{v}) = 0$ if $v > v_{\text{esc}}$. The constant k in eq. (1.16) becomes then [63]:

$$k = \text{erf}\Big(\frac{v_{\text{esc}}}{v_0}\Big) - \frac{2}{\sqrt{\pi}}\frac{v_{\text{esc}}}{v_0}e^{-(\frac{\mathbf{v}}{v_0})^2}. \tag{1.18}$$

The escape velocity is taken as $544\,\text{km}\,\text{s}^{-1}$ and the most probably velocity is given as $220\,\text{km}\,\text{s}^{-1}$ [64].
For an earth-bound detector the velocity distribution has to be adjusted due to the relative movement within the galaxy. The earth moves along the sun with a velocity of v_E, which is at $232\,\text{km}\,\text{s}^{-1}$. Furthermore, Earth's orbital velocity around the sun ($\sim 30\,\text{km}\,\text{s}^{-1}$) has to be included as well. The time dependence of the velocity v_E is included by [6]

$$\mathbf{v}_E(t) = \mathbf{v}_E\Big[1.05 + 0.07\cos\Big(\frac{2\pi(t-t_p)}{1\text{yr}}\Big)\Big], \tag{1.19}$$

where t_p is the event rate peak due to the maximal net velocity and it is expected to be around the 2nd June each year. The final velocity distribution $f(\mathbf{v},t)$ in the local frame of reference has to account for all the relative movements (see [65] for a comparison). While more refined halo models and more recent measurements exist, the values for ρ_0, v_{esc}, v_0 and v_E are used as stated here as a consensus among experiments to ensure comparability (see [66] for a discussion on this and modern values).

1.3.2 Kinematics

The observable of a direct detection experiment is the energy E_R deposited within the detector, which is given in this non-relativistic scenario by the momentum transfered $|\mathbf{q}|$ and the target nucleus mass m_N:

$$E_R = \frac{|\mathbf{q}|^2}{2m_N}. \tag{1.20}$$

The momentum transfer

$$|\mathbf{q}|^2 = 2\mu_N^2 v^2(1 - cos\theta) \tag{1.21}$$

is a function of the WIMP velocity v, the scattering angle in the center-of-mass system θ and the reduced mass of the WIMP-nucleus system μ_N defined as:

$$\mu_N = \frac{m_\chi m_N}{(m_\chi + m_N)}, \tag{1.22}$$

where m_χ is the mass of the WIMP. If $\cos\theta$ is assumed to be homogeneously distributed between [-1,1], the energy transfered E_R from a WIMP of a given velocity is also homogeneously distributed between 0 and E_{max}. This is the maximum energy deposited ($\theta = 180°$) for a given WIMP mass and velocity, and is defined as:

$$E_{\text{max}} = \frac{2\mu_N^2 v^2}{m_N}. \tag{1.23}$$

1.3.3 Nuclear form factor

This is only valid if the interaction would be an isotropic hard-sphere scattering. This is not correctly describing the situation as soon as the momentum transfer is large enough that the de-Broglie wavelength is no longer large compared to the radius of the nucleus. For the actual description the nuclear physics have to be addressed by introducing the nuclear form[5] factor $\mathcal{F}$. It encodes the interaction mechanism between the WIMP and the underlying nuclear structure. In order to express the WIMP-nucleus cross section $\sigma_{\chi N}$ in dependence of the underlying nuclear physics, the differential cross section is written as [67]

$$\frac{\mathrm{d}\sigma_{\chi N}}{\mathrm{d}\mathbf{q}^2} = \frac{8G_F^2}{\mathbf{v}^2(2J+1)}[S_S(\mathbf{q}^2) + S_A(\mathbf{q}^2)], \tag{1.24}$$

where G_F expresses Fermi´s constant, J the spin of the target nucleus and S_S and S_A are structure factors for the scalar and axial-vector coupling and are defined as:

$$S_S(0) = \frac{2J+1}{4\pi}|c_0 A + c_1(Z-N)|^2 \tag{1.25}$$

$$S_A(0) = \frac{(2J+1)(J+1)}{4\pi J}|(a_0+a_1)\langle \mathbf{S_p}\rangle + (a_0-a_1)\langle \mathbf{S_n}\rangle|^2. \tag{1.26}$$

Here Z is the number of protons, N is the number of neutrons and $\langle \mathbf{S_{p,n}}\rangle$ are the respective spin expectation values for protons and neutrons. The coefficients a_i,c_i embody the information of the nucleon matrix elements and any coefficients describing the physics beyond the Standard Model. In the common approach only the part which is independent of the spin, referred to as spin-independent interaction, (SI), is investigated. Therefore, the spin-dependent (SD) component (S_A) is set to zero. In addition to this, c_1 is assumed to be zero as well, since only the purely isoscalar coupling is considered. As this leaves only the component which is proportional to A^2, the motivation of the simplification can be understood. This coherent enhancement makes it by far the dominating contribution. For the further evaluation eq. (1.24) is usually separated in a cross section at zero momentum transfer σ_0 and the nuclear physics incorporated into a nuclear form factor $\mathcal{F}_{SI}$

$$\frac{\mathrm{d}\sigma_{\chi N}}{\mathrm{d}\mathbf{q}^2} = \frac{\sigma_0}{4\mathbf{v}^2\mu_N^2}|\mathcal{F}_{SI}(q^2)|^2 \tag{1.27}$$

This is usually further transformed into a cross section normalized to the single nucleon in order to enable comparisons between experiments utilizing different target isotopes. Therefore

$$\sigma_0 = \sigma_{nn}\frac{\mu_N^2}{\mu_{nn}^2} \tag{1.28}$$

is inserted in eq. (1.27). Here σ_{nn} is the cross-section of the WIMP-nucleon interaction and μ_{nn} is the reduced mass between nucleon and WIMP. Notably, eq. (1.28) is usually

[5] Sometimes in the field the term nuclear structure factor is used interchangeably, see e.g. [11]

expressed in terms of A^2, representing the coherent enhancement. Throughout this work the factor is absorbed into the respective nuclear form factor following the notation in [11].
In the low-momentum regime the nuclear form factor $\mathcal{F}_{SI}$ represents approximately the Fourier transform of the spatial distribution of the scattering centers within the nucleus. In the standard WIMP scenario it can be assumed the same as the charge density distribution [63]. The form factor accounts for the coherence loss at increasing momentum transfers depending on the size of the nucleus. For the momentum transfer window of interest in dark matter experiments ($\mathcal{O} \sim 10\,\mathrm{MeV} - 100\,\mathrm{MeV}$) this is successfully approximated by using the so called Helm form factor $|\mathcal{F}_{SI}^{\mathrm{Helm}}|$, defined as:

$$|\mathcal{F}_{SI}^{\mathrm{Helm}}| = A\frac{3j_1(|\mathbf{q}|r_N)}{|\mathbf{q}|r_N}e^{\frac{(-\mathbf{q}s)^2}{2}}, \tag{1.29}$$

where j_1 is the first order spherical Bessel function and A is the total number of nucleons. The parameter r_N corresponds to the radius of the spheric nucleus and the parameter s is a measure of the skin thickness and they are given as [63]:

$$r_N^2 = c^2 + \frac{7}{3}\pi^2 a^2 - 5s^2 \tag{1.30}$$

$$s = 1\,\mathrm{fm} \tag{1.31}$$

$$c = (1.23A^{\frac{1}{3}} - 0.60)\mathrm{fm} \tag{1.32}$$

$$a = 0.52\,\mathrm{fm} \tag{1.33}$$

A first step beyond the standard assumptions is considering the SD component of eq. (1.24). Any experimental evaluation of this interaction channel, as performed by [68, 69], has to assume that the SI component is non-existing or heavily suppressed. Otherwise the SD standard interaction which is not coherently enhanced would only be detected after the SI interaction is detectable at large statistics. Recently, due to the absence of a detection of the standard isoscalar SI interaction, more attention has been devoted to disentangle the interaction modes and corrections in both channels [11]. One approach is to describe the corrections through effective field theories (EFT). First limits on the operators arising from non-relativistic EFT (NREFT) have been explored experimentally [70, 71] but in order to build a relation between the NREFT operators and the parameter space of a physics model, quantum chromodynamics (QCD) has to be included again [72]. This is pursued within the framework of chiral effective field theories (ChEFT), which in particular include the spontaneous symmetry breaking of chiral symmetry [73]. These give rise to various sub-dominant corrections of the isoscalar and also isovector SI interactions [11]. One particular novelty here is the inclusion of interactions not only with a single nucleon of the target nucleus, but with the pion exchanged between two nucleons. These are referred to as two-body interactions and the respective schematic diagram is shown in fig. 1.11.
Exploring this in terms of the differential cross section leads to a minimal extension

of eq. (1.24) [74]:

$$\frac{\mathrm{d}\sigma_{\chi N}}{\mathrm{d}q^2} = \frac{1}{4\pi v^2}\left|c_+^M \mathcal{F}_+^M(q^2) + c_-^M \mathcal{F}_-^M(q^2) + c_\pi \mathcal{F}_\pi(q^2)\right|^2. \tag{1.34}$$

In this notation the isoscalar form factor $\mathcal{F}_+^M(q^2)$ corresponds to $\mathcal{F}_{SI}(q^2)$ in eq. (1.24). Furthermore $\mathcal{F}_-^M(q^2)$ denotes the form factor of the isovector counter part. The additional term $\mathcal{F}_\pi$ is the underlying form factor of the scalar WIMP-Pion interaction. The coefficients $c_\pm^M$ and c_π are so called Wilson coefficients, which govern the included particle physics beyond the Standard Model (SM) and the nucleon matrix elements.

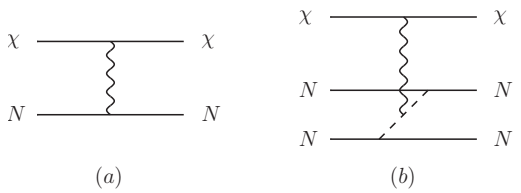

Figure 1.11.: Diagrams of the standard interaction and the two-body interaction. Solid lines refer to the WIMP (χ) and nucleon (N) fields, wavy lines to the mediating current, and the dashed line indicates the exchange of a virtual pion between two nucleons. Left: Leading iso-scalar WIMP coupling to one nucleon. Right: WIMP coupling to the exchange pions between two nucleons. Figure provided by the Co-Authors of [74].

A possible experimental detection of the pion channel involves the same assumption as for the SD case: The dominating interaction channel $c_\pm^M \approx 0$ has to be suppressed [11]. In this case the WIMP-pion interaction is promising compared to the SD case as it is also coherently enhanced and supposedly provides higher interaction rates (see section 3.3 and [74]).
The relative strength of this correction and the SI isovector coupling is shown in comparison with the isoscalar interaction $\mathcal{F}_+^M(q^2)$ in fig. 1.12. The full set of possible corrections up to third order in ChEFT can be found in [11]. A closer investigation on the two-body correction is pursued in section 3.3. Another important piece of information can be extracted from fig. 1.12 as well, namely the correlation between the interaction strength and the momentum transfer. While at low momentum transfers the standard interaction is dominating this is not always the case for larger momentum transfers. The possibility to discriminate the underlying nuclear form factors along their interaction strength at different momentum transfers is elaborated in section 3.2.

1.3.4 Differential recoil rate

Since the observable in a direct dark matter detector is the recoil energy E_R, the rate per unit energy $\frac{\mathrm{d}R}{\mathrm{d}E_R}$ is the input signal model one needs as a starting point to interpret a particular result from an experiment. The differential recoil energy is given as:

$$\frac{\mathrm{d}R}{\mathrm{d}E_R} = \frac{\rho_0 \sigma_0}{2 m_\chi \mu_N^2} |F(q^2)|^2 \int_{v_{\min}}^{v_{\mathrm{esc}}} \frac{f(\mathbf{v},t)}{v} \mathrm{d}^3 v. \tag{1.35}$$

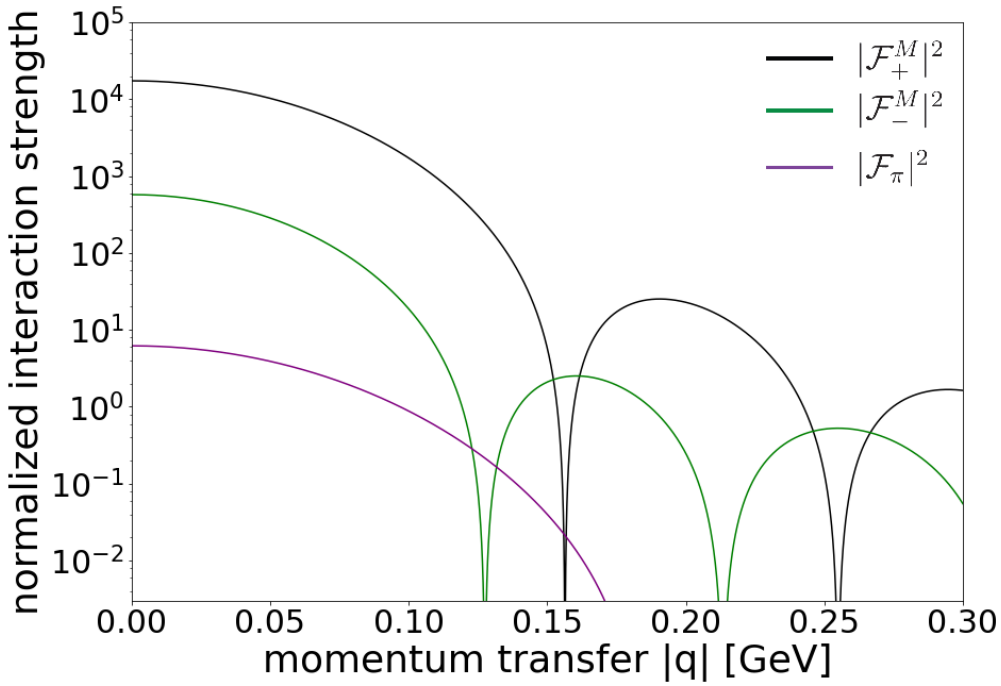

Figure 1.12.: Comparison of the interaction strength of selected form factor contributions. The standard isoscalar SI coupling (black) is shown with its corrections calculated from ChEFT. The SI isovector response (green) and the two-body response from the scalar pion exchange (purple) are selected for a comparison. All three are shown as function of the momentum transfer. The normalization is such that $\mathcal{F}(q^2)(0) = A$. While all three responses are enhanced coherently, the isoscalar has the highest relative interaction strength at low momentum transfers. The decrease at higher momentum transfers corresponds to the Fourier transform of the charge distribution and represents the size of the nucleus. Data from [11].

The velocity distribution is defined time dependent in the local frame of reference, where v_{min} is given as:

$$v_{\text{min}} = \sqrt{\frac{E_{\text{thr}} m_N}{2\mu_N}}, \tag{1.36}$$

corresponding to the minimal velocity at a given WIMP mass to produce a recoil larger than the energy threshold E_{thr} [7]. The quantities measured are often reported as a cross-section σ_0 for a given WIMP mass m_χ, where the former is often transfered by eq. (1.28) for comparability among different targets. This is only an approximation under the assumption that the standard isoscalar SI interaction is the underlying mechanism. In fact any experiment measures always the combinatiom $\sigma_0 \times \mathcal{F}$ as the interaction strength of a given WIMP mass not the pure cross section σ_0. Figure 1.13 shows the differential recoil spectrum calculated for the standard form factor and the previously described coupling of the WIMP to the pion using the same cross section. Within the dark matter search region both are featureless exponential falling spectra but with a different scattering rate.

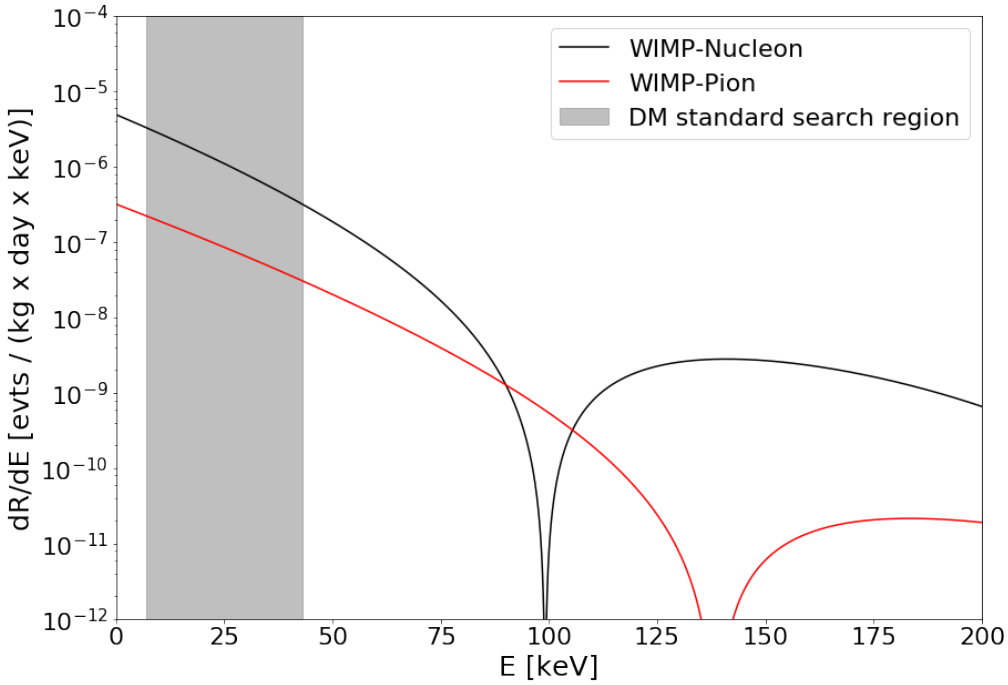

Figure 1.13.: Differential WIMP recoil spectrum for a xenon target. Two different form factors are assumed: The standard isoscalar SI interaction (black) and the pure scalar coupling to the exchange pions of two nucleons (red). Indicated is the region of interest in a standard dark matter search (e.g. LUX, XENON1T). The assumed cross section is $\sigma_0 = 1 \cdot 10^{-46}\,\mathrm{cm}^2$ and the exemplary mass is $m_\chi = 200\,\mathrm{GeV}$. Further details on this in section 3.3

.

1.4 Two-Neutrino double electron capture

Isotopes with the longest-half lives are those, where the direct beta decay is energetically forbidden[6], but a simultaneous transformation of two nucleons can overcome the barrier. This is illustrated in fig. 1.14. There, the exemplary masses from both mass parabolas - for even-even and odd-odd isotopes - are expressed as a function of the so-called mass excess. It is defined as the difference between the expected mass number from the number of nucleons and its actual mass in atomic mass units (amu). This corresponds directly to the binding energy per nucleon. The process,

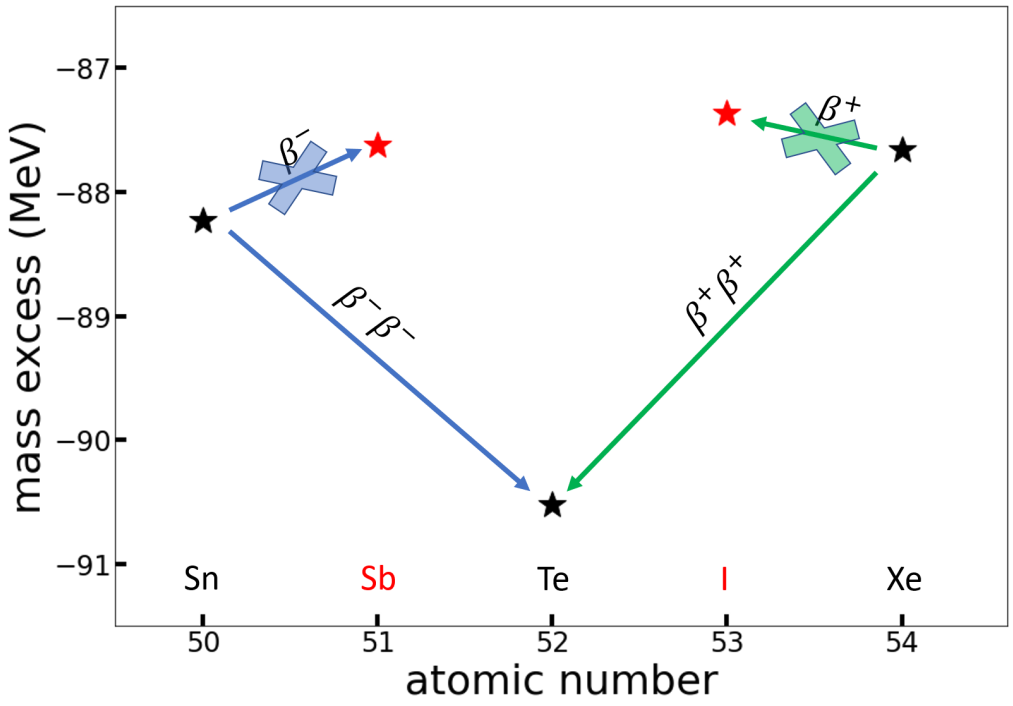

Figure 1.14.: Mass excess of different isobars for A = 124. The mass excess (description in the text) is shown for different isotopes with the same number of nucleons (mass number A). Asterisks in red denote odd-odd isotopes and asterisks in black denote even-even isotopes. The decay of the selected even-even isotopes into odd-odd isotopes is energetically forbidden and thus, the β^--decay (blue) and the β^+-decay (green) are impossible. A second-order decay into the energetically favored even-even isotope ^{124}Te is possible via the emission of two β-particles. The allowed β-decays of the odd-odd isotopes are omitted for clarity. Data taken from [75].)

where two neutrons in the nucleus decay simultaneously into two protons emitting two anti-neutrinos and two electrons is commonly referred to as two-neutrino double beta decay ($2\nu\beta\beta$). Although, this process has drawn interest since its first prediction in 1935 [76] a first direct observation was only possible in 1987 [77] due to the

[6] Sometimes single-β-decay is still less likely, although energetically allowed. This is the case e.g. for ^{48}Ca, where the single beta is extremely hindered by the large angular momentum change involved in a decay.

long half-live. Nowadays, the decay was observed directly in a couple of isotopes all with half-lives between $10^{18}\,\mathrm{yr}$ to $10^{21}\,\mathrm{yr}$ [20, 78]. Even more interest is put into a more speculative variation of this decay mode, where no neutrinos are emitted. This neutrinoless decay, usually referred to as $0\nu\beta\beta$, would demonstrate the Majorana nature (anti-particle = particle) of neutrinos as first concluded by [79]. Moreover, this would require an extension to the standard model of electroweak interactions since it violates the lepton number conservation. This would be helpful to understand the matter–anti-matter asymmetry in our universe. If the annihilation of Majorana neutrinos causes the decay, the obtained half-life is sensitive to the absolute mass scale and hierarchy of the neutrinos as well. Since, the impact of this decay would be groundbreaking there are large experimental efforts to observe this decay in a variety of isotopes [80].
Less attention has been put in transitions on the proton-rich side of the mass parabola, where two protons are simultaneously transformed into neutrons. Depending on the available phase space, this process can occur via three different modes:

$$(\mathrm{Z,A}) \rightarrow (\mathrm{Z\text{-}2,A}) + 2\mathrm{e}^{+} + 2\nu_{\mathrm{e}} \tag{1.37}$$

$$\mathrm{e}^{-} + (\mathrm{Z,A}) \rightarrow (\mathrm{Z\text{-}2,A})^{*} + \mathrm{e}^{+} + 2\nu_{\mathrm{e}} \tag{1.38}$$

$$2\mathrm{e}^{-} + (\mathrm{Z,A}) \rightarrow (\mathrm{Z\text{-}2,A})^{**} + 2\nu_{\mathrm{e}}. \tag{1.39}$$

Here Z is the atomic number and A is the mass number. Holes in the atomic shell caused by the electron capture are denoted by an asterisk. The decay in eq. (1.37) is the simultaneous two-neutrino double positron emission ($2\nu\beta^{+}\beta^{+}$) and only possible if the Q-value of the respective isotope is at least larger than $4\,m_e c^2 = 2044\,\mathrm{keV}$. A mix of an electron capture accompanied by an emission of a positron ($2\nu\mathrm{EC}\beta^{+}$) is possible as soon as the Q-value is larger than $2\,m_e c^2 = 1022\,\mathrm{keV}$ and is shown in eq. (1.38). The process without such an energy requirement is the two-neutrino double electron capture (2νECEC), shown in eq. (1.39). Hereby, two electrons from the atomic shells are captured simultaneously. The daughter isotope remains with two holes, which are filled with electrons from sub-sequent atomic shells. Electrons from shells closer to the nucleus have higher probabilities to be captured due to the higher likelihood to be within the proton´s reach.
An isotope which is predicted to decay via all three channels is $^{124}\mathrm{Xe}$. This isotope is observably stable so far, which is explainable since the direct decay into $^{124}\mathrm{I}$ would require an energy of $295\,\mathrm{keV}$ [75] and hence is not realized in nature. Nevertheless, the mentioned second-order decay into $^{124}\mathrm{Te}$ has a Q-value of $(2856.73 \pm 0.12)\,\mathrm{keV}$. Hereby, the Q-value for the double electron capture is defined by the difference in mass for the daughter and mother isotope. It is of particular importance, when calculating the half-life $T_{1/2}$ of the decay[7]:

$$T_{1/2}^{-1} = G_{2\nu}^{\mathrm{ECEC}} g_A^4 |m_e c^2 M^{(2\nu)}|^2. \tag{1.40}$$

[7] There is a significant discrepancy between the value given by the measurements used for the survey in [75] yielding $(2863.9 \pm 2.2)\,\mathrm{keV}$ and the value stated here taken from [81]. A discussion of this issue is provided within [81] and the decision towards the latter value is due to its more recent method with presumably higher precision.

Here m_e is the mass of the electron and c is the speed of light. The term g_A represents the strength of the weak axial-vector coupling. From the free neutron decay its value is determined to be 1.2723 ± 0.0023 [20]. For a decay in a nucleus, there is the hypothesis that the coupling constant is smaller due to quenching caused by influence from the many-body currents and other nuclear medium effects [82]. Theoretical calculations providing predictions on the half-life usually assume a value between 1 and the value for a free nucleon. The term $M^{(2\nu)}$ represents the nuclear matrix element (NME) involved in the decay. It is defined as the transition amplitude from the initial nuclear state of the mother isotope to the final nuclear state of the daughter isotope. For $^{124}\mathrm{Xe}$ it is considered to be a pure Gamow-Teller transition up to small corrections for Coulomb effects. The matrix element calculation has to include the intermediate states which are involved due to the momentum transfer of few MeV. Several methods exist for calculating the NME for the different decay modes, but their predicted half-lifes for a given isotope differ by a few orders of magnitude. This is mainly caused by the limited computational resources given in comparison to what is needed due to the high number of intermediate states involved. This difficulty is shared with the extensively studied $2\nu\beta\beta$ decay and is even more pronounced for neutrinoless modes of the decays due to the higher momentum transfers ($\sim \mathcal{O}(100\,\mathrm{MeV})$). A review of the different strategies to overcome the computational limitation is given in [28]. For the NME of the 2νECEC mode of $^{124}\mathrm{Xe}$ a few calculations are available [83, 25, 84, 24, 85, 26]. The corresponding half-lives are shown in fig. 1.15. The last term determining the half-life of the process is the phase-space factor (PSF) $G_{2\nu}^{\mathrm{ECEC}}$. Here, the aforementioned Q-value enters with the fifth power. Additionally, it is based on the bound-state electron wave function and therefore, includes the probability of an electron to be found at the nucleus. As this is largely increased for the K-shell electrons, the most likely process is a double electron capture of the two electrons from this shell. Therefore, most experimental efforts are targeting this particular branch of the decay mode, which is often referred to as 2νKK. Derivations of the PSF are done in [87] and [88], where from the latter a probability P_{KK} for the 2νKK is derived to be around $76.7\,\%$. For the decays from the proton-rich side of the mass parabola neutrinoless modes are also predicted within diverse theories, but are experimentally not well investigated due to disfavored half-life predictions in comparison with the decays from the neutron-rich side [89]. However, with the growing interest but lack of successful observation in the standard neutrinoless channel of double beta decay, those process become more interesting. Especially, a resonant degeneracy between the initial and final state could boost the half-life to measurable values in certain isotopes [90, 91, 92, 93].

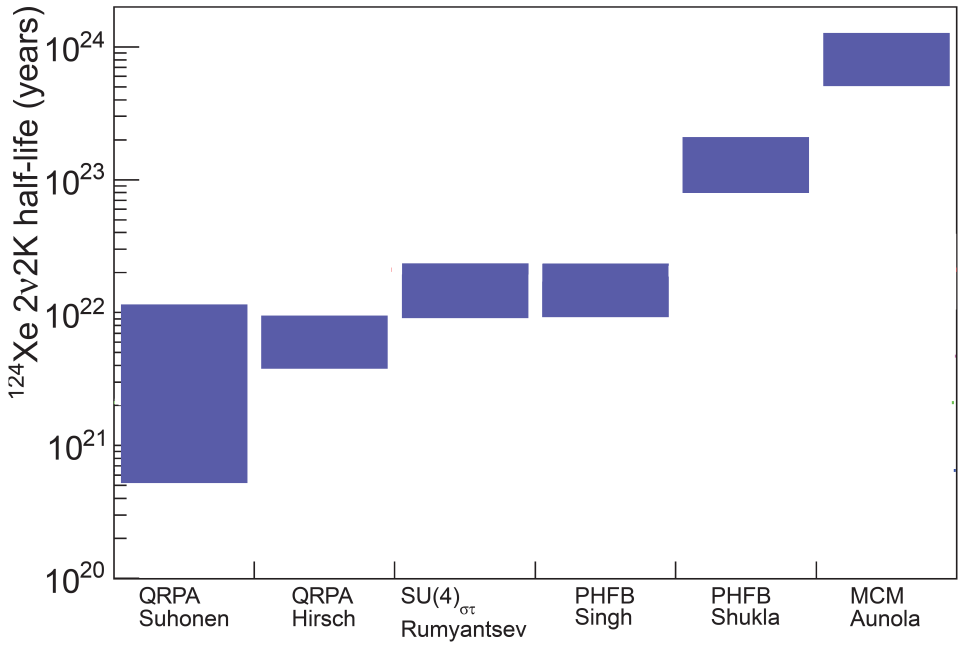

Figure 1.15.: Predictions of the theoretical NME for the half-life of ^{124}Xe . The expectation of the half-life of the 2νECEC is shown (blue boxes) as calculated by different NME framekworks [83, 25, 84, 24, 85, 26]. The lower edge corresponds a weak axial-vector coupling of $g_A = 1.26$ and the upper edge to $g_A = 1$. The theoretical values are scaled by the branching ratio ($P_{KK} = 0.767$) for the capture of two K-shell electrons (2νKK) as the experimental efforts are focused on this decay mode. Figure is adapted from [86].

Chapter 2

XENON Dark Matter Project

The idea for the XENON dark matter project was conceived in 2004 [94] and the first realization was the XENON10 detector. It started the first dark matter search in October 2006 using $14\,\mathrm{kg}$ of LXe as an active volume [95]. This prototype dual-phase TPC was followed by XENON100 in 2008, which utilized $62\,\mathrm{kg}$ of LXe [57], and in 2015 by XENON1T using an active volume of $2000\,\mathrm{kg}$ [96]. All of these experiments operated at Laboratori Nazionale del Gran Sasso (LNGS), which is an underground laboratory located at a depth equivalent to $3600\,\mathrm{m}$ of water that reduces the muon flux by about $\sim 10^6$ compared to sea level [97, 98]. This reduction, together with the addition of other background mitigation and removal strategies, and the advantage of liquid xenon dual-phase technology, made each of these detectors the most sensitive dark matter detector at their time of operation. Data from XENON100 and XENON1T will be used within this work, and therefore, both detectors will be introduced briefly. A detailed description can be found in the instrumentation publications of XENON100 [57] and of XENON1T [96].

2.1 XENON100

The core piece of the XENON100 experiment was a cylindrical dual-phase TPC with a height of $30.5\,\mathrm{cm}$ and a radius of $15.3\,\mathrm{cm}$. The inner walls of the TPC were covered with highly reflective polytetrafluorethylene (PTFE) section 1.1 only interrupted by copper wires for field shaping.
It was filled with a total amount of $161\,\mathrm{kg}$ liquid xenon (LXe). $62\,\mathrm{kg}$ were used as target material and monitored by in total 178 R8520-AL 1 inch PMTs in a top and a bottom array. In addition, the target was surrounded by an optically separated active veto containing $99\,\mathrm{kg}$ of LXe, which was monitored by 62 additional PMTs. This provided additional shielding and also allowed tagging of coincident events. The detector itself was contained in a cylindrical vessel made of low radioactivity stainless steel. A

shielding by successive layers of oxygen free high conductivity copper, polyethylene, lead, and water/polyethylene was in place to suppress environmental and cosmogenic radiation. By constantly flushing nitrogen trough the inner part of the shielding a further reduction of radon contamination from ambient air was achieved.
Cooling of the LXe was ensured by a pulse tube refrigerator (PTR), which was operated outside the shield, maintaining a temperature of about $182\,\mathrm{K}$ with sub-percent fluctuations over the time scale of a measurement ($\sim 6\,\mathrm{months}$). As described in section 1.1 it is necessary to maintain a high purity in order to maximize the electron yield from the ionization channel of the interaction. This was achieved by continuous purification trough a hot zirconium getter, which efficiently adsorbs electronegative impurities.
A different step of purification was performed by processing the gas trough a cryogenic distillation column once before a scientific run to remove the isotope $^{85}\mathrm{Kr}$. It is a β-emitter with an end point energy of $687\,\mathrm{keV}$ and a half-life of $T_{1/2} = 10.76\,\mathrm{yr}$. Although, its abundance in natural krypton is only at the $10^{-11}\,\mathrm{mol/mol}$ [99] it was a major background source for the XENON100 experiment even after reduction of the natural krypton content in the xenon to the ppt-level[1]. All these efforts with the addition of careful material selection lead to an ER background rate as low as $5.3 \cdot 10^{-3}\,\mathrm{events/kg/d/keV}$ in an inner fiducial volume of $34\,\mathrm{kg}$ during the science run II. Here about $40\,\%$ were contributed by the intrinsic backgrounds $^{85}\mathrm{Kr}$ and $^{222}\mathrm{Rn}$, where the daughter isotope $^{214}\mathrm{Pb}$ is the most important part of the chain due to its beta decay with an endpoint energy of $1024\,\mathrm{keV}$. The other $60\,\%$ came from external radiation mainly produced by the detector materials [100].
Background sources producing NR are the crucial part for direct dark matter searches. These originate from muon-induced neutrons, which are present despite the strong reduction from the rock overburden in the underground laboratory. In addition, neutrons emitted from (α,n)-reactions or spontaneous fission in the detector materials add to possible signals. However, for the dark matter search these are a smaller contribution than ER [101], regardless the discrimination ability by the S2/S1-ratio with an efficiency of $99.75\,\%$ [102]. Therefore, NR background are also negligible for the search for most of the ER physic channels such as double electron capture.
The energy reconstruction parameter $g1$ and $g2$ needed for the combined energy scale (CES) as shown in eq. (1.8) were determined to:

$$\mathrm{g_1(XE100)} = (0.0661 \pm 0.0004)\,\mathrm{pe/ph} \tag{2.1}$$
$$\mathrm{g_2(XE100)} = (10.12 \pm 0.07)\,\mathrm{pe/}, \tag{2.2}$$
$$\tag{2.3}$$

using calibration sources of known energy at $39.6\,\mathrm{keV}$, $80.2\,\mathrm{keV}$, $163.9\,\mathrm{keV}$, $236.2\,\mathrm{keV}$ and $319.9\,\mathrm{keV}$. The given uncertainty is purely statistical. At an energy of $164\,\mathrm{keV}$ XENON100 had a light yield of about $2.07\,\mathrm{pe/keV}$ and a charge yield of $332\,\mathrm{pe/keV}$

[1] ppt (parts per trillion= = 10^{-12}

estimated from the 2D-elliptical fit in ($cS1$,$cS2b$)-space[2]. The energy resolution[3] has been determined following eq. (1.12) to be

$$\sigma_{\mathrm{XE100}}(E) = ((0.405 \pm 0.010)\sqrt{\mathrm{keV}}) \cdot \sqrt{E} + (0.0261 \pm 0.0008) \cdot E, \tag{2.4}$$

with purely statistical uncertainties from the fit to the same energies as for the energy reconstruction with the exception of the line at $163.9\,\mathrm{keV}$, as this line showed an overlap with another line from activated fluorine.

2.2 XENON1T

In 2015 the commissioning of the first multi-ton liquid xenon detector XENON1T took place in Hall B of the LNGS (see fig. 2.1). The scientific data taking for the detector analyzed in this work was conducted from 22nd November 2016, and ended on the 8th February 2018. The data sets were separated in two sequences, differing by the electric field which was applied, due to an earthquake affecting the whole experiment on the 18th January 2017. Within this work, these datasets are referred to science run 0 (SR0) for the 32.1 days before the earthquake and science run 1 (SR1) for the 246.7 days after the earthquake.[4]
In addition to the 3600 meter water equivalent overburden by the rock of the Gran Sasso massive, the detector is placed within a water tank with a height and diameter of about $10\,\mathrm{m}$. This water tank is actively monitored by 84 *Hamamatsu R5912ASSY* PMTs in order to detect Cerenkov light from muons penetrating towards the TPC on the one hand, and neutrons induced my muon scattering on the other hand. This way any contribution of muons is basically eliminated completely for the course of the dark matter operation of XENON1T [103]. Additionally the de-mineralized water shields against other external γ- and neutron radiation. The cryostat vessel inside the tank contains the TPC. It features a total drift length of $97\,\mathrm{cm}$ and is $96\,\mathrm{cm}$ in diameter and contains about $2000\,\mathrm{kg}$ of active liquid xenon. Full wall coverage by PTFE ensures a high light yield, which necessitates the copper field shape rings to be installed on the outside of the active volume. The light is detected by 248 *Hamamatsu R-11410* PMTs which are installed at the top in a concentric array and packed with highest density at the bottom of the detector [104]. These optimized photo sensors provide an average quantum efficiency of $34.5\,\%$ at room temperature for the xenon scintillation light wave length of $178\,\mathrm{nm}$. The photo collection efficiency is measured to be about $90\,\%$ [105, 106, 107]. A regular LED calibration using blue light extracts the PMT gains individually for each PMT. The gains are spread between $2.0 \cdot 10^6$ to $5.0 \cdot 10^6$ and are measured to be stable at the $2\,\%$-level.

[2] In literature usually the $122\,\mathrm{keV}$ reference line from $^{57}\mathrm{Co}$ is used, which is however not accessible for a large detector. The chosen $163.9\,\mathrm{keV}$ is a homogeneous mono-energetic source generated by a single γ-emission is comparable among the XENON experiments

[3] A multiplication by 100 transforms it into a percentage.

[4] The times are given as livetime with DAQ correction applied and only runs without any calibration source present or other operation undertaken are included.

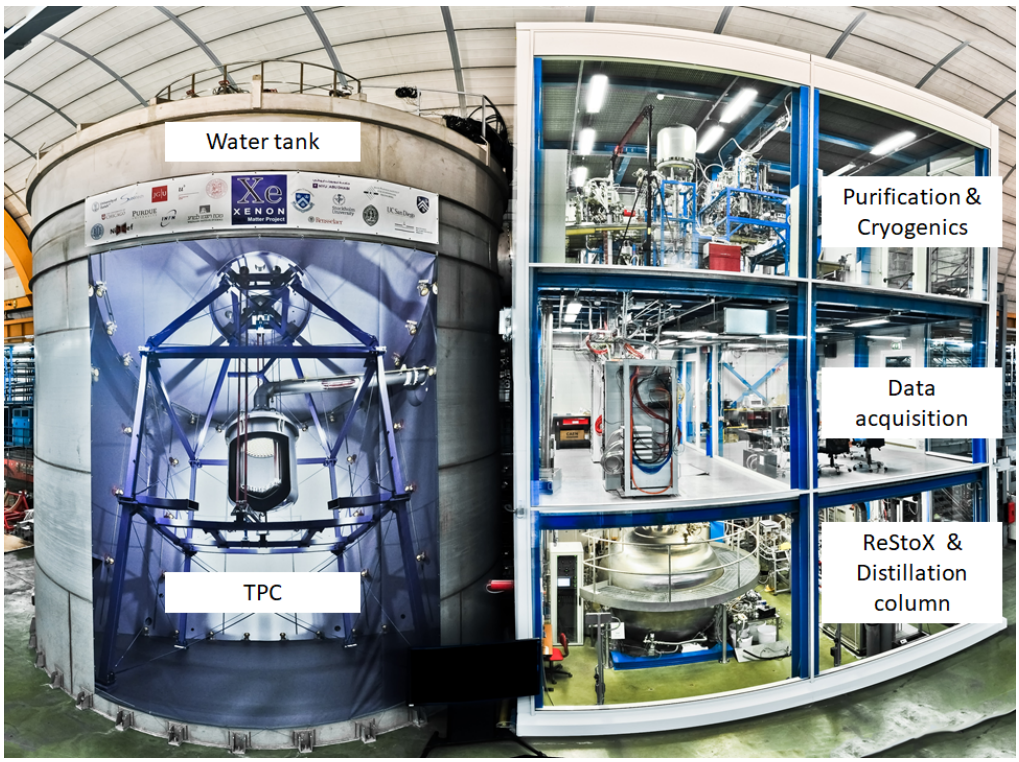

Figure 2.1.: XENON1T in Hall B. Left: Water tank filled with de-mineralized water. A poster on the outside wall sketches the inner part: a cryostat containing the TPC and its holding structure. Right: The support building. On the first floor it contains the xenon storage and recovery system (ReStoX), the gas chromatography system used for filling the detector and the first part of the distillation column, which continues to the second floor. Here the on-site shifters have space for work and also the data acquistion system as well as the slow-control of the system is located there. On the third floor there is the purification loop and the cryogenic system located. Additionally, there is the access to the calibration sources controlled from the top of the water tank and the calibration source box at the purification system. Picture taken with a fisheye lens by Patrick de Perio and Roberto Corrieri.

$1200\,\mathrm{kg}$ additional LXe is contained within the supporting cryogenic system of the detector. The full xenon content is liquefied outside of the water tank using two pulse refrigerator tubes (PTR, *Iwatani PC-150*) supported by a heat exchanger. During the detector operation the temperature was kept at $-96.3\,°\mathrm{C}$ with deviations less than $1\,\%$ and the pressure was measured to be at $1.935\,\mathrm{bar}$ stable within $1\,\%$.
Any detector parameter is controlled and monitored by a slow control system based on industry standard process control hardware and software from *General Electric*. If any parameter exceeds a pre-set threshold, an alarm is triggered to inform the required experts on-site and off-site and to automatically initiate necessary steps as for example start the liquid nitrogen (LN_2) cooling. In case of a severe emergency, but also for the initial filling, the entire xenon content can be stored in ReStoX (*Recovery and Storage of Xenon*), a custom-made storage system, which can hold up to $7.6\,\mathrm{t}$ of xenon in any aggregate state.

The level of the liquid within the TPC is controlled by a pressurized *diving bell* and measured by four parallel-plate-capacitive level-meter with a precision of about $30\,\mu\mathrm{m}$. Before liquefication the xenon gas is passed to the purification system, which consists of two independent loops. Each loop is equipped with one rare gas purifier (*SAES PS4-MT50-R*). These devices remove electronegative impurities via chemical bonding to hot zirconium. A monitoring system, the *Tiger Optics HALO+ H2O monitor*, enables measurements of the purity in terms of water, with a sensitivity down to the ppb-level. The gas is actively pumped by three magnetic-resonance pumps (*CHART QDrive*) and the flows are controlled via mass flow controller *(MKS 1579A)*. Given by the flow of about $50\,\mathrm{slpm}$, the total xenon content is revolved once every $7.5\,\mathrm{d}$. After the initial cleaning period, the flow becomes the limiting factor for the increase of the electron lifetime (see eq. (1.1)) as the removal speed balances the out-gassing rate of electronegative impurities within the LXe. Figure 2.2 shows the development of the electron lifetime measured with $^{83m}\mathrm{Kr}$. A plateau is reached at about $660\,\mu\mathrm{s}$ towards the end of SR1. Given the electric field strength for SR0 of about $120\,\mathrm{V\,cm^{-1}}$ the drift time for an electron traveling through the entire TPC is at $673\,\mu\mathrm{s}$ and with the reduced field in SR1 of about ($80\,\mathrm{V\,cm^{-1}}$) this value increases to about $707\,\mu\mathrm{s}$.
The inter-phase between liquid and gas is placed in the middle of the gap between the gate electrode and the anode, which is $5\,\mathrm{mm}$ wide and biased with about $4\,\mathrm{kV}$.

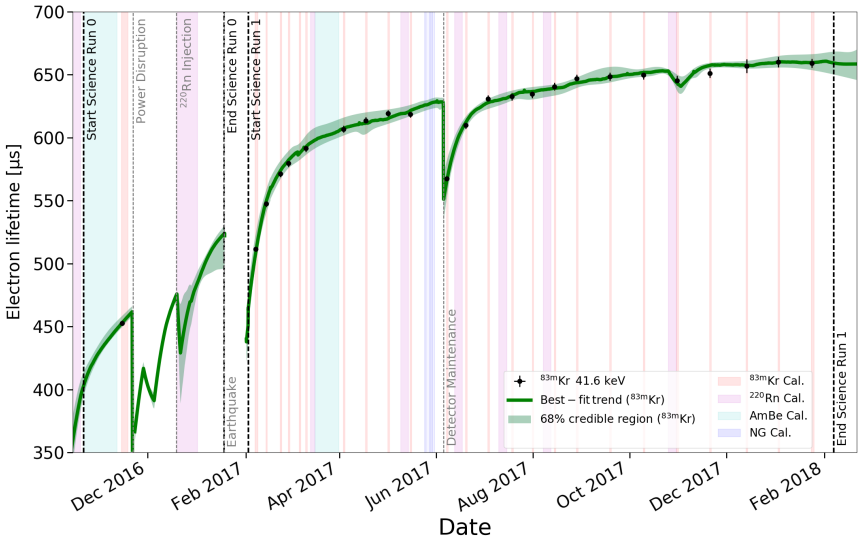

Figure 2.2.: Electron lifetime evolution for the full scientific data taking. The electron lifetime is measured throughout the two detector runs using $^{83m}\mathrm{Kr}$. Various interruptions from the normal conditions lead to repeatedly drops, but the lifetime recovers fast from this. The long stable operation to the end allows the system to achieve the equilibrium between removal of the impurities by the getters and out-gassing from the detector materials. See [108] for a description of the fit model. Data for this plot provided by Zach Greene.

The task of krypton removal was performed by a cryogenic distillation column designed especially for the needs of the experiment [109]. Hereby the krypton is removed utilizing the difference of vapor pressures of krypton and xenon. A technical drawing of the distillation column can be seen in fig. 2.3. A new way of operation was tested for XENON1T. Instead of an extensive removal campaign prior a run (so called offline distillation), the distillation was operated continuously in the commissioning phase of the experiment (online distillation). As the offline option would have taken about a month without being able to use the xenon content, the most important advantage was the possibility of taking data during the online operation. Details on the operation can be found in [110] and the resulting reduction in krypton concentration during the operation is shown in fig. 2.3 leading to a final value as low as $0.36\,\mathrm{ppt}$. Since the krypton concentration was measured in a time expensive procedure using residual gas mass spectrometry (RGMS) at the MPIK in Heidelberg, Germany [111], an on-site measurement system was installed next to the cryogenic distillation column, which is described in [112]. However, in its current configuration it is unable to measure the concentrations achieved during the XENON1T operation. In appendix A.1 a rough description of an improvement as well as first indicative results are shown in order to enable the system to be sensitive to krypton concentrations on the sub-ppt level.
The krypton removal reduced the contribution of krypton to the total event background rate, which leaves the subsequent isotopes of the decay chain of $^{222}\mathrm{Rn}$ being the main challenge for the experiment. As the distillation technique is capable of removing this component as well if the extraction port for the clean gas is changed from the bottom to the top of the column [113], a test run was performed during SR0, which reduced the contribution by $20\,\%$ for a period of 15 days [110]. In addition to the active removal of intrinsic impurities and to the intensive shielding, a careful material screening campaign before detector building was undertaken [114]. These efforts led to a background rate lower than $2.0 \cdot 10^{-4}\,\mathrm{events/kg/d/keV}$ in the inner fiducial cylinder [115]. More details on the background will be given in section 4.2. While the natural krypton content was removed to reduce the long-lived $^{85}\mathrm{Kr}$ ($T_{1/2} = 10.76\,\mathrm{yr}$), the short-lived $^{83m}\mathrm{Kr}$ ($T_{1/2} = 1.83\,\mathrm{h}$) is introduced to the system regularly. Produced by electron capture of a $^{83}\mathrm{Rb}$-zeolith source in a designated box at the purification system, $^{83m}\mathrm{Kr}$ is injected in the detector and distributes homogeneously within the TPC [118]. It decays via internal conversion in a two step process depositing in total $41.5\,\mathrm{keV}$. However, due to the lifetime of $154\,\mathrm{ns}$ of the intermediate state a distinction of a part of the decays is possible, leading to two distinct energy depositions at $32.1\,\mathrm{keV}$ and $9.4\,\mathrm{keV}$. The source is used for the determination of the electron lifetime, the mapping of the light response of the detector, for the energy calibration and for the correction of the field distortion (as described in section 1.1). The calibration box also contains a $^{228}\mathrm{Th}$ source, which emanates only $^{220}\mathrm{Rn}$. This isotope also distributes homogeneously in the detector and its daughter isotope $^{212}\mathrm{Pb}$ is utilized to calibrate the ER-band of the detector. The half-life of $T_{1/2} = 10.6\,\mathrm{h}$ ensures no impact on the rare event search within a week after source closing. In addition to this application, an analysis of the full chain can point towards the possible convection patterns in the

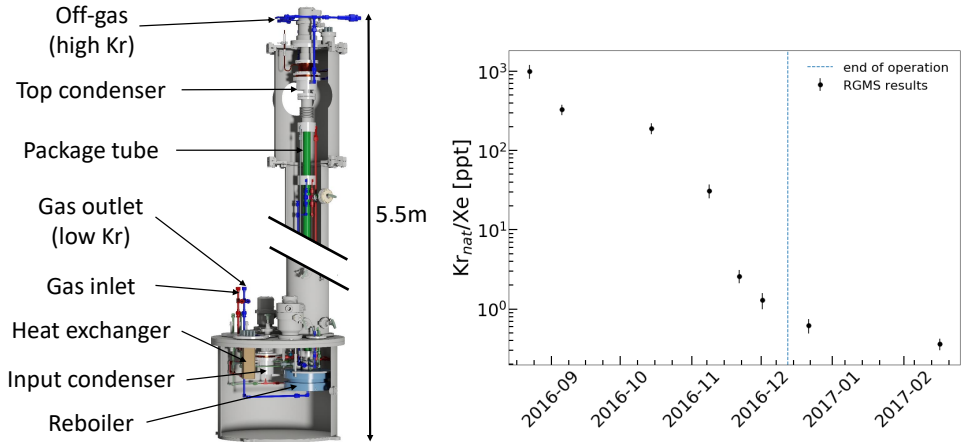

Figure 2.3.: Krypton removal in SR0. Left: Technical drawing of the XENON1T distillation column. The gas at the inlet is liquefied by a first input condenser, which is supported by a heat exchanger. After this first separation [116] the gas is injected in the final column. Here it streams upwards, getting liquefied again by the second condenser. The liquid xenon drips down the package material within the column and is collected at the reboiler. Due to the higher vapor pressure of kryton, it is depleted in the and enhanced in the gas phase at the top. The cleaner xenon from the reboiler is extracted trough the heat exchanger and a small fraction of the gas phase at the top is removed to a gas bottle. Technical details of the system can be found in [110, 117]. Drawing provided by Christian Huhmann. Right: Development of the natural krypton concentration in the XENON1T detector during the operation of online distillation as described in the text. The actual operation was stopped at the 12th December 2016 (blue, dashed line). Measured by MPIK Heidelberg as described in [111].

detector [119]. Besides these internal sources, also external calibration is used within XENON1T. However, due to the large target mass, this is only feasible for neutron calibration sources. Two different sources are used: a deuterium-deuterium-fusion generator and an $^{241}\mathrm{AmBe}$ source. The first one provides an adjustable neutron flux and the ability turn it off and on and is thus, the favored option, but was not available during the full operation time [120]. Therefore, also two campaigns were performed using the $^{241}\mathrm{AmBe}$-source, which emits constantly 160 n/s [58]. These neutrons are used to calibrate the NR response of the detector as well as for studies on activated isotopes, mainly for the purpose of energy calibration.
Both, energy calibrations and regular data taking mode, are handled by the same data acquisition system (DAQ). It can be operated in different modes, where a maximum of about $100\,\mathrm{Hz}$ can be recorded. However, in regular operation mode events at $5\,\mathrm{Hz}$ rate are registered. For the TPC this is considered trigger-less. This means that every pulse above a digitization threshold ($\sim 0.3\,\mathrm{PE}$) in any PMT is read independently from any other channel. The decision, if the pulse is stored and an event is built,

is made in real-time by an external software event-builder. In the regular mode, a time-clustering of pulses looking for $S2$-signals in individual PMT channels achieves a trigger efficiency of >$99\,\%$ at $200\,\mathrm{PE}$. This corresponds to approximately 7 electrons. Once an event is successfully stored, it is passed to the *Processor for Analyzing XENON* (PAX), which reconstructs the physical events with all their properties (e.g. size, width, timing) [121]. It transforms the raw pulses recorded in mV to classified signals in units of PE, corrected for the various detector effects explained in section 1.1, using the processing chain shown in fig. 2.4. After data processing, HAX (*Handy Analysis for XENON*) makes the various different signal properties accessible in so called *minitrees*. Depending on the needs of the particular analysis, only a few properties are available in order to reduce data load. For the energy calibration

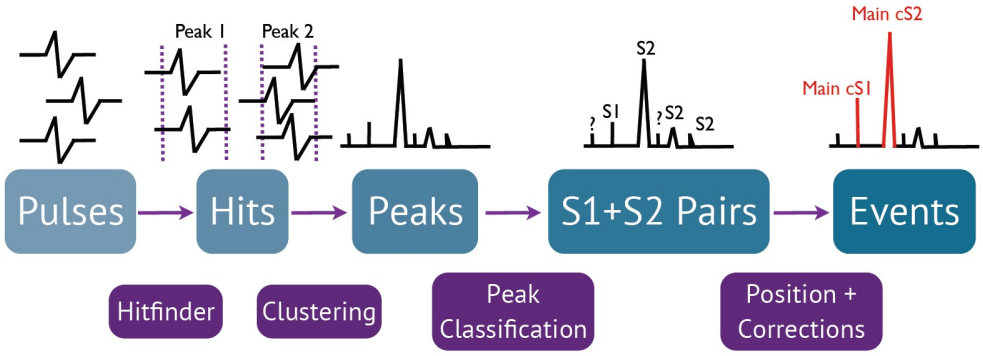

Figure 2.4.: Processing chain of PAX Raw event pulses in different PMTs are grouped by their timely proximity into so called hits. Coincident hits among different PMTs are then grouped into peaks, which are first classified into $S1$ and $S2$ signals and then the various corrections are applied depending on the interaction type. Sketch taken from [53].

of XENON1T various sources of known energy were available as summarized in table 2.1. According to eq. (1.8) the combined energy scale (CES) can be denoted by the g_1 and g_2 value. Figure 2.5 shows the linear behavior of the energy scale as used for the dark matter search in SR0 and the obtained values for $\mathrm{g_1(XE1T)}$ and $\mathrm{g_2(XE1T)}$ used in the SR1 dark matter analysis are:

$$\mathrm{g_1(XE1T)} = 0.1426 \pm 0.0001(\mathrm{stat.}) \pm 0.0017(\mathrm{sys.})\,\mathrm{pe/ph} \tag{2.5}$$

$$\mathrm{g_2(XE1T)} = 11.56 \pm 0.01(\mathrm{stat.}) \pm 0.24(\mathrm{sys.})\,\mathrm{pe/.} \tag{2.6}$$

The systematics are derived from spatial variation of the calibration fits. While the energy reconstruction is independent on the field strength and therefor did not change between the scientific runs, the energy resolution is affected. The comparison of the energy resolution function between the two runs can be seen in fig. 2.6.

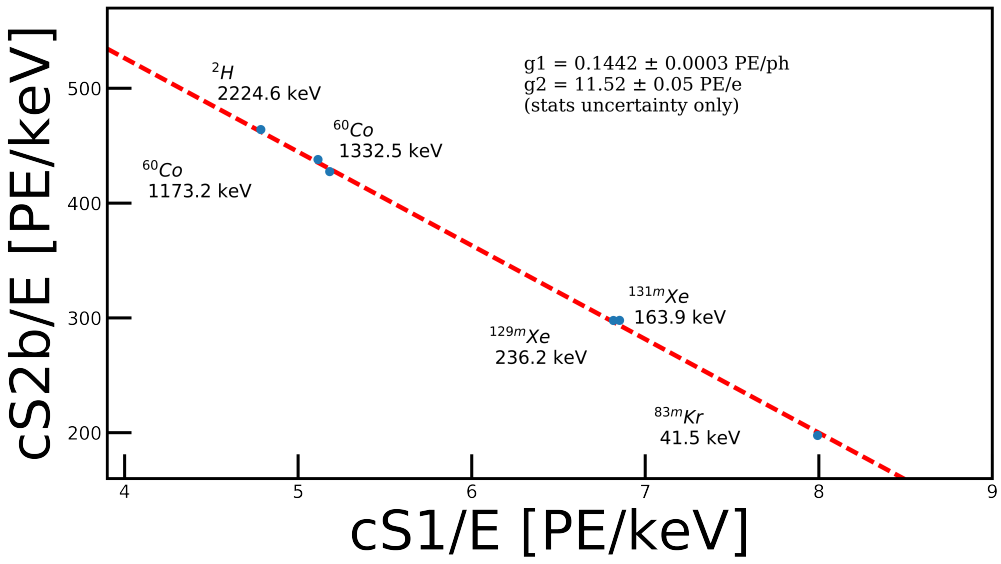

Figure 2.5.: Energy calibration in SR0. Various sources as described in table 2.1. The linear fit to the response function (red, dashed) of the two signal $cS1$ and $cS2$ was performed on all lines but the deuterium line ^{2}H. This is added for illustration of the linear energy response at high energies, where the detector was not optimized. The discrepancy between the values given in eq. (2.5) arises from the fact that only statistical uncertainties were studied in SR0 and that the systematic uncertainties at the time of the dark matter search were rather large due to lacking corrections for the field distortion.

Table 2.1.: Sources in XENON1T useable for energy reconstruction.

Isotope	Energy [keV]	Origin
^{83m}Kr	41.5	Calibration
^{131m}Xe	163.9	Neutron acitvation
^{129m}Xe	236.2	Neutron activation
^{60}Co	1173.2	Materials
^{60}Co	1332.5	Materials
^{40}K	1460.8	Materials
^{2}H	2224.6	Neutron activation

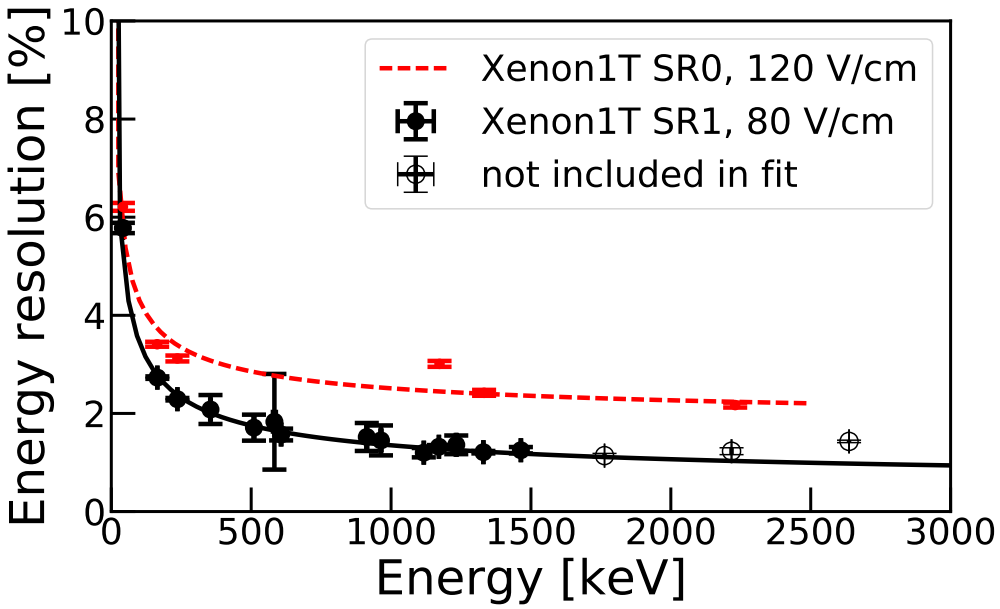

Figure 2.6.: Energy resolution in both science runs. Comparison of the energy resolution as defined in eq. (1.12) for SR0 (red) and SR1(black). The improvement in SR1 is based on a deeper understanding of the detector and the necessary corrections (e.g. for field distortion, saturation) especially at higher energies, but also on the lower field, which enhances the light signal compared to the charge signal. Data for SR0 obtained in co-operation with Jingqiang Ye. Data for SR1 provided by Christian Wittweg and Jialing Fei.

2.3 Future detectors

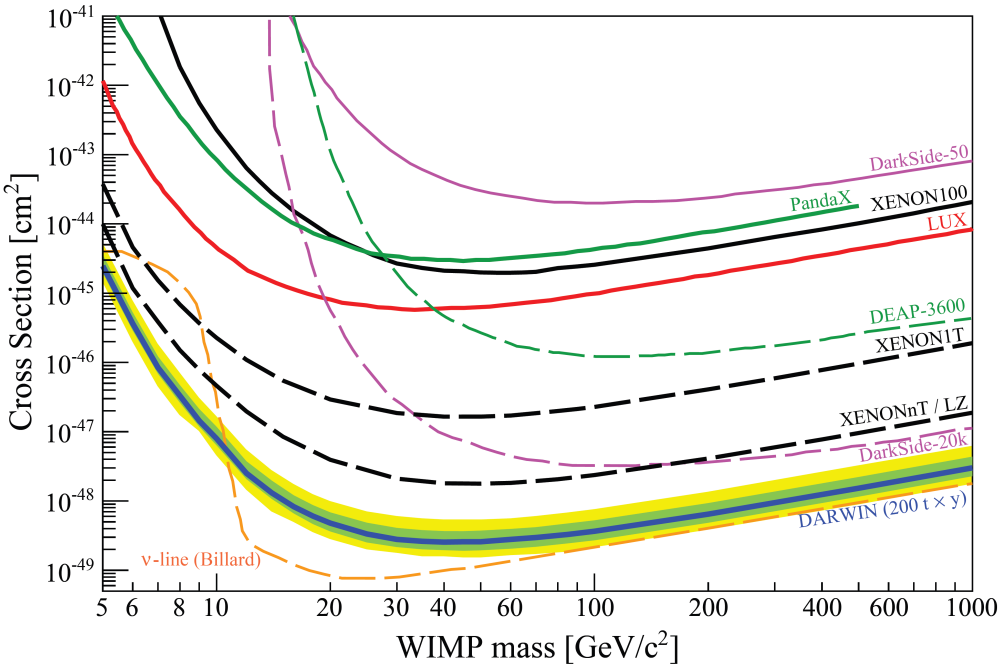

Figure 2.7.: Different experimental sensitivities for the WIMP-nucleon cross section in dependence of the WIMP mass. The status prior to the first results of XENON1T is shown for the experimental exclusion limits (solid lines). The sensitivities of the future experiments are denoted by dashed lines and for the DARWIN experiment a sensitivity band is given with 1σ (2σ) contours in green (yellow). The ultimate limit for the direct dark matter search given the coherent elastic neutrino nucleus scattering is marked with the dashed orange line taken from [122]. Figure from [65].

When planning XENON1T the inclusion of a larger TPC in the future was already foreseen. This project named XENONnT will enlarge the active LXe volume to $\sim 6\,\mathrm{t}$ in a TPC with approximately $1.3\,\mathrm{m}$ diameter and a height of about $1.5\,\mathrm{m}$. The active volume is planned to be monitored by 454 PMTs. The advantage of the system is the re-use of large parts of the existing structure of XENON1T [123]. In addition to the benefits from the enlarged target mass, upgrades are planned building on lessons learned from the previous detectors. In particular it is aimed for adding a liquid purification facility supporting the gas purification in order to achiever higher flows. This will help to overcome the limitation in terms of electron lifetime, which is growing in importance with enlarged detectors. The inclusion of new gas pumps, e.g., a custom developed magnetically coupled piston pump [124], will support this further. In addition, these efforts are also targeting a decrease in the background contribution from $^{222}\mathrm{Rn}$ daughters compared to the existing pump solutions [124]. Not only the reduction but also the active removal is pursued for the XENONnT. Therefore, a custom high-throughput radon distillation column is under development utilizing the principle successfully proven in XENON100 and XENON1T [113]. Furthermore, an

active liquid scintillator neutron veto is foreseen. All these efforts are projected to push the sensitivity for the standard WIMP search to $10^{-48}\,\mathrm{cm}^2$ at $50\,\mathrm{GeV/c}^2$ assuming a radon concentration of $1\,\mu\mathrm{Bq\,kg}^{-1}$ and a relative krypton content of $0.02\,\mathrm{ppt}$. A detector of similar size is planned by the LZ collaboration [125]. For XENONnT it is aimed to provide first scientific data at the end of 2019.
The time scale for the start of DARWIN is set around 2023. This detector design concept developed by a dedicated collaboration is projected to contain $50\,\mathrm{t}$ LXe, where $40\,\mathrm{t}$ are actively monitored [126]. In combination with a further reduction in background it will explore the parameter space in terms of WIMP-nucleon cross section down to $10^{-49}\,\mathrm{cm}^2$. This marks an important point as the coherent elastic neutrino scattering off the entire xenon nucleus occurs at these probed cross sections and poses an indistinguishable background from the standard WIMP without the possibility of shielding [126, 122]. A summary of the sensitivities of the present and future detectors are given prior to the XENON1T results, which will be described in the next chapter, in fig. 2.7.

Chapter 3

Direct dark matter detection

The earthbound search for WIMPs is lead for WIMP masses above a few GeV by dual-phase liquid xenon TPCs. Among them, the TPCs of the XENON dark matter project were always on top of the field at their time of operation. The results of the XENON1T-phase of the project are presented here. In the first section the complete dark matter search for the standard WIMP is presented. This effort is the work of the entire XENON collaboration. The second section moves away from the standard assumption in terms of the underlying nuclear mechanisms. A set of different structure factors is used to test if a present or future XENON-like detector would be able to discriminate between the standard assumption and the respective non-standard mechanism once a WIMP signal is found. This work is based on the theoretical basis provided by Martin Hoferichter, Javier Menéndez, Philipp Klos and Achim Schwenk and it is published in [127].
One of the non-standard structure factors, namely the coupling of the WIMP to the exchange pions, is elaborated further and inserted into the standard analysis machinery of XENON1T in order to derive the first limit on this interaction in a one-operator-at-a-time approach. This analysis relies on the same theoretical groundwork and is prepared for publication [74].

3.1 Spin-independent WIMP-nucleon interaction

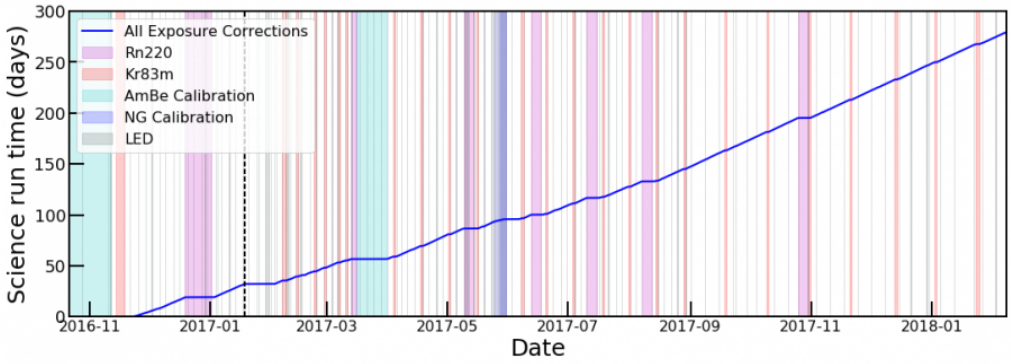

Figure 3.1.: Science run time of XENON1T. The data taking for dark matter is shown (blue line) in dead-time corrected days (live days) as a function of the calendar days. Additionally, diverse calibration data campaigns are indicated: LED calibration for PMT gain evaluation (gray), ^{83m}Kr for detector stability monitoring and signal reconstruction studies (orange), ^{241}AmBe (green) and neutron generator (purple) data to calibrate the NR band and respective cuts on NR and ^{220}Rn (pink) to determine the ER band. Plot generated using code provided by D.Coderre.

The main dark matter search data set of the XENON1T detector consists of $278.8\,\mathrm{days}$ separated into two time periods (details on the experiment in chapter 2). These two are referred to as science runs SR0 with $32.1\,\mathrm{days}$ of data and SR1 with $246.7\,\mathrm{days}$. They are separated due to an earthquake, which stopped the operation of the detector for about two weeks. The detector run history inclusive several calibration campaigns of the detector is shown in fig. 3.1. The major difference between the two runs is the applied electric drift field, which was set to $12\,\mathrm{kV}$ for SR0 and $8\,\mathrm{kV}$ for SR1. Initially, the data of SR0 was analyzed blindly and a first result was published in [115]. However, due to improvements in signal correction, reconstruction, and detector understanding in general, the data was re-blinded and re-analyzed for a combined data analysis with the blinded data set of SR1, which is published in [128].
The blinding of the data was done in order to prevent the analyzers to bias themselves during the analysis. In this way the selection criteria are not driven by the actual result itself but are exclusively based on first principles and calibration data. As a further step to evaluate the full analysis chain artificial events were added to the data before unblinding. The number and the nature of these events (commonly referred to as *salt*) was not known to the analyzers a priori. The intention behind this is to evaluate possible changes after unblinding. Furthermore, it allows to cross check whether the acceptances of the cut selections are consistent with the removal of these salt events. The selection of the blinded region was done in the two dimensional signal space $(cS1,cS2b)$. For this reason calibration data was used to determine the mean of the electronic recoil (ER) band. Anything below the -2σ–quantile of the ER band was then removed from the data analysis and only made accessible after

the entire analysis machinery was in place. A summary of the band determination and the resulting blinded region for the dark matter search is shown in fig. 3.2. The calibration data used for the ER band determination was obtained from the daughters of the short-lived calibration source $^{220}\mathrm{Rn}$. A total of $17.1\,\mathrm{days}$ were recorded for this purpose. Any tests of the selection criteria targeting WIMPs, which are assumed to recoil directly from the nucleus (NR), were performed on calibration data acquired using $30\,\mathrm{days}$ of $^{241}\mathrm{AmBe}$-data and additionally, $1.9\,\mathrm{days}$ of data from a deuterium-deuterium neutron generator. For both science runs only data is used, where the data acquistion (DAQ) system was ready to take data on all channels (deadtime correction). Furthermore, the active muon veto was not allowed to show a correlated event at the same time, as this would strongly point towards a muon-induced event.

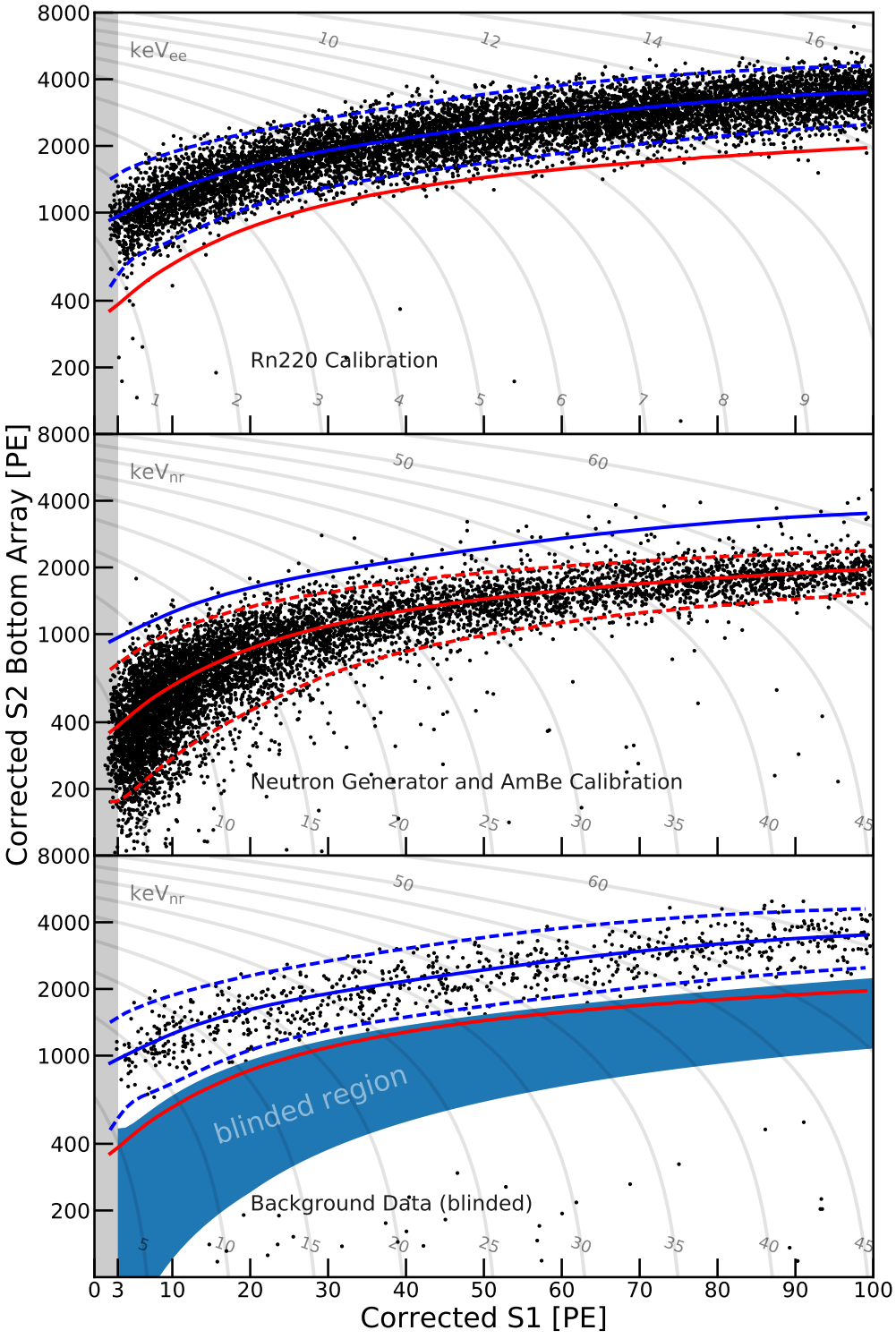

Figure 3.2.: Electronic and nuclear recoil bands in XENON1T. Top: Determination of the mean of the ER distribution (blue) in the $(cS2b,cs1)$-space using ^{220}Rn. The dashed lines indicate the 2σ-quantiles of the distribution. Middle: Determination of the mean of the NR distribution (red) using both neutron calibration sources. Dashed lines indicate the same quantiles as above and the ER band mean is shown for comparison (blue). Bottom: Dark matter search data with the blinded region (shaded blue) determined from the lower 2σ-quantile of the ER band. The area below the blinded region was initially blinded as well but was revealed in a step prior to the final unblinding to test background models. Figure generated by D.Coderre and S.Kazama.

The event selection criteria to discriminate real WIMP-like events from noise or background contributions range from simple data quality thresholds to sophisticated physics models. Firstly, any event has to include both signals ($S1$ and $S2$). The $S1$ signal has to be seen coincidentally by at least 3 PMTs within $100\,\mathrm{ns}$ and the uncorrected $S2$ signal has to overcome a threshold of $200\,\mathrm{pe}$. For the standard SI interaction an energy window of $4.9\,\mathrm{keV_{NR}}$ to $40.9\,\mathrm{keV_{NR}}$ is chosen [1], which corresponds to 3-70pe in $cS1$. Finally an $S1$ is discarded if its properties are to similar to the frequent $S2$ signal of single electrons. The expected detection efficiency from simulation based on these data quality criteria is shown in fig. 3.3 as a function of the energy. Especially at low energies the coincidence criterion reduces the detection efficiency significantly. Further selection criteria target the fraction of both signals in the respective array of PMTs (top and bottom). For the $S1$-signal, the fraction seen by the top array is compared to the expectation based on the interaction position within the detector using the knowledge about the light collection. Additionally, the maximal area seen by a single PMT is not allowed to surpass (0.052 $\times$ total-S1-size (pe) + 4.15 (pe)). This is demanded in order to prohibit artificial events from a single malfunctioning PMT. For the $S2$-signal of a real event, the fraction of the signal area seen by the top PMT is always between $50\,\%$ and $72\,\%$ as obtained from calibration data and simulations. The requirement to fall within this range targets effectively so-called gas events, where an interaction occurred in the small gas-phase on top of the detector, generating most of the light in the top of the TPC. If an interaction contains an un-resolved multi scatter (e.g. for a neutron) or occurs from accidentally paired signals, it produces an inconsistent hit pattern in both signal channels. Therefore, the hit patterns of each event are compared to expectations from simulation and rejected if inconclusive. Naturally, as WIMPs are expected to scatter exactly one time, any resolved multi-scatter event is removed. This is done by comparing the size of the second largest $S1$ or $S2$ to energy-dependent thresholds obtained from calibration and simulation data. A further sanity check is performed by comparing the width of the $S2$ signal and the reconstructed interaction depth of the interaction. This is motivated by the fact that the electron cloud produced after an interaction undergoes diffusion along the way. Hereby, the longitudinal component of the diffusion affects the width of the $S2$ signal as it is a measure of the arrival time of the electrons at the gas-phase. The temporal broadening Δt_σ caused by Brownian motion of a point-like source can be described by:

$$\Delta t_\sigma = \sqrt{\frac{2Dt_d}{v_d^2} + \sigma_0^2}, \tag{3.1}$$

where t_d is the mean drift time of the electron cloud, which is directly related to the interaction depth when the drift velocity v_d is taken into account. The term σ_0 is describing the signal width of a $S2$ signal induced by a single electron and the diffusion constant D incorporates detector parameters like temperature, density and electric field strength. By comparing the expected broadening Δt_σ with the reconstructed interaction depth non-physical signals, multi-scatter events, gas events

[1] For ER this corresponds $1.4\,\mathrm{keV_{ee}}$ to $10.6\,\mathrm{keV_{ee}}$.

and accidental coincides can be rejected. Details on this selection cut can be found in [65]. Finally, a comparison of the (x,y)-position reconstructed from the hit pattern using the standard neural network and the one using a likelihood-fit method is used to reject signals energy-dependently. Therefore, any event has to be reconstructed within $2\,\mathrm{cm}$ to $5\,\mathrm{cm}$ by both methods. The resulting total efficiency, derived from simulations and calibration data, is shown in fig. 3.3 as a function of nuclear recoil energy. The acceptance is reliably above $80\,\%$ except for low energies.

The most important part in order to confidentially claim a WIMP signal is to avoid the

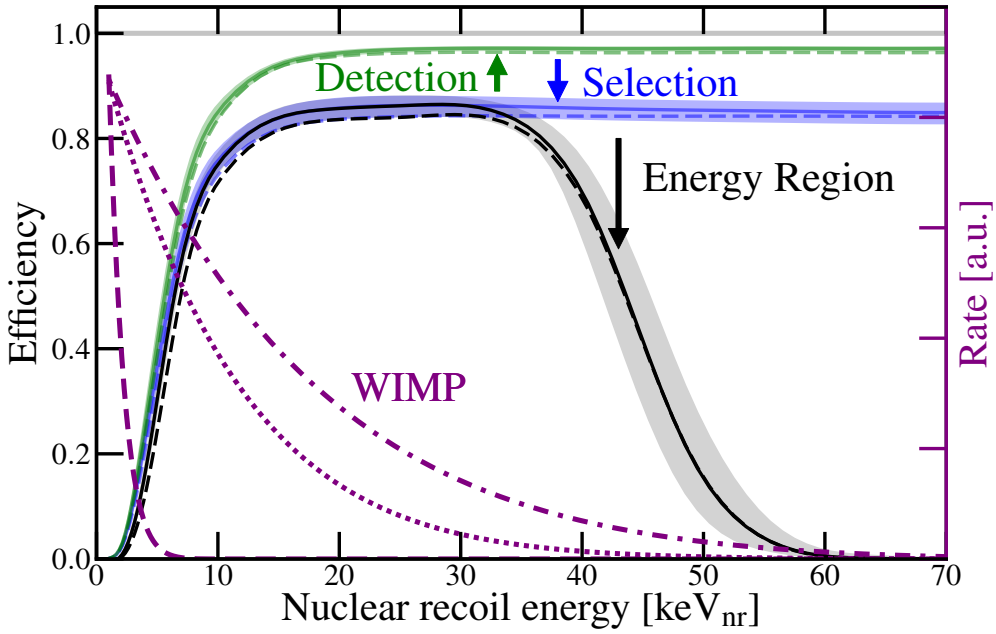

Figure 3.3.: Detection efficiency (acceptance) in XENON1T. Best-fit total efficiencies (black), including the energy ROI selection, for SR0 (dashed) and SR1 (solid) as a function of true NR energy (keV$_{NR}$). The efficiency of S1 detection (green) and that of S1 detection and selection (blue) are shown. The shaded bands show the $68\,\%$ credible regions for SR1. The expected spectral shapes (purple) of $10\,\mathrm{GeVc}^2$ (dashed), $50\,\mathrm{GeVc}^2$ (dotted), and $200\,\mathrm{GeVc}^2$ (dashed dotted) WIMPs are overlaid for reference. Figure and caption from [128]

possibility of a false claim caused by unexpected background. This requires complete knowledge of the background and especially a profound understanding of sources which could mimic a WIMP signal. As described in chapter 2 substantial efforts were undertaken to avoid, reduce and remove any kind of background sources. This lead to an ER background rate measured to be lower than $2.0 \cdot 10^{-4}\,\mathrm{events/kg/d/keV}$ in the inner one-ton cylinder used in [115]. For the updated analysis a larger fiducial volume (see below) could be used due to a better understanding of corrections to the applied electric field. Here an ER rate of $(82^{+5}_{-3}\,(\mathrm{sys}) \pm 3\,(\mathrm{stat})\,\mathrm{events/yr/ton/keV})$ is measured, which corresponds to about $2.2 \cdot 10^{-4}\,\mathrm{events/kg/d/keV}$. From these events, about $(7.7 \pm 1.3)\,\mathrm{events/yr/ton/keV}$ are contributed from $^{85}\mathrm{Kr}$. This corresponds to a concentration of natural krypton in xenon of about $0.66\,\mathrm{ppt}$. The obtained value is

about a factor of two higher than the lowest measured concentration during SR0 at the end of the krypton distillation campaign. An explanation for this could be either in the fact that small air leaks within the entire gas system add krypton over the time or that the concentration equilibrium was not reached at the time of sample extraction for the external krypton measurements during SR0. Another possibility would be outgassing from the detector materials in contact with the LXe.
Nonetheless, the contribution from $^{222}\mathrm{Rn}$ daughters, mainly $^{214}\mathrm{Pb}$, is the larger contribution with an expected event count of $(29 \pm 4)\,\mathrm{events/yr/ton/keV}$ to $(71 \pm 8)\,\mathrm{events/yr/ton/keV}$. The large spread is caused by the two different methods, which are both only capable to set a lower or upper limit on the $^{214}\mathrm{Pb}$ concentration. Insights into this background component will be given in section 4.2. Although, ER can be discriminated from NR with an efficiency of about $99.7\,\%$, the small remaining leakage still has to be considered for the later evaluation.
The second large type of background are the NR backgrounds, which mimic the WIMP signal directly. Here the largest contribution results from single scatter neutrons. These mostly originate from the detector materials (radiogenic), since the muon-induced neutrons are efficiently reduced by the active muon veto in the water tank [103]. While the radiogenic neutrons are not likely to be found in the inner center of the detector due to their origin at the edges of the TPC and their short mean free path of $15\,\mathrm{cm}$, the contribution from coherent elastic neutrino nucleus scattering (CEνNs) is distributed homogeneously over the detector. These NR are induced by solar neutrinos which scatter off the entire nucleus. This process is expected from standard model and has been observed for the first time by the COHERENT experiment in 2017 [129]. As its cross section depends on the energy, the main contributor for XENON1T are neutrinos originating from $^{8}\mathrm{B}$.
In addition to the ER and NR contributions, two further background sources have to be considered: accidental coincidences (AC) and surface background events. The former are caused by randomly paired lone $S1$ and lone $S2$ signals. These lone signals are mainly caused by energy depositions in regions of the detector which are not sensitive for both signal channels, e.g., an interaction in the liquid below the cathode will not produce an $S2$ but only an $S1$ signal. Surface background events are decays which happen at the wall but have a position reconstructed into the fiducial volume. These are usually decays producing an ER (e.g. $^{210}\mathrm{Pb}$), but due to charge-loss at the surface, they are detected with an $S2$-over-$S1$-ratio compatible with an NR. The contribution of this type ultimately dictates the limits of the fiducial volume, which is shown in fig. 3.4 (magenta line). The mass enclosed by it corresponds to $(1.30 \pm 0.01)\,\mathrm{t}$ and only events within this boundary are considered for the statistical inference. For this an extended unbinned likelihood in three dimensions ($cS1$,$cS2$,R) is used. In this case the likelihood $\mathcal{L}$ is defined as

$$\mathcal{L} = \mathrm{Poisson}(N_{\mathrm{tot}}|\mu) \prod_{i}^{\mathrm{events}} \left(\sum_{j}^{\mathrm{sources}} \frac{\mu^{(j)}}{\mu} \mathrm{pdf}^{(j)}(\text{event i}) \right), \tag{3.2}$$

where N_{tot} refers to the total number of observed events and μ to the total number of expected events. The number of expected events from a particular source j is

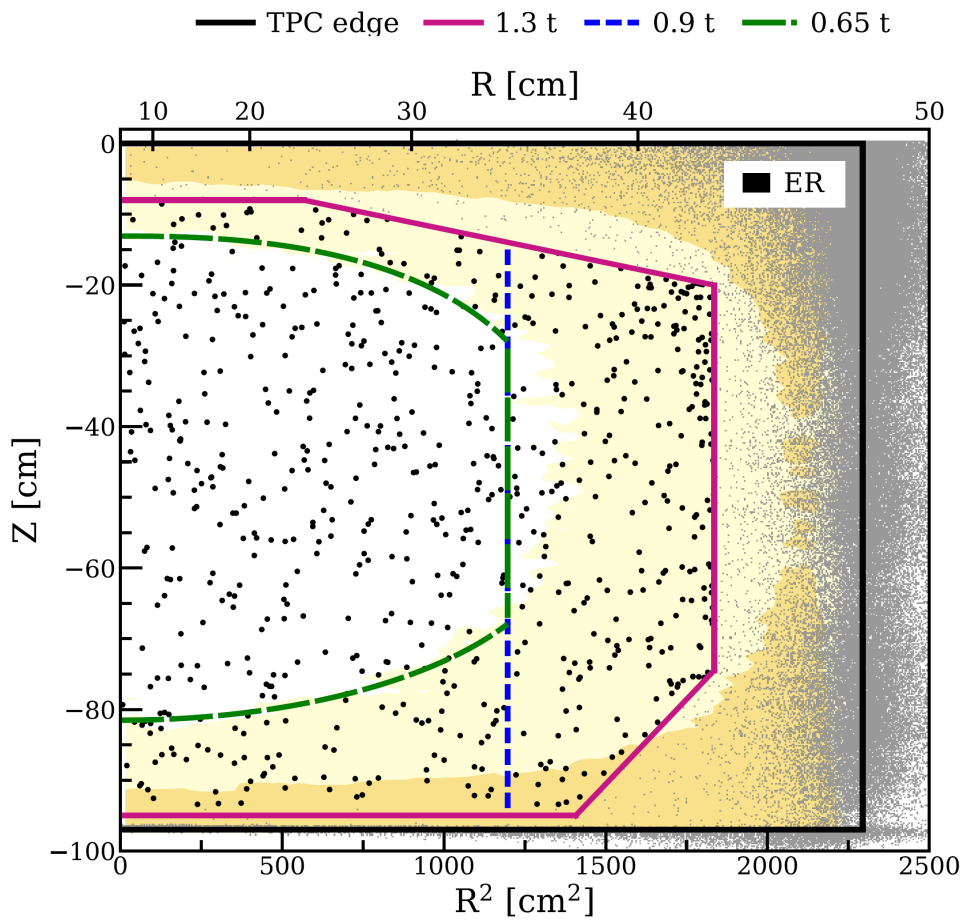

Figure 3.4.: Fiducial volume design in XENON1T. The blinded data is shown in their spatial distribution (Z,R^2). TPC boundaries are indicated in black and the $1.3\,\mathrm{t}$ fiducial volume is denoted by the magenta-colored line. Any event within this fiducial volume is shown in black, while events outside are represented by gray dots. These are just ER events as the blinding cut is still applied. An inner core of $0.65\,\mathrm{t}$ is marked in green. This volume was chosen based on the models for the radiogenic neutron contribution, which probability density is indicated in yellow shades (dark for 1σ and light for 2σ). A reference region similar to the previous results of SR0 is marked by the blue-dashed line. It corresponds to $0.9\,\mathrm{t}$. Figure with courtesy of the XENON collaboration.

denoted by $\mu^{(j)}$ and $\mathrm{pdf}^{(j)}$ is the probability density function for the respective source in the three-dimensional parameter space. From various studies of the detector response and background model constraints are derived and added to the likelihood multiplicatively. As only the number of extracted signal events is of interest, this likelihood is profiled and the other parameters are treated as nuisance parameters [130, 131, 65]. A modified profile likelihood test statistic ratio is used to derive the best-fit for the cross-section σ for a given signal model of a specific WIMP mass m_χ in order to account for the number of extracted signal events. The signal models are

built by using the standard astrophysical parameter as well as the approximation of the Helm form factor for the isoscalar spin-independent WIMP interaction (cf. 1.3). From the statistical inference confidence intervals ($90\,\%$ C.L.) can derived in the (σ,m_χ)-space according to [132, 20]. For the combined results in [128] a full Monte Carlo construction was used and the coverage was tested for varying values of the nuisance parameter. This avoids undercoverage by falsely applying the assumption of the asymptotic case of infinite events and no nuisance parameter, as it was done in [115]. This lead to an overestimated limit on the WIMP cross section for certain WIMP masses in this previous analysis (details in [65, 133]). The likelihood needs the input of the pdf's of each source as well as their model uncertainty, which are incorporated as nuisance parameter. These pdf´s are derived from models fitted to all calibration data sets simultaneously. Furthermore, simulations have been used to evaluate the neutron distribution and the model for the surface events has been build on control samples in the data. If now the region of interest is unblinded, the likelihood of origin for each event can be calculated depending on their position in the ($cS1$,$cS2$,R)-space. Additionally, in order to account for the radiogenic neutron distribution an inner core volume has been selected with a fiducial mass of $0.65\,\mathrm{t}$ as shown in fig. 3.4 (green line). This volume is used to classify the origin of the events in addition to the spatial likelihood in the radial dimension.
The unblinded data set is shown in fig. 3.5 in the ($cS1$,$cS2$)-space as well as in ($cS2$,R)-space. Two artificially introduced events (salt) were removed beforehand. For a comprehensive cross check of the results, a classical approach can be used by defining a reference region and compare the expectation from background alone with the measured data. This reference region corresponds to the blinded data in ($cS1$,$cS2$)-space, meaning anything below the -2σ-quantile of the ER band and above the -2σ-quantile of the NR band. Spatially, the reference regions are separated into the three volumes shown in fig. 3.4. The background expectation in the $1.3\,\mathrm{t}$ volume was determined to be $(7.36 \pm 0.61)\,\mathrm{events}$, and the data contained $14\,\mathrm{events}$. For the reference volume of $0.9\,\mathrm{t}$ in total $(1.62 \pm 0.28)\,\mathrm{events}$ were expected and $2\,\mathrm{events}$ were observed and for the inner core volume of $0.65\,\mathrm{ton}$ an expectation of $(0.80 \pm 0.14)\,\mathrm{events}$ is compared against $2\,\mathrm{events}$ in the data. While every reference region includes more events then expected, the gain in signal events should be proportional to the mass. This is not the case due to the large increase in outer volume. Additionally, this simple method does not account for the particular signal model and thus, the distribution of WIMPs in the energy space. This illustrates the benefits of the analysis in the full three-dimensional parameter space. It provides a likelihood of all possible sources and allows to calculate the p-value of the particular signal model in comparison with the background-only hypothesis. For this analysis in the full parameter space it was a priori decided to set a two-sided limit only in the case, where the event observation exceeds a 3σ-significance. The statistical inference shows no such excess in the analyzed data. As a result of this, only an upper limit with $90\,\%$ C.L. on the cross-section can be established, which is shown in fig. 3.6. The limit set by XENON1T is the most stringent for masses above $6\,\mathrm{GeV/c^2}$ and its most-strict exclusion for the WIMP-nucleon cross section σ_{nn} is $4.1 \cdot 10^{-47}\,\mathrm{cm}$ at $30\,\mathrm{GeV/c^2}$ WIMP mass. While the

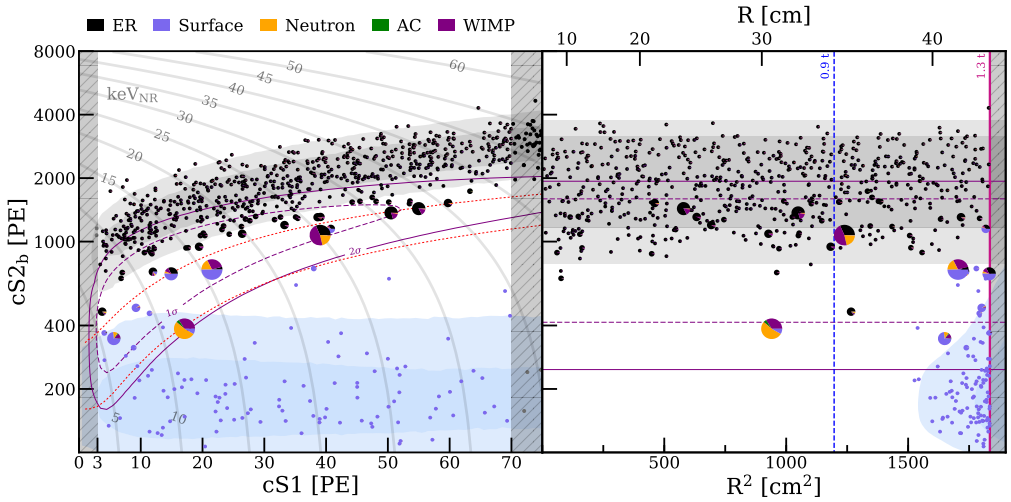

Figure 3.5.: Full data set (unblinded, desalted) in the respective parameter spaces. DM search data in the $1.3\,\mathrm{t}$ fiducial mass distributed in ($cS1$, $cS2b$) (left) and (R, $cS2b$) (right) parameter spaces. Events in the fiducial volume that pass all selection criteria are shown as pie charts representing the relative probabilities of the background and signal components for each event under the best-fit model. Here a $200\,\mathrm{GeV/c^2}$ WIMP was used with a resulting best-fit cross section of $\sigma_{nn} = 4.7 \cdot 10^{-47}\,\mathrm{cm}$. The color code for the respective sources in the pie chart is given in the legend. The size of the pie charts represents the probability of corresponding to a WIMP and for clearly identified background events small single-colored dots are used. The respective quantiles of the models for surface events (blue) and ER (gray) are denoted light colors (1σ-quantile) and dark colors (2σ-quantile). Additionally, the contours of the used WIMP model are drawn with the 1σ-percentile as dashed purple line and with the 2σ-percentile as solid purple line. An NR signal reference region (left, red dotted lines) and the maximum radii (right) of the $0.9\,\mathrm{t}$ (blue dashed) and $1.3\,\mathrm{t}$ (magenta solid) masses are shown. Gray lines correspond to iso-energy contours in terms of NR. Figure adapted from [128].

sensitivity of the experiment is about 7 times better than previous experiments (above $50\,\mathrm{GeV/c^2}$), as shown in fig. 3.6, the limit has less improved at higher WIMP masses. This points towards a statistical over-fluctuation of the background, which is expected in 50 percent of the cases.

Optimistic minds could interpret this as a first sign of an upcoming dark matter signal, but there is no scientific foundation for this. Nevertheless, future experiments as XENONnT or LZ will probe the parameter space further and clarify this easily due to the improved sensitivity by about an order of magnitude.

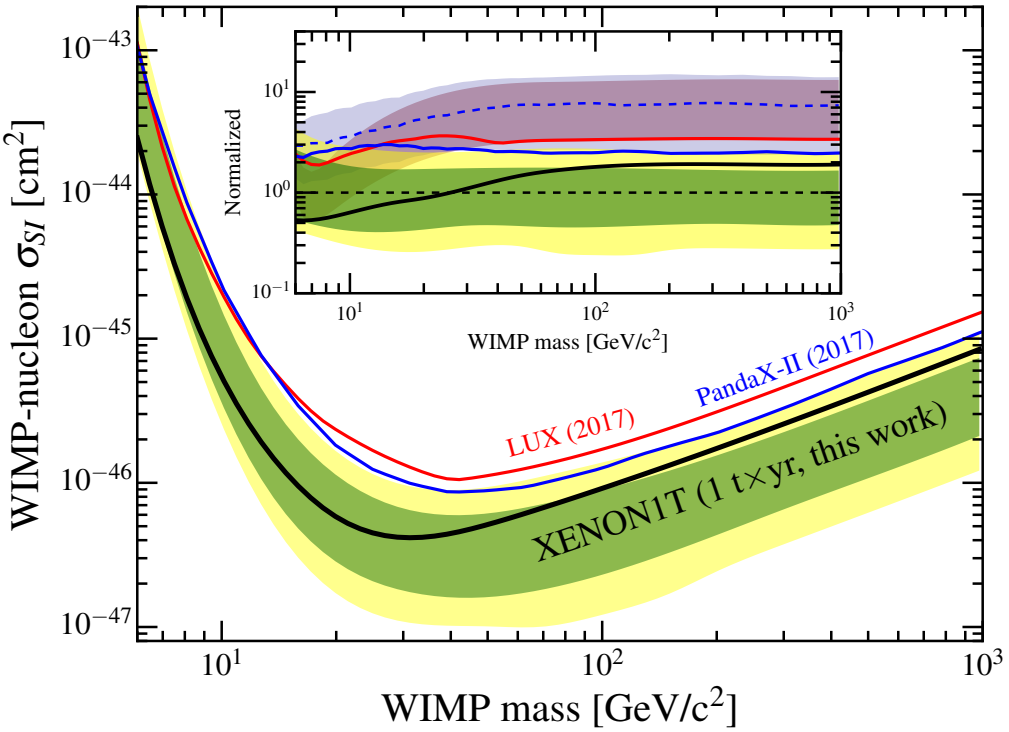

Figure 3.6.: Experimental exclusion limits on the WIMP-nucleon cross section σ_{SI} in dependence of the WIMP mass m_χ.) The cross section of the interaction between WIMP and nucleon (note: $\sigma_{SI} = \sigma_{nn}$ in eq. (1.28)) shown for the results presented in this section using the full exposure of XENON1T (black). Further experimental limits from the full exposure of LUX (red) [134] and PandaX-II (blue) are displayed as well. Emphasized in the subplot are the expected normalized sensitivities (bands) in comparison with the obtained limits (solid lines) for all three experiments. For XENON1T green denotes the 1σ-contour and yellow represents the 2σ-contour and it is remarkably the only experiment with a limit set above its sensitivity. Figure taken from [128].

3.2 Discrimination of different nuclear form factors

The standard analysis described in the previous section follows the common approach assuming an isoscalar spin-independent (SI) interaction between the WIMP and the xenon nucleus, with the underlying nuclear structure approximated by a so-called Helm form factor [135]. However, as shown in section 1.3.3 the limit given on the WIMP-nucleon cross section σ_{nn} for a given WIMP mass is related to the shape of the form factor $\mathcal{F}$ as well as on its normalization. This implies that standard limits on σ_{nn} are only valid if the SI interaction is indeed the dominant contribution to WIMP-nucleus scattering. If the isoscalar SI interaction is suppressed, e.g., in some supersymmetric models [136, 137, 138], other channels can not be neglected anymore. Models including the dynamics of the underlying strong interaction (QCD) as implemented in the framework of chiral effective field theory (ChEFT) introduce further classes of interaction channels as a correction to the dominant isoscalar SI interaction [11]. In case of a vanishing isoscalar component, the responses which can be still coherently enhanced are of particular interest.
In the event of a confirmed WIMP detection the nature of dark matter can be encrypted from the underlying WIMP-nucleus interaction. Naturally the questions arise if different interaction mechanisms could be distinguished and how much events are needed in order to achieve sufficient discrimination. This translates directly to the question which present or future experiment is able to provide the necessary discrimination for a given interaction strength of WIMPs with ordinary matter. One possibility for discrimination arises from the different momentum transfer q-dependences of the nuclear form factors involved. The study described below was published in [127] and is based on the most stringent limits at the time of publication, which are the SR0 results of XENON1T [115]. As described in the previous section the limits on the WIMP-nucleon cross section were pushed further by XENON1T in [128]. The implications on the updated results for this study are discussed where applicable. The other authors of [127] also contributed to the work presented in this section.

3.2.1 Set of nuclear form factors

For the analysis presented here and in [127] the nuclear form factors derived in [11] are considered and tested in a one-at-a-time approach. In a first step all contributions but the one operator of interest are neglected, which provides a pure signal model. In a second step it is evaluated if the different q-dependence allows to distinguish it from the standard Helm form factor.
Interactions calculated by ChEFT can be categorized into three different classes as presented in fig. 3.7. The diagram (a) represents contributions from single nucleons as they would arise from non-relativistic effective field theory (NREFT). These corrections

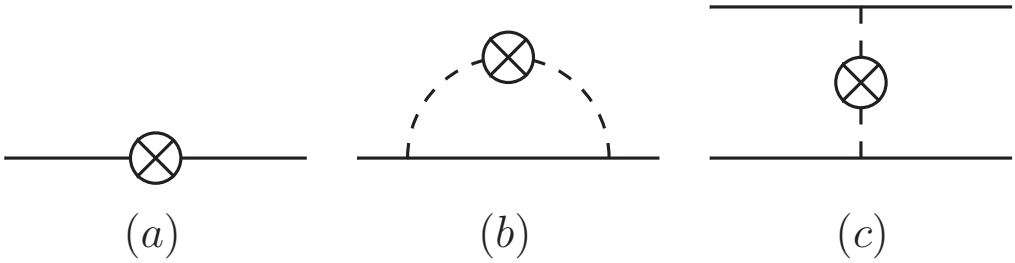

Figure 3.7.: Diagrams for WIMP–nucleon interactions in chiral EFT. Solid (dashed) lines refer to nucleons (pions) and crosses indicate the coupling to the WIMP. Diagram (a) represents a single-nucleon contribution, (b) a momentum-dependent radius correction, and (c) the coupling via a two-body current. Figure and caption from [127].

have been cataloged in terms of NREFT operators $\mathcal{O}_i$ in [139, 140, 141]. These are translated to a distinct set of nuclear responses, canonically referred to as M, Δ, Σ', Σ'', $\tilde{\Phi}'$, Φ''. Notably, the isoscalar M response is the standard response, which is commonly approximated by the Helm form factor.
Diagram (b) in fig. 3.7 illustrates so-called radius corrections which are related to momentum-dependent loop effects. While these terms share the same set of nuclear form factors as the single-nucleon contributions, they are suppressed by the momentum transfer q. The third category of contributions are two-body currents, which are described in section 1.3.3. These are shown in diagram (c) in fig. 3.7 and represent the coupling of the WIMP to two nucleons via their exchange pions leading to an exclusive set of nuclear responses.
Using these three categories of responses as elaborated in [11], the coherent enhanced contributions to the differential cross section (extended version of eq. (1.34)) can be written as:

$$\frac{\mathrm{d}\sigma}{\mathrm{d}q^2} = \frac{1}{4\pi v^2}\left|\sum_{I=\pm}\left(c_I^M - \frac{q^2}{m_N^2}\dot{c}_I^M\right)\mathcal{F}_I^M(q^2) + c_\pi\mathcal{F}_\pi(q^2) + \frac{q^2}{2m_N^2}\sum_{I=\pm} c_I^{\Phi''}\mathcal{F}_I^{\Phi''}(q^2)\right|^2 + \frac{1}{4\pi v^2}\left|\sum_{I=\pm}\frac{q}{2m_\chi}\tilde{c}_I^M\mathcal{F}_I^M(q^2)\right|^2. \tag{3.3}$$

Here, the form factors $\mathcal{F}_\pm^M$ and $\mathcal{F}_\pm^{\Phi''}$ correspond to the M and Φ'' responses. They can either couple in the same way to protons and neutrons (isoscalar, denoted by $+$) or have opposite coupling for protons and neutrons (isovector, denoted by $-$). $\mathcal{F}_\pi$ relates to the coupling to the exchange pions as described in section 1.3.3. More details on this particular form factor are given in the next section. The terms suppressed by q^2 in the first line of eq. (3.3) lead to the radius corrections. All remaining terms are produced by subleading NREFT operators. Following [11] two of those NREFT operators, which are numerically dominant, were selected to be included into the investigation. These are $\mathcal{O}_3$ (leading to the Φ'' response) and $\mathcal{O}_{11}$ (generating the non-interfering M response in the last line). In reference [11] the form factors $\mathcal{F}_\pm^M$, $\mathcal{F}_\pm^{\Phi''}$, and $\mathcal{F}_\pi$ are derived by using large-scale nuclear shell calculations for all stable

xenon isotopes. As a cross check, the nuclear excitation spectra of the xenon isotopes were calculated within the same framework and agreed with experimental data. Also, references [142, 143] showed that the relevant coherent form factors at low momentum transfer are not sensitive to the nuclear structure details of the nuclei involved. Therefore, the associated uncertainties are considered less relevant than the astrophysical ones [144] and are neglected within this work.
The q-dependences of the form factor used in the evaluation are shown in fig. 3.8 ordered by their respective amplitude in the region of interest.

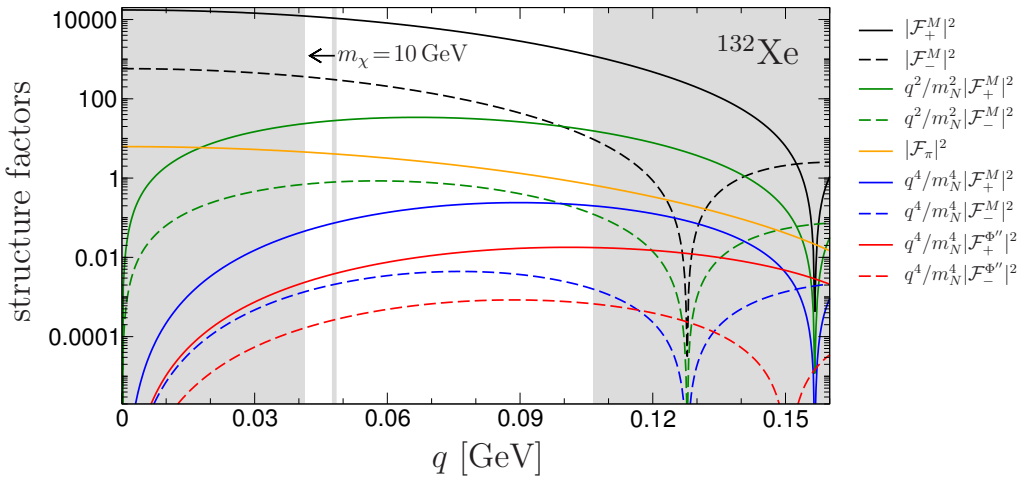

Figure 3.8.: Nuclear form factors for ^{132}Xe from [11] Solid/dashed lines refer to isoscalar/isovector nucleon couplings. The energy thresholds at $6.6\,\mathrm{keV_{NR}}$ to $43.3\,\mathrm{keV_{NR}}$, from the search window of the XENON100 detector, translate into the solid gray bands indicating the momentum transfers below the lower (above the upper) detector threshold at $q_{\mathrm{thr}}^{\mathrm{low}} = 0.0412\,\mathrm{GeV/c}$ ($q_{\mathrm{thr}}^{\mathrm{up}} = 0.1065\,\mathrm{GeV/c}$). The vertical gray line indicates the maximum momentum transfer for a WIMP with a mass of $m_\chi = 10\,\mathrm{GeV/c^2}$. For $m_\chi = 100\,\mathrm{GeV/c^2}$ and $m_\chi = 1\,\mathrm{TeV/c^2}$ the maximum momentum transfer exceeds $q_{\mathrm{thr}}^{\mathrm{up}}$. The ordering of the solid lines in the legend follows the ordering of the form factors in the search window of the detector. Figure and modified caption from [127].

3.2.2 Experimental setting

In order to compare present experimental efforts (XENON1T [96]) and future experimental programs (XENONnT [123, 40], DARWIN [126]) efficiently, a basic configuration has been chosen, which relies on publicly available XENON100 data [39]. This choice was motivated by the fact that only XENON100 had enough dedicated published analysis providing all necessary information [71]. The following assumptions are directly used from XENON100: the ER and NR background composition, its distribution in the ($cS1$,$cS2$)-space and the lower energy threshold ($6.6\,\mathrm{keV_{NR}}$). Additionally, the upper energy threshold ($43.3\,\mathrm{keV_{NR}}$) from the analysis of the main data set of XENON100 recorded between 2011 and 2012 is used [39]. The upper

energy threshold is not a detector property by itself, but could be adjusted for the specific analysis needs. It is fixed within this study since the aim of it is to answer the question whether a detector could distinguish an underlying non-standard nuclear form factor from the standard hypothesis without any change to its analysis. In fig. 3.8 the energy thresholds are indicated in dependence of momentum transfer q for three selected masses: $10\,\mathrm{GeV/c^2}$, $100\,\mathrm{GeV/c^2}$ and $1\,\mathrm{TeV/c^2}$. It has to be noted, that the energy thresholds do not correspond to a strict cut in energy or momentum space, but are smeared out due to Poisson fluctuations of the signals. This is important since the NR differential spectrum corresponding to a standard isoscalar SI WIMP-nucleus interaction is a falling exponential, and thus, the highest rate is expected at the lowest energies [7]. A significant fraction of information is lost below the detector's energy threshold, especially compared with a form factor that vanishes at $q = 0$. For this reason, the smearing at the energy threshold provides a bit of information below and has a non-negligible influence on the possibility of discrimination between different form factors. There are small further experimental differences of a XENON100-like detector used for the study and the other experimental-settings. One important example is the increase in light yield by more than a factor of 2 in XENON1T with respect to XENON100. This enhances the measurable quanta at the lower energy threshold, which extends the information at the most important part of the spectrum. Since these parameters and others are not yet known for the future detectors and are not fully publicly available for XENON1T, the study in this work uses the experimental parameters from XENON100. This will result in a conservative assumption on the discrimination power as experiments improve with additional experience.

3.2.3 Background model

The shape of the background event distribution in ($cS1$-$cS2b$)-space from the XENON100 data for both channels (ER and NR) is shown in fig. 3.9. The expected event rate (color scale in fig. 3.9) is normalized to the total number of generated events and thus, represents the probability for each bin. While the shape is fixed for all experimental settings, the rate has to be adjusted in order to account for the three experimental scenarios of interest (XENON1T-like, XENONnT-like, DARWIN-like). As the NR rate is a few orders of magnitude lower than the ER rate and its composition changes among the detectors, the ER contributions are used for scaling the absolute background rate b to the respective experiments. For the basic XENON100 configuration the ER background rate b_{XENON100} is given in [39] as $5.3 \cdot 10^{-3}\,\mathrm{events/kg/keV/d}$. From this the other experiments are scaled in order to adjust the rate to the different situations. For a XENON1T-like detector the rate is taken from the measurements in [115]. Since it is given as $1.9 \cdot 10^{-4}\,\mathrm{events/kg/keV/d}$, the scale factor from the ratio to XENON100 is $b_{\mathrm{XENON1T}} = 0.036\, b_{\mathrm{XENON100}}$. For a XENONnT-like detector the rate assumed in [40] is derived using an expected reduction of a factor of 100 for the dominant backgrounds induced by $^{222}\mathrm{Rn}$ daughters. Experience from XENON1T showed that this assumption is too optimistic. Therefore, a reduction factor of 10 is estimated with respect to XENON1T. Since the changes in other ER background components

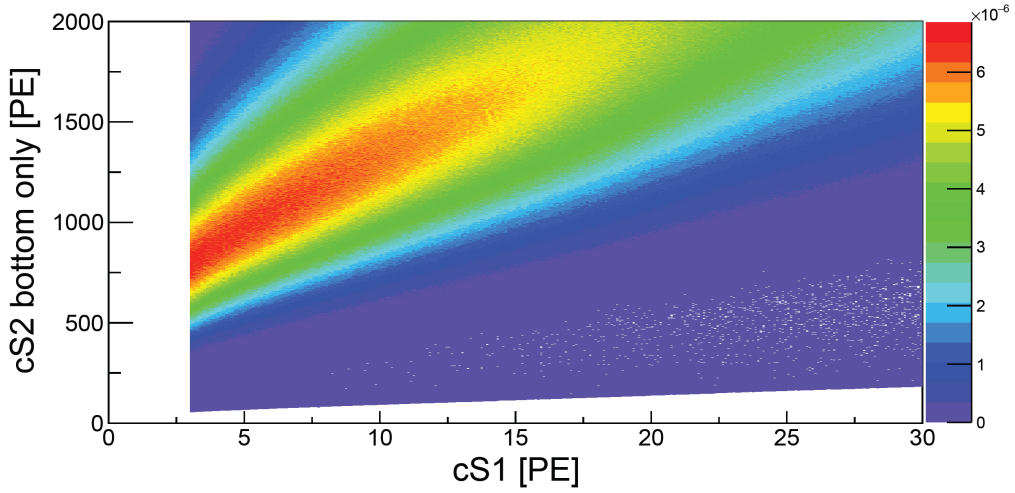

Figure 3.9.: Background event distribution according to XENON100. The event distribution is shown in ($cS2b$,$cS1$)-space. This histogram corresponds to the probability density function (pdf) of the background distribution. The probability for each bin is given by code and the binning is $0.1\,\mathrm{pe}$ for $cS1$ and $1\,\mathrm{pe}$-bins for $cS2b$. The sharp cut at low $cS1$ is given by the detector threshold.

are negligble, this translates directly into a scaling factor $b_{\mathrm{XENONnT}} = 0.0036\, b_{\mathrm{XENON100}}$. For the DARWIN-like setting a rate of $5.8 \cdot 10^{-6}\,\mathrm{events/kg/keV/d}$ is taken from [126]. The value is based only on the ER rate from xenon-intrinsic contaminations, which is a valid assumption for the selected mass cross section range in this study. This leads to a scaling factor of $b_{\mathrm{DARWIN}} = 0.0011\, b_{\mathrm{XENON100}}$. In table 3.1 the scale factors with respect to XENON100 are summarized next to the absolute background rates. A few aspects have to be considered given this choice of background scaling. First, the rate of NR backgrounds, which can be the more challenging component for certain form factors, decreases more pronounced than the ER background. For example, in XENON1T the fraction of NR events is about $8\,\%$ in SR0 in comparison to $17\,\%$ to XENON100 [115, 39]. This effect scales with the fiducial volume due to the self-shielding and is enhanced by active veto techniques in future dark matter detectors. Consequently, the ER scaling is a conservative assumption.

Table 3.1.: Background scaling for different experimental settings with respect to XENON100 ($5.3 \cdot 10^{-3}\,\mathrm{events/kg/keV/d}$)

Experiment	Event rate [$\mathrm{kg^{-1}\,keV^{-1}\,d^{-1}}$]	Scaling factor s
XENON1T	$1.9 \cdot 10^{-4}$	$3.6 \cdot 10^{-2}$
XENONnT	$1.9 \cdot 10^{-5}$	$3.6 \cdot 10^{-3}$
DARWIN	$5.8 \cdot 10^{-6}$	$1.1 \cdot 10^{-3}$

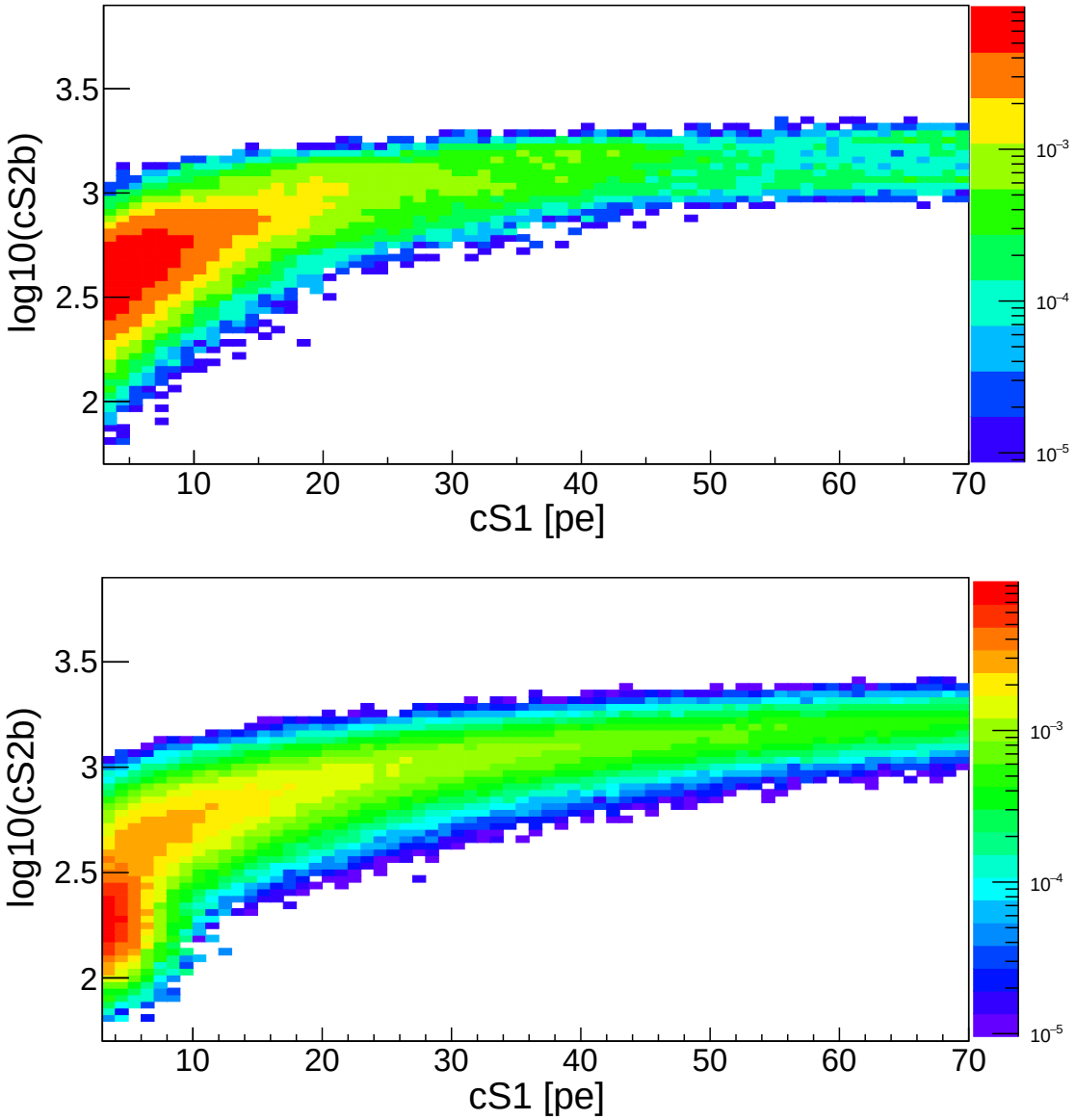

Figure 3.10.: Distribution of NR backgrounds in ($cS1$,$log_{10}(cS2b)$)-space in XENON100 and XENON1T. Top: Distribution of NR induced background events in XENON100. The color scale corresponds to the probability of an event per bin. The spectrum of XENON100 is dominated by neutrons induced from muons (>70 %) and radiogenic neutrons [101]. Bottom: Distribution of NR events in XENON1T. The main contributions are radiogenic neutrons and CEνNS events [115].

This is illustrated in fig. 3.10, where the overall NR compositions of XENON100 and XENON1T are shown. The change is related to two described properties: The active muon veto reduces the muon-induced NR to a negligible minimum [103] and the larger target mass reduces the radiogenic induced neutrons from the surrounding materials. Future detectors plan to use active neutron veto techniques [126] with liquid scintillators, which reduces the NR contributions further. However, at higher sensitivities coherent elastic neutrino–nucleus scattering (CEνNS) occurs, further changing the composition of the background in a way that depends on the source of the neutrinos and their respective energy.
As all these changes are difficult to quantify on the existing data and are also mostly based on Monte Carlo (MC) simulations, they are not taken into account in the study. Nevertheless, due to the increased drop in NR rate compared with ER, an incorporation of the exact NR contributions is expected to improve a possible discrimination between the underlying nuclear form factors in future detectors.
The actual background probability density function (pdf) in the further study is based on the full background model derived from data and simulations as used in [39]. This model is given in events per unit of exposure and energy and is defined up to $4000\,\mathrm{pe}$ in $cS2b$ and $30\,\mathrm{pe}$ in $cS1$ and is attached in fig. B.1. In order to transform it into a pdf a random generator was used with the input of the background model. This way $5 \cdot 10^8$ events were produced accordingly to the model using the *GetRandom2* function in the *TH2* class of the software package *ROOT* [145]. Afterwards the full distribution is divided by the total number of events, which ensures that the total integral is equal to one. Since the original model had events included below the energy threshold, these are correctly reproduced by the random fluctuations, which put the respective fraction of these events above the threshold. This threshold is then introduced as a strict cut at $3\,\mathrm{pe}$ in $cS1$-space. Additionally, any event with a $cS2b$ above $2000\,\mathrm{pe}$ after the random generation is removed since the signal models are not available for larger signals[2].

3.2.4 Signal model

The signal models for the respective form factor are generated using the same XEPHYR software package as employed in [146]. This framework takes the differential recoil spectrum (as given by eq. (1.35)) and convolves it with the statistical fluctuations of signal carriers as well as with the detector response function. The change from the input to the output in one dimension is shown in fig. 3.11. The further translation into ($cS1$,$cS2b$)-space is done by XEPHYR as well. The output is given in events per unit exposure and energy and thus, has to be normalized analogous to the background model to derive a probability density function. An outcome of this procedure is shown exemplary for the signal model derived for the standard Helm form factor assumption and for one momentum transfer dependent form factor in fig. 3.12. Signal models for the other seven form factors can be found in the appendix appendix B.1.

[2] As all signals predict vanishing likelihoods for signals this large, the choice of this cut has no impact on the discrimination power.

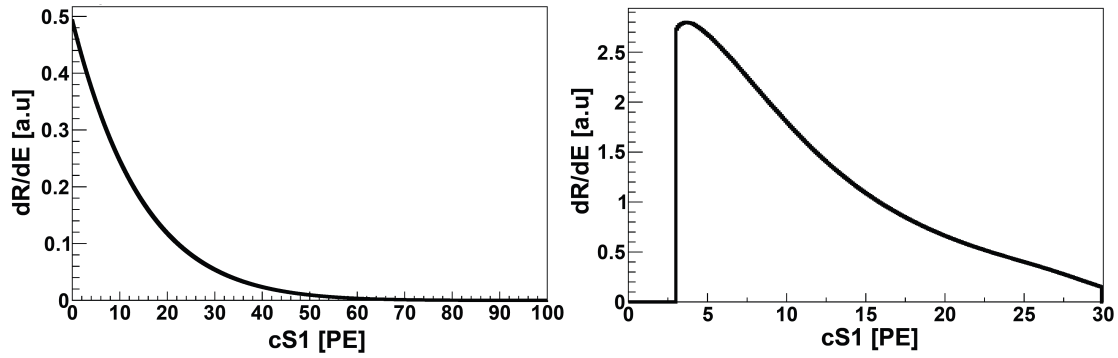

Figure 3.11.: Differential recoil spectra before and after XEPHYR. Left: Exemplary input of a featureless exponential differential recoil spectrum as given by eq. (1.35). The recoil energy is transformed into the $cS1$ signal using eq. (1.13). Right: The expected differential recoil spectrum in the real detector. Here, the statistical fluctuations, the detector response function as well as the detector energy threshold are included.

3.2.5 Monte Carlo and likelihood analysis

To answer the question, whether a present or future experiment could disentangle the underlying nuclear form factor without changing its analysis, a toy-Monte-Carlo (toy-MC) study will be performed. Starting point are the aforementioned signal models (8 new ones + Helm form factor) and one general background model. The outcome of any experiment is always a superposition of signal and background, where the fraction of each depends on different factors. While the background rate is given by the respective experiment (XENON1T-like, XENONnT-like, DARWIN-like), the signal rate depends on the interaction mechanism and is unknown so far. Nevertheless, for a given detector setting (material and energy window) a particular WIMP event rate can be calculated for each interaction based on the WIMP mass m_χ and cross section σ_0 (see eq. (1.35)). As the cross section for the standard isoscalar SI WIMP-nucleon interaction σ_{nn} is the most studied, it seems natural to express the interaction strength in equivalence to this cross section. So based on σ_{nn} a total mean number of expected signal events $\langle N_{\text{sig}} \rangle$ can be calculated as a function of the exposure with the target mass M and the measurement time t. So while $\langle N_{\text{sig}} \rangle$ is kept constant when investigating the different underlying nuclear form factors one-at-a-time, the shape of the signal model will differ in the ($cS1$,$cS2b$)-plane due to the different q-dependence of each term. In addition to this, the mean number of expected background events $\langle N_{\text{bkg}} \rangle$ is derived from the exposure as well as from the respective background rate (b_{XENON1T}, b_{XENONnT}, or b_{DARWIN}). From the mean number of signal and background events experimental outcomes are generated via toy-MC simulations using the respective probability density function for the two-dimensional distribution. Therefore, the resulting total pdfs are generated as following:

$$f_{\text{Hs+b/nHs+b}} = \frac{\langle N_{\text{sig}} \rangle \times f_{\text{Hs/nHs}} + \langle N_{\text{bkg}} \rangle \times f_{\text{b}}}{\langle N_{\text{sig}} \rangle + \langle N_{\text{bkg}} \rangle} \,. \tag{3.4}$$

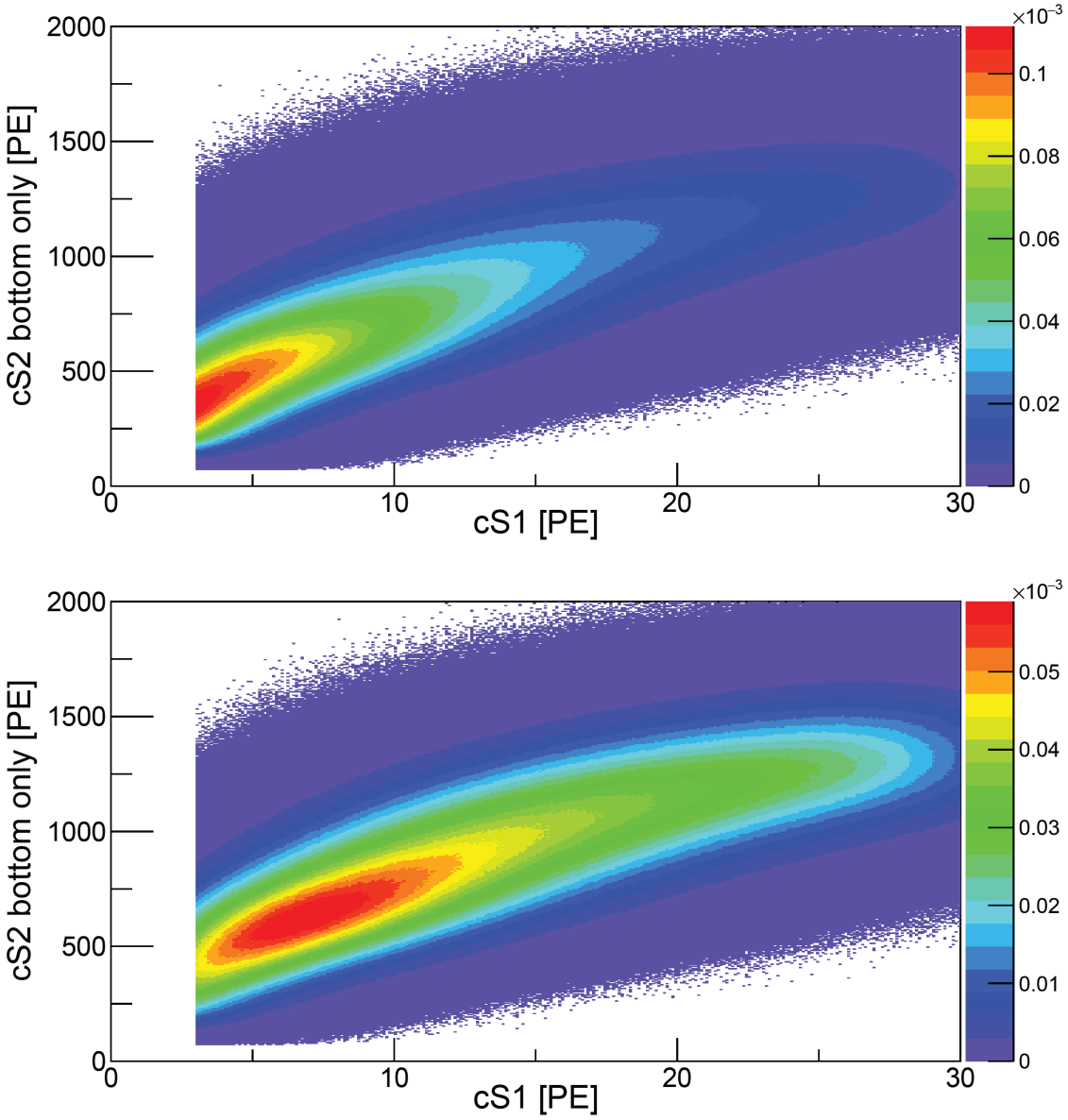

Figure 3.12.: Exemplary comparison of two signal models. Top: Probability density function based on the signal model using the standard isoscalar form factor $|\mathcal{F}_+^M|^2$, corresponding to the Helm form factor. The parameter space shows the scintillation signal ($cS1$) vs. the part of the ionization signal ($cS2$) that is seen in the bottom of the detector. The color code give the probability for each bin. Bottom: Probability density function for the signal with the underlying form factor $q^2/4m_\chi^2|\mathcal{F}_+^M|^2$ as well normalized to 1 in the given parameter space. Figure also published in [127].

Here, the pdfs of the chosen signal model for either the standard interaction (f_{Hs}) or the particular non-standard form factor (f_{nHs}) and the background model (f_{b}) are weighted with their expected mean number of events and normalized to the total number of events. An unbinned likelihood-ratio test is used to judge whether a signal of a non-standard form factor can be distinguished from the Helm form factor. So, the hypothesis of a Helm form factor signal acts as the null model and accordingly, the alternative model is the hypothesis of the respective different form factor. As a cross-check an analogous analysis is performed to investigate if a discrimination of the non-standard form factor signal model from a background-only signal is possible. This is necessary especially for q-dependent nuclear form factors (e.g. bottom figure in fig. 3.12). Their expected signal is shifted closer to the ER background dominated area, leading to an obvious discrimination from the standard expected signal. However, it would be rejected as a signal in the standard analysis due to its similarity to the background-only scenario.
For both cases the procedure is equivalent and exemplary it is carried out as following: Firstly, the toyMC generates an event distribution with a total number of events $N_{\mathrm{tot}} = \langle N_{\mathrm{sig}} \rangle + \langle N_{\mathrm{bkg}} \rangle$ drawn from the pdf with the Helm form factor signal and added background. Afterwards the total likelihood-ratio $Q_{N_{\mathrm{Hs}}}$ is computed by:

$$Q_{N_{\mathrm{Hs}}} = \prod_{i=1}^{N_{\mathrm{tot}}} \frac{p(x_i|f_{\mathrm{nHs+b}})}{p(x_i|f_{\mathrm{Hs+b}})} \,. \tag{3.5}$$

Here p denotes the probability of the event x_i given the respective probability density function f. The generation of this ratio for each of the n-trials in the toy-MC provides the null distribution, shown in fig. 3.13. For this distribution the $1.28\,\sigma$ quantile is derived, corresponding to the one-sided 90%-quantile. In a second step a data set with events y_i is created. These are distributed according to the non-Helm form factor signal model of interest with background added from the same background model as before. In this case the likelihood-ratio $Q_{N_{\mathrm{nHs}}}$ is given as

$$Q_{N_{\mathrm{nHs}}} = \prod_{i=1}^{N_{\mathrm{tot}}} \frac{p(y_i|f_{\mathrm{nHs+b}})}{p(y_i|f_{\mathrm{Hs+b}})} \,. \tag{3.6}$$

By repeating this for each trial an alternative distribution with n entries is generated. It is also illustrated in fig. 3.13 and has to be compared to the null distribution. This is done by determination of the fraction of entries above the previously-derived $1.28\,\sigma$ quantile, which is interpreted as discrimination power. So for the limiting case, where the underlying nuclear form factors are completely indistinguishable, the discrimination power is at $10\,\%$. The result can be interpreted in the following way: If n-experiments have been built, and all run for the given exposure, the discrimination power corresponds to the experiments which report an excess of $1.28\,\sigma$ in their data. The discrimination power is now calculated for different experimental settings and signal strengths expressed by σ_{nn} for each form factor of interest. Test of the alternative hypothesis against the background-only scenario is performed in the same fashion. For all calculations the sum of the logarithms of the likelihood ratios was used in order to overcome computational limitations.

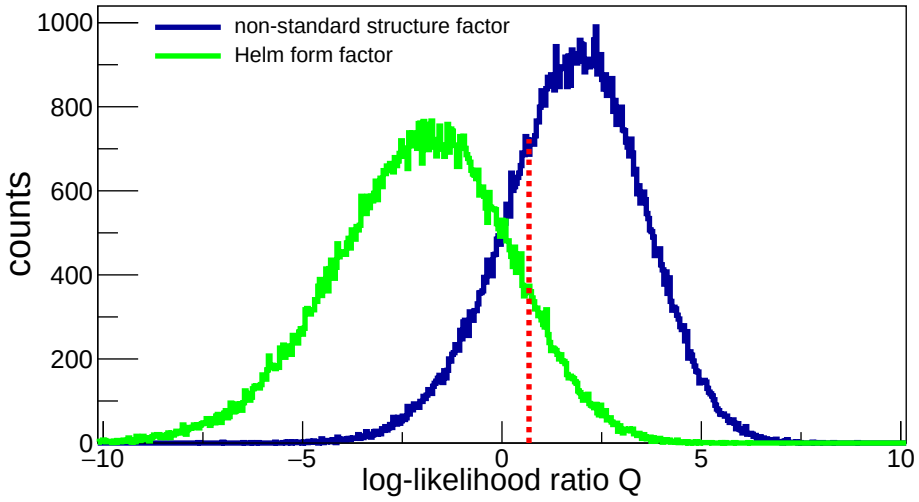

Figure 3.13.: Exemplary determination of the discrimination power of one particular parameter pair (exposure and experimental setting). Log-likelihood ratio distributions for the null distribution (green, based on the Helm form factor) and the alternative distribution (blue, based on a non-standard form factor). The $1.28\,\sigma$-line for the null distribution is marked in red. The discrimination power is given by integration of the alternative distribution from the reference red line towards infinity. In this case this yields a discrimination power of 74%. Figure and caption also in [127].

.

3.2.6 Results

Initially, three different WIMP masses: $m_\chi = 10\,\mathrm{GeV/c^2}$, $m_\chi = 100\,\mathrm{GeV/c^2}$, and $m_\chi = 1\,\mathrm{TeV/c^2}$ were included in the investigation. However, as illustrated in fig. 3.8 for the lightest mass the corridor of allowed momentum transfers is narrow. For this reason, there is no discrimination power for any of the form factors tested within this study at $m_\chi = 10\,\mathrm{GeV/c^2}$. This is even valid for the form factors with the largest difference due to their q-dependence probed in a future DARWIN-like detector. The results for the discrimination power at the other two WIMP masses[3] are shown in table 3.2 for XENON1T-like experiments, in table 3.3 for XENONnT-like experiments and table 3.4 for DARWIN-like experiments. Here the discrimination power is given for certain cross sections σ_{nn}.
The considered interaction strengths for each experiment, based on these cross sections, start from the sensitivity limits of the cutting-edge experiment at the time of the study [115]. Subsequently, they are lowered towards smaller cross sections as long as a significant discrimination power was found for one of the eight form

[3] In principle direct-detection dark matter experiments cannot accurately reconstruct the WIMP mass for large WIMP masses. However, the features in the recoil spectra, which allow one to differentiate between the form factors, do not depend strongly on the WIMP mass. Therefore, a scan in detail over the entire WIMP mass range is not needed.

factors. The starting point was therefore set to $\sigma_{nn} = 10^{-46}\,\mathrm{cm}^2$ for $m_\chi = 100\,\mathrm{GeV/c}^2$ and $\sigma_{nn} = 10^{-45}\,\mathrm{cm}^2$ for $m_\chi = 1\,\mathrm{TeV/c}^2$. The discrimination power is scanned as a function of exposure in a different range for each experiment: A XENON1T-like experiment was probed up in to $10\,\mathrm{t\,yr}$, a XENONnT-like (also LZ-like or PandaX-xT-like) experiment up to $30\,\mathrm{t\,yr}$, and for a DARWIN-like experiment was tested up to $200\,\mathrm{t\,yr}$. This corresponds roughly to $6\,\mathrm{years}$ of run time for all experiments, but depends on the achievable fiducial volume. The values given in the table are the respective discrimination powers after the full run time.

Exemplary, the discrimination power as a function of exposure for three non-standard

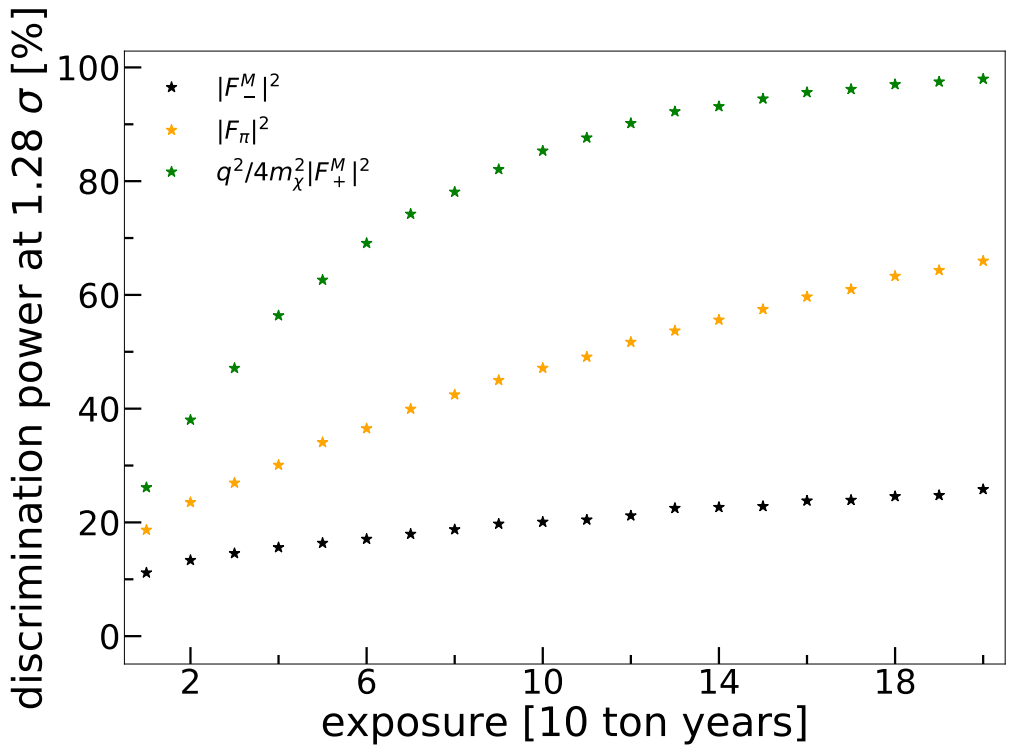

Figure 3.14.: Discrimination power versus exposure for three representative form factors. The isovector interaction $|\mathcal{F}_-^M|^2$ (black), the coupling to the exchange pion $|\mathcal{F}_\pi|^2$ (orange), and a momentum-dependent form factor $q^2/4m_\chi^2|\mathcal{F}_-^M|^2$ (green). The detector setting is DARWIN-like, with $m_\chi = 100\,\mathrm{GeV/c}^2$ and $\sigma_{nn} = 10^{-47}\,\mathrm{cm}^2$. The figure appeared also in [127].

form factors in the most optimistic DARWIN-like setting is shown in fig. 3.14. The selected WIMP mass is $m_\chi = 100\,\mathrm{GeV/c}^2$ and the corresponding cross section is $\sigma_{nn} = 10^{-47}\,\mathrm{cm}^2$. The pure isovector interaction $|\mathcal{F}_-^M|^2$ is the least distinguishable case, with only 26% of the experiments being able to report an excess after the full exposure. This can be explained by its similar shape as a function of q compared to the isoscalar case $|\mathcal{F}_+^M|^2$ as shown in fig. 3.8. For $|\mathcal{F}_\pi|^2$ (orange) the discrimination power is larger, reaching up to 66% for the full exposure of $200\,\mathrm{t\,yr}$. This makes it an interesting case which will be discussed in the next section. The most promising candidate for a discrimination, is a WIMP coupling purely via the interaction based

on $q^2/4m_\chi^2|\mathcal{F}_-^M|^2$ (green), which can be distinguished with $1.28\,\sigma$ in 98% of the cases at full exposure. This is representative for all form factors with a similar momentum dependence as seen within the tables 3.2–3.4. This pattern is fully consistent with the expectation from fig. 3.8: The more the q-behavior of a given form factor differs from $|\mathcal{F}_+^M|^2$, the better the two responses can be discriminated. For that reason, form factors that vanish at $q = 0$ always offer the highest discrimination power for a given exposure. This could be enhanced by expanding the energy window of the analysis, since the signal models based on these form factors usually have a non-negligible signal strength at energies above the standard search window. The comparison of the different experimental settings can be made from the comparison between the tables 3.2–3.4. Table 3.2 shows that if SR1 of XENON1T would have observed WIMP scattering corresponding to a σ_{nn} slightly higher than the previous limits from SR0 – close to $10^{-46}\,\mathrm{cm}^2$ for $m_\chi = 100\,\mathrm{GeV/c}^2$ and $10^{-45}\,\mathrm{cm}^2$ for $m_\chi = 1\,\mathrm{TeV/c}^2$ – a discrimination would have been possible if the underlying form factor actually corresponded to a signal vanishing at $q = 0$. Naturally, this would have needed a longer run time, which would have been provided since such a cross section would have been present as a large signal in SR1. In turn, future experimental efforts of XENONnT-like

Table 3.2.: Discrimination power (in $\%$) of the XENON1T settings after $10\,\mathrm{t\,yr}$ of exposure.

m_χ	$100\,\mathrm{GeV}$		$1\,\mathrm{TeV}$	
$\sigma_{nn}\,[\mathrm{cm}^2]$	10^{-46}	10^{-47}	10^{-45}	10^{-46}
$\lvert\mathcal{F}_-^M\rvert^2$	17	10	21	11
$q^2/4m_\chi^2\lvert\mathcal{F}_+^M\rvert^2$	94	19	98	20
$q^2/4m_\chi^2\lvert\mathcal{F}_-^M\rvert^2$	74	16	90	17
$q^4/m_{nn}^4\lvert\mathcal{F}_+^M\rvert^2$	100	25	100	28
$q^4/m_{nn}^4\lvert\mathcal{F}_-^M\rvert^2$	100	23	100	25
$\lvert\mathcal{F}_\pi\rvert^2$	38	13	48	14
$q^4/4m_{nn}^4\lvert\mathcal{F}_+^{\Phi''}\rvert^2$	100	26	100	30
$q^4/4m_{nn}^4\lvert\mathcal{F}_-^{\Phi''}\rvert^2$	100	25	100	29

experiments are needed as shown in table 3.3. The form factors vanishing at $q = 0$ have the highest probability of being discriminated in this experimental setting. The chance of discrimination of $|\mathcal{F}_\pi|^2$ from the Helm form factor was given prior the SR1 results, but now a discrimination including $|\mathcal{F}_\pi|^2$ would only be reliably possible in a DARWIN-like experiment. For the isovector $|\mathcal{F}_-^M|^2$ interaction the new results from XENON1T put even the DARWIN experiment to its limit, and a discrimination in only about $40\,\%$ of the cases would still be possible at high WIMP masses. So in order to separate the leading isoscalar and isovector interaction the study of only one target isotope appears insufficient and, thus, a comparison of different target nuclei will be needed to disentangle these two mechanisms.

The advantage of the DARWIN-like experiment is shown in fig. 3.15, which illustrates the discrimination power as a function of run time for all three experiment generations in the case of a form factor $q^2/4m_\chi^2|\mathcal{F}_+^M|^2$ and a WIMP mass of $m_\chi = 1\,\mathrm{TeV/c^2}$. The chosen cross section ($\sigma_{nn} = 10^{-46}\,\mathrm{cm}$) is currently not excluded by any experimental result.

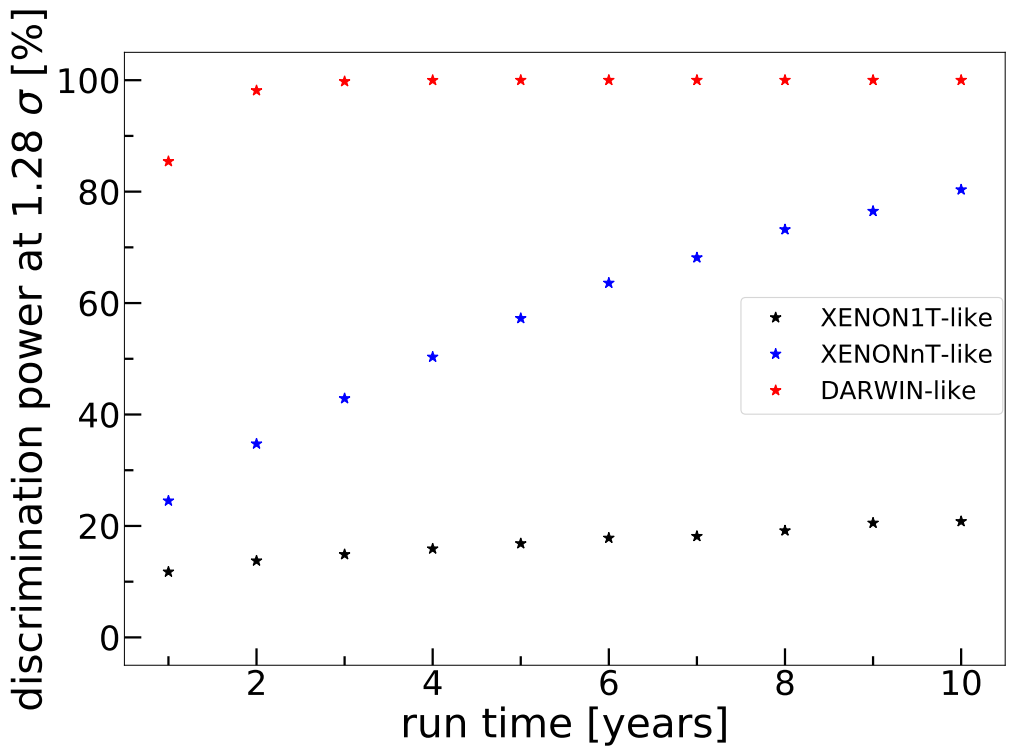

Figure 3.15.: Comparison of the discrimination power during the run time of the three different experimental settings. For the XENON1T-like setting (black) a fiducial target of $1\,\mathrm{t}$ is assumed, for the XENONnT-like (blue) a $4\,\mathrm{t}$ fiducial target, and for the DARWIN-like setting (red) we assumed $30\,\mathrm{t}$ fiducial volume. The signal is generated using the form factor $q^2/4m_\chi^2|\mathcal{F}_+^M|^2$, a WIMP mass $m_\chi = 1\,\mathrm{TeV/c^2}$, and the mean number of events equivalent to $\sigma_{nn} = 10^{-46}\,\mathrm{cm^2}$. Figure is also printed in [127].

Table 3.3.: Discrimination power (in %) of a XENONnT-like experiment after $30\,\mathrm{t\,yr}$ of exposure.

m_χ	100 GeV			1 TeV		
$\sigma_{nn}\,[\mathrm{cm}^2]$	10^{-46}	10^{-47}	10^{-48}	10^{-45}	10^{-46}	10^{-47}
$\lvert\mathcal{F}_-^M\rvert^2$	37	13	10	21	15	11
$q^2/4m_\chi^2\lvert\mathcal{F}_+^M\rvert^2$	100	59	14	100	71	15
$q^2/4m_\chi^2\lvert\mathcal{F}_-^M\rvert^2$	100	39	13	100	53	13
$q^4/m_{nn}^4\lvert\mathcal{F}_+^M\rvert^2$	100	90	16	100	95	17
$q^4/m_{nn}^4\lvert\mathcal{F}_-^M\rvert^2$	100	81	15	100	87	16
$\lvert\mathcal{F}_\pi\rvert^2$	89	23	12	98	28	12
$q^4/4m_{nn}^4\lvert\mathcal{F}_+^{\Phi''}\rvert^2$	100	93	17	100	98	19
$q^4/4m_{nn}^4\lvert\mathcal{F}_-^{\Phi''}\rvert^2$	100	89	17	100	96	17

Table 3.4.: Discrimination power (in %) of a DARWIN-like experiment after $200\,\mathrm{t\,yr}$ of exposure.

m_χ	100 GeV			1 TeV		
$\sigma_{nn}\,[\mathrm{cm}^2]$	10^{-46}	10^{-47}	10^{-48}	10^{-45}	10^{-46}	10^{-47}
$\lvert\mathcal{F}_-^M\rvert^2$	94	26	12	100	35	13
$q^2/4m_\chi^2\lvert\mathcal{F}_+^M\rvert^2$	100	100	34	100	100	41
$q^2/4m\chi^2\lvert\mathcal{F}_-^M\rvert^2$	100	98	25	100	100	32
$q^4/m_{nn}^4\lvert\mathcal{F}_+^M\rvert^2$	100	100	55	100	100	63
$q^4/m_{nn}^4\lvert\mathcal{F}_-^M\rvert^2$	100	100	47	100	100	53
$\lvert\mathcal{F}_\pi\rvert^2$	100	66	17	100	81	20
$q^4/4m_{nn}^4\lvert\mathcal{F}_+^{\Phi''}\rvert^2$	100	100	58	100	100	69
$q^4/4m_{nn}^4\lvert\mathcal{F}_-^{\Phi''}\rvert^2$	100	100	55	100	100	64

So far the results in terms of the discrimination power with respect to the Helm form factor do not take the discrimination power with respect to the pure background into account. This discrimination power for the non-Helm form factors in comparison to the background-only hypothesis is larger for all form factors, with the exception of the nuclear form factors involving a kinematic q^4 suppression (see appendix B.2). There the capability of discrimination for the Helm form factor signal with background is greater than for the background only scenario. This is shown in fig. 3.16 for a given example. The observation of this behavior for the q^4-dependent form factors has important consequences for the interpretation of direct-detection limits since a true dark matter signal could be rejected if its interaction mechanism were based on one of these underlying form factors as long as the Helm form factor signal is the only hypothesis tested in the experimental analysis. This illustrates that the consideration of subleading responses is not only important to potentially extract further information on the nature of the WIMP, but that in some cases a signal could be missed if the analysis were restricted to the standard Helm form factor.

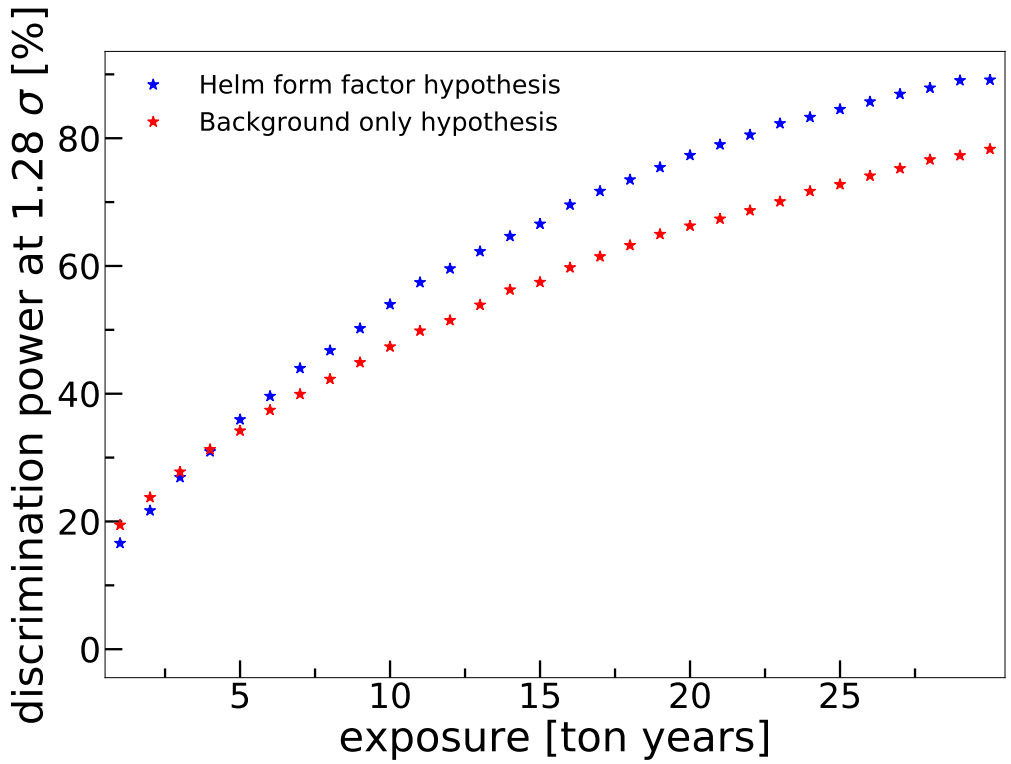

Figure 3.16.: Exemplary discrimination power with respect to the background. The comparison of the discrimination power is taken from a XENONnT-like experiment for a signal based on the form factor $q^4/4m_N^4|\mathcal{F}_-^{\Phi''}|^2$ with respect the Helm form factor signal (blue) and for the same signal versus a pure background signal hypothesis (red). Here $\sigma_{nn} = 10^{-47}\,\mathrm{cm}^2$ is chosen for a mass of $m_\chi = 100\,\mathrm{GeV/c}^2$. Figure appeared also in [127].

3.3 WIMP-pion coupling

From the selection of interaction mechanisms in the previous section the direct isoscalar coupling to the exchange pions of two nucleons within the xenon nucleus is an interesting case to study. Although the WIMP-pion coupling is sub-dominant with respect to the leading SI isoscalar interaction, the interaction strength is larger than the one for the well-studied SD cases[69, 68]. For typical nuclear targets with about 100 nucleons (A = 100) the coupling strength scales as

$$A^2 \gg 4\left(\frac{m_\pi}{\Lambda_\chi}\right)^6\left(\frac{m_{nn}}{m_\pi}\right)^2 A^2 \gg \frac{4}{3}\frac{J+1}{J}\langle \mathbf{S}_{n/p}\rangle^2, \tag{3.7}$$

where the isoscalar SI case is directly related to A^2, while the WIMP–pion coupling in the middle term is suppressed but still coherently enhanced. The masses m_π correspond to the pion mass and m_{nn} to the mass of the nucleon The suppression factor $(m_\pi/\Lambda_\chi)^6$ arises from the subleading Q^3 nature of two-body currents entering squared in the cross section. $\Lambda_\chi \sim 500 - 600\,\mathrm{MeV}$ corresponds to the breakdown scale of ChEFT. For the two xenon isotopes with non-vanishing spin, necessary for the SD coupling, the above scaling is well reflected by the actual hierarchy of the structure factors with relative strengths $1.7 \cdot 10^4 \gg 1.1 \cdot 10^3 \gg 0.34{,}0.13$, for ^{129,131}Xe [147, 11]. Despite this fact, no experimental limit exist on the WIMP-pion coupling. The first result will be presented within this section using the entire XENON1T data set (as in [128]). They have been derived in collaboration with Martin Hoferichter, Javier Menéndez, Achim Schwenk and Philipp Klos on the theoretical part and Knut Mora on the statistical part [74].
In order to provide the first result on the WIMP-pion interaction, a transition from the WIMP-nucleus interaction presented in section 3.1 has to be performed. Therefore, the differential recoil spectrum in eq. (1.35) has to be rewritten in terms of the cross section of the WIMP-pion coupling σ_π:

$$\sigma_0 = 4\sigma_\pi \frac{\mu_N^2}{\mu_\pi^2}. \tag{3.8}$$

Here, the reduced mass between the WIMP and the pion is given by μ_π. The additional factor four in comparison with eq. (3.8) is included due to different hadronic couplings for the pion [11]. The coherent enhancement A^2 is absorbed into the form factor $\mathcal{F}_\pi$. Inserting now σ_π into eq. (1.35) and changing from $\mathcal{F}_+^M$ to $\mathcal{F}_\pi$, the differential recoil spectrum is obtained:

$$\frac{\mathrm{d}R}{\mathrm{d}E_\mathrm{r}} = \frac{2\rho_0\sigma_\pi}{m_\chi \mu_\pi^2}\left|\mathcal{F}_\pi(q^2)\right|^2 \int_{v_\mathrm{min}}^{v_\mathrm{esc}} \frac{f(\mathbf{v},t)}{v} d^3v. \tag{3.9}$$

Here, v_min is still valid as defined in eq. (1.36) since the nucleus is still involved in the momentum transfer. The differential recoil spectrum (illustrated in fig. 1.13) is now fed into the signal model generator of XENON1T used also for the SI WIMP-nucleon limit. This framework accounts for the detector smearing as well as the statistical

fluctuations in the photon detection. The signal model for a WIMP with an exemplary mass of $m_\chi = 1\,\mathrm{TeV/c^2}$ is shown for the WIMP-pion interaction and the WIMP-nucleon interaction in fig. 3.17. The same statistical inference is used as in the standard

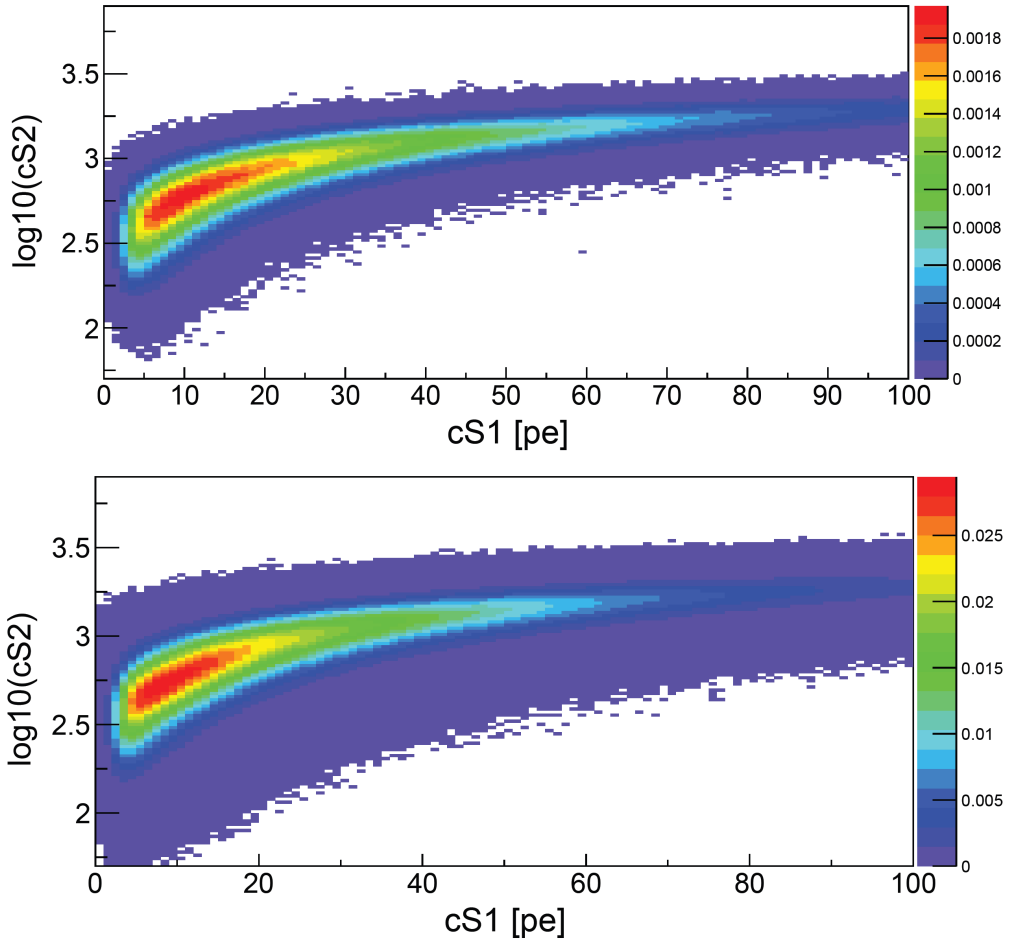

Figure 3.17.: Signal model distribution for a 1 TeV/c^2-WIMP in ($\log_{10}(cS2)$,$cS1$)-space in XENON1T. Top: Probability density function for the signal model based on the nuclear form factor related to the exchange pion coupling $\mathcal{F}_\pi$. The color bar indicates the probability for each bin. Bottom: Probability density function for the signal model based on the standard isoscalar SI interaction ($\mathcal{F}_+^M$). As the lower part was simulated with higher statistics a few more bins are populated with negligible probabilities. Only slight differences can be seen as the WIMP-pion coupling signal is a more washed out towards higher $cS1$.

SI search (see section 3.1 and [128]) to derive a result comparing the respective signal hypothesis for each mass to the background only hypothesis. No significant excess has been found, which was completely expected given the results from the standard search and the similarity of the signal models. The respective limit on the cross-section as a function of mass is presented in fig. 3.18 together with the expected sensitivity of the one ton year exposure data of XENON1T. It has been derived using

ten different masses with interpolation between them and an extrapolation towards higher WIMP masses. This is a valid approximation as the shape of the recoil spectrum does not change anymore after $200\,\mathrm{GeV/c^2}$. The best exclusion using the full statistical inference method from XENON1T is found at $\sigma_\pi = 6.4 \cdot 10^{-46}\,\mathrm{cm}^2$ for a WIMP of about $30\,\mathrm{GeV/c^2}$ coupling to the exchange pions. The lowest p-value for the background only

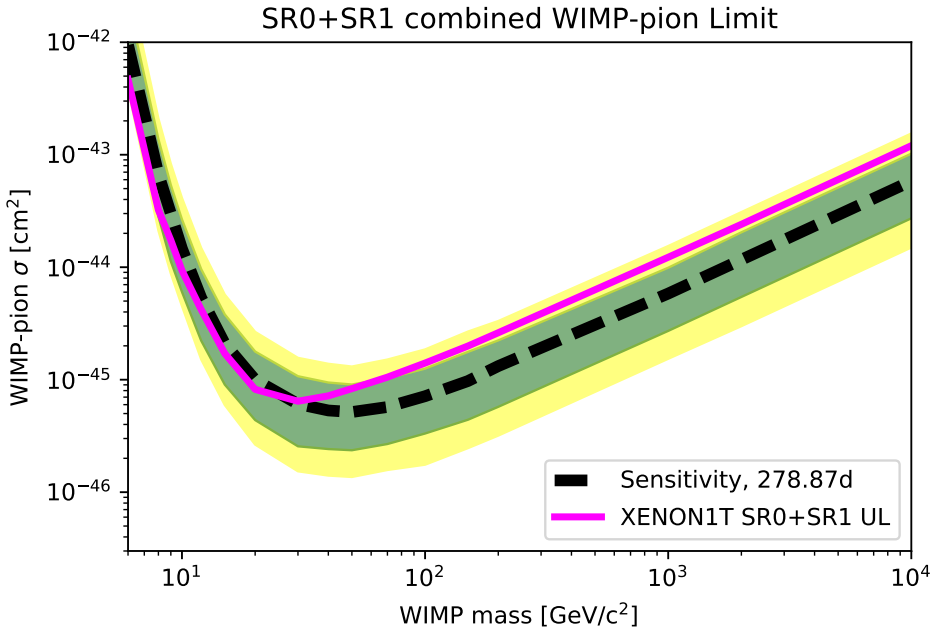

Figure 3.18.: Exclusion limits on the WIMP-pion cross section σ_π as a function of the WIMP mass m_χ. The derived limit (pink) is shown with the projected mean sensitivity (dashed black). Furthermore, the 1σ and 2σ-band of the sensitivity projection are denoted in green and yellow.

hypothesis is reached at masses above of $200\,\mathrm{GeV/c^2}$ with $p = 0.14$. As for the WIMP-nucleon case the excess at higher masses seems to result from the overfluctuation of the background contributions. In general the shape of the limit and the sensitivity is similar to the standard analysis with an increase of about $8\,\%$ in comparison with a simple scaling, which is expected given the similarities of the signal distribution shapes.

Chapter 4

Search for Two-Neutrino double electron capture of ^{124}Xe

Rare double beta decays have been explored with different detector technologies for various isotopes. While the neutrinoless decay mode ($0\nu\beta\beta$) has not been observed so far [80], there are a few direct observations of the two-neutrino mode ($2\nu\beta\beta$) of the decay [148]. For xenon there is an observation of the $2\nu\beta\beta$ of $^{136}\mathrm{Xe}$ with a half-life of $\sim T_{1/2} > 2.2 \times 10^{21}$ yr [149, 150]. In contrast to the electron emission double beta decays, the positron emission or electron capture processes are not directly observed yet. Only in the case of the two-neutrino double electron capture (2νECEC) there is an indirect observation from geochemical surveys for $^{130}\mathrm{Ba}$ [21, 151] and an direct indication for the decay in $^{78}\mathrm{Kr}$ [22, 23]. For xenon two isotopes, namely $^{124}\mathrm{Xe}$ (Q = 2856.73 keV [81]) and $^{126}\mathrm{Xe}$ (Q = 920 keV [75]), are predicted to decay via this mode. So far, only lower limits on the half-life have been derived [152, 86], which are given at $T_{1/2} > 2.1 \times 10^{22}$ yr for $^{124}\mathrm{Xe}$ and $T_{1/2} > 1.9 \times 10^{22}$ yr for $^{126}\mathrm{Xe}$ with $90\,\%$ confidence level.

The dark matter detectors of the XENON project fulfill all the criteria that are needed for a 2νECEC search: large amounts of xenon, keV energy resolution, stable long-term operation and low background rates in the energy region of interest as well as a threshold below the energy of interest.

The 2νECEC of $^{124}\mathrm{Xe}$ results in a particle cascade from the refilling of two holes in the atomic shell. Since the simultaneous capture of two K-shell electrons has the highest probability ($76.7\,\%$ [153]), only this process is considered in the further analysis denoted as 2νKK. Also, both isotopes provide a non-distinguishable signature. The further part will focus on $^{124}\mathrm{Xe}$, as its predicted decay rate is higher caused by the larger phase space ($\Gamma \propto Q^5$) and slightly higher abundance.

The detailed calculation of the decay's signature has to take into account which quanta are emitted following the capture processes. Therefore, a simulation for the single electron capture using the RELAX code [154] has been performed yielding that $78.4\,\%$ of the binding energy per K-shell vacancy ($31.8\,\mathrm{keV}$) is released in a single

x-ray followed by a cascade of Auger electrons that carry $21.1\,\%$ of the energy. The remaining energy is released when the daughter isotope $^{124}\mathrm{Te}$ returns to a neutral state by capturing electrons from the continuum. This way $0.2\,\%$ of the energy is released via electrons and x-rays, which do not exceed the average energy ($13.7\,\mathrm{eV}$, see section 1.2) to produce a signal carrier in xenon.
All quanta are released within time scales below nanoseconds. This is to close in time to be separated from each other given the time resolution of the XENON detectors. Moreover, no spatial distinction is possible as the attenuation length of electrons or x-rays at this energy range is below below the spatial resolution of the detector [155]. Therefore, a single peak is expected, which has its mean value not at the expected position of two times the energy per K-shell vacancy ($63.6\,\mathrm{keV}$), but, as direct studies of the two-shell vacancy suggest, at $(64.457 \pm 0.012)\,\mathrm{keV}$ [81]. The reason for this is a changing binding energy for the second K-shell electron once the first one is captured. Since this changes the energy of each released quantum only slightly, it is assumed that the same amount of energy is released as derived previously in the single electron capture case including the fraction which is lost per K-shell vacancy. So in total the signal from the 2νKK is expected at $(64.33 \pm 0.13)\,\mathrm{keV}$. The uncertainty is derived from the systematic error of the RELAX code.
The search for this energy signature with XENON100 and XENON1T will be presented in the two following sections. For XENON100 the analysis has been published in [156] and the results obtained from XENON1T are prepared for publication [157].

4.1 Search for Two-Neutrino Double Electron Capture with XENON100

A previous investigation of 2νKK has been carried out by researchers outside the XENON collaboration using publicly available XENON100 data [158]. However, due to lack of insight into the full information the limit on the half-life of $T_{1/2} > 1.6 \times 10^{21}$ yr at $90\,\%$ C.L. left open questions. First of all, the available data was not well suited for a signal search due to the coarse binning. Second, the limit was calculated from the average background rate outside the expected signal region and, third, the assumed isotopic abundance of ^{124}Xe did not match the real situation.
The correct value from the full analysis that is presented here has been derived in collaboration with Moritz von Sievers and has been published in [156]. Data from the second science run[1] of XENON100 [39] was used. In total $224.6\,\mathrm{d}$ of data, taken between 28th February 2011 and 31st March 2012, were analyzed. With the same fiducial volume selection of $(34.0 \pm 0.2)\,\mathrm{kg}$ as in the dark matter search a total exposure of $(20.9 \pm 0.1)\,\mathrm{kg\,yr}$ xenon was used. This corresponds to $(17.6 \pm 0.1)\,\mathrm{g\,yr}$ of $^{124}\mathrm{Xe}$ exposure and was derived from the abundance $\eta_{\mathrm{Xe100}} = (8.40 \pm 0.07) \times 10^{-4}$ of $^{124}\mathrm{Xe}$ in the xenon target. The slight difference with respect to the natural abundance $\eta_{\mathrm{nat}} = (9.52 \pm 0.03) \times 10^{-4}$ [159] was caused by a mixture of $86.9\,\%$ natural xenon gas with $13.1\,\%$ gas, which had especially been reduced in $^{124}\mathrm{Xe}$ and $^{136}\mathrm{Xe}$. The uncertainty of the abundance was given by the uncertainty on the natural abundance and by the uncertainty on the weight measurement of the filled xenon.
Since the energy reconstruction adds an uncertainty to the one already given by the systematic uncertainty from the relaxation, the peak position of the decay signature the uncertainty was revisited. As shown eq. (2.1) it adds a statistical uncertainty of $0.35\,\mathrm{keV}$ leading to a total uncertainty of $0.37\,\mathrm{keV}$. The expected peak width, assuming a Gaussian distribution, was determined using eq. (2.4). For the calculation it had to be considered that the energy is deposited by several quanta. Using the energy width function $\sigma_{\mathrm{XE100}}(E)$, a signal width $\sigma^{2\nu\mathrm{KK}}_{\mathrm{XE100}}$ was obtained by

$$\sigma^{2\nu\mathrm{KK}}_{\mathrm{XE100}} = \sqrt{2 \cdot (n_\gamma \cdot \sigma^2_{\mathrm{Xe100}}(E_\gamma) + n_{e^-} \cdot \sigma^2_{\mathrm{Xe100}}(E_{e^-}))} \tag{4.1}$$

taking the average number of released quanta $n_\gamma = 0.96$ for x-rays at an energy E_γ of $25.9\,\mathrm{keV}$ and $n_{e^-} = 11.7$ for emitted Auger electrons with an average energy E_{e^-} of $0.57\,\mathrm{keV}$. This yielded a value of $(4.10 \pm 0.27)\,\mathrm{keV}$ with the uncertainty given by the fit uncertainty of the resolution function and a systematic uncertainty. The latter one was estimated from the difference of the calculated energy resolution in eq. (4.1), from the one which was obtained using only the most common de-excitation branch as described previously. As described in [81] the expected peak position is at $(64.457 \pm 0.012)\,\mathrm{keV}$. From the RELAX simulations it was estimated that two times $64\,\mathrm{eV}$ are released through sub-excitation quanta and therefore the expected peak position is set to $\mu^{2\nu\mathrm{KK}}_{\mathrm{XE100}} = (64.33 \pm 0.37)\,\mathrm{keV}$. The uncertainty is derived from the described systematic shift by the de-excitation simulation as well as from the

[1] Internally referred to as *run10*

statistical uncertainty from the determination of the combined energy scale.
Next to the total numbers of $^{124}\mathrm{Xe}$ particles, given by the abundance η_{XE100}, the target mass m_{XE100} and the molar mass M_{Xe}, the number of observable decay events depends on the acceptance $\epsilon_{\mathrm{XE100}}$ of the detector for ER in the energy region of interest. This value depends on the expected fraction of false rejections of the selection criteria (cuts). In order to calculate this, each selection cut was tested with the N-1 method as used in [102]. Here, all selection cuts but the one of interest are applied, providing a presumably clean subset of data. Now by applying the remaining cut of interest a fraction of supposedly valid events is removed. This is considered a false rejection, given by:

$$\epsilon_i = \frac{\text{number of events without using the i-th cut}}{\text{number of events, using all cuts}}, \tag{4.2}$$

with the acceptance ϵ_i for the i-th-cut of interest. This method is based on the assumption that any unphysical event would be removed by at least two cuts. However, as this assumption is not always correct, e.g. multiple scatters in $S2$, the method only provides a lower limit on the acceptance. Moreover, the correlation of two cuts can only be accounted for by using the N-1 method on the correlated cuts simultaneously. Basic selections were omitted from the acceptance calculation as they are supposed to have no false rejections and were necessary to provide a clean subset of ER data. These criteria were: the existence of an $S2$ and an $S2$ area above $150\,\mathrm{pe}$, at least a two-fold PMT-coincidence for the main $S1$ signal, the fiducial volume selection and the restriction to single scatters in both signal channels. For all other cuts listed in table 4.1 an energy dependent acceptance was derived using ER calibration data from external was determined by multiplying the N-1 value of each cut in every energy bin, which resulted in the acceptance spectrum in fig. 4.1. The respective errors

Table 4.1.: All cuts used for the double electron capture search and used for the acceptance calculation

Name	Target
Xsignalnoise4	Noise via the area ratio outside and inside the peaks
Xentropy0	Noise via the entropy
Xlownoise0	Gas events via S2 symmetry between top and bottom
Xs1width0	Noise based on the width of the S1
Xs2widther3	Noise and gas events via depth-size correlation
Xs2top0	Hotspots in the bottom array by requiring signal seen in top
Xveto2	External events scattering in the veto

per bin entry were calculated using the *Divide* function from the *ROOT* package which provides the possibility of asymmetrical errors utilizing Bayesian statistics giving credibility intervals on lower limits. This becomes necessary for acceptances close to $100\,\%$ [160]. A linear fit function can be used to approximate the total acceptance in the region of interest, which was chosen to be $\pm 3\,\sigma$-interval around the

expected peak position. With a reduced χ^2_{red} of 1.1 a value for the total acceptance of $\epsilon_{\text{XE100}} = (98.3 \pm 0.1)\,\%$ has been obtained. Here, the uncertainty is purely statistical. The fit is shown in fig. 4.1. The data after applying all selection cuts in an energy

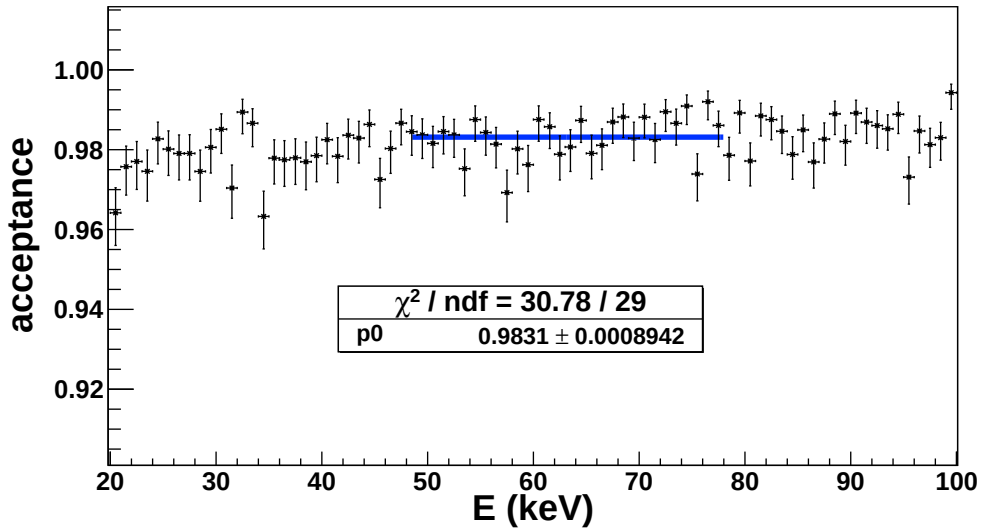

Figure 4.1.: Combined acceptance for ER in XENON100. The acceptance of each cut in table 4.1 derived by the N-1 method is combined per energy unit in $1\,\text{keV}$ bins. The $\pm 3\,\sigma$ region around the expected peak position ($64.33\,\text{keV}$) is fitted with a zero degree polynomial (blue) yielding an average acceptance of 0.983 ± 0.001.

range from $0\,\text{keV}$ to $200\,\text{keV}$ is shown in fig. 4.2. Besides a Gaussian peak at $163.9\,\text{keV}$ caused by the de-excitation of ^{131m}Xe the background is expected to be featureless. Therefore, a combination of a constant background component c_{bkg} and a linear a_{bkg} component were used for its description as shown in eq. (4.3).

$$f_{\text{bkg}}(E) = a_{\text{bkg}} E + c_{\text{bkg}}\,. \tag{4.3}$$

For the signal a Gaussian function was added to the background model. The signal mean μ_{sig} is given by the expected peak position and the standard deviation is given by the energy resolution $\sigma^{2\nu\text{KK}}_{\text{XE100}}$. The model to describe a possible peak can then be written as:

$$f_{\text{sig}}(E) = \frac{\Gamma \epsilon \eta m t N_A}{\sqrt{2\pi}\sigma_{\text{sig}} M_{\text{Xe}}} \exp\left(-\frac{(E-\mu_{\text{sig}})^2}{2\sigma^2_{\text{sig}}}\right) + f_{\text{bkg}}(E)\,. \tag{4.4}$$

All input parameters used for the determination of the decay rate Γ are summarized with their uncertainties in table 4.2. For the statistical analysis the Bayesian Analysis Toolkit (BAT) was used, which is described in [161]. Two models were tested: the “background only” hypothesis using the function from eq. (4.3) and a “signal+background” hypothesis as described in eq. (4.4). Both models were fitted to the data in an energy window from $10\,\text{keV}$ to $135\,\text{keV}$. The fit was performed using a

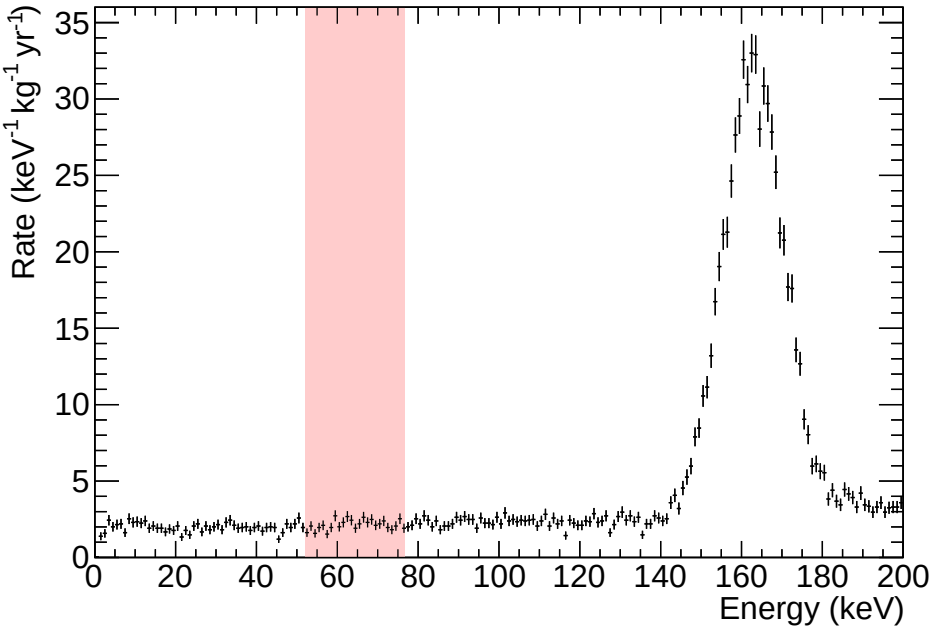

Figure 4.2.: Remaining events after all selection cuts. Event rate per unit energy in $1\,\mathrm{keV}$ bins. The $\pm 3\,\sigma$ region around $64.33\,\mathrm{keV}$ is marked in red. Besides the peak from activated $^{131m}\mathrm{Xe}$ at $163.9\,\mathrm{keV}$ the background spectrum is expected to be featureless.

binned likelihood, which assumes independent Poisson fluctuations of the bin entries. It is defined as

$$\mathcal{L} = \prod_{i=1}^{N_{\mathrm{bin}}} \frac{\lambda_i^{n_i} e^{-\lambda_i}}{n_i!}\,, \tag{4.5}$$

where N_{bin} is the total number of bins, λ_i is the expected number of events and n_i is the observed number of events in the ith bin. Uncertainties were included into the fit as Gaussian priors for the values given in table 4.2, with the exception of the two constants N_A and M_{Xe}. For the free fit parameters Γ, a_{bkg} and c_{bkg} uniform priors were chosen, with restriction to physically allowed positive values. As a decision criterion the results were evaluated using the Bayes Factor BF, which is defined according to [162] as:

$$BF = \frac{P(f_{\mathrm{bkg}} \mid \vec{D})}{P(f_{\mathrm{sig}} \mid \vec{D})}\,, \tag{4.6}$$

where $P(f \mid \vec{D})$ is the posterior probability of the best-fit model f and $\vec{D}$ is the recorded data. The resulting best-fit functions can be seen in fig. 4.3 and the obtained values are shown in table 4.3.

Table 4.2.: Input parameters for the signal amplitude, position and shape.

Parameter f_{sig}	Value
acceptance ϵ	$(98.3 \pm 0.1)\,\%$
abundance η	$(8.40 \pm 0.07) \times 10^{-4}$
exposure mt	$(20.9 \pm 0.1)\,\mathrm{kg\,yr}$
Avogadro constant N_A	$6.0221 \cdot 10^{23}\,\mathrm{mol}^{-1}$
Molar mass M_{Xe}	$(131.293 \pm 0.006)\,\mathrm{g\,mol}^{-1}$
peak position μ_{sig}	$(64.33 \pm 0.36)\,\mathrm{keV}$
peak width σ_{sig}	$(4.10 \pm 0.37)\,\mathrm{keV}$

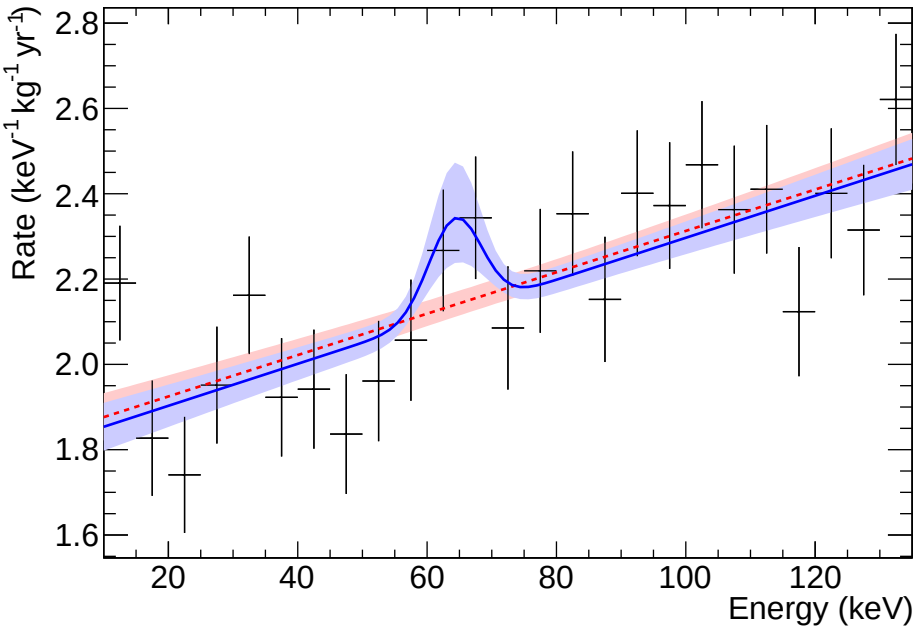

Figure 4.3.: Best-fit results. Event rate normalized to energy and exposure versus the reconstructed energy with $5\,\mathrm{keV}$ per bin. The best-fits for the "signal+background" model f_{sig} (blue solid line) and "background only" f_{bkg} (red solid line) are given with their respective $1\,\sigma$ uncertainty bands (shaded).

P-values were calculated by BAT accordingly to [163] to 0.92 for f_{sig} and 0.89 for f_{bkg} and the evaluation using the Bayes Factor provides a value of:

$$BF = 1.2. \tag{4.7}$$

A value above one points towards a favored "background only" model, so an upper credibility limit on the decay rate was derived. Hence, the marginalized posterior probability of the decay rate Γ was integrated as seen in fig. 4.4. The quantile from

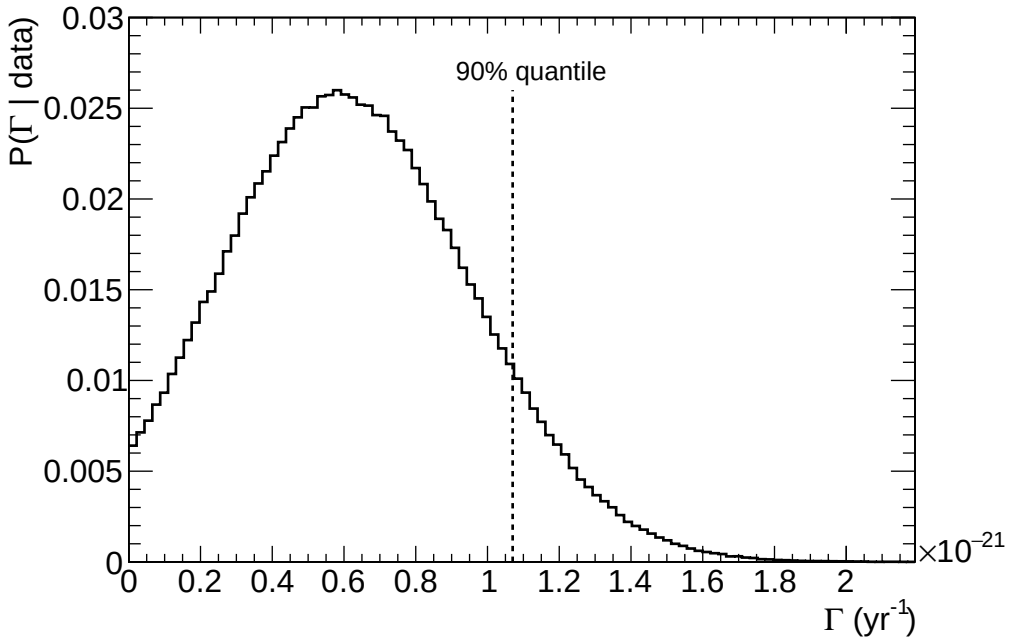

Figure 4.4.: Marginalized posterior probability distribution for the decay rate Γ. Probability for different values of the decay rate. The vertical line denotes the 90% quantile from which the lower limit on the half-life was derived.

$0\,\%$ to $90\,\%$ of the distribution corresponds to the $90\,\%$ credibility interval in a Bayesian interpretation. For a better comparison to literature values the $90\,\%$ credibility limit on the decay rate Γ was transformed to a half-life $T_{1/2}$ of

$$T_{1/2} > \frac{\ln(2)}{\Gamma_{\text{lim}}} = 6.5 \cdot 10^{20}\,\text{yr}\,. \tag{4.8}$$

This value is a factor of 2.55 lower than the previously derived value from the external investigation [158]. In order to cross check this, a statistical evaluation in the frequentist spirit was performed using the method explained in [132]. Two different approaches have been pursued to obtain a limit here. First, a box-counting method for a Poisson process with known background, where the $3\,\sigma$-region around the expected peak position is defined as the boundary of the box. The events within were counted, giving $N_{\text{meas}} = 1386$. This was then compared with the expected background events by averaging over equally sized energy windows before and after the box, which

gave $N_{\mathrm{bkg}} = 1379$. For the calculation of the maximum number of signal events, the *TFeldmanCousins* class in the *ROOT* framework was used [164]. This provides a limit on the observed events of $N_{\mathrm{lim}} = 70.7$ at $90\,\%$ C.L., which has been translated into a lower limit on the half-life of $T_{1/2} > 7.8 \times 10^{20}$ yr at $90\,\%$ C.L. In addition, the procedure for a Gaussian with a fixed boundary also given in [132] was also applicable. Therefore the mean and the uncertainty for the decay rate Γ have been obtained by the fit and are given in table 4.3. An upper limit on the the decay rate according to Table X in [132] was calculated. This puts a lower limit on the half-life of $T_{1/2} > 7.1 \times 10^{20}$ yr at $90\,\%$ C.L. The difference of the two methods of about $10\,\%$ can be explained by background fluctuations within the sideband energy windows in the box-counting. Nevertheless, both values are compatible with the one inferred using the Bayesian method. As this is the more conservative value it is used as the final value. During the follow-up analysis in XENON1T, a new background was identified. A merged decay structure from ^{125}I , which is produced via neutron activation, could possibly produce a Gaussian signal close to the 2νKK signal. As no dedicated analysis was performed in XENON100, it cannot be clarified anymore if it contributed significantly. Details will be provided in the following section.

Table 4.3.: Best fit parameters obtained for the data with the "signal+background" model f_{sig} and the "background-only" model f_{bkg}.

Parameter f$_{sig}$	Value
decay rate Γ	$(1.64 \pm 0.95) \times 10^{-24}\,\mathrm{d}^{-1}$
acceptance ϵ	$(98.3 \pm 0.1)\,\%$
abundance η	$(8.40 \pm 0.07) \times 10^{-4}$
exposure mt	$(7636 \pm 45)\,\mathrm{kg{\cdot}d}$
peak position μ_{sig}	$(64.34 \pm 0.36)\,\mathrm{keV}$
peak width σ_{sig}	$(4.08 \pm 0.26)\,\mathrm{keV}$
background slope a_{bkg}	$(0.103 \pm 0.016)\,\mathrm{counts{\cdot}\,keV^{-1}}$
background constant c_{bkg}	$37.73 \pm 1.31\,\mathrm{counts}$

Parameter f$_{bkg}$	Value
background slope a_{bkg}	$(0.101 \pm 0.016)\,\mathrm{counts{\cdot}\,keV^{-1}}$
background constant c_{bkg}	$38.22 \pm 1.29\,\mathrm{counts}$

4.2 Search for Two-Neutrino Double Electron Capture with XENON1T

Unlike XENON100, the successor experiment explores a new frontier in the half-life parameter space. Therefore, additional effort is necessary to ensure not only a robust limit setting but also allow for the possibility of an unambiguous discovery. Therefore, an extensive part of the work presented in this section is dedicated to the background model building and the assessment of a particular source capable of mimicking the double electron capture signature. The analysis performed in this section was done in close collaboration with Christian Wittweg and will appear in his thesis as well [165]. The analysis is intended to appear in a publication in 2018 [157].

4.2.1 Data set

The data set used for this analysis is from the SR1 data described in section 3.1. However, it differs from the dark matter search data in some respects: Data sets recorded between the[2] 31th March 2017 and the 14th April 2017 are removed from the investigation as they were unblinded beforehand in order to study the contribution of ^{125}I (see section 4.2.5). Furthermore, as a result of the investigation and due to repeated neutron generator tests, the data taken from the 1st May 2017 to the 8th June 2017[3] is excluded. This minimizes possible contamination with ^{125}I by taking data only after any possible contribution has dropped to minimal values. In addition, data is included regardless of the status of the muon veto as muon backgrounds do not contribute to the background expectation for the double electron capture search. Lastly, instead of relying on a selection criterion on the data sets containing PMT flashes, the entire data sets tagged with *Flash* are not considered. The total live time of the data selection including the correction for dead time is $214.3\,\mathrm{days}$. For these data, the region between $56\,\mathrm{keV}$ to $72\,\mathrm{keV}$ is removed[4] from the analysis and only added once the entire background and signal model was in place. This blinding cut establishes an unbiased analysis analogous to the procedure in the dark matter search.

4.2.2 Fiducial volume

The fiducial volume of the double electron capture search has different requirements than the one chosen for dark matter search. In particular the surface background events, which limit the dark matter search volume are not of any concern for such

[2] Runs: 8340 to 8728.

[3] Runs: 9175 to 10 300.

[4] The unblinding was a two-step process with a first unblinding between $50\,\mathrm{keV}$ to $56\,\mathrm{keV}$ and from $72\,\mathrm{keV}$ to $80\,\mathrm{keV}$. As the background model was changed depending on the outcome of this sidebands, it will not considered as blinded in the further discussion, but still a few parts of the analysis were performed with the stricter cut in place.

a line search. Sources decaying at the walls and falsely reconstructed into the fiducial volume within the energy range of the 2νECEC-signal, would have a reduced $cS2$-signal, and hence, would be identified at lower energies. This process is also dependent on the exact position at the surface, which would wash out any Gaussian signal. In addition, nuclear recoils do not play a role as they can be discriminated efficiently at this energy. Also, accidental coincidences do not contribute to the backgrounds at all in this analysis, as they are too low in energy and randomly paired, and thus, not forming a particular shape.
The measure to investigate the optimal fiducial volume is the sensitivity S_{fid}, which is defined as

$$S_{\text{fid}} = \frac{M}{\sqrt{N_{\text{bkg}}}}. \tag{4.9}$$

The enumerator is given by the target mass M, which is directly proportional to the spatially homogeneously distributed amount of ^{124}Xe particles and this way to the number of signal events. The denominator represents the statistical limitation due to N_{bkg} background events following a Poisson distribution. Using this measure the fiducial volume is optimized for discovery potential.

Energy range selection

As the analysis cannot be done on the energy region of interest directly due to the blinding cut, a sideband in energy is chosen. In an ideal case one would try to take the largest symmetrical energy range possible in order to increase the statistics and reduce the uncertainty. This is not feasible on both sides of the signal as visible in the energy spectrum shown in fig. 4.5. Firstly, there is an upper threshold on the energy needed in order to account for the energy dependent mean free path of γ and β-radiation from sources at the walls. Naturally, any high-energy source is able to penetrate deeper into the detector and optimizing on sources with longer mean free paths than the one in the energy region of interest, will select a too conservative fiducial volume. Secondly, any spatially homogeneous source which is not present in the energy region of interest ($50\,\text{keV}$ to $80\,\text{keV}$), will increase the fiducial volume and therefore, has to be excluded from the sensitivity study. This can be understood comparing the contributions of the dominating background in the energy region of interest, which is caused by β-radiation from the ^{222}Rn progeny ^{214}Pb, with material backgrounds as shown in fig. 4.5. For the spatially homogeneous sources any increase in fiducial volume would increase the sensitivity as also seen in eq. (4.9). Nevertheless, this increase stops as soon as the added background from external sources is able to contribute stronger than the gain from the increased number of signal nuclei[5]. If now any other source is added in a sideband, e.g. an inclusion of ^{83m}Kr in the energy from $30\,\text{keV}$ to $50\,\text{keV}$, the turning point where materials dominate over the intrinsic backgrounds would be pushed to higher masses. So, this removes the possibility to

[5] This is the moment, when the total contribution changes with mass differently than the ^{214}Pb.

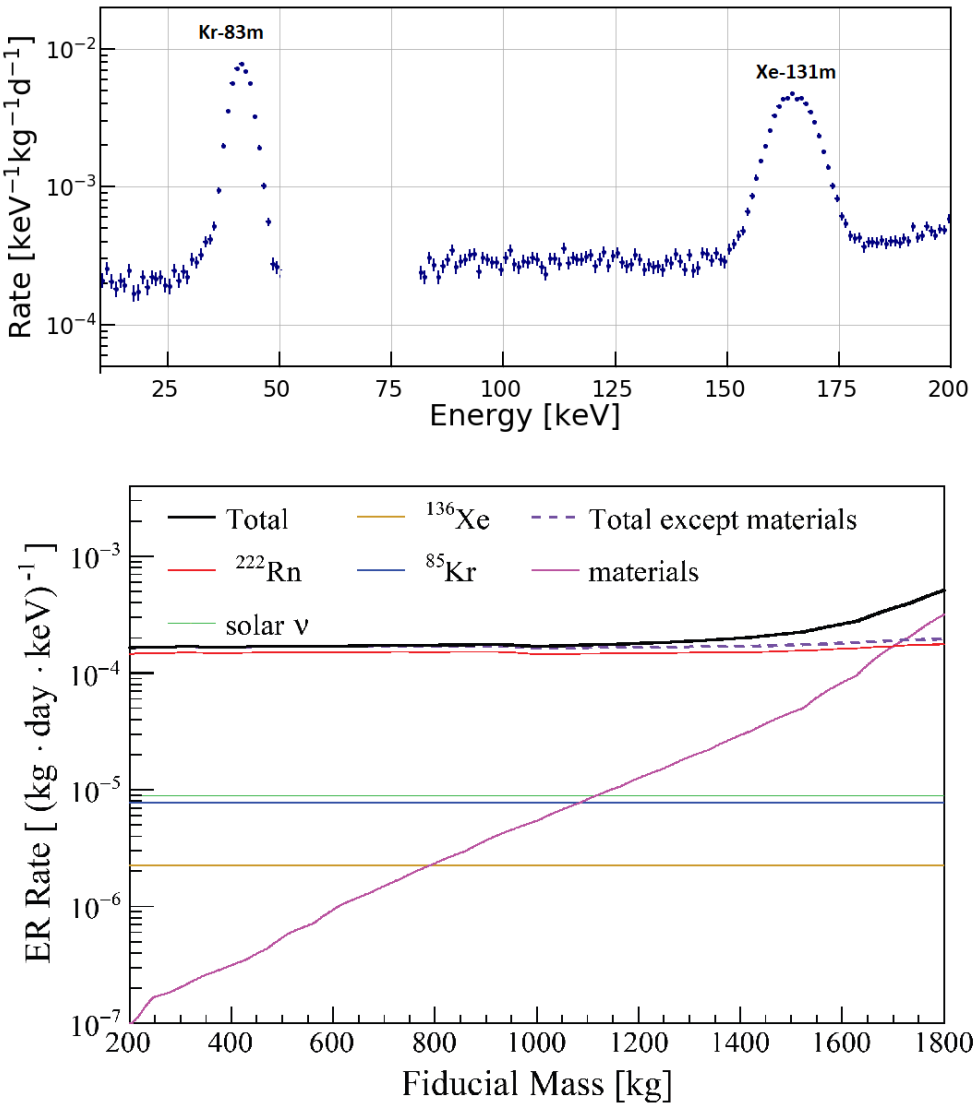

Figure 4.5.: Considerations for the energy range selection. Top: Energy spectrum around the region of interest. No data is shown between $50\,\mathrm{keV}$ to $80\,\mathrm{keV}$ as the blinding cut is still applied. Two peaks are visible at both ends of the spectrum. Bottom: Monte Carlo (MC) simulations for the different background contributions (normalized to exposure and energy range) as a function of chosen fiducial mass. Here, super-elliptical volumes have been used to illustrate the behavior for energies below $12\,\mathrm{keV}$. While most of the backgrounds are linear with the increased mass, the γ-radiation from the materials increases in rate as soon as the mass is enlarged towards the detector surfaces. For this example, the best sensitivity would be around $1700\,\mathrm{kg}$, which points towards the bias of low energy sidebands. Any additional source increasing the flat level would shift this sensitivity towards higher masses. Figure taken from [40].

use the neighboring part of the energy spectrum due to the permanent contribution of ^{83m}Kr (compare fig. 4.5). Including energies below $30\,\mathrm{keV}$ can lead to bias, as

the mean free path in this energy region is shorter than for the region of interest. Therefore, only the neighboring part above the blinding cut is chosen. Here, the upper edge is naturally given by the neutron-activated isotope $^{131m}\mathrm{Xe}$, which decays via aγ or conversion electrons with an energy of $163.9\,\mathrm{keV}$.
For this reasons, the energy region used for this study is from $80\,\mathrm{keV}$ to $140\,\mathrm{keV}$.
A further caveat is the contribution of $^{133m}\mathrm{Xe}$, which produces a continuous and spatially homogeneous signal starting from $80\,\mathrm{keV}$ and following a β-decay spectrum up to $507\,\mathrm{keV}$. The shift in the starting energy is caused by a coincident de-excitation γ, which is always merged with the following β-decay. This signal with a half-life of $T_{1/2} = 5.243\,\mathrm{d}$ is not naturally occurring in the xenon, but is activated by the neutron calibration campaigns. This way a selection of data before and a couple of half-lives after the calibration campaign provides a clean data set. Two chunks of data were selected: before the first neutron calibration and about 17 half-lives after the last calibration starting from the 1st September 2017 and ending at the 6th January 2018. The comparison of both data sets shows no difference, which points towards the independence of the $^{133m}\mathrm{Xe}$ contribution.

Shape optimization

In order to decide on the most sensitive volumes two different shapes are tested and optimized. The first is the cylindrical shape similar to [115] which is entirely defined by its size in Z and its maximum value in R. The second is a super-ellipsoid defined as function of (Z,R) in the following way:

$$\left(\left|\frac{-Z - Z_0}{v_Z}\right|\right)^p + \left(\frac{R^2}{v_R}\right)^p < 1. \tag{4.10}$$

Z_0 is defined as the central value for the depth, v_R is the maximum radius squared and v_Z the maximum deviation in one direction of Z. The curvature of the ellipse is described by p. For both shapes the parameters are varied and the two quantities of interest (M, S_{fid}) are obtained. The target mass M is calculated using the density[6] $\rho_{\mathrm{LXe}} = 2.862\,\mathrm{g\,cm^{-2}}$ and the geometrical volume of liquid xenon at the given iteration of the shape. The sensitivity S_{fid} is then calculated using eq. (4.9) with the total counts of background events between $80\,\mathrm{keV}$ to $140\,\mathrm{keV}$. Figure 4.6 shows the sensitivity for both shapes as a function of target mass and the expected behavior is reflected: In the beginning the sensitivity scales linearly to the point where external sources (materials) cannot be neglected anymore and a maximum is reached. Going further outside then decreases the sensitivity due to increasing contributions from the walls. Also, it is found that the super-elliptical volume has a higher sensitivity throughout the entire mass range. This is expected given the background distribution within the detector (see fig. 4.7). The sensitivity for a few exemplary target masses for the super-elliptical shaped volumes with their respective parameters is given in table 4.4. Since the difference between the maximum found at $1433\,\mathrm{kg}$ and the volume with

[6] For the measured detector temperature of $T = -96.1\,°\mathrm{C}$ [166].

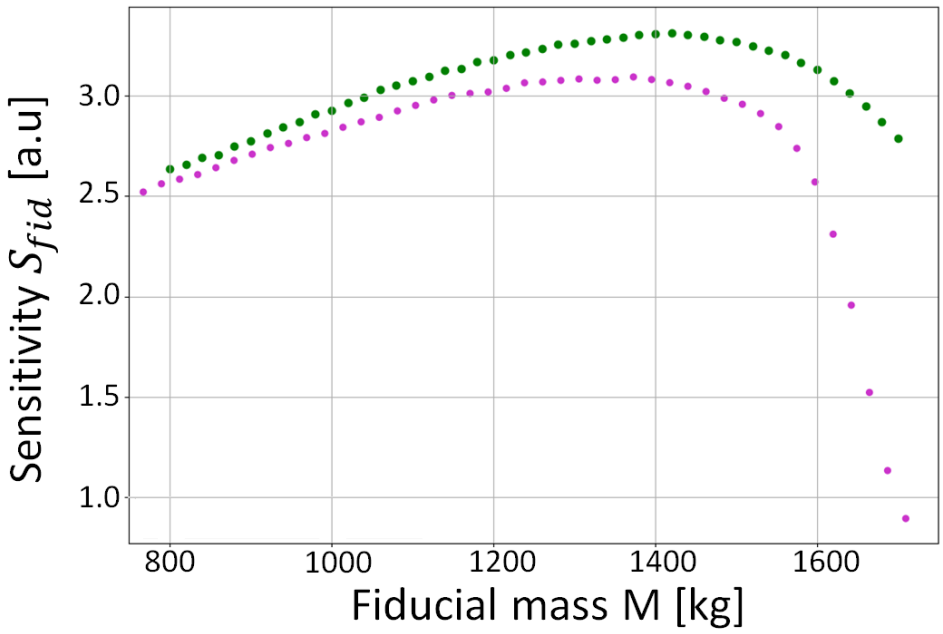

Figure 4.6.: Optimization of the fiducial volume. By varying the shape parameters for the super-elliptical volume (green) and the cylindrical parameters (purple) the sensitivity is scanned for various fiducial masses. Different shape parameters can lead to the same fiducial volume but only the optimal for each mass is shown. For the study the background data between $80\,\mathrm{keV}$ to $140\,\mathrm{keV}$ was used. The entire detector would correspond to $2000\,\mathrm{kg}$.

$1494\,\mathrm{kg}$ is less than $1\,\%$, the larger volume was chosen, as it is expected that the sideband with higher energy provides a small bias towards smaller fiducial volumes. The target mass corresponding to this volume is $1493.1\,\mathrm{kg}$ and shown in fig. 4.7. In order to cross check this target mass, data from the spatially homogeneous source ^{83m}Kr is used ($90\,\mathrm{hours}$ in total). By comparing the events in the total active target volume[7] ($M_{\mathrm{tot}} = 2003.0\,\mathrm{kg}$) to the event count in the chosen super-ellipsoid a relative mass size can be derived. Since 4473382 events are measured in the total detector, the 3374198 events in the chosen super-ellipsoid are used to calculate the mass M to be $1510.8\,\mathrm{kg}$. As this method could suffer from irregularities of the krypton concentration at the walls, it is combined with the prior calculation from the density and the geometric dimensions. The average of both values is taken and the difference towards each of them is taken as the uncertainty. This yields to a final fiducial volume with a target mass of

$$M_{\mathrm{fid}} = (1502.0 \pm 8.9)\,\mathrm{kg} \tag{4.11}$$

with $Z_0 = -50.5\,\mathrm{cm}$, $v_R = 2047.6\,\mathrm{cm}^2$, $v_Z = 45.3\,\mathrm{cm}$ and $p = 3.218$. Finally, the obtained fiducial volume was compared to a fiducial volume derived from bin-wise machine

[7] Derived from the geometrical dimensions and the density.

Table 4.4.: Selected fiducial volumes shaped according to the super-ellipsoid.

M [kg]	S_{fid} [a.u.]	Z_0 [cm]	v_Z [cm]	v_R [cm^2]	p
1011	29.3	−50.5	39.9	1785	2.03
1213	31.8	−51.1	44.6	1884	2.13
1332	32.7	−52.5	43.6	1965	2.72
1433	33.1	−51.0	45.0	2034	2.81
1494	32.8	−50.5	45.3	2048	3.22
1574	32.0	−51.2	45.1	2093	4.02
1657	30.1	−50.4	45.8	2105	5.31

optimization. No substantial sensitivity gain was found, and therefore, the simpler choice was kept.

4.2.3 Signal model

For the analysis of XENON1T the assumption of a single Gaussian signal in the detector despite the multi-quanta emission is examined. Therefore, the extreme case of a submission of two $31.8\,\text{keV}$ x-rays is considered. If these most energetic relaxation quanta are not separable in the detector, all others are not separable as well, due to the smaller mean free path at lower energies. In order to demonstrate this, the *Decay0* package is used. This is a *C++*-framework developed in [167], which simulates the emission of particles accounting for the angular correlation after various decays. ^{124}Xe was added to the package and limited to the emission of the two selected K-shell x-rays. The outcome of this event generator is fed into the *GEANT4*[8]-framework of XENON1T [168, 40]. In total 10^4 events have been passed to the framework and were homogeneously distributed within the detector. From this part of the simulation chain it is already concluded that only in about $0.2\,\%$ of the events a reduced energy is measured due to an x-ray, which scatters outside the sensitive region. Since this is only possible closely to the walls of the detector, this effect disappears as soon as only the fiducial volume is considered. The output of the *GEANT4*-simulation is now passed to the *nSort*-framework. This package is developed by the XENON collaboration to convert energy depositions into the final measured signal in $(cS1,cS2)$-space. For this study the most interesting part is the functionality, which checks if two energy depositions provided by *GEANT4* will be merged into a single signal by the XENON1T data processor or if they can be separated. The output of *nSort* shows that within the fiducial volume no separation is possible and the signal will be measured in $99\,\%$ of the cases at about $64\,\text{keV}$. It is presented in fig. 4.8. A sub-percent effect is found, which moves the energy slightly towards lower energies ($\sim 60\,\text{keV}$). This is not fully understood, but may be caused by an unwanted effect of

[8] Version *p9.5.01*.

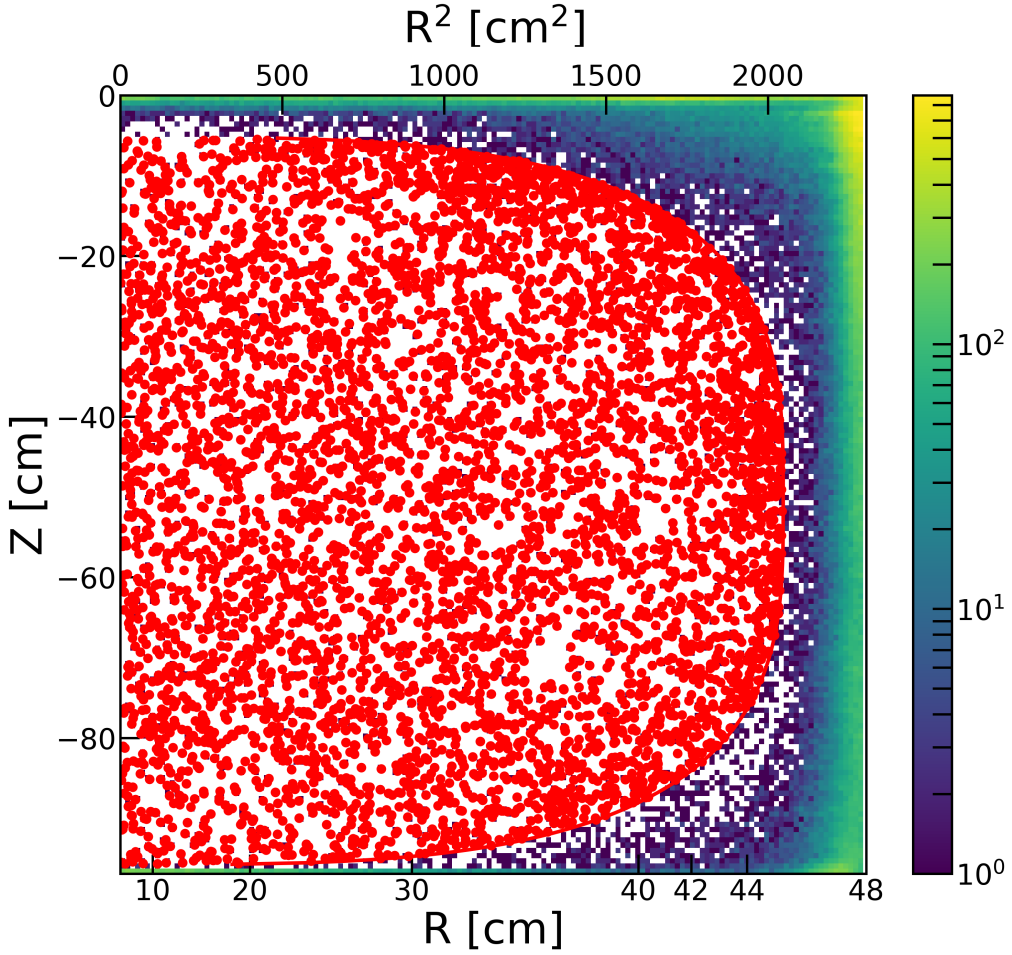

Figure 4.7.: Fiducial volume selection for the double electron capture search. Distribution of the measured counts is shown in a histogram in (Z,R) and (Z,R^2)-space. The optimized super-ellipsoid volume is indicated within the detector (red line) and all events falling into it are marked (red dots). The energy range is $80\,\mathrm{keV}$ to $140\,\mathrm{keV}$.

the nSort packages, which was not evaluated to the last precision for energies outside the dark matter search region.
The effect plays no role as the smearing of the obtained merged energies with the resolution function given in eq. (4.15) provide a Gaussian shape verified by a χ^2-fit. Therefore, the Gaussian signal will assumed for the following analysis is valid.

Peak position

To relate the signal in the detector to the deposited energy, the energy reconstruction is performed using different sources introduced to the detector as well as intrinsic sources according to the Doke method (as described in section 1.2.1). The result for the entire SR1 as used in [128] can be seen in fig. 4.9. As the energy reconstruction

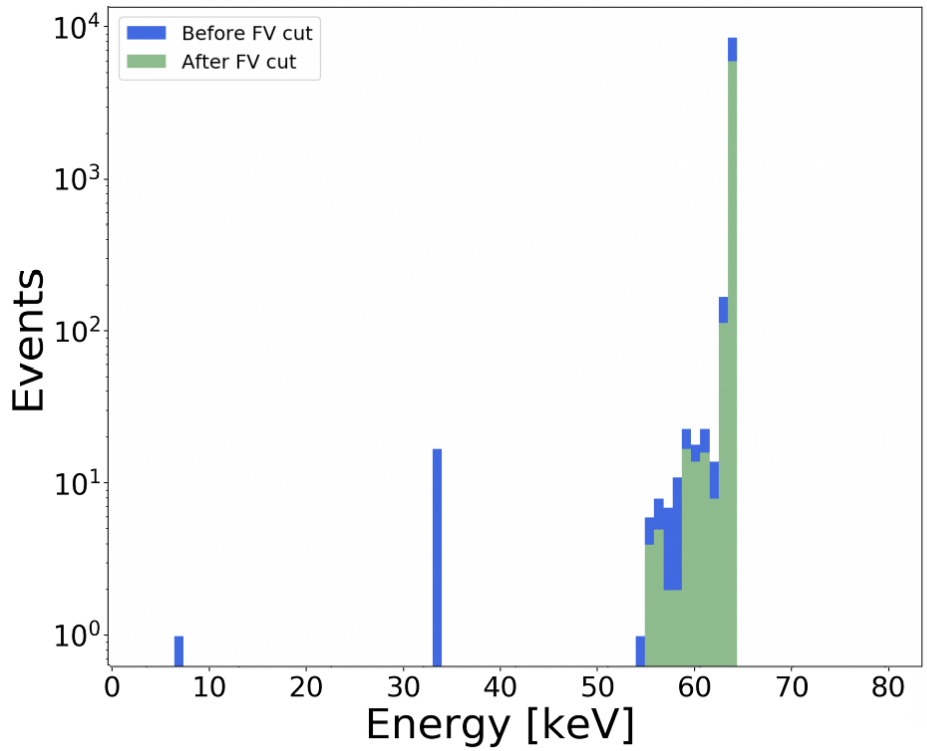

Figure 4.8.: Comparison of the energy depositions as provided by the simulation chain. The energy depositions are shown in the full TPC (blue) and after the fiducial volume selection (green). The major part of the depositions is not separable and thus, centered around $63.8\,\mathrm{keV}$. A sub-percent fraction of events deposits less energy. The reason for this is not quite clear, but does not have an influence on the shape of the signal as the detector resolution is at this point at about $6.5\,\mathrm{keV}$ (full width at half maximum). In a single case one of the photons scattered once and left the detector, in about 10 of the cases one of the photons left the detector without a deposition. Both signatures are not visible within the fiducial volume.

plays a major role in the search of a peak centered at a known energy, the energy reconstruction is extended by the depth dimension. The fiducial volume is divided into 10 equidistant slices along the z-axis[9] and for each slice the Doke method is applied to all possible sources. The advantage of this extension lies in the inclusion of spatial inhomogeneities in the energy reconstruction. This is important for spatially localized high energy sources, such as $^{40}\mathrm{K}$ in the PMT arrays. Due to its contributions from the very top and very bottom any Z-dependence leads to a washed out Gaussian peak, when fitted without taking the difference at the respective position into account. The inclusion of the depth mainly improves the resolution of the signal, but also has a slight influence on the reconstructed energy.
A g_1 and g_2 value is extracted for each slice and their relation to the depth Z is

[9] Equidistant does not correspond to equally sized. In fact more area is included in the slices in the middle. However, due to the origin of the background calibration sources, the statistics is increased at the top and bottom part.

approximated with a linear function as shown in fig. 4.10. This way the following values for $g_1(2\nu\mathrm{KK})(Z)$ and $g_2(2\nu\mathrm{KK})(Z)$ are obtained:

$$\mathrm{g_1(2\nu KK)(Z)} = 0.145306 \pm 0.000137\,\mathrm{pe/ph} + Z \cdot (6.7 \pm 0.2) \cdot 10^{-5}\,\mathrm{pe/ph/cm} \tag{4.12}$$

$$\mathrm{g_2(2\nu KK)(Z)} = 11.1103 \pm 0.0160\,\mathrm{pe/} - Z \cdot (1.3 \pm 0.1) \cdot 10^{-2}\,\mathrm{pe//cm}. \tag{4.13}$$

Since the Doke method is a global survey of the energy scale, a test of its impact on

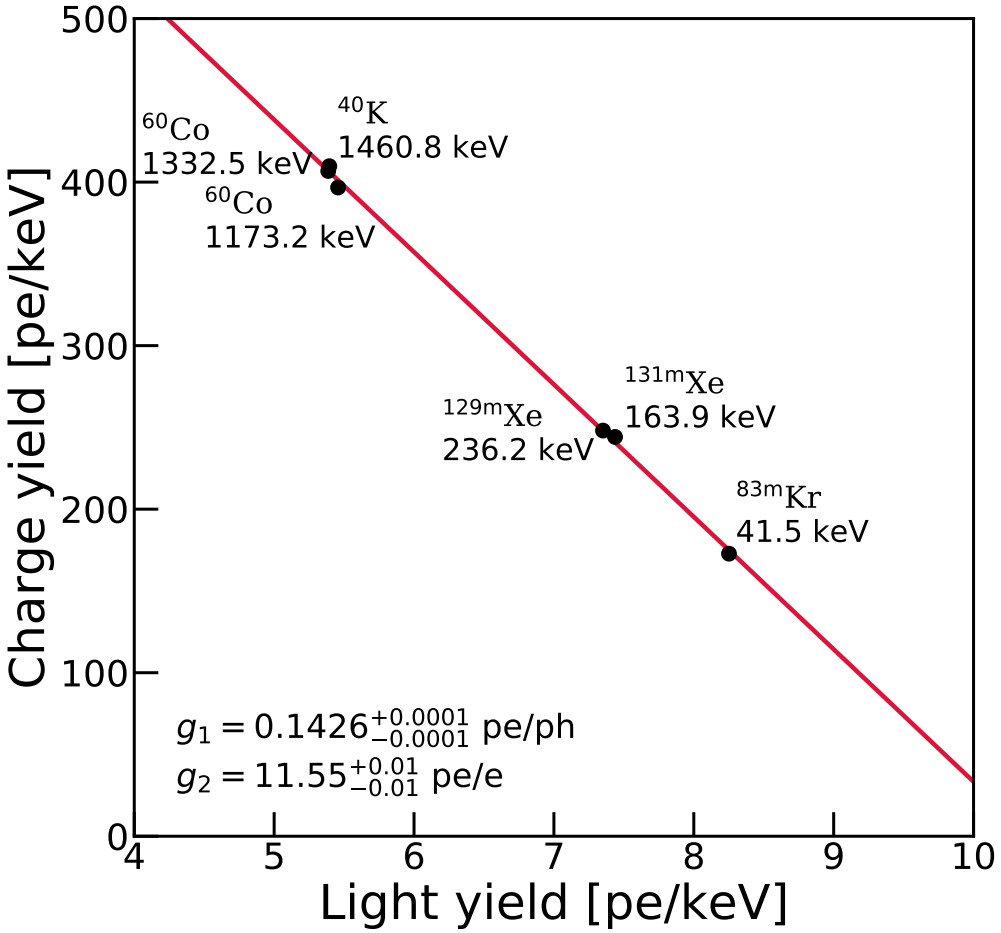

Figure 4.9.: Energy reconstruction using multiple sources (Doke method) in the 1 t fiducial volume in SR1. The energy calibration fit as used for the results in [128]. Only statistical uncertainties are indicated for g_1 and g_2. The reduced χ^2 is at 164.3 with four degrees of freedom. This large deviation is due to the missing incorporation of the systematic spatial and temporal dependence. Nevertheless, the derived energy scale reproduces the energy position of calibration sources with a deviation of less than a percent as shown in fig. 4.11.

the respective sources is performed by reconstruction of the entire energy spectrum and application of Gaussian fits to each source. The obtained Gaussian mean from these fits is then compared to the literature energy of each source as shown in

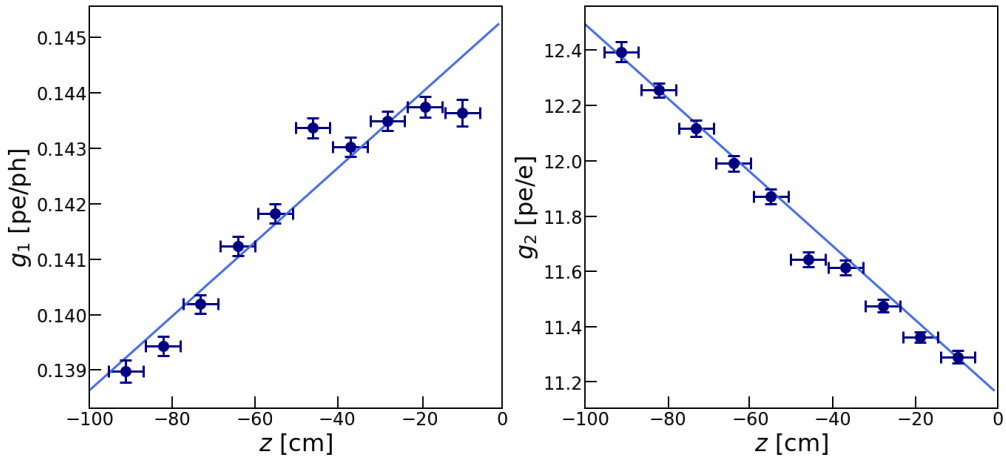

Figure 4.10.: Energy reconstruction using the Doke method in different Z-slices of the $1.5\,\mathrm{t}$ fiducial volume. Left: g_1 is determined in each of the 10 Z-slices according to the method indicate in fig. 4.9. The χ^2 is 70.3 at for eight degrees of freedom. The error bars on the x-axis are indicating the bin size in Z, while the error bars on the y-axis are the statistical uncertainties of the respective fit. A deviation at the top of the Z distorts the fit result, but is negligible as only few events are expected there. Right: g_2 derived accordingly. The χ^2 is for 19.0 for eight degrees of freedom. Unlike in g_1 the linear fit seems to describe the situation better, and makes the deviations for the light yield negligible on the final result as the deviations on the known sources show in fig. 4.11.

fig. 4.11. From the derived relations for g_1 and g_2 an additional statistical uncertainty on the peak position is given. Furthermore, a systematic uncertainty is included by building a second energy scale only using the low-energy part of the spectrum: $^{83m}\mathrm{Kr}$ at $41.5\,\mathrm{keV}$, $^{131m}\mathrm{Xe}$ at $163.9\,\mathrm{keV}$ and $^{129m}\mathrm{Xe}$ at $236.2\,\mathrm{keV}$. A comparison of the reconstructed position of the line closest to the 2νKK, $^{83m}\mathrm{Kr}$, shows a $0.87\,\%$ difference, which decreases with increasing energies. An incorporation of this as systematic uncertainty accounts for the incomplete knowledge introduced by the larger energy range and possible non-linearity at higher energy due to saturation effects. Nevertheless, the full calibration, using all sources given in fig. 4.9, is applied since this provides more information on the detector response. The inclusion of the statistical uncertainties on g_1,g_2 and the systematic uncertainty derived from the lower part of the energy calibration is quadratically added to the uncertainty from the K-edge energy measurement ($0.012\,\mathrm{keV}$ [81]) and the uncertainty of ($0.064\,\mathrm{keV}$) from the sub-excitation quanta provided by the RELAX code [154]. This yields a final expected peak position $\mu^{2\nu\mathrm{KK}}_{\mathrm{XE1T}}$ for the 2νKK of:

$$\mu^{2\nu\mathrm{KK}}_{\mathrm{XE1T}} = (64.33 \pm 0.58)\,\mathrm{keV} \tag{4.14}$$

Peak width

Next to the peak position a resolution function is extracted from the energy calibration as well. This function is used to estimate the Gaussian signal width of the double

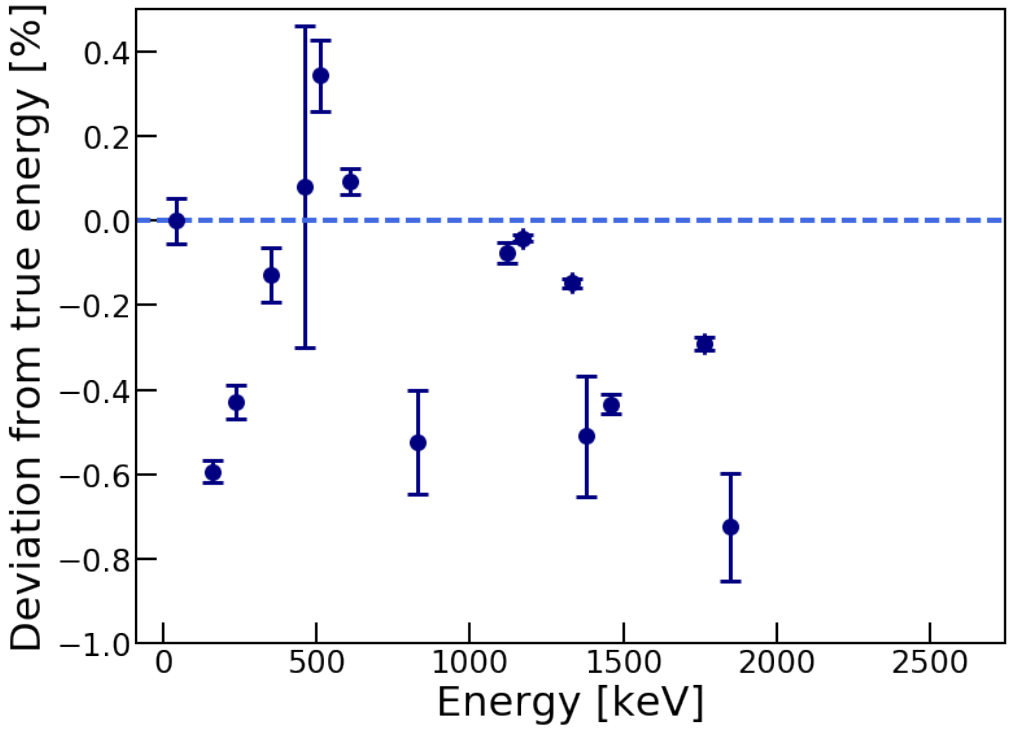

Figure 4.11.: Deviation from true energy after energy reconstruction. A Gaussian fit for each source after the energy reconstruction is performed. The obtained mean is subtracted from the literature value and the difference is divided by the literature value. The zero-difference line is indicated. All deviations from true energy are within $1\,\%$ and arise from non-linearities of the energy response.

electron capture. Hence, the resolution function R_E in dependence of the deposited energy E from SR1 (see fig. 2.6) can be used[10], which is parametrized according to eq. (1.12) by:

$$R_E = \frac{(30.98 \pm 0.43)\,\%\sqrt{\mathrm{keV}}}{\sqrt{E}} + (0.37 \pm 0.03)\,\%. \tag{4.15}$$

The resolution can be translated into an expected signal width $\sigma^{2\nu\mathrm{KK}}_{\mathrm{XE1T}}$ at the given energy $\mu^{2\nu\mathrm{KK}}_{\mathrm{XE1T}}$ by eq. (1.11). Analogous to the procedure in the previous section (see eq. (4.1)) the signal width is not evaluated for the all possible relaxation processes but accounts for the most-prominent branching ratio. This yields $\sigma^{2\nu\mathrm{KK}}_{\mathrm{XE1T}} = (2.64 \pm 0.21)\,\mathrm{keV}$. In addition to the statistical uncertainty from the fit function, a systematic uncertainty is added in the same way as for the peak position determination. The result to the signal width obtained from using low energy lines only is compared to the full fit result. This adds an additional uncertainty of $0.12\,\mathrm{keV}$, which is added quadratically and the final expected signal width is at

$$\sigma^{2\nu\mathrm{KK}}_{\mathrm{XE1T}} = (2.64 \pm 0.24)\,\mathrm{keV}, \tag{4.16}$$

[10] An evaluation showed no significant dependence on the fiducial volume selection, so the SR1 fit could be re-used.

which corresponds to $4.1\,\%$ energy resolution. This value is improved compared to XENON100 by a factor of 0.65.
All in all the expected signal is a Gaussian peak described by

$$f_{\text{sig}} = \frac{N_0}{\sqrt{2\pi\sigma^2}} \times e^{-(x-\mu)^2/(2\sigma^2)}, \tag{4.17}$$

where the expected peak position μ and its width σ are given by the values in eq. (4.14), respective eq. (4.16). N_0 is the amount of signal events obtained by fit, corresponding to the area covered by the Gaussian signal.

4.2.4 Abundance of ^{124}Xe

In order to relate a measured event count N_0 to a decay rate or the inverse proportional half-life, the number of $^{124}\mathrm{Xe}$ atoms has to be known. The total xenon atom count is given by the fiducial volume, the molar mass M_{Xe} of $^{124}\mathrm{Xe}$, Avogadro's constant N_A and the abundance η of $^{124}\mathrm{Xe}$ in the xenon filled into the detector. In order to evaluate the latter a straightforward assumption is to assume the natural composition, which would yield $\eta_{\text{nat}} = (9.52 \pm 0.03) \cdot 10^{-4}$ [159]. Nonetheless, due to the existence of xenon which is changed in its composition[11], only a measurement of the actual fractions of the respective isotopes minimizes the systematic uncertainty. This measurement has been performed using an on-site residual gas analyzer system (RGA) mainly consisting of an *Inficon Transpector H200M* described in detail in [112]. This quadrupole mass filter measures the mass-over-charge ratio of ionized atoms and molecules. The device was set to measure the ratio in steps of $0.1\,\mathrm{amu}$ (10ppAMU).
In total, three batches of gas were extracted from a dedicated port at the gas system and measured using the electron multiplier (EM) mode. In total 35 measurements were taken from three batches and only those were kept, where the total inlet pressure, which is proportional to the flow of xenon atoms in the measurement chamber, was stable within $2\,\%$. Although no influence of the integration time was found, a changing inlet pressure could possibly cause a shift in the amplitude during a scan over the mass range. The eight measurements fulfilling this criterion are presented in fig. 4.12. In order to derive the fraction $f_{\text{Xe-124}}$ of $^{124}\mathrm{Xe}$ all isotopes of xenon were integrated $0.7\,\mathrm{amu}$ around the expected center and the fraction of $^{124}\mathrm{Xe}$ was calculated as following

$$f_{\text{Xe-124}} = \frac{S_{124}}{\sum\limits_i S_i} \text{ with } i = (124,..,134,136). \tag{4.18}$$

Here the integrated signal of $^{124}\mathrm{Xe}$ is denoted by S_{124} and it is divided by the sum of the integrated signals of all isotopes S_i with i iterating through the nine long-lived isotopes of xenon. As it can be seen in fig. 4.12 the abundance[12] η_{XE1T} from the set of

[11] The xenon bought on the market is sometimes depleted in $^{136}\mathrm{Xe}$, due to the extraction for double beta decay experiments.
[12] The abundance is equal to the mean fraction.

measurements lies above the natural abundance. It is determined as

$$\eta_{\mathrm{XE1T}} = (9.94 \pm 0.14\,(\mathrm{stat.}) \pm 0.15\,(\mathrm{sys.})) \cdot 10^{-4}. \tag{4.19}$$

The statistical uncertainty is derived from the standard deviation of the eight different measurements. The systematic uncertainty accounts for the fact that the peak separation is finite in the RGA. In order to evaluate this, an integration of the entire mass range between the mass-over-charge ratios 122 and 138 was performed and compared to the integrated signal of $^{124}\mathrm{Xe}$. The maximum deviation that was found was included as a systematic uncertainty.
The comparison of the complete isotopic composition of the detector gas and the expectation from natural abundance for all isotopes revealed a gradient increase towards lower masses in comparison to the expected natural abundance. Hence, it was necessary to exclude a systematic effect. This was done by cross checking a xenon gas sample with known isotopic composition. While the precision of the given isotopic composition of the known gas sample made a direct verification not feasible, the gradient behavior was not reproduced in this sample. Therefore, it is concluded to be a real effect in the detector gas sample. The deviation of the measured abundance compared to the natural abundance is less than $4\,\%$ and it could be explainable by a single gas bottle with an increased $^{124}\mathrm{Xe}$ content.

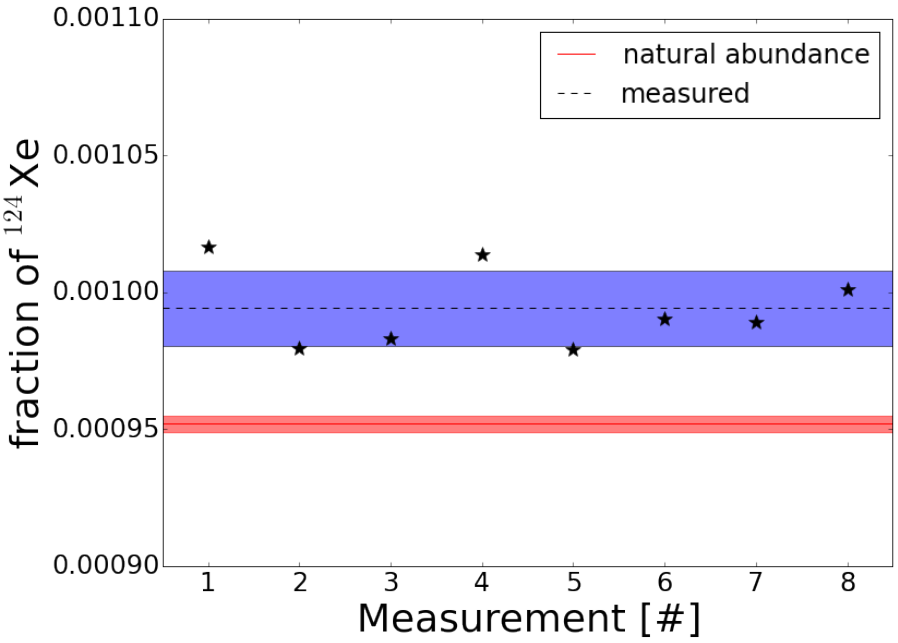

Figure 4.12.: Measurements of the ^{124}Xe abundance in the detector gas. The fraction of ^{124}Xe was derived as described in the text for eight independent measurements. For each measurement the result is shown (black asterisks) including statistical uncertainties for each point and the mean is indicated (black dashed line). Further the standard deviation of all measurements is shown (blue band) and the expected fraction from the natural abundance with the uncertainty from literature is indicated (red).

4.2.5 Background model

A successful search for the double electron capture requires knowledge of any background signals. While this is not crucial for setting a limit on the half-life, a signal claim can only be made on an understood background. Two parts are necessary to consider: the underlying background level, which sets the sensitivity, and any potential source in the energy region of interest, which could be misinterpreted as the signal. For this study only ER backgrounds are of any importance, as the discrimination at these energies is sufficient to reduce any NR contribution to almost zero events. The ER backgrounds can be separated into intrinsic sources, which are homogeneously distributed over the entire detector and external sources, which arise from the detector edges. The latter will be summarized as material contribution. Intrinsic sources present in the xenon gas ordered by the size of contribution within the energy region of interest are:

- β-decay from $^{214}\mathrm{Pb}$
- $2\nu\beta\beta$-decay from $^{136}\mathrm{Xe}$
- β-decay from $^{85}\mathrm{Kr}$
- Elastic scattering from solar neutrinos

Furthermore, due to thermal activation but mostly due to neutron calibration campaigns, background sources created artificially are considered as well.

MC/data matching

In order to get a handle on the background composition not only the energy region around the double electron capture is useful, but in fact the entire energy spectrum of the detector. This can be seen in fig. 4.13, where the full ER background spectrum is shown.

There are more features (peaks, edges) present at higher energies and all of them contain information on the isotopic composition behind the background signal spectrum. In order to extract the contribution of each isotope a comparison with Monte Carlo (MC) simulations of the different sources in the detector using the *GEANT4* framework of XENON1T is performed[13]. For the isotopes in the detector materials the origin is of particular importance, as their contributions depend on the penetration depth. The simulations are separated into six different parts: the entire stainless-steel cryostat, the PTFE panels of the TPC, the copper from the field-shaping rings of the detector and the PMT support structures, the stainless-steel bell and electrode support rings in the TPC, the PMTs and their bases. Each component was screened before the detector operation started [114]. This provides values for the isotopic composition of the material contributions with uncertainties given or if no traceable amount was measured it states an upper limit on the specific isotopic

[13] For all contributions but $^{214}\mathrm{Pb}$ the GEANT version 4.9 was used. Due to an error in the branching ratio of the decay into the $^{214}\mathrm{Bi}$ ground state, 4.10 has been used for $^{214}\mathrm{Pb}$.

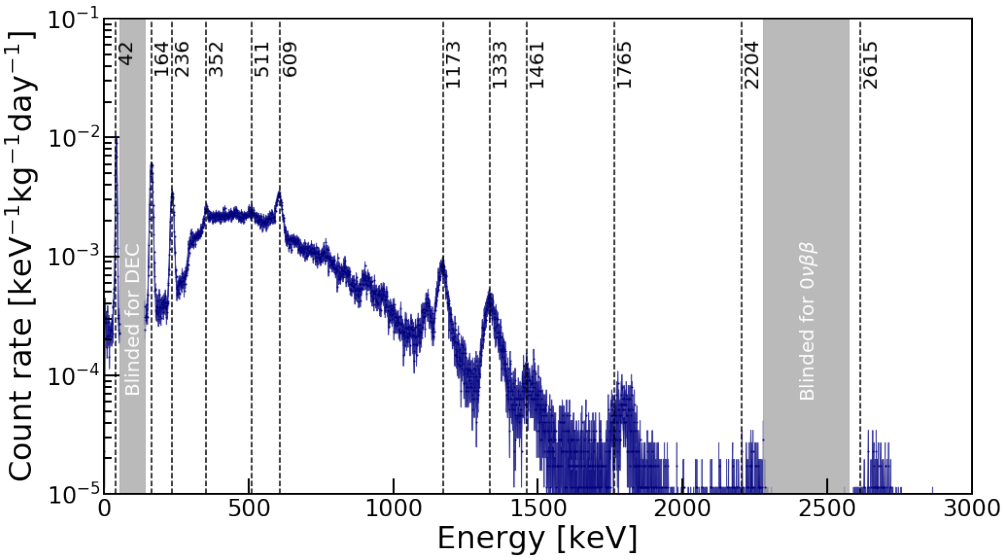

Figure 4.13.: Exemplary energy spectrum in $1\,\mathrm{t}$ fiducial volume. The event counts are normalized to the target mass and exposure and are shown as a function of the energy. The binning is $1\,\mathrm{keV}$. Various lines indicate identified external sources and their expected energy. A particular source has usually several lines in the spectrum from subsequent decays. Selected peak energies, usable for energy calibration from various isotopes are indicated. The spectrum is only shown up to $3\,\mathrm{MeV}$. Above this energy mostly α-decays contribute further. Two blinding cuts are indicated (grey shaded): $50\,\mathrm{keV}$ to $80\,\mathrm{keV}$ blinded for the double electron capture and $2.3\,\mathrm{MeV}$ to $2.6\,\mathrm{MeV}$ for the neutrino-less double beta decay.

abundance. The relative fractions are summarized in table 4.5 and are based on the values given in [40].

A simulation of the deposited energy spectrum for each component as it would be measured in the TPC was performed with 10^7 to 10^9 events for any possible pairing of material background isotopes and detector components (48 in total). From this two isotopes, ^{137}Cs and ^{235}U, have been found to be completely negligible as already indicated by the screening campaign. In addition, the intrinsic sources were simulated with a comparable event count. The output of all *GEANT4* simulations were fed into the *nSort* MC framework of XENON1T to evaluate single and multiple scattering in the detector. Only the single interactions identified by *nSort* are considered for the further evaluation, as the measured data is treated in the same way.

All simulated material contributions are then normalized to their specific activity by the component mass and total simulated events such that the spectra correspond to $1\,\mathrm{mBq\,kg^{-1}}$ within the simulated component. As the majority of the material contribution is self-shielded at low energies the statistics from the simulation decrease drastically. This introduces statistical fluctuations that look like peaks. In order to avoid them to be misinterpreted as physics structures in the low energy regime, the

Table 4.5.: Weighting factors of each component for the respective isotope derived from material screening [40]. The contributions for $^{137}\mathrm{Cs}$ and $^{235}\mathrm{U}$ are neglected since they do not contribute significantly.

Component	$^{238}\mathrm{U}$	$^{226}\mathrm{Ra}$	$^{232}\mathrm{Th}$	$^{228}\mathrm{Th}$	$^{60}\mathrm{Co}$	$^{40}\mathrm{K}$
Cryostat (SS)	2.00	2.00	0.21	1.98	20.5	3.80
Panels (PTFE)	1.20	$3.3 \cdot 10^{-2}$	$4.3 \cdot 10^{-2}$	$3.4 \cdot 10^{-2}$	0.10	0.28
Field rings (Cu)	0.25	0.12	$4.1 \cdot 10^{-2}$	$6.5 \cdot 10^{-2}$	$2.7 \cdot 10^{-2}$	0.34
Bell & Structure (SS)	2.40	0.64	0.21	0.36	9.70	2.70
PMT Base	8.00	0.50	0.50	0.50	0.71	13.0
PMTs	0.82	0.32	0.20	$1.53 \cdot 10^{-1}$	$5.2 \cdot 10^{-3}$	0.36

contributions at low energies ($10\,\mathrm{keV}$ to $100\,\mathrm{keV}$) are flattened by linear interpolation[14]. Intrinsic sources are normalized differently in order to reflect the knowledge from independent measurements, except for $^{214}\mathrm{Pb}$, which is normalized to $1\,\mu\mathrm{Bq\,kg^{-1}}$.The contribution from $^{136}\mathrm{Xe}$ is normalized such that unity corresponds to the activity expected from the measured abundance of the isotope in the detector ($\eta_{\text{Xe-136}} = (8.49 \pm 0.04\,(\text{stat.}) \pm 0.13\,(\text{sys.})) \cdot 10^{-2}$.) and the measured half-life of the decay ($T_{1/2} = 2.165 \cdot 10^{21}\,\mathrm{yr}$ [149]). The contribution from solar neutrinos is normalized such that unity corresponds to $8.9 \cdot 10^{-9}\,\mathrm{events/kg/s}$. This is the value obtained in [40] mostly based on the solar flux from [169] and taking flavor oscillations into account as well as the respective cross sections[15]. The simulated spectrum of $^{85}\mathrm{Kr}$ is normalized such that unity corresponds to a signal given by $0.1\,\mathrm{ppt}$ of natural krypton in xenon using a fraction of $^{85}\mathrm{Kr}$ in natural krypton of $1.65 \cdot 10^{-11}\,\mathrm{mol/mol}$. In addition to the described contributions, a set of peaks and sources artificially introduced to the detector has to be considered for a full description, although none of them is directly related to the region of interest. There is a permanent mono-energetic contribution of the calibration source $^{83m}\mathrm{Kr}$ centered at $41.5\,\mathrm{keV}$. Due to misidentification of the two-fold decay process a small second contribution centered at $32.2\,\mathrm{keV}$ is present in the spectrum as well. Further peaks are from long-lived activation lines of xenon, namely $^{131m}\mathrm{Xe}$ at $163.9\,\mathrm{keV}$ and $^{129m}\mathrm{Xe}$ at $236.2\,\mathrm{keV}$. Another, rather short-lived contribution is from $^{133m}\mathrm{Xe}$, which provides a special signature. The β-decay of the isotope is always accompanied by a de-excitation γ of about $81\,\mathrm{keV}$ [171]. As this is not separable in the detector, the β-spectrum starts from the point of the γ-energy. This was simulated as well and normalized to $1\,\mu\mathrm{Bq\,kg^{-1}}$. In order to match the output of all these simulations to the actual data spectrum as shown in fig. 4.13, the discrete energy depositions have to be smeared with the detector response function. This is achieved by a convolution

[14] A check on the final fit showed no significant difference in the best-fit parameters with and without interpolation.

[15] Recent studies have shown that the solar neutrino cross section is about $25\,\%$ lower if not calculated for free electrons but for bound electrons in the xenon nucleus [170]. The results within this section do not change if taking this into account as expected for such a sub-dominant component and thus, the assumptions of [40] will be used.

Table 4.6.: Summary of background sources.

Source	Signature type	Energy range [keV]	Normalization
Materials	continuous + peaks	0-3000	$1\,\mathrm{mBq\,kg^{-1}}$
Pb-214	β+γ	0-1024	$1\,\mu\mathrm{Bq\,kg^{-1}}$
Kr-85	β	0-687	$0.1\,\mathrm{ppt}$
Xe-136	$2\nu\beta\beta$	0-2458	$4.0 \cdot 10^{-3}\,\mu\mathrm{Bq\,kg^{-1}}$
solar ν	continuous	0-1250s	$8.9 \cdot 10^{-9}\,\mathrm{counts/s/kg}$
Xe-133	shifted β	81-507	$\mathrm{counts/keV/kg/d}$
Xe-131m	peak	163.9	$\mathrm{counts/keV/kg/d}$
Xe-129m	peak	236.2	$\mathrm{counts/keV/kg/d}$
Kr-83m	peak	41.5	$\mathrm{counts/keV/kg/d}$
Kr-83m$_{\mathrm{mis}}$	peak	32.2	$\mathrm{counts/keV/kg/d}$

of each bin with a Gaussian built whose width is given by the resolution function in eq. (4.15). A summary of all background contributions can be found in table 4.6

Fit model

With the simulated spectra in place a matching of them with the actual data is possible. To this end, a χ^2-function is minimized by the *migrad*-method in the python-based software package *iMinuit* [172, 173]. It is constructed of the form

$$\chi^2_{\mathrm{basic}} = \sum_{i}^{E_{\mathrm{max}}} \frac{(r_i - f_i)^2}{(\Delta r_i)^2}. \tag{4.20}$$

This function compares the actual measured rate in the i-th energy bin from data r_i with the one given by the smeared MC simulation f_i and normalizes it to the uncertainty of the measurement Δr_i. The maximum energy range E_{max} is ideally the end of the entire energy spectrum, but can be constrained as well. This is usually necessary due to saturation effects within the PMTs for large signals or due to acceptance losses at high energies, which a. Theoretically, one could minimize the χ^2-function by varying all fit parameters. However, since this would yield over 70 correlated parameters, the result would be highly degenerated as various (unphysical) combinations could provide suitable results in the absence of sufficient limitation. Therefore, constraints are added in order to reduce fit parameters and narrow the parameter space for the remaining fit parameters to reasonable values. In a first assumption, the ratio between the components for each of the isotopes was fixed to the values obtained from the material screening. In case the radio-assay provided only upper limits, these were used as central values. This fixation of the ratios effectively

reduces the material part of the fit to six parameters[16]. These describe the summed contribution over all detector components from each of the isotopes and represent the list given in table 4.5. A particular specialty is given by the two simulated progeny $^{226}\mathrm{Ra}$ and $^{228}\mathrm{Th}$. Both long-lived isotopes are simulated along their parent isotopes in order to account for any decay chain disequilibrium, e.g., due to any specific treatment of the materials. In the first case the parent decay chain $^{238}\mathrm{U}$ is only simulated up to the daughter isotope and from there the second simulation takes over for all further progeny. In the second case this was not possible and therefore the full decay chain is included in $^{232}\mathrm{Th}$ as well. This leads to the possibility of a negative fit value for $^{228}\mathrm{Th}$, if the equilibrium is distorted within the decay chain.
For the materials the relative size of each component is dependent on the fiducial volume, so the amplitude of each isotope is left free in the fit. This is different for the various other sources, which are constrained by external knowledge. This is incorporated in eq. (4.20) by introducing Lagrange multipliers (quadratic χ^2-penalties) changing the χ^2-function to

$$\chi^2_{\mathrm{extended}} = \chi^2_{\mathrm{basic}} + \sum_j \frac{(\mu_j - p_j)^2}{(\Delta\mu_j)^2}. \tag{4.21}$$

Here, μ_j denotes the expected value for the j-th parameter, which is given by external constraints including an uncertainty $\Delta\mu_j$. The fit parameter is expressed by p_j. This way the χ^2 is increased if the fit tries to shift from the expectations. The expected value for the χ^2-penalty for the intrinsic isotopes is set to unity and the uncertainties are given by external studies. For $^{136}\mathrm{Xe}$ the uncertainty from the abundance measurement ($5\,\%$) dominates, so it is included into the constraint. For solar neutrinos an uncertainty of $20\,\%$ was taken according to [174]. For $^{85}\mathrm{Kr}$ input for the expected value is given by concentration measurements from the RGMS system and by the isotopic fraction within natural krypton. The respective values are $(0.66 \pm 0.11)\,\mathrm{ppt}$ for the concentration and $1.65 \cdot 10^{-11}\,\mathrm{mol/mol}$ for the isotopic fraction of $^{85}\mathrm{Kr}$. The latter is derived from RGMS measurements prior to the krypton distillation and an actual measurement of the ER rate at this time [111]. The systematic uncertainty of the RGMS is dominating in both quantities. Although there could be a cancellation of the uncertainty, it is included conservatively and accounts for the $17\,\%$ uncertainty in the concentration measurement. Since $^{85}\mathrm{Kr}$ is normalized to $0.1\,\mathrm{ppt}$, the expectation value for the Lagrange multiplier is at 6.6 and the uncertainty at 1.1.
No constraint can be introduced on $^{214}\mathrm{Pb}$, the major background source in the energy region of interest. The only information available on its contribution is from an upper limit of $(12.6 \pm 0.8)\,\mathrm{Bq\,kg^{-1}}$ from the counting of α-decays of its parent isotope $^{218}\mathrm{Po}$ and from a lower limit of $(5.1 \pm 0.5)\,\mathrm{Bq\,kg^{-1}}$ from a delayed coincidence study on subsequent decays of its progeny $^{214}\mathrm{Bi}$ and $^{214}\mathrm{Po}$. The difference between both methods is caused by plate-out of decay products at the walls and the cathode and no mean value can be assumed, as this process is not well understood.
The different peaks introduced artificially to the detector cannot be constrained in

[16] The isotopes $^{235}\mathrm{U}$ and $^{137}\mathrm{Cs}$ are not expected to contribute significantly and are omitted in the entire consideration.

amplitude as this is not known precisely. Their expected energy position is constrained using the knowledge of the uncertainty of the energy calibration and the literature values for the position. For simplicity the peak position uncertainty of all activated peaks is set to $0.6\,\mathrm{keV}$, which corresponds to the average uncertainty for the energy reconstruction in this range. The width is not constrained as no independent measurements exist and the internal uncertainty on the resolution function is derived from exactly these sources. Nevertheless, a value derived from the resolution function can be compared to the fit result later.
The matching of the MC and the data is performed up to a maximum energy of $E_{\mathrm{max}} = 300\,\mathrm{keV}$. This limitation arises from the lack of knowledge about the efficiencies of multi-scatter cuts at higher energies. More details on the fit range will be given in section 4.2.7. The result of the χ^2-fit and all background contributions obtained this way are illustrated in fig. 4.14. Before the results of the fit can be discussed a few adjustments are introduced in section 4.2.7.

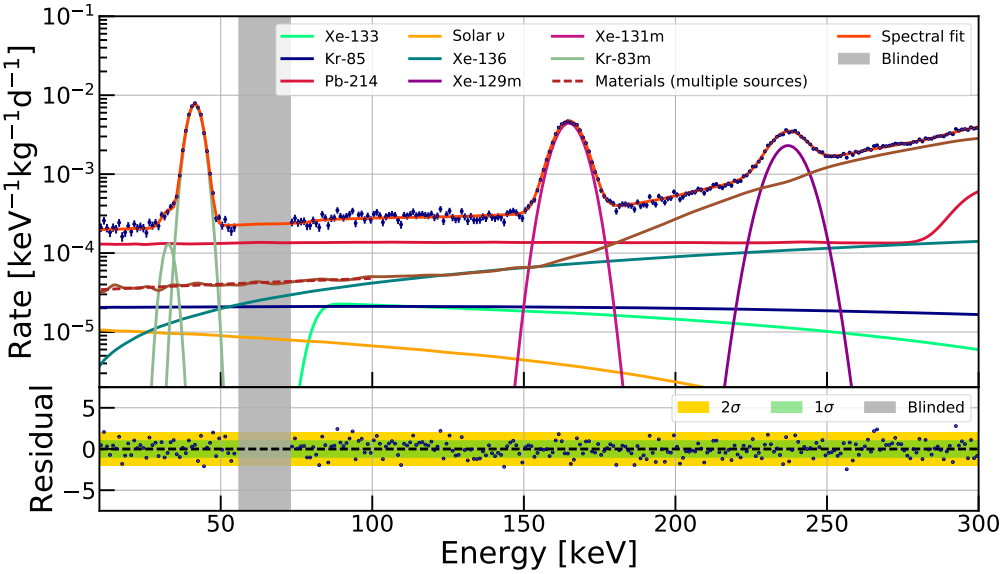

Figure 4.14.: MC/data matching of the background model in the $1.5\,\mathrm{t}$ fiducial volume from $10\,\mathrm{keV}$ to $300\,\mathrm{keV}$ The described background components are fitted simultaneously according to the constraints given in the text. The summed spectrum of the best-fit is shown (orange) overlaid on the data (blue crosses). A region between $56\,\mathrm{keV}$ to $72\,\mathrm{keV}$ is still blinded. The reduced χ^2 is 1.10 with 254 degrees of freedom.

I-125

While all sources mentioned so far increase the general background level, a potentially dangerous background source would be one that deposits an energy close to $64.33\,\mathrm{keV}$ in a single signal. Due to the short mean free path of γ or β-particles at these energies, the source would have to be homogeneously distributed in the detector. The only source identified able to mimic the double electron capture signal in this way is the

iodine isotope $^{125}\mathrm{I}$. It decays via electron capture ($T_{1/2} = 59.4\,\mathrm{d}$) into a short-lived excited state of $^{125}\mathrm{Te}$, which is at $35.5\,\mathrm{keV}$ above the ground state [175]. The K-shell capture is the most probable ($P_K = 87.5\,\%$ [176]) and, therefore, the relaxation of the process releases the energy of the K-edge of $^{125}\mathrm{Te}$, which is at $31.8\,\mathrm{keV}$ [177]. As the detector is not able to separate the signals of the atomic relaxation and the de-excitation γ or conversion electrons of $^{125}\mathrm{Te}$, the entire energy is recorded in a single signal (c.f. double electron capture signal) at $67.3\,\mathrm{keV}$. Given the resolution at these energies, this is about 1σ away from the double K-shell electron capture signal. So, a separation of the two signals is difficult and can limit the sensitivity of the search (see [86]). The $^{125}\mathrm{I}$ is produced via neutron activation of $^{124}\mathrm{Xe}$ by the capture of thermal neutrons:

$$\begin{aligned} {}^{124}\mathrm{Xe} + n &\rightarrow {}^{125}\mathrm{Xe} + \gamma, \\ {}^{125}\mathrm{Xe} + e^- &\rightarrow {}^{125}\mathrm{I}^* + \nu_e, \\ {}^{125}\mathrm{I} + e^- &\rightarrow {}^{125}\mathrm{Te}^* + \nu_e. \end{aligned} \tag{4.22}$$

The created $^{125}\mathrm{Xe}$ disintegrates via electron capture ($T_{1/2} = 16.9\,\mathrm{h}$) into excited states of only $^{125}\mathrm{I}$. Mostly, it populates the excited states at $243.4\,\mathrm{keV}$ ($66.6\,\%$) or at $188.4\,\mathrm{keV}$ ($25.4\,\%$). Due to the short half-life of these states ($\mathcal{O}(\mathrm{ps})$) they are merged with the relaxation quanta of the atomic shell vacancies of $^{125}\mathrm{I}$ left after the electron capture of $^{125}\mathrm{Xe}$. Nevertheless, the energy deposition of $^{125}\mathrm{Xe}$ can be separated completely from the subsequent decay of $^{125}\mathrm{I}$ due to its long half-life.
The activation of xenon through thermal neutrons is possible by two different sources: environmental neutrons activating xenon in the gas system outside of the water tank and neutrons from the calibration campaigns moderated by the water in the water tank. While the former would constitute a continuous source in time, the latter is limited to the two neutron calibration campaigns using $^{241}\mathrm{AmBe}$ and the deuterium-deuterium-neutron generator. A substantial advantage of the XENON1T detector compared to similar searches (see [86]) is the fast continuous purification of the entire xenon inventory with hot-zirconium getters. These are expected to be extremely efficient in terms of removing halogens as iodine from xenon gas. Two studies are conducted in order to investigate whether $^{125}\mathrm{I}$ is a potential threat to the double electron capture search in XENON1T. Both are based on the idea that an activation rate A within the calibration campaigns can be determined using the decay signature of $^{125}\mathrm{Xe}$. This provides an expectation value for the $^{125}\mathrm{I}$ signatures in the region of interest. A comparison of the obtained data after the neutron calibration campaigns with the expectation provides a handle on the efficiency of iodine removal. This can then be used to estimate the contribution of $^{125}\mathrm{I}$ within the double electron capture search data.
The contribution of the decay can be modeled in terms of $^{125}\mathrm{Te}$ particles $N_{\text{Te-125}}$

registered in the active detector volume as a function of time in the following way:

$$\begin{aligned}\frac{N_{\text{Xe-125}}}{\mathrm{d}t} &= A - \lambda_{\text{Xe-125}} N_{\text{Xe-125}}(t),\\ \frac{N_{\text{I-125}}}{\mathrm{d}t} &= \lambda_{\text{Xe-125}} N_{\text{Xe-125}}(t) - \lambda_{\text{I-125}} N_{\text{I-125}}(t) - \lambda_{\text{rem}} N_{\text{I-125}}(t),\\ \frac{N_{\text{Te-125}}}{\mathrm{d}t} &= \lambda_{\text{I-125}} N_{\text{I-125}}(t).\end{aligned} \tag{4.23}$$

The neutron activation rate A denotes the number of created $^{125}\mathrm{Xe}$ nuclei per unit time in the observed volume, N the respective particle number and λ the respective decay constants. A translation from decay constant to half-life or lifetime is given by:

$$\lambda = \frac{\ln(2)}{T_{1/2}} = \frac{1}{\tau_{\text{rem}}}. \tag{4.24}$$

The two decay terms, $\lambda_{\text{I-125}}$ and λ_{rem} cannot be distinguished in the measurement and are subsumed in an effective decay constant λ_{eff}. Nevertheless, for fast removal times, λ_{rem} dominates the process. If the purification of the getters works with a perfect efficiency, the removal decay constant is defined by the time wherein the entire detector content is revolved once through them. For SR1 the according removal time constant [96] would be

$$\tau_{\text{rem}} = 7.5\,\mathrm{d} \approxeq \tau_{\text{eff}}. \tag{4.25}$$

The behavior of the decay rates as extracted for a few sample expectations is shown in fig. 4.15. In addition, by integration of eq. (4.23) the total number of expected counts as a function of time can be obtained, as shown exemplary in fig. 4.16. In order to determine the effective lifetime within the detector two separate data sets were analyzed. In a first step, the $^{241}\mathrm{AmBe}$ calibration campaign within SR1 was used. Therefore, $14\,\mathrm{days}$ of data were unblinded and excluded from the final data set directly after the calibration. The only quantity which has to be determined beforehand is the activation rate as shown in eq. (4.23). This is extracted by using the decay of the parent nucleus $^{125}\mathrm{Xe}$ while the neutron source is present. Here, the most prominent decay branch is chosen and the signal at $276.7\,\mathrm{keV}$ (de-excitation γ + $K-$shell vacancy) is fitted with a Gaussian function. In order to reduce the background contribution and enhance the precision, the fit is performed on a differential spectrum. This obtained by subtracting the regular background rate prior to the AmBe-calibration from the normalized rate during the AmBe-calibration. The obtained number of events has to be corrected for the branching ratio (0.666 [175]) and the probability of a K-shell electron capture (0.889 [176]). By normalizing it with the activation time ($13.7\,\mathrm{days}$) the activation rate A_{AmBe} for the $^{241}\mathrm{AmBe}$-source was found to be

$$A_{\text{AmBe}} = (60 \pm 7)\,\mathrm{d}^{-1}. \tag{4.26}$$

Notably, this is the activation rate in the chosen fiducial volume corresponding to the cylinder from SR0 containing $1042\,\mathrm{kg}$ of xenon.
The analogous procedure is performed for a second data set, which was dedicated to

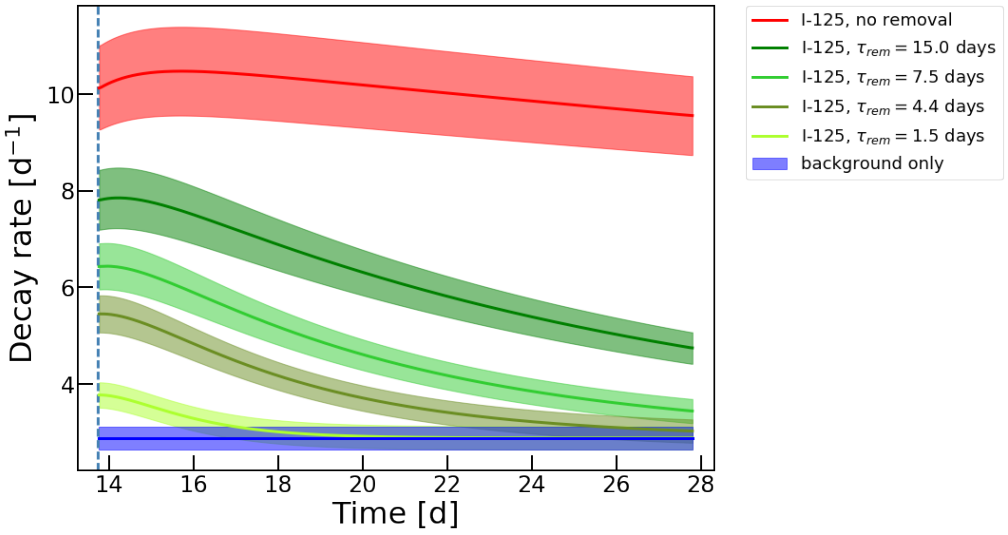

Figure 4.15.: Evolution of the ^{125}I decay rate for various effective lifetimes τ_{rem}. The recorded decay rate for ^{125}I per day is shown as a function of time in the given post-AmBe data set (see eq. (4.26)). The comparison of no-removal (red) of ^{125}I and different removal lifetimes are shown (various green). The background rate is added for each of the curves and a background-only scenario is indicated in blue. Each band around the mean curve represents the uncertainty on the activation and background rates.

the purpose of determining the ^{125}I removal efficiency. Here, the neutron generator (NG) was used after SR1 was concluded[17]. The NG was continuously running for $2.83\,\mathrm{days}$ and $5.96\,\mathrm{days}$ of data were taken continuously afterwards in order to quantify the ^{125}I signal. The activation rate was determined according to the analysis before and yielded:

$$A_{\mathrm{NG}} = (411 \pm 35)\,\mathrm{d}^{-1}. \tag{4.27}$$

By insertion of this number and the activation time for each of the two studies in eq. (4.23) the total number of expected ^{125}I events is calculated and compared with the measured events as obtained from a Gaussian fit with linear background R_b constrained at the expected energy ($67.5\,\mathrm{keV}$) and width ($2.8\,\mathrm{keV}$). The fit results of both studies are illustrated in fig. 4.17 and given in table 4.7. While the fit for the post-AmBe data set only gives a signal count in agreement with zero, the results from the NG data actually correspond to a signal from ^{125}I. Both results can be transformed into a removal lifetime by using the integration of eq. (4.23) as shown in fig. 4.16. In the case of AmBe only an upper limit can be set of $\tau_{\mathrm{rem}} < 4.8\,\mathrm{d}$ at $90\,\%$ C.L. using the method of Feldman and Cousins [132] and the uncertainty from the fit result. From the NG data a value of

$$\tau_{\mathrm{rem}} = 4.2^{+2.1(\mathrm{stat.})+0.7(\mathrm{sys.})}_{-1.6(\mathrm{stat.})-0.5(\mathrm{sys.})}\mathrm{d}, \tag{4.28}$$

[17] The neutron generator calibration within SR1 could not be used due to interrupted usage of the neutron generator as well as messy data in its aftermath due to a light emission hot spot.

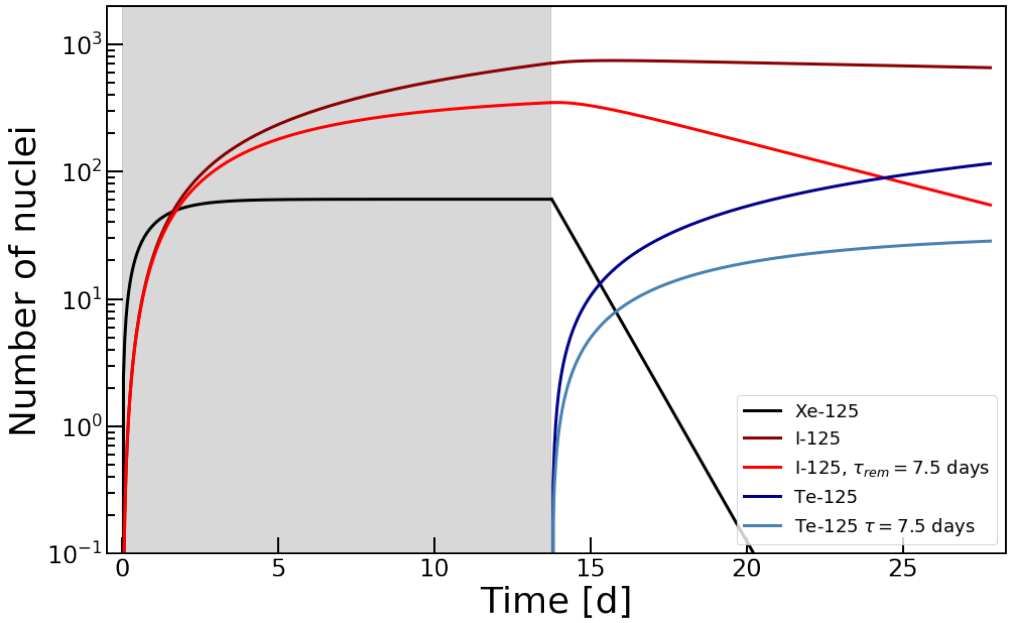

Figure 4.16.: Integrated number of ^{125}Xe and its progeny within the AmBe calibration study. The neutron calibration with ^{241}AmBe lasted for $13.7\,\mathrm{days}$ (gray shaded area). During this time ^{125}Xe is generated (black) and reaches an equilibrium with its decay with a half-life of $\mathrm{T}_{1/2} = 16.9\,\mathrm{h}$. As soon as the source is removed, only the decay takes place. The progeny ^{125}I is produced by this decay during calibration and its behavior is shown for two cases: No removal through the getters or any other process (dark red) and removal with an effective lifetime of $\tau = 7.5\,\mathrm{d}$ (red). The number of ^{125}Te particles corresponds to the integrated number of ^{125}I decays within the detector. They are only recorded in the background data after the calibration campaign due to increased background during the calibration. The evolution in case of no removal of the iodine is shown (dark blue) as well as an exemplary removal with $\tau = 7.5\,\mathrm{d}$ (light blue).

is derived, which is in agreement with the upper limit from the AmBe evaluation. The statistical uncertainties on the removal lifetime are derived from the fit uncertainty, while the systematic uncertainty is defined by varying the activation rate according to the uncertainty given in eq. (4.27). All results from this integral analysis are summarized in table 4.7.
The time distribution of the events is compared for a further extraction of the effective lifetime. Therefore, a binned log-likelihood of the form

$$\log \mathcal{L}_{\mathrm{rem}} = \sum_{i}^{\mathrm{t_{max}}} \ln\left(\frac{f_i(\tau_{\mathrm{rem}})^{x_i}}{x_i!} e^{-f_i(\tau_{\mathrm{rem}})}\right) \tag{4.29}$$

is used to compare the measured behavior in the time dimension with the expected values from eq. (4.23). Here, the expected number of events f_i in the i-th time bin is compared with to measured event count x_i in the respective bin assuming a Poisson distribution. The expectation is derived from eq. (4.23) and is dependent on the effective lifetime τ_{rem} of ^{125}I. In order to incorporate the uncertainties on

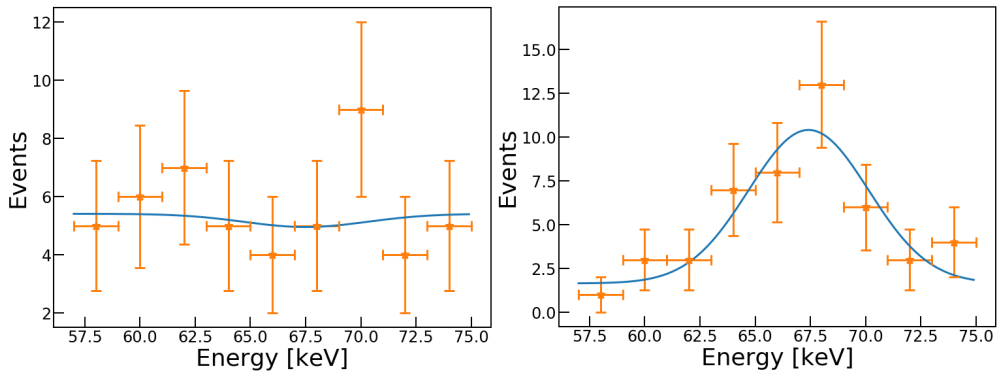

Figure 4.17.: Fit results of both post neutron calibration data sets. Left: The events from $57\,\mathrm{keV}$ to $75\,\mathrm{keV}$ in $14\,\mathrm{days}$ of post-AmBe data are fitted in $2\,\mathrm{keV}$ bins (orange). A likelihood fit of a Gaussian signal plus a constant background is added (blue). The position and width were constrained using Lagrange multiplier. Right: The events from $57\,\mathrm{keV}$ to $75\,\mathrm{keV}$ in the $5.96\,\mathrm{days}$ of post-NG data. The fit is the same as for the other data set but due to the different detector conditions the background rate is not shared and left free in the fit.

Table 4.7.: Fit results for both data sets with the calculated τ_{rem} from the model in eq. (4.23). The uncertainties are taken from the fit result.

Data set	R_b [evts/keV/d]	Counts	Mean [keV]	Width [keV]	τ_{rem} [d]
AmBe	0.24 ± 0.05	-1.5 ± 7.5	67.5 ± 0.5	2.8 ± 0.2	<4.8
NG	0.14 ± 0.06	30.0 ± 7.8	67.4 ± 0.4	2.7 ± 0.2	$4.2^{+2.1}_{-1.6}$

the activation rate A and the background rate R_b, Lagrange multipliers are added to the log-likelihood. The *migrad*-function is used to minimize $-2\log\mathcal{L}_{\mathrm{rem}}$ with the given constraints. In total 143 bins were compared (hourly binning) for events in an energy window[18] between $62\,\mathrm{keV}$ to $74\,\mathrm{keV}$. The best-fit values in case of the NG are $A = (407 \pm 35)\,\mathrm{d}^{-1}$ for the activation rate, and $R_b = (0.17 \pm 0.06)\,\mathrm{events/d/keV}$ for the background rate, which are both in agreement with the previous derived values. For the removal lifetime the fit provides:

$$\tau_{\mathrm{rem}} = 4.7^{+2.5}_{-1.9}\,\mathrm{d}. \tag{4.30}$$

The uncertainties are provided by the *minos*-method of *iMinuit* and are cross-checked using the negative log-likelihood distribution as a function of τ_{rem}. In fig. 4.18 the best-fit result is shown together with the data and two other scenarios: no-removal and background-only. Clearly, it describes the data better then the other two and confirms the removal of ^{125}I within the detector. For the further treatment of the expected contribution of the source the value in eq. (4.30) is used, as it incorporates the most knowledge. Notably, the result would correspond to a cleaning efficiency

[18] This energy window is more narrow compared to the integrated analysis as the differential analysis suffers from background-only bins. By choosing a rough 2σ band around the peak center, it was tried to maximize the signal-to-noise-ratio.

greater than $100\,\%$ from the assumption of $7.5\,\mathrm{days}$ revolving time for the detector, a homogeneous distribution of the ^{125}I and perfect iodine removal by the getters. This cannot be explained by the getter removal alone and a possible explanation lies in the fact, that the iodine is created via an electron capture. The filling of the vacancy leads to a positively charged ion. Any positive charge in the detector is drifted towards the cathode[19], and thus, is removed from the fiducial volume. As the background level at the cathode is increased, this hypothesis cannot be easily tested, given the few expected ^{125}I events.

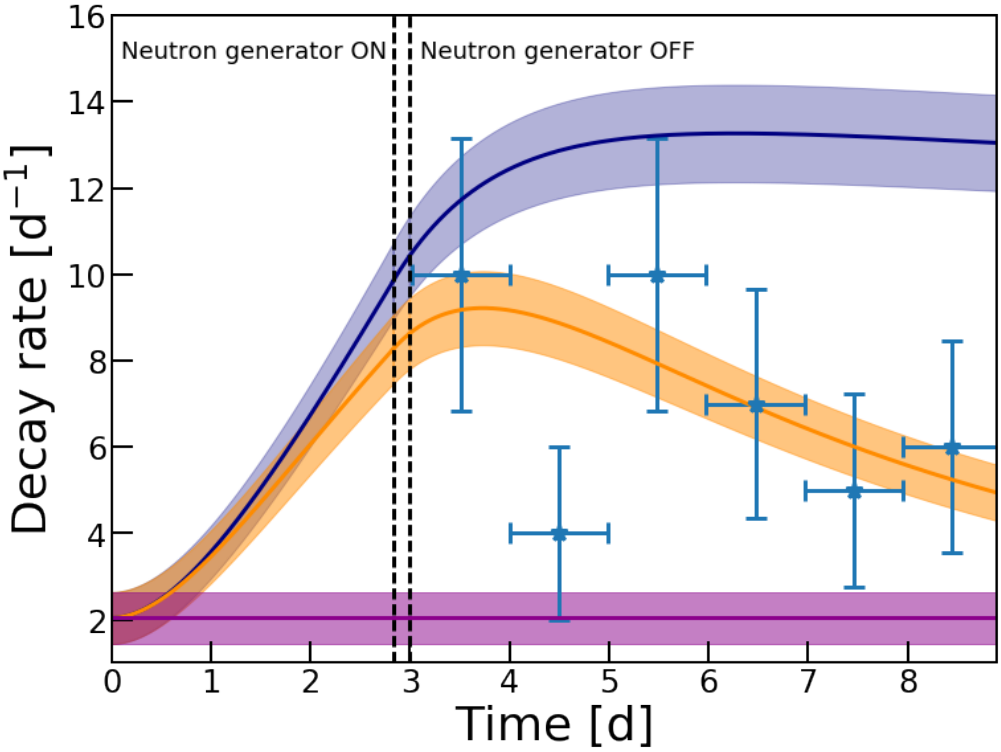

Figure 4.18.: Decay rate evolution of ^{125}I in the NG data set. The decay rate per day is shown during and after the neutron generator activation. The scenario of no removal (blue), the evolution with the best-fit value for a removal time of $\tau_{\mathrm{rem}} = 4.7\,\mathrm{d}$ (orange) and a pure background-rate scenario (purple) are compared to the data (blue crosses). Dashed lines denote the small time period, where no data was recorded during removal of the neutron generator. The uncertainties on the data are purely statistical for the decay rate and the width of the time bins is indicated by the horizontal bars. An uncertainty band incorporating the uncertainty on the background rate as well as on the activation rate is shown around each curve. The data was binned daily for illustration.

[19] To some extent they should also drift to the wall since they presumably accumulate negative charges. This effect could be sub-dominant due to the smaller electric fields compared to the strength of the electric field towards the cathode.

As outlined before the estimation of ^{125}I in the entire data set targets the two possible contributions: continuous activation from thermal neutrons and time localized activation from calibration campaigns. For the first, the amount of xenon (m_{out}) outside of the water tank has to be estimated, as this is the only xenon which can be activated. A conservative assumption is about $10\,\text{kg}$, which will clearly overestimate the contribution but can be used as an upper limit[20]. From this, the number of xenon particles $N_{\text{Xe-124}}$ can be calculated using the abundance η_{XE1T} and number of xenon nuclei per mass unit ($4.6 \cdot 10^{24}\,\text{nuclei/kg}$). The thermal neutron flux Φ_n at LNGS is measured by different experiments, which do not provide a conclusive number [178, 179, 180, 181]. Reference [182] derives from MC simulations that this disagreement could be caused by seasonal changes of the water flow within the mountain rock and could, thus, change moderation rates of produced environmental neutrons depending strongly on the time of measurement. By taking the average of all measurements a value for the thermal neutron flux at LNGS is assumed as

$$\Phi_n = (1.00 \pm 0.67) \cdot 10^{-6}\,\text{cm}^{-2}\,\text{s}^{-1}, \tag{4.31}$$

where the uncertainty is the standard deviation of the measurements. Using this flux, the amount of xenon outside the detector $N^{\text{out}}_{\text{Xe-124}}$ and the thermal neutron capture cross-section for ^{124}Xe ($\sigma_{nc} = 165 \cdot 10^{-24}\,\text{cm}^{-2}$) the expected activation rate A_{thermal} can be calculated using:

$$A_{\text{thermal}} = \Phi_n \cdot N^{\text{out}}_{\text{Xe-124}} \cdot \sigma_{nc}. \tag{4.32}$$

A value of $(0.65 \pm 0.44)\,\text{d}^{-1}$ for the activation rate is found, which can be translated to an upper limit on the expected amount of ^{125}I decays in the fiducial volume using the measurement time ($214.3\,\text{days}$) and the effective lifetime derived from the previous studies:

$$N^{\text{t}}_{\text{I-125}} < 6.2\,\text{events} \tag{4.33}$$

An upper limit is chosen, as this value is based on an overestimated amount of xenon outside the water tank.
The contribution from the neutron calibration campaigns can be calculated by integrating eq. (4.23). Since there was no measurable signal after the AmBe calibration, the only concern is the neutron generator campaign in the end of May, 2017. The calibration lasted for five days in total, but only two days live time of the neutron generator with alternating on-off-phases were acquired. In order to estimate the contribution from ^{125}I due to this campaign conservatively, it is assumed that the neutron generator ran for two days consecutively. While the first 7 days after the campaign were not usable for any science search due to insufficient detector conditions, 3 additional days are removed from the search here. This was done for two reasons: After 10 days the first detector calibration with ^{83m}Kr was performed, ensuring stable

[20] This value is in the right ball park, but no actual value could be determined reliably. A rough estimation based on the geometrical dimensions and the densities of xenon at the given temperatures yields about $5\,\text{kg}$ of xenon outside the water tank, but conservatively the larger value is chosen.

detector assembly, and, in addition, this way, any contribution of ^{125}I is reduced to about $10\,\%$ of the initial activation given the obtained removal lifetime. From this point on, the calculation yields an upper limit of:

$$N^{\mathrm{c}}_{\text{I-125}} < 2.5\,\mathrm{events} \tag{4.34}$$

Also, in this case only an upper limit is derived since the assumption on the continuous operation neglects the removal during the entire five days of the calibration campaign. A validation of the expected counts of ^{125}I is accomplished by extracting the expected number of ^{125}I events in the full data set from the number of decays of its short-lived parent ^{125}Xe. Therefore, the signal of ^{125}Xe is simulated with a normalization such that unity is equal to $1\,\mu\mathrm{Bq\,kg^{-1}}$ and added to the background model. The outcome of the fit can be translated to an expected number of ^{125}I signal counts produced through thermal neutrons outside of the water tank as well. Notably, it does not correspond to the calibration campaign part of the ^{125}I contribution, since the data sets right after and during calibration are not included in the data set used for the double electron capture search. So the short-lived ^{125}Xe has decayed away but its daughter isotope still contributes to the overall rate. This method will be used to derive the final expectation value for the ^{125}I contribution from the environmental activation after a few additions are added to the fit routine (see section 4.2.7).

4.2.6 Selection criteria and acceptances

The shift towards higher energies as well as the transition from NR to ER requires an evaluation of all event selection criteria (referred to as cuts) from the dark matter search analysis and possibly introducing new cuts. Furthermore, the mindset for this analysis in terms of cut efficiencies and signal acceptances is different than for the dark matter search. There, the removal of a single noise event is of crucial importance due to the low background expectation and low expected rate of the WIMP interaction. Here, the main background sources cannot be removed anyway and, thus, the search is mainly about finding a signal above the statistical fluctuations of the background contributions. This makes signal acceptance more important than rejection of (unphysical) background, especially as these kinds of backgrounds, e.g. gas events, are not expected to mimic the double electron capture signal.
When removing the selection criteria which target only the low-energy nuclear recoil parameters, the left-over cut set is shown in table 4.8. Basic cuts as the require that an interaction exists and that the interaction is the main one within the event are negligible due to the high energy character of the search. Also the *S2Threshold* criterion is obsolete as the energy requirement is already demanding way larger S2s. Any selection due to dead time correction is implemented already in the live time correction of the data set and needs no further acceptance evaluation. Clearly identified noise events are removed based on the integrated signal size before the actual $S2$ (*PreS2Junk*). Any proper event is required to have at least $50\,\%$, but not more than $72\,\%$ of its $S2$ signal registered by the top array (*S2AreaFractionTop*). This effectively removes events produced in the gas phase and spurious noise from the anode. A similar criterion ensures that the registered fraction of the $S1$ signal in the top array matches the binomial distribution expected from the interaction position (*S1AreaFractionTop*). Also, the general hit distribution of the $S1$ signal in both PMT arrays is compared to the expectation from a physical single scatter (*S1PatternLikelihood*). In general, an event is only allowed to pass if only one scatter is identified in the detector in both signal channels (*S1SingleScatter* & *S2SingleScatter*). This targets multi-energy depositions at different positions within the detector (mainly Compton scattering) as well as delayed coincident decay processes. Additionally, pile-up events are removed. Furthermore, the width of the $S2$ signal of the event has to match its interaction depth (*S2Width* c.f. section 3.1). Finally, it has to occur within the fiducial volume as described above.
For each cut, the respective parameter space in an energy region between $20\,\mathrm{keV}$ to $200\,\mathrm{keV}$ was checked for its acceptance of signal events. The study was performed in two data sets: Background (dark matter search) with the energy region of the double electron capture ($50\,\mathrm{keV}$ to $80\,\mathrm{keV}$) omitted due to the blinding cut and data from the $^{220}\mathrm{Rn}$ calibration, which provides a continuous ER source in the entire energy range. For both data sets, different time periods throughout SR1 have been used in order to account for possibly time dependent acceptance changes.
The *S2PatternLikelihood* selection from dark matter analysis is the only ER cut not viable for the double electron capture search. It removes up to $30\,\%$ of the $^{220}\mathrm{Rn}$ data

of which most are real ER events, as found by investigating the discarded events. For all other cuts as listed in table 4.8 no acceptance problems were encountered. In addition to this, the fiducial volume cut as derived above is added and furthermore, an ER band criterion requiring any event to be between:

$$1 < log_{10}\left(\frac{cS2b}{cS1}\right) < 2, \tag{4.35}$$

was introduced for the removal of NR and surface events. It has been verified using $^{220}\mathrm{Rn}$ calibration data that this cut has an acceptance at unity but rejects noise and NR efficiently. For the other cuts the acceptance has been individually evaluated with the best possible method. There are three ways available to determine the acceptance: evaluation using simulation or external information (referred to as *analytics*), the N-1 method described by eq. (4.2) and used in [102] and the iterative method applied on the $^{220}\mathrm{Rn}$ calibration data set. The first one is always the method of choice if available, as it provides an independent input and allows to infer the actual acceptance. The N-1 method, introduced in the previous chapter, is performed in the best case on calibration data, but can also be used on the search data itself. However, in both cases it yields only a lower limit for the acceptance. The iterative method is only used, where the N-1 method is not applicable due to correlation of the selection criteria. This method applies all cuts successively to calibration data and the removed events with each selection step are used as a lower limit on the acceptance. So, only the analytical methods derive an actual acceptance, while the other two methods set a lower limit on the acceptance. The method applied for each selection criterion is shown in table 4.8. Hereby, the acceptance is defined in energy bins with $1\,\mathrm{keV}$ width and with binomial uncertainties accounting for the limitation of the acceptance to values between zero and unity. A total acceptance is derived by bin-wise multiplication as shown in fig. 4.19. A continuous acceptance function $\epsilon_{\mathrm{XE1T}}(E)$ itself is then obtained with a first order polynomial fit:

$$\epsilon_{\mathrm{XE1T}(E)} \geq ((-1.48 \cdot 10^{-2} \cdot E + 94.28) \pm 0.73))\,\%. \tag{4.36}$$

This can be further approximated in a small energy region around the double electron capture signal ($50\,\mathrm{keV}$ to $75\,\mathrm{keV}$)[21], where the acceptance $\epsilon_{2\nu\mathrm{KK}}$ is fitted by a polynomial of 0th order which yields

$$\epsilon_{2\nu\mathrm{KK}} \geq (93.4 \pm 0.7)\,\%. \tag{4.37}$$

The uncertainty is taken from the fit function since the standard deviation from the data points is negligible ($0.1\,\%$).

[21] The energy intervall was selected due to the limitation by $^{83m}\mathrm{Kr}$ on the lower energy side of the central expectation value of the double electron capture and due to the limitation by $^{133}\mathrm{Xe}$ on the upper energy side.

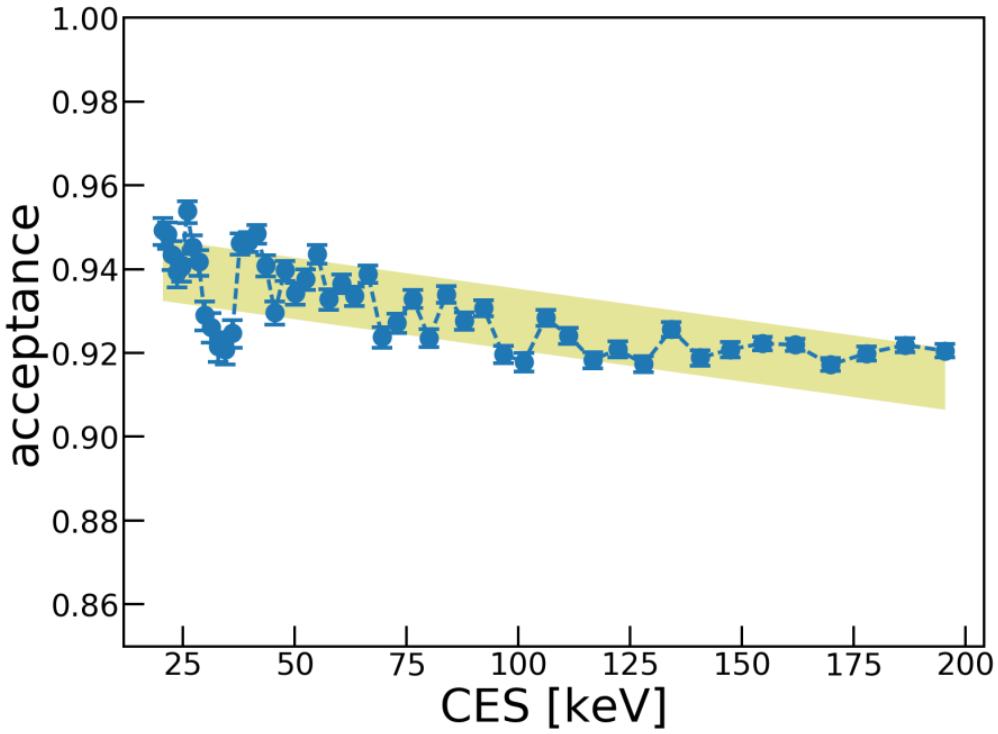

Figure 4.19.: Event acceptance between $20\,\mathrm{keV}$ to $200\,\mathrm{keV}$. The bin-wise acceptance obtained from the multiplication of the different cut acceptances in each bin is shown (blue). The structure around $30\,\mathrm{keV}$ is related to two-fold krypton signals and the conservative N-1 method. The acceptance is approximated by a polynominal of first order (yellow), which is indicated with a symmetric uncertainty band of $0.73\,\%$.

Table 4.8.: Selection criteria for the double electron capture search.

Cut name	Description	Acceptance method
DAQVeto	Dead time correction	Live time
InteractionPeakBiggest	No larger peak	Analytics
S2Tails	Dead time correction	Live time
S2Width	Depth-size correlation	Analytics
PreS2Junk	Noise threshold	N-1(BKG)
S2AreaFractionTop	Signal size fraction	N-1(Rn-220)
S2SingleScatter	Single scatter	N-1(BKG)
S1AreaFractionTop	Signal size fraction	Iterative (Rn-220)
S1PatternLikelihood	Photon distribution check	Iterative (Rn-220)
S1SingleScatter	Single scatter	Iterative (Rn-220)
ER criterion	Removing NR	Analytics

4.2.7 Fit model

In order to fit a combination of the background and signal model, a few adjustments have to be made in the definition of the χ^2-function. Firstly, instead of a matching in the full volume, two separate volumes are cut out of the $1.5\,\mathrm{t}$ total volume as illustrated in fig. 4.20. This separation is done in order to enhance the information for the background and signal model. For the background model it provides additional information on the intrinsic components as the background contributions from the different materials are suppressed in the inner volume due to the self-shielding of xenon. By fitting the two volumes simultaneously with shared parameters for each isotope, the extra information on the intrinsic components is also passed to the outer layer and consistency is ensured. This is also the case for the signal model. The decay of $^{124}\mathrm{Xe}$ is homogeneously distributed and so a combined fit of the two volumes has to yield the same value within uncertainties. If this is not the case, e.g., due to an unforeseen background source at the walls, the goodness-of-fit would deteriorate.
The mass of the two selected volumes was estimated using the $^{83m}\mathrm{Kr}$ event counts in both of the volumes as a ratio of the total volume and they are determined to $M_{\mathrm{inner}} = 1052\,\mathrm{kg}$ and $M_{\mathrm{outer}} = 448\,\mathrm{kg}$. This differs by $1\,\%$ from what would be expected from the geometrical considerations and in order to incorporate this uncertainty to the fit, a mass factor was included in the fit function for each volume as a constrained parameter with the expectation normalized to unity. Each constraint is added as a Lagrange multiplier to the χ^2-function

$$\chi^2_{\mathrm{vol}}(i) = \frac{(M_i - 1)^2}{(0.01)^2} \quad \text{with i} = (\text{inner}, \text{outer}), \tag{4.38}$$

where the expectation value is set to one and the uncertainty to $1\,\%$ as given by the event counting with $^{83m}\mathrm{Kr}$.
The next adjustment targets the uncertainty for acceptances above $200\,\mathrm{keV}$. Around these energies a few of the selection criteria decrease in acceptance for any true physical event. This is caused by the fact that the selection criteria are designed for the low energy part of the spectrum, but also by entering a different physics regime around these energies. In case of the cuts targeting the single scatter selection, an acceptance drop within the N-1 method is expected as the Compton scattering starts to dominate over the photoelectric absorption, thus leading to more multi scatters. For higher energies pair production complicates the processes further. As this purely physics driven process cannot be distinguished from any noise removal, this cannot be treated as an acceptance loss. The fraction of falsely identified multi-scatters is not easily extractable anymore as this would require simulation studies since any calibration source introduced is not able to produce single scatters at this energy. An evaluation of this is the task of future studies, especially for any search of high energy signatures but can not be implemented here. For two other cuts, a different approach is pursued. The *PreS2Junk* as well as the *S2Width* cut show dropping acceptances at higher energies. As the former is related to spurious signals before the main $S2$, it can be possibly explained by increased noise, e.g., due to photoionization by the

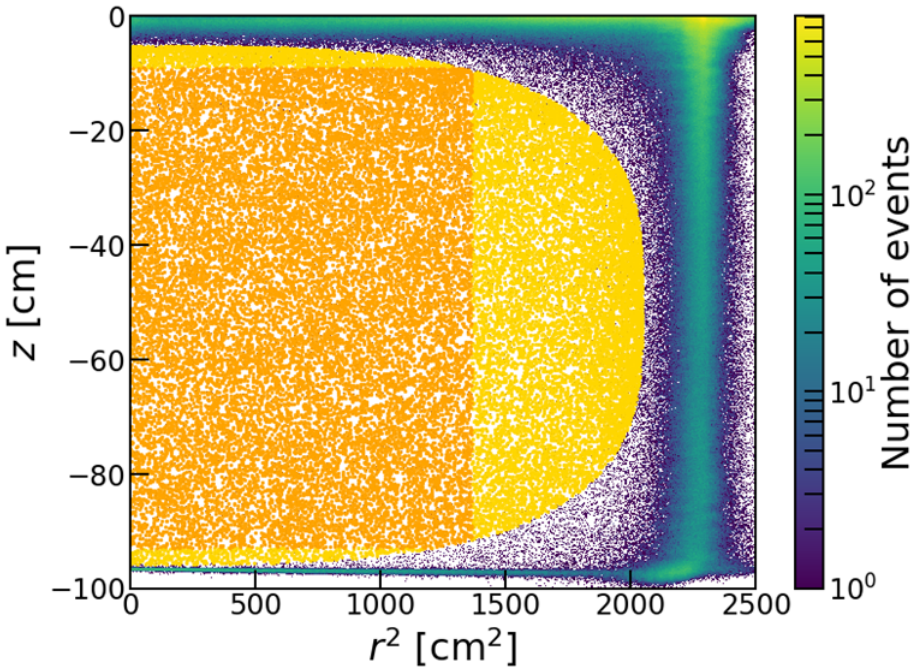

Figure 4.20.: Fiducial volume separation for combined fitting. The two separated volumes are indicated. The outer volume (yellow) corresponds to $448\,\mathrm{kg}$ and the inner volume (orange) is a cylinder of about $1052\,\mathrm{kg}$. The mass factor of these two is separately included in the fit as a constrained parameter. The energy range of the data used for this plot is $80\,\mathrm{keV}$ to $140\,\mathrm{keV}$.

photons of the $S1$ signals. The width of the signals can be related to this as well and a removal of valid signals due to increased single electrons or photoionization would indeed be an acceptance loss. Furthermore, it is assumed that the width of the S2 signals suffers from saturation effects, changing the parameter in a way the cut is not optimized for. This has to be taken into account for the MC/data matching as the simulated spectra do not suffer from such problems at high energies, since they are not implemented in the simulation yet, but a lot of information is contained within the peaks at these energies.

In order toa account for the high energy acceptance loss, the N-1 method is used on $^{220}\mathrm{Rn}$ data for each of the cuts. The results are then multiplicatively bin wise combined up to $500\,\mathrm{keV}$. This is performed for both volumes separately in order to include a possible spatial dependence. The resulting spectrum is shown in fig. 4.21 for each of the volumes. In order to model the acceptance losses, an effective function is introduced. It is defined as unity up to a changeable cross-over point, above $100\,\mathrm{keV}$, and then approximated by a fourth order polynomial. This way the low energy part (including the signal) is not affected and the full acceptance, including all cuts, can be later evaluated when determining the half-life using eq. (4.37). Figure 4.21 includes the respective fourth order polynomial fit. These two fits are now implemented as correction functions $\epsilon^{\mathrm{lin}}_{\mathrm{high}}$ to the MC spectra of the respective volume. However, as the N-1 method only provides a lower limit on the acceptance it is not clear to which

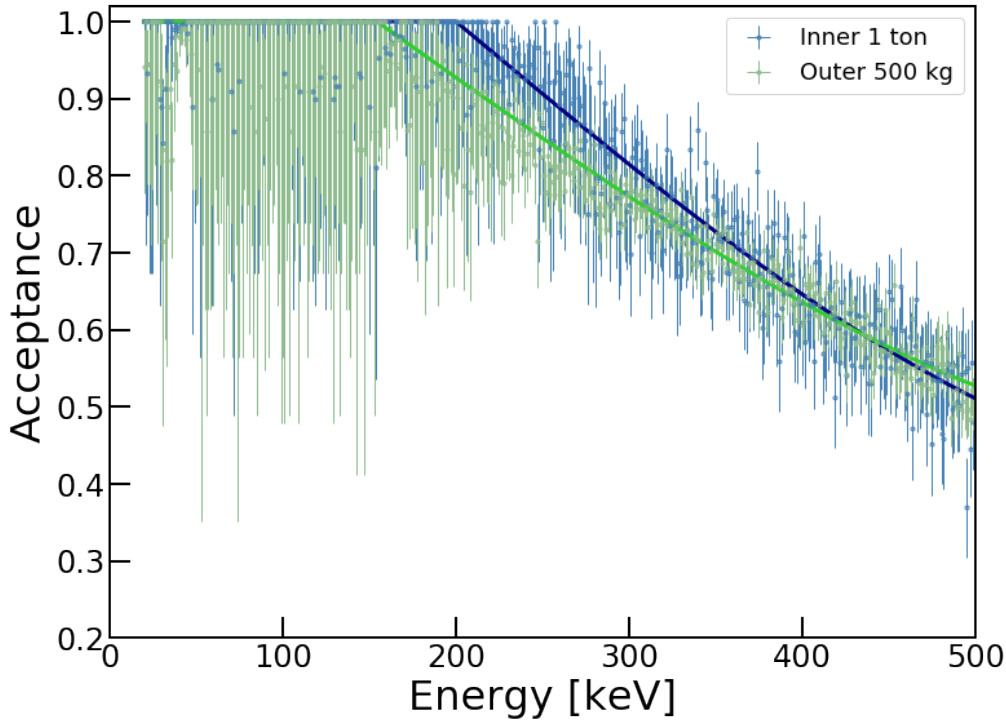

Figure 4.21.: Approximation of the acceptance loss at high energies. The acceptance as derived by the N-1 method is shown for the inner (blue) and outer (green) volume. Only two cuts were multiplicatively combined: The *PreS2Junk* and the *S2Width* cut. The bin-wise estimated acceptance is approximated by a polynomial of fourth order for each volume (blue and green line) in order to reduce the influence of statistical fluctuations.

extent the changed physics account for a real acceptance loss or if the different situation at high energy is causing the large removal of data. For this reason, the acceptance functions are varied within the fit and so, the entire acceptance function in each volume is modified to:

$$\epsilon_{\text{high}}(E) = \kappa \cdot \epsilon_{\text{high}}^{\text{lin}} + (1 - \kappa). \tag{4.39}$$

Here the parameter κ allows the acceptance to float between the lower limit derived from the fit $\epsilon_{\text{high}}^{\text{lin}}$ and unity. The latter would be the choice if all of the additional acceptance loss is due the eligible removal of non-physical events. The expectation of the parameter is set to $\kappa = 2/3$ and its uncertainty is given as $1/3$. This way the full parameter space is within 2σ. The constraint is defined in each volume (inner, outer) as:

$$\chi^2_{\text{acc}}(i) = \frac{(\kappa_i - 2/3)^2}{(1/3)^2} \quad \text{with i = (inner, outer).} \tag{4.40}$$

With these adjustments in place the matching fit to the sidebands (with the double electron capture region still blinded) is applied in order to infer the expected counts

of ^{125}I from the decays of its parent isotope ^{125}Xe as described. Therefore, the contribution from ^{125}Xe is simulated as well and added to the fit. The full side-band results are illustrated in fig. 4.22 for each volume. Notably, the energy range of both volumes differs. This is necessary since the outer volume suffers from the proximity to the wall and the related incomplete knowledge on the acceptance is enhanced. The parameter of interest extracted from the fit is the contribution from

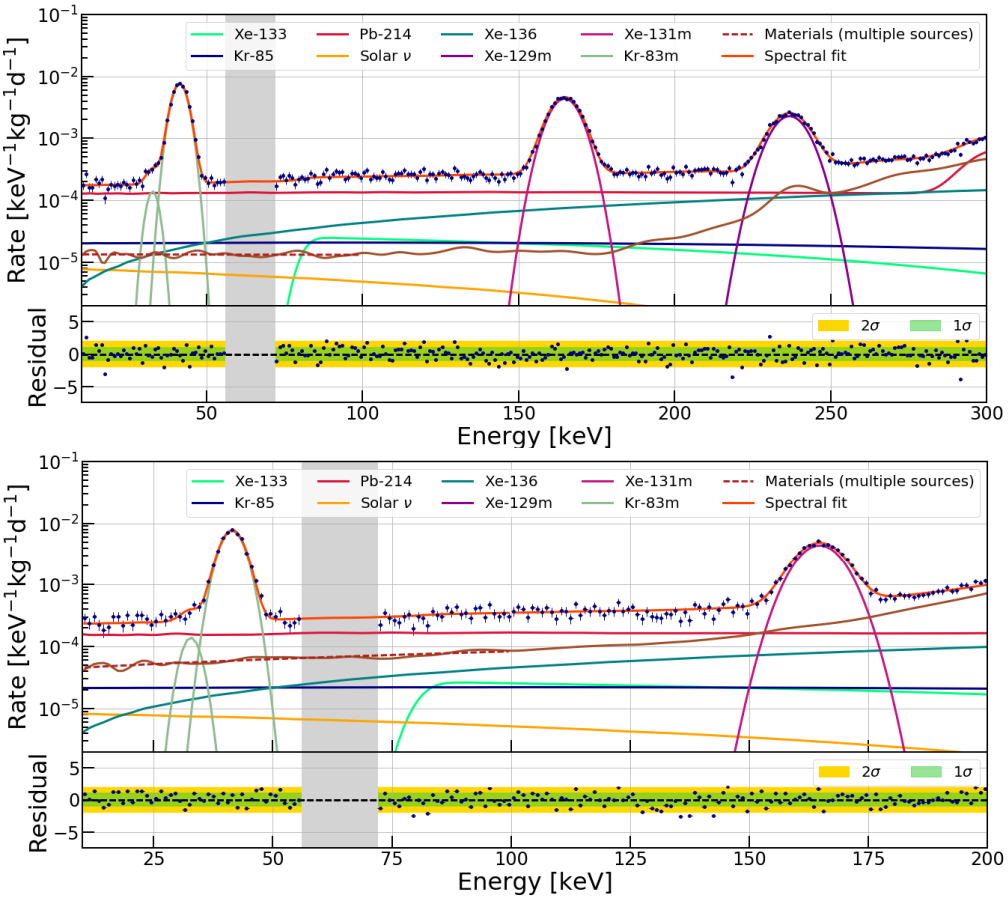

Figure 4.22.: Sideband fit result of the simultaneous two-volume matching. Top: Matching of the MC to the data in the inner volume ($1052\,\mathrm{kg}$). The normalized rate is shown as a function of energy from $10\,\mathrm{keV}$ to $300\,\mathrm{keV}$. All background sources are shown with their respective contribution and the summed spectrum (orange) is compared with the data (blue), illustrated as residuals (deviations) normalized on the uncertainty. For the residuals the 1σ band (green) and the 2σ band (yellow) are added. The energy region of interest is still blinded. Bottom: Analogous result for the outer volume ($448\,\mathrm{kg}$) in an energy range from $10\,\mathrm{keV}$ to $200\,\mathrm{keV}$. The combined reduced χ^2 is 1.04 for 431 degrees of freedom. The fit yields a negative value for the contribution from ^{125}Xe and is therefore not shown on the logarithmic plot (see text for the results) and find the full results in the table C.1.

^{125}Xe, which is determined by the fit function to $(-0.0320 \pm 0.0157)\,\mu\mathrm{Bq\,kg^{-1}}$. In a procedure according to Feldman and Cousins [132] an upper limit on the activity of $0.0064\,\mu\mathrm{Bq\,kg^{-1}}$ at $90\,\%$ C.L is determined. Using the best-fit removal lifetime of

$\tau_{\mathrm{rem}} = 4.7\,\mathrm{d}$ this translates into an upper limit of

$$N^{\mathrm{d}}_{\text{I-125}} < 7.8\,\mathrm{events} \tag{4.41}$$

consistent with the calculation in eq. (4.33). As described, this value can be used in addition to the calibration campaign estimation in eq. (4.34) as a constraint on the possible ^{125}I-signal in the entire data set. Since both are upper limits, the area for the Gaussian signal of ^{125}I is constrained by taking the mean between zero and the sum of $N^{\mathrm{c}}_{\text{I-125}}$ and $N^{\mathrm{d}}_{\text{I-125}}$ and the difference from the mean to the respective value is used as the uncertainty $\Delta_{\mathrm{N_{I\text{-}125}}}$ for the Lagrange multiplier. Lastly, the knowledge of its mean energy position $\mu_{\mathrm{I}-125}$ and the Gaussian signal width $\sigma_{\mathrm{I}-125}$ are implemented as well, which leads to a χ^2 constraint for ^{125}I of the following form:

$$\chi^2_{\text{I-125}} = \frac{\left(N_{\text{I-125}} - 5.15\right)^2}{5.15^2} + \frac{\left(\mu_{\text{I-125}} - 67.5\,\mathrm{keV}\right)^2}{0.5^2} + \frac{\left(\sigma_{\text{I-125}} - 2.8\,\mathrm{keV}\right)^2}{0.5^2}. \tag{4.42}$$

Adding this to the full function we obtain a fit with 34 parameters, where 16 parameters are constrained by external knowledge. The entire list of parameters is shown in table 4.9 and the results for the sideband fit can be found in table C.1

Table 4.9.: Summary of the fit parameters used for the background and signal model.

Parameter	Origin	Constraint/Limit	Unit
M_{inner}	mass factor	1.00 ± 0.01	$1052\,kg$
M_{outer}	mass factor	1.00 ± 0.01	$448\,kg$
κ_{inner}	acceptance	0.67 ± 0.33	scale factor
κ_{outer}	acceptance	0.67 ± 0.33	scale factor
Co-60	materials	only positive	scale factor
K-40	materials	only positive	scale factor
U-238	materials	only positive	scale factor
Ra-226	materials	only positive	scale factor
Th-232	materials	only positive	scale factor
Th-228	materials	no	scale factor
Xe-125	n activation	no	$\mu Bq\,kg^{-1}$
Xe-133	n activation	no	$\mu Bq\,kg^{-1}$
Pb-214	intrinsic	no	$\mu Bq\,kg^{-1}$
Kr-85	intrinsic	6.6 ± 1.1	$0.1\,ppt$
Solar ν	external	1.0 ± 0.2	$8.9 \cdot 10^{-9}\,events/s/kg$
Xe-136	intrinsic	1.00 ± 0.05	$4.0 \cdot 10^{-3}\,\mu Bq\,kg^{-1}$
$N_{Kr\text{-}83m}$	intrinsic	no	$events/kg/d$
$\mu_{Kr\text{-}83m}$	position	41.5 ± 0.6	keV
$\sigma_{Kr\text{-}83m}$	width	no	keV
$N_{Kr\text{-}83m\text{-}miss}$	mis-modelled	no	$events/kg/d$
$\mu_{Kr\text{-}83m\text{-}miss}$	position	32.2 ± 0.6	keV
$\sigma_{Kr\text{-}83m\text{-}miss}$	width	no	keV
$N_{Xe\text{-}131m}$	n activation	no	$events/kg/d$
$\mu_{Xe\text{-}131m}$	position	163.9 ± 0.6	keV
$\sigma_{Xe\text{-}131m}$	width	no	keV
$N_{Xe\text{-}129m}$	n activation	no	$events/kg/d$
$\mu_{Xe\text{-}129m}$	position	236.2 ± 0.6	keV
$\sigma_{Xe\text{-}129m}$	width	no	keV
$N_{I\text{-}125}$	n activation	5.15 ± 5.15	$events$
$\mu_{I\text{-}125}$	position	67.5 ± 0.5	keV
$\sigma_{I\text{-}125}$	width	2.8 ± 0.5	keV
$N_{Xe\text{-}124}$	signal	no	$events$
$\mu_{Xe\text{-}124}$	position	64.33 ± 0.58	keV
$\sigma_{Xe\text{-}124}$	width	2.64 ± 0.24	keV

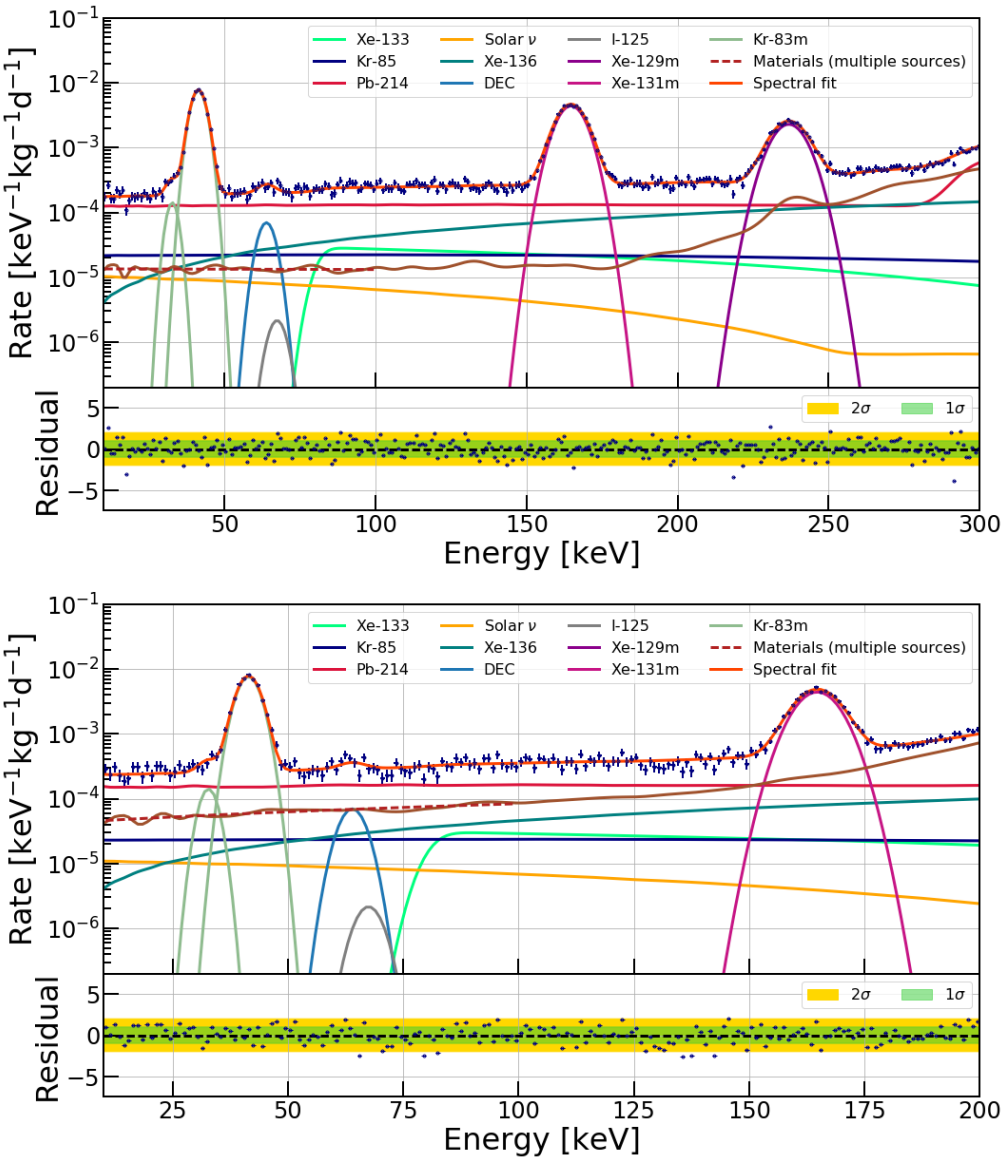

Figure 4.23.: Combined fit result of the two-volume matching with the fully unblinded data. Top: Inner volume fit with the signal region revealed and two additional Gaussian signals added for the decay of ^{124}Xe and ^{125}I. Bottom: Fit result in the outer volume. The reduced χ^2 is 1.05 with 462 degrees of freedom.

4.2.8 Fit results

With the final background and signal model, the signal region is unblinded and included into the fit. The resulting fit spectrum in both volumes is shown in fig. 4.23 and the best-fit parameters are listed in table 4.10. The sum of the fit results in the two distinct volumes is shown for illustration in fig. 4.24 in the entire fiducial volume. A zoom into the energy region of interest is given in fig. 4.25. Additionally, the best-fit from the sideband fit is included. The clear excess at the energy of interest is visible.

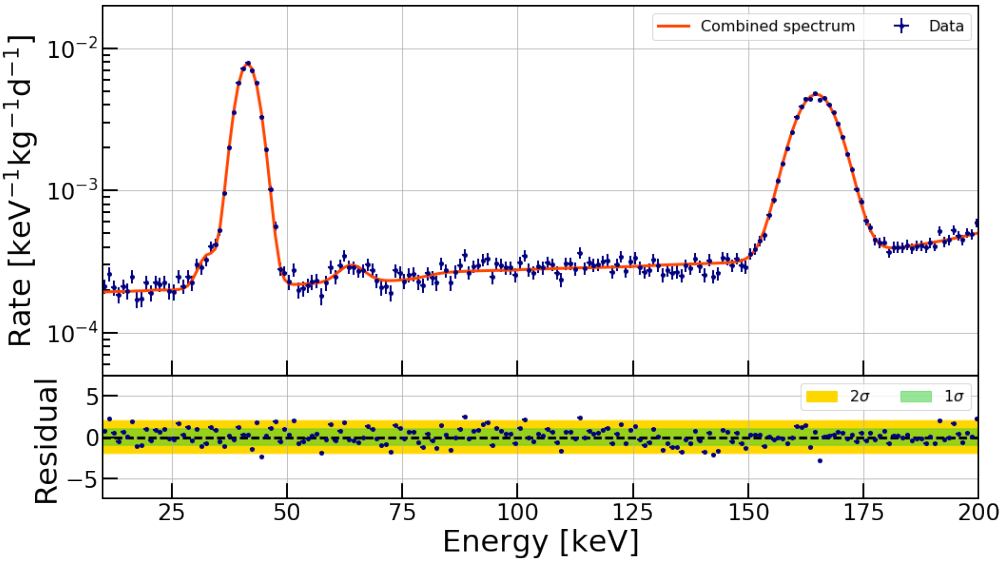

Figure 4.24.: Sum fit in the complete fiducial volume. The normalized rate is shown in the energy window from $20\,\mathrm{keV}$ to $200\,\mathrm{keV}$ with the sum from the two-volume fits (orange) for illustration. The residuals are given accordingly.

A value for the signal events $N_{\text{Xe-124}}$ from 2νKK is extracted at:

$$N_{\text{Xe-124}} = 150.6^{+33.5}_{-32.9}\,\text{events} \tag{4.43}$$

The uncertainties are given by the *minos*-routine from the *iMinuit*-framework and are cross-checked on the χ^2-distribution itself. In order to clarify the validity of the result, a first check is to investigate the pull on the constrained parameters. This pull is defined as:

$$\frac{p - p_{\text{lit}}}{\Delta p}, \tag{4.44}$$

where p is the best-fit value for a given parameter. It is compared to the expectation in the respective constraint p_{lit} and weighted by the uncertainty on the constraint Δp. This way the pull is measured in units of the uncertainty σ. The result is displayed in fig. 4.27. If the fit needs a strong adjustment, this would manifest itself in a strong pull on a given fit parameter. No pull above 2σ has been found.
The significance of the signal is a measure how unlikely the measured events correspond to a background-only scenario. In order to investigate this, the χ^2-distribution of the fit parameter is scanned up to the value at zero events, which corresponds to the best-fit for the background only scenario. The significance is then defined as

$$\sqrt{\Delta\chi^2} = \sqrt{\chi^2(0) - \chi^2(\text{best-fit})}. \tag{4.45}$$

The best-fit value yields $\chi^2(\text{best-fit}) = 485.7$ and at 0 a $\chi^2(0)$ of 507.4 is obtained. The significance (in units of σ) is therefore given as:

$$\sqrt{\Delta\chi^2} = 4.7. \tag{4.46}$$

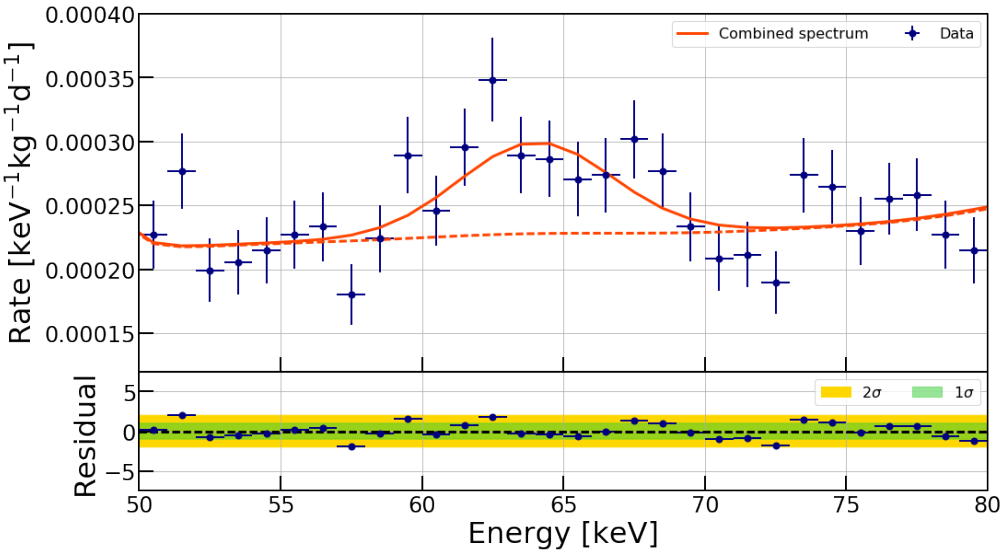

Figure 4.25.: Zoom into the summed spectrum with a comparison of the best-fit with the background-only scenario. The rate as a function of energy is shown for the measured data (blue). The fit from the two-volume matchin is shown (solid orange) in comparison to the sideband result (dashed orange). The residuals normalized on the uncertainty are given together with the 1σ (green) and 2σ (yellow) bands.)

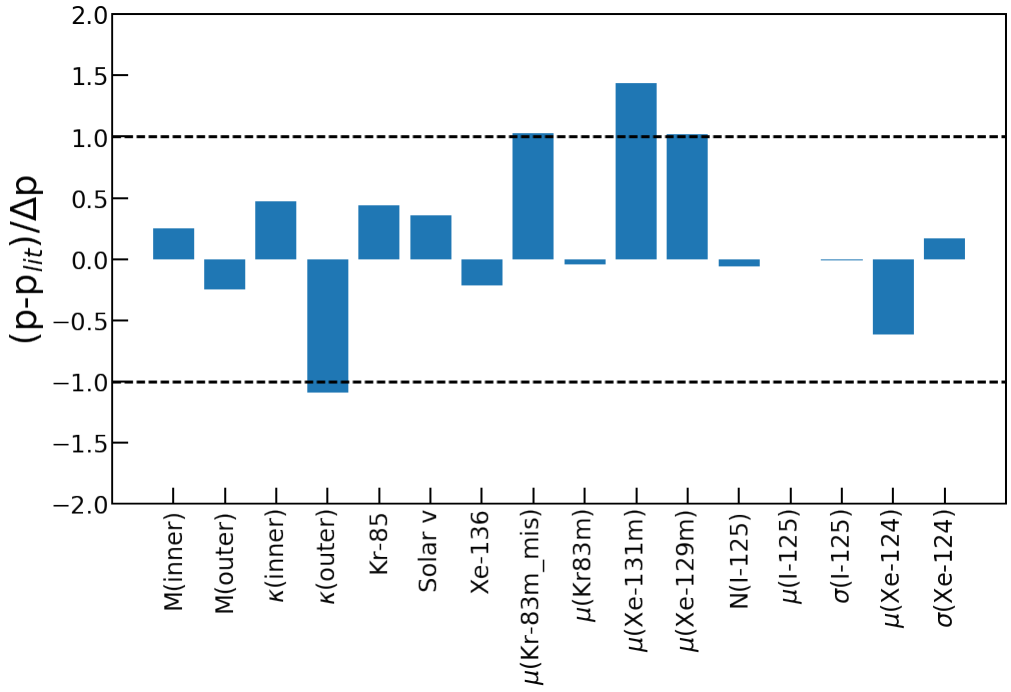

Figure 4.26.: Parameter pull on the constrained parameters. The pull (as defined in eq. (4.44)) is shown for each parameter with initial constraints. No significant excess can be found.

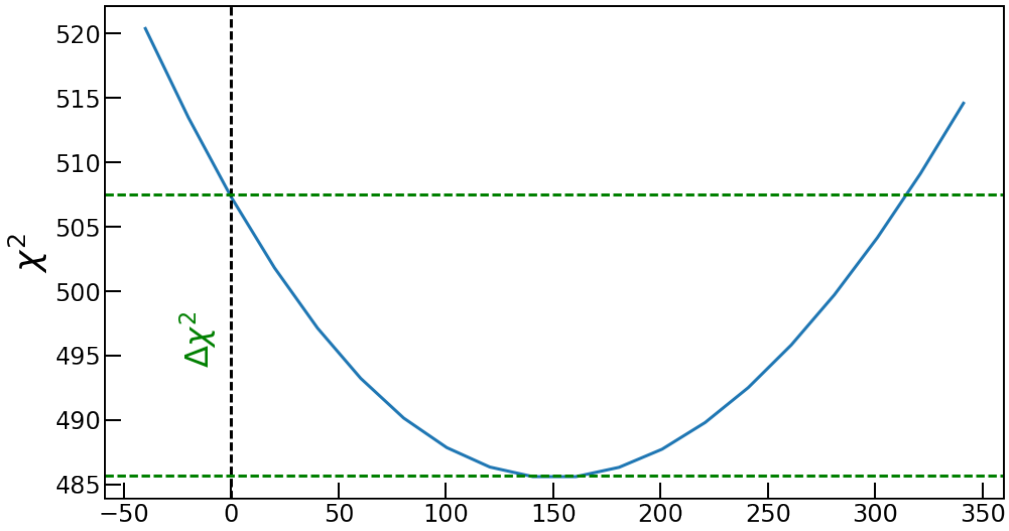

Figure 4.27.: Mapping of the χ^2-distribution. The χ^2-distribution is scanned given the best-fit for each number of signal events. The significance is determined by calculating the difference between the minimum of the distribution and the intersection at 0 events. It yields a $\Delta\chi^2$ of 21.7.

A crucial part of the investigation is the validation whether the signal shows the expected behavior of a source homogeneously distributed in space and time. Therefore, a look into different parameter spaces is necessary. The spatial distribution in the (R^2,Z)-plane is shown in fig. 4.28 next to the distribution in the (x,y)-plane for an extracted energy region of about[22] $59\,\mathrm{keV}$ to $70\,\mathrm{keV}$. Both distributions show small regions with increased event counts (hot spots). An investigation on this (see appendix C.2) reveals that these hot spots are also present in sideband energy regions, but move slightly. As it is expected that the outer volume has an increased event count from material contributions due to the proximity to the walls, this can be attributed to an increased background. The separation of the fit into two volumes acts as a safeguard against these problems, since an increase in the outer region would not be matched by the inner volume and, thus, the goodness-of-fit would deteriorate. Within the (x,y)-plane there should be no distinguished spot. This is checked by separating the detector along a diagonal axis ($x = -y$) and count the fraction of total events ($n = 919$) in each of the halves. Using a Binomial distribution (fixed n) an expectation value of 459.5 is obtained from expected probability of $50\,\%$ per half ($p = 0.5$). The uncertainty is determined to be 15.2 from $\sqrt{p \cdot n \cdot (1-p)}$. A comparison with the measured counts of 470 (upper right part) and 449 (lower left part) reveals an agreement with the expectation. The energy distribution of the two halves can be found in fig. C.2.

The next investigation is on the distribution of the signal in the time dimension. In order to avoid a bias introduced by periods, where the detector was not taking usable data, a consecutive run number is introduced. Each run number corresponds

[22] The energy range is chosen such as it corresponds to roughly 2σ in both directs around the signal.

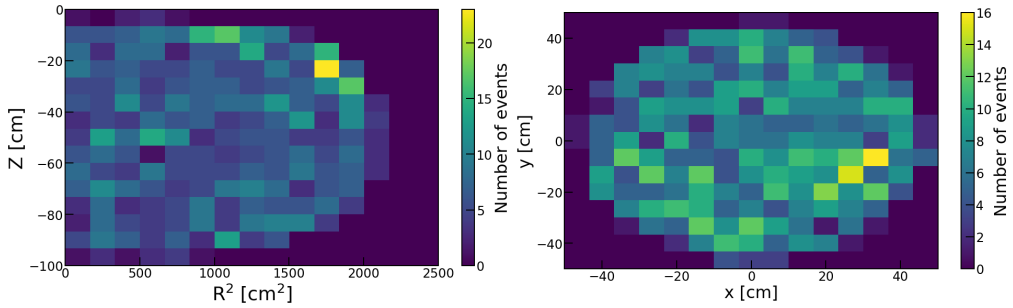

Figure 4.28.: Spatial distribution of events in the energy region of $59\,\mathrm{keV}$ to $71\,\mathrm{keV}$. Left: Distribution in the (R^2,Z)-space. The color bar indicates the number of events. Right: Distribution in the (x,y)-space.

to one hour of data. Then it is expected to find the signal of interest homogeneously distributed along the axis of this consecutive run number. The behavior is shown in fig. 4.29 as a function of energy and no particular clustering has been found. In order to further investigate this, the data set was separated into three time bins and the region of interest in the $1.5\,\mathrm{t}$ fiducial volume was fitted with an simplified model consisting of a Gaussian signal model with a constant background. The signal parameter were constrained between the time bins, while the background was allowed to float. A signal was confirmed to be present in each time bin and it was found that the background is slightly decreasing over time. Results of this can be found in appendix C.2. Remarkably, if the constraints on the position and width of the signal from $^{124}\mathrm{Xe}$ are removed, the fit result is in agreement with the constrained fit in all three parameters describing the signal ($\mathrm{N_{Xe\text{-}124}} = (153 \pm 38)\,\mathrm{events}$, $\mu_{\mathrm{Xe\text{-}124}} = (63.4 \pm 0.8)\,\mathrm{keV}$ and $\sigma_{\mathrm{Xe\text{-}124}} = (2.7 \pm 0.7)\,\mathrm{keV}$).

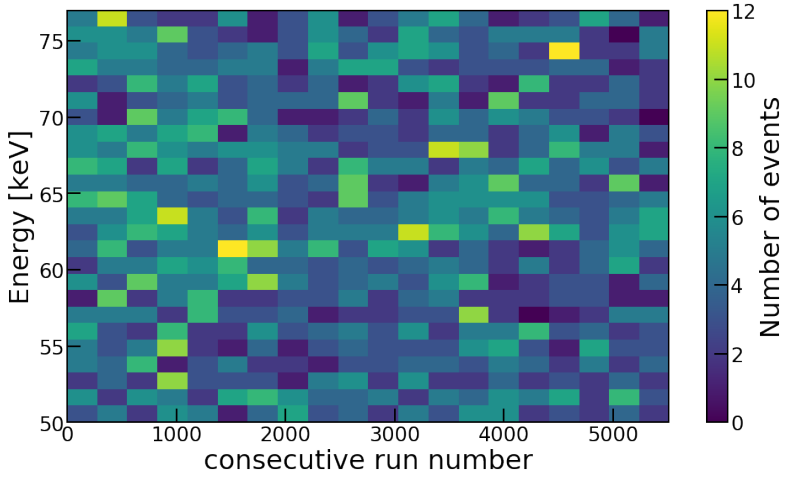

Figure 4.29.: Temporal distribution of events in the energy region of interest. The energies between $50\,\mathrm{keV}$ to $75\,\mathrm{keV}$ are shown as a function of the consecutive run number. This is a continuous measure for the run time, and translated directly to the distribution of the events in time.

Table 4.10.: Fit results from the unblinded spectrum.

Parameter	Fit result
M_{inner}	1.00 ± 0.01
M_{outer}	1.00 ± 0.01
κ_{inner}	0.82 ± 0.16
κ_{outer}	0.31 ± 0.28
Co-60	$2 \cdot 10^{-4} \pm 2 \cdot 10^{-2}$
K-40	$4 \cdot 10^{-9} \pm 3 \cdot 10^{-2}$
U-238	$5 \cdot 10^{-3} \pm 5 \cdot 10^{-2}$
Ra-226	$1 \cdot 10^{-8} \pm 4 \cdot 10^{-2}$
Th-232	134.1 ± 20.8
Th-228	-3.2 ± 11.7
Xe-125	$(-3.40 \pm 0.16) \cdot 10^{-2}$
Xe-133	$(5.2 \pm 1.0) \cdot 10^{-2}$
Pb-214	8.3 ± 0.3
Kr-85	7.1 ± 1.0
Solar ν	1.07 ± 0.19
Xe-136	0.99 ± 0.04
$N_{Kr\text{-}83m}$	$(4.47 \pm 0.04) \cdot 10^{-2}$
$\mu_{Kr\text{-}83m}$	41.48 ± 0.02
$\sigma_{Kr\text{-}83m}$	2.33 ± 0.02
$N_{Kr\text{-}83m\text{-}miss}$	$(6.6 \pm 1.1) \cdot 10^{-5}$
$\mu_{Kr\text{-}83m\text{-}miss}$	32.8 ± 0.3
$\sigma_{Kr\text{-}83m\text{-}miss}$	1.8 ± 0.4
$N_{Xe\text{-}131m}$	$(5.02 \pm 0.05) \cdot 10^{-2}$
$\mu_{Xe\text{-}131m}$	164.76 ± 0.04
$\sigma_{Xe\text{-}131m}$	4.45 ± 0.04
$N_{Xe\text{-}129m}$	$(3.12 \pm 0.07) \cdot 10^{-2}$
$\mu_{Xe\text{-}129m}$	236.81 ± 0.08
$\sigma_{Xe\text{-}129m}$	5.43 ± 0.07
$N_{I\text{-}125}$	4.86 ± 5.07
$\mu_{I\text{-}125}$	67.5 ± 0.5
$\sigma_{I\text{-}125}$	2.8 ± 0.5
$N_{Xe\text{-}124}$	$150.58^{+33.52}_{-32.87}$
$\mu_{Xe\text{-}124}$	63.98 ± 0.46
$\sigma_{Xe\text{-}124}$	2.68 ± 0.21

Table 4.11.: Input parameter for half-life calculation.

Parameter	Value	Uncertainty (stat.)	Uncertainty (sys.)
acceptance $\epsilon_{2\nu\mathrm{KK}}$	0.967	0.007	0.033
abundance η_{XE1T}	$9.94 \cdot 10^{-4}$	$0.14 \cdot 10^{-4}$	$0.15 \cdot 10^{-4}$
Mass M_{fid}	1502.0 kg	-	8.9 kg
live time t	214.3 d	-	-
events $N_{\text{Xe-124}}$	150.6	$^{+33.5}_{-32.9}$	-

4.2.9 Half-life calculation

The decay rate $\Gamma^{2\nu\mathrm{KK}}$ is related to the number of measured signal events via eq. (4.8)

$$\Gamma^{2\nu\mathrm{KK}} = \frac{N_{\text{Xe-124}} M_{\mathrm{Xe}}}{\epsilon \eta N_A m t}. \tag{4.47}$$

Here, the abundance is taken from the measured value η_{XE1T} in eq. (4.19). The exposure mt is given by the mass M_{fid} in eq. (4.11) and the live time of 214.3 days. M_{Xe} is the average molar mass of xenon (131.293 amu) and N_A Avogadro's constant. For the acceptance, the value of $\epsilon_{2\nu\mathrm{KK}}$ from eq. (4.36) has to be adjusted since due to the involved N-1 method, this yields only a lower limit instead of the precise value. The true value lies between $\epsilon_{2\nu\mathrm{KK}}$ and unity and so the mean is taken with a systematic uncertainty on top of the statistical uncertainty given by the difference between the mean and the two limits. All input parameters with their statistical and systematic uncertainties are listed in table 4.11. The statistical and systematic uncertainties are separately propagated. This yields a decay rate $\Gamma^{2\nu\mathrm{KK}}$ of

$$\Gamma^{2\nu\mathrm{KK}} = 3.87^{+0.86(\text{stat.})+0.13(\text{sys.})}_{-0.85(\text{stat.})-0.13(\text{sys.})}\, 10^{-23}\,\mathrm{yr}^{-1}, \tag{4.48}$$

and can be translated (see eq. (4.8)) into a half-life of

$$T^{2\nu\mathrm{KK}}_{1/2} = 1.80^{+0.40(\text{stat.})+0.07(\text{sys.})}_{-0.39(\text{stat.})-0.07(\text{sys.})}\, 10^{22}\,\mathrm{yr}. \tag{4.49}$$

Chapter 5

Conclusion and Outlook

5.1 Dark matter search

The ongoing search for elusive WIMPs is reaching deeper into the parameter space of the WIMP-nucleon cross section with each new experiment. Currently, the largest detector XENON1T has set the most stringent limits for direct dark matter interaction via isoscalar spin-independent (SI) scattering at $4.1 \cdot 10^{-47}\,\mathrm{cm}^2$ for a $30\,\mathrm{GeV/c}^2$ WIMP with $90\,\%$ C.L. from an analysis of a one tonne$\times$year exposure. The limit is less strict compared to the expected sensitivity at masses above $200\,\mathrm{GeV/c}^2$. This points rather to a statistical upward fluctuation of the background than to a real WIMP signal. In order to probe this, larger detectors are needed but also technical difficulties have to be overcome for further improvements. Especially, in terms of background reduction new paths have to be opened up. XENONnT, the successive detector is projected to start in 2019 and will provide another order of magnitude in sensitivity (see fig. 5.1). To achieve this, not only an enlargement but also a further background reduction is necessary. In particular the removal and mitigation of radon progeny is required.

All exclusion limits shown in fig. 5.1 share the common assumption of a standard isoscalar SI interaction as the underlying nuclear interaction mechanism between WIMP particles and ordinary matter. Other interaction channels could contribute as corrections - or if the isoscalar interaction is suppressed - could be the interaction channel realized in nature. If a WIMP signal will be detected, the interaction mechanism can be tested using the difference in the expected signal distribution due to the different q-dependency. The Monte Carlo study presented here revealed that for nuclear interaction mechanisms, where the signal vanishes at low momentum transfers, a distinction from the standard assumption would be possible already in XENONnT. For other channels a discrimination becomes more difficult and only the DARWIN experiment will have the chance to discriminate between them given the most recent exclusion limits on the general interaction strength. Especially, a spin-independent isovector contribution would not be distinguishable even by a DARWIN-like detector, and thus, a separation from the isoscalar case would need a comparison of a signal

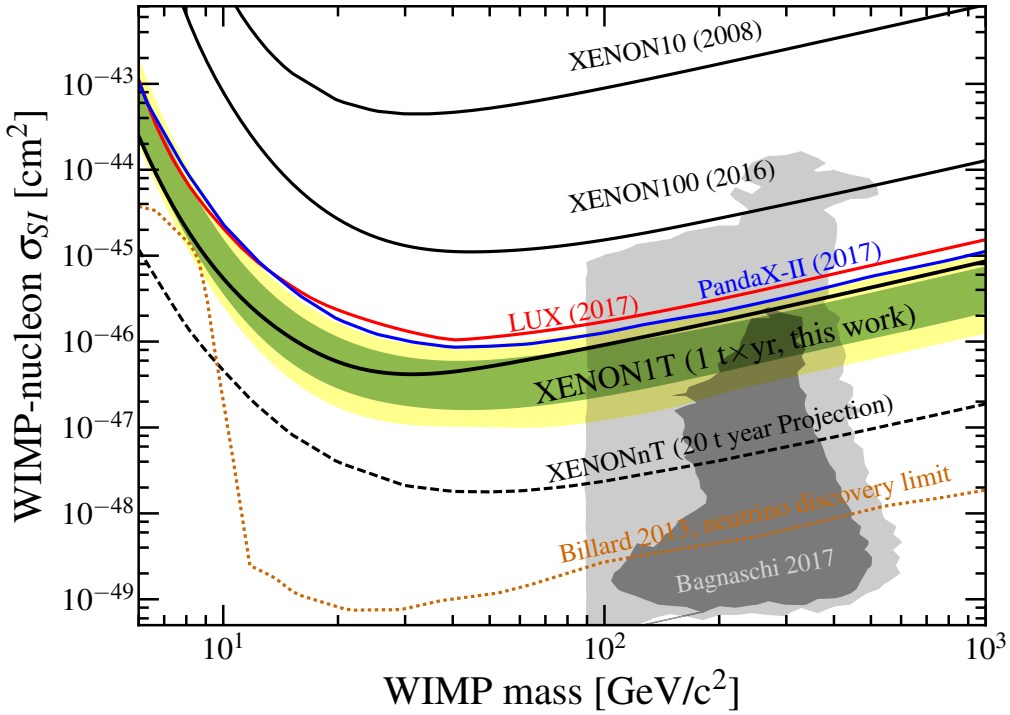

Figure 5.1.: Experimental exclusion limits on the WIMP-nucleon cross section σ_{SI} in dependence of the WIMP mass m_χ. The cross section of the interaction between WIMP and nucleon (note: $\sigma_{SI} = \sigma_{nn}$ in eq. (1.28)) as probed by the different XENON experiments (black) with the most sensitive search using the results presented within this work is shown. The expected sensitivity is given for this particular result as bands: green denotes the 1σ-contour and yellow represents the 2σ-contour. Additionally, results from the other large dual-phase LXe TPCs (LUX [134] and PandaX-II [183]) are included (red and blue). While the best limit XENON1T has set is at $4.1 \cdot 10^{-47}\,\mathrm{cm}^2$ for a $30\,\mathrm{GeV/c}^2$ WIMP with $90\,\%$ C.L., the future experiment XENONnT is projected to probe the cross section about $10^{-48}\,\mathrm{cm}^2$. This is still mainly above the calculated cross section for the limiting background of coherent elastic neutrino nucleus scattering (CEνNs) [122]. In addition to the experimental results, theoretically predicted parameters (gray shaded area) are added from a phenomenological MSSM model [184]. Plot with courtesy of the XENON collaboration based on the results in [128].

with different target isotopes.
One of the channels, which can only be distinguished by a DARWIN-like experiment, is the interaction of the WIMP with the exchange pions of the nucleons. This two-body interaction process described by chiral effective field theory and arising from quantum chromodynamics is at least an important correction once a WIMP signal is detectable with sufficient statistics. If the coupling to the pion would be a dominate process, in view of a suppression of the isoscalar channel, its coherent enhancement would lead to a way stronger interaction than the well-studied spin-dependent interaction channel. The first limit on this interaction mechanism has been set within this work with its most strict result at $6.4 \cdot 10^{-46}\,\mathrm{cm}^2$ for a $30\,\mathrm{GeV/c}^2$ WIMP with $90\,\%$ C.L. using the

same data as for the standard analysis. This opens up the possibility of a comparison for future theoretical calculations and studies starting with the assumption of a pure WIMP-pion interaction.

5.2 Double electron capture search

The spread in half-life calculations for the simultaneous electron capture of two K-shell electrons with the emission of two neutrinos (2νKK) spans a few orders of magnitude. Only indirect detection of the process is available in order to verify the different many-body calculations used for the half-life estimation. First parts of the parameter space for the unobserved double electron capture of ^{124}Xe were probed using XENON100 data, where at this point more stringent limits from other experiments were already in place. Nevertheless, a derivation of the limit using only public information by an external group gave a too optimistic limit, which had been corrected within this work using the actual data with the full detector insights. The half-life limit on the decay obtained at $6.5 \cdot 10^{20}\,\mathrm{yr}$ with $90\,\%$ C.I. corrected the result by a factor of two. This analysis introduced the tools necessary for the investigation in its successor experiment XENON1T. There, an actual peak containing 150.6^{+33}_{-34} events was found at the expected position ($64.33\,\mathrm{keV}$) and with the predicted signal width ($2.64\,\mathrm{keV}$). The corresponding half-life of the 2νKK was measured to

$$T_{1/2}^{2\nu\mathrm{KK}} = 1.80^{+0.40(\mathrm{stat.})+0.07(\mathrm{sys.})}_{-0.39(\mathrm{stat.})-0.07(\mathrm{sys.})}\,10^{22}\,\mathrm{yr}. \tag{5.1}$$

A measurement of the decay was only possible due to extensive work on understanding the background composition of the detector. Especially, the mitigation of the possibly dangerous contribution of ^{125}I is a profound advantage of the XENON1T detector. This decay with a summed energy deposition of $67.5\,\mathrm{keV}$ was found to be removed by purification getters and possible charge follow-up drift processes with a removal life-time of $4.7^{+2.5}_{-1.9}\,d$ reducing the impact from the long lived isotope ($\mathrm{T}_{1/2} = 59.4\,\mathrm{d}$) to a negligible amount. Taking advantage of the removal of this crucial background together with the general low background level at this energy range in the detector allowed to observe the double electron capture signature with a significance of 4.7σ. A direct observation of a decay with such a long half-life has never been made directly at this precision. The measured half-life can be put in context to the experimental limit obtained from the XMASS collaboration at $2.1 \cdot 10^{22}\,\mathrm{yr}$ at $90\,\%$ C.L. Within uncertainties the two values agree with each other and it can be stated that the XMASS experiment suffered strongly from the lack of purification methods to remove the ^{125}I contribution. These two values are shown in comparison to various theories in fig. 5.2. This new result will help to evaluate the many-body methods used to calculate the proper nuclear matrix element for the two-neutrino decay mode. As the same methods are used for the neutrino-less mode, this will also help to shed light on the suitable method to predict half-lives for this impactful decay.
Future detectors such as XENONnT will be able to probe the decay itself further by

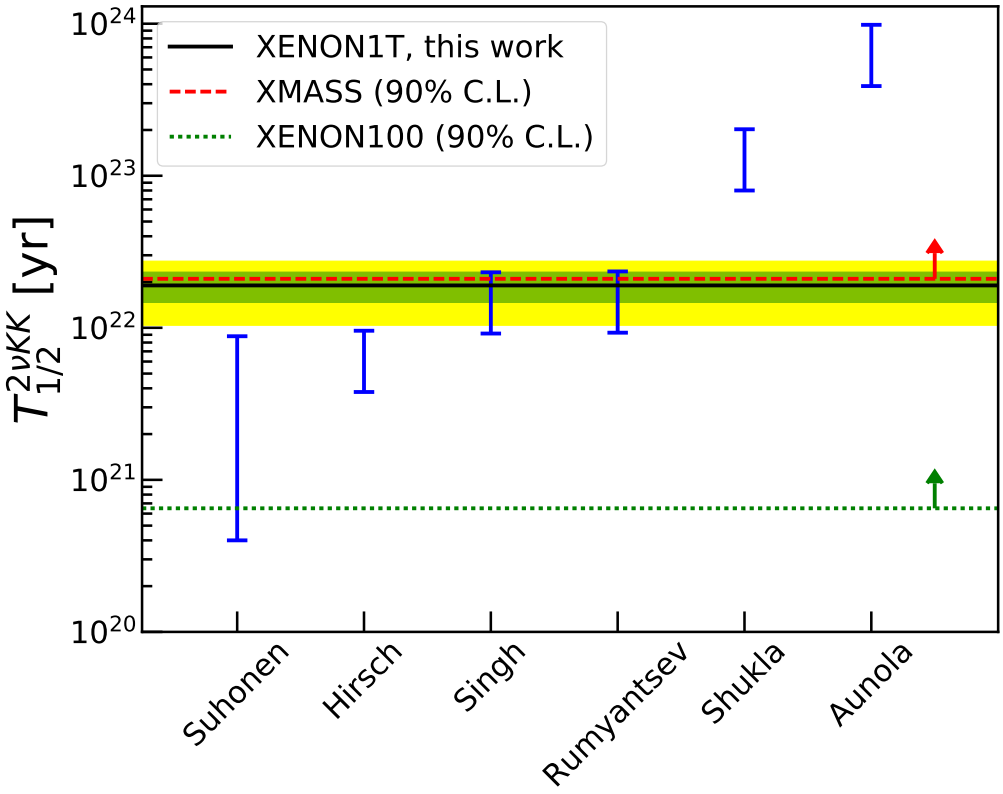

Figure 5.2.: Comparison of the measured half-life with experimental lower limits and theoretical predictions. The result derived in this work is presented (black) with the 1σ (green) and 2σ (yellow) uncertainties shown as well. The lower limit derived from the XENON100 data is added (green, dotted) together with the lower limit from the XMASS experiment (red, dashed). The result is compatible with the 1σ-uncertainty of the results from XENON1T. This is also the case for the theoretical predictions by [24] and [84] (blue), while others are clearly off ([85, 26]). The theoretical predictions are shown with a range limited by the axial-vector coupling constant $g_A = 1$ for the lower edge and $g_A = 1.26$ for the upper edge. Notably, for the results of [83] the values given by [24] were used due to the g_A-scaling performed there. All theoretical values, which were given for the entire double electron capture, were scaled by the double K-shell capture fraction of the decay.

investigating not only the 2νKK but also signatures of the 2νKL and 2νLL captures. These two channels would provide a smoking gun evidence for the double electron capture. Although, they make up only $23\,\%$ of the decay, they are measurable with a reduced background, larger exposure and especially the removal of a permanent calibration with ^{83m}Kr, which is the crucial background in XENON1T at the energies of the two decay branches.
The observation of the double electron capture is also a start point for valid searches for the competing decay modes as well as a possible begin to look into the search for the neutrino-less decay mode counterparts.
All in all the observation shows that the XENON1T detector and its successors are

capable of contributing to physics searches beyond the standard direct dark matter search.

5.3 Search for other decay channels of ^{124}Xe

Due to the large Q-value ($2856\,\mathrm{keV}$) of the decay of $^{124}\mathrm{Xe}$ all competing decay modes involving the emission of one or two positrons are allowed as well. Although, the signature differs for each of them, they all share a release of a detectable energy above the $64\,\mathrm{keV}$ from the two-neutrino double electron capture. A summary of the different decay channels can be found in table 5.1. All of them require a profound knowledge of the signature left in the detector, which demands a working Monte Carlo simulation with an extensive understanding of high energy signals. The latter is not existing yet since the focus of XENON1T lied in the low energy window but future efforts in this direction are foreseen. A crucial part of high energy simulations is to understand whether different energy depositions can be distinguished by the detector in one of the two signal channels and if so, the efficiency has to be determined precisely. If this simulation is in place, the XENON1T detector has the highest sensitivity for all of the decay channels. A special case is the neutrino-less double electron capture. This decay mode requires an additional particle to release the energy in order to fulfill momentum conservation. A single release of a Bremsstrahlung photon could be one possibility (0νECEC) but the predicted half-life is heavily suppressed [185]. Another possibility is a resonance enhancement, where the $^{124}\mathrm{Xe}$ decay leads not into the ground state of $^{124}\mathrm{Te}$ but into an excited state (0νRECEC) [89, 91]. Unfortunately, the gap between those two states is still at $1.86\,\mathrm{keV}$[81] but the decay would provide a clear signature in the detector. This is caused by the different high-energy γs released during the de-excitation process in combination with the double K-hole relaxation. Hence, a coincidence signature could be measured providing a strong background suppression.
For any of the decays which involve a positron, the question to be answered by Monte Carlo studies is, if the annihilation gamma emission can be used to provide a background suppressed sample as well. In this case, depending on the efficiency of this separation, a search for each of the channels would be promising. Especially, the $0\nu\mathrm{EC}\beta^+$ is an interesting case with this regard due to the multi-fold signature with a mono-energetic positron ($1.8\,\mathrm{MeV}$), the vacancy refill at $31.8\,\mathrm{keV}$ and the additional γ's from electron-positron annihilation. Nevertheless, its predicted half-life at $10^{27}\,\mathrm{yr}$ would be problematic due to the largest weakness of $^{124}\mathrm{Xe}$ [25]. The low abundance of only about $0.1\,\%$ would make a dedicated detector necessary with enriched amounts of the isotope. This is rather expensive and for this reason all the measurements on $^{124}\mathrm{Xe}$ are so far side products of dark matter searches. Nevertheless, for a DARWIN-like experiment the amount could be enough to probe interesting parameter space and at least detect the remaining two-neutrino decay modes.

Table 5.1.: Possible further decay searches using XENON1T and future detectors.

Decay mode	Signature
$2\nu\mathrm{EC}\beta^+$	e^+, annihilation $\gamma's$, X-ray/Auger ($31.8\,\mathrm{keV}$)
$2\nu\beta^+\beta^+$	$2\mathrm{e}^+$,annihilation $\gamma's$
0νECEC	Bremsstrahlung photon ($2.8\,\mathrm{MeV}$),X-ray/Auger ($64\,\mathrm{keV}$)
0νRECEC	multiple γ, X-ray/Auger ($64\,\mathrm{keV}$)
$0\nu\mathrm{EC}\beta^+$	mono-energetic e^+, annihilation γ, X-ray/Auger ($31.8\,\mathrm{keV}$)
$0\nu\beta^+\beta^+$	$2\mathrm{e}^+$, annihilation $\gamma's$

List of Figures

List of Tables

Bibliography

[1] J. Beringer et al. “Review of Particle Physics (RPP).” In: *Phys. Rev.* D86 (2012), p. 010001. DOI: 10.1103/PhysRevD.86.010001.

[2] P. A. R. Ade et al. “Planck 2015 results. XIII. Cosmological parameters.” In: *Astron. Astrophys.* 594 (2016), A13. DOI: 10.1051/0004-6361/201525830. arXiv: 1502.01589 [astro-ph.CO].

[3] Vera C. Rubin, W. Kent Ford Jr., and Norbert Thonnard. “Extended rotation curves of high-luminosity spiral galaxies. IV. Systematic dynamical properties, Sa through Sc.” In: *Astrophys. J.* 225 (1978), pp. L107–L111. DOI: 10.1086/182804.

[4] Douglas Clowe et al. “A direct empirical proof of the existence of dark matter.” In: *Astrophys. J.* 648 (2006), pp. L109–L113. DOI: 10.1086/508162. arXiv: astro-ph/0608407 [astro-ph].

[5] J. Silk et al. *Particle Dark Matter: Observations, Models and Searches*. Ed. by Gianfranco Bertone. Cambridge: Cambridge Univ. Press, 2010. ISBN: 9781107653924. DOI: 10.1017/CBO9780511770739. URL: http://www.cambridge.org/uk/catalogue/catalogue.asp?isbn=9780521763684.

[6] Gerard Jungman, Marc Kamionkowski, and Kim Griest. “Supersymmetric dark matter.” In: *Phys. Rept.* 267 (1996), pp. 195–373. DOI: 10.1016/0370-1573(95)00058-5. arXiv: hep-ph/9506380 [hep-ph].

[7] Teresa Marrodán Undagoitia and Ludwig Rauch. “Dark matter direct-detection experiments.” In: *J. Phys.* G43.1 (2016), p. 013001. DOI: 10.1088/0954-3899/43/1/013001. arXiv: 1509.08767 [physics.ins-det].

[8] Andrea De Simone, Gian Francesco Giudice, and Alessandro Strumia. “Benchmarks for Dark Matter Searches at the LHC.” In: *JHEP* 06 (2014), p. 081. DOI: 10.1007/JHEP06(2014)081. arXiv: 1402.6287 [hep-ph].

[9] Jan Conrad and Olaf Reimer. “Indirect dark matter searches in gamma and cosmic rays.” In: *Nature Phys.* 13.3 (2017), pp. 224–231. DOI: 10.1038/nphys4049. arXiv: 1705.11165 [astro-ph.HE].

[10] A. Liam Fitzpatrick et al. “Model Independent Direct Detection Analyses.” In: (2012). arXiv: 1211.2818 [hep-ph].

[11] Martin Hoferichter et al. “Analysis strategies for general spin-independent WIMP-nucleus scattering.” In: *Phys. Rev.* D94.6 (2016), p. 063505. DOI: 10.1103/PhysRevD.94.063505. arXiv: 1605.08043 [hep-ph].

[12] Riccardo Catena and Paolo Gondolo. “Global limits and interference patterns in dark matter direct detection.” In: *JCAP* 1508.08 (2015), p. 022. DOI: 10.1088/1475-7516/2015/08/022. arXiv: 1504.06554 [hep-ph].

[13] Y. Fukuda et al. “Evidence for oscillation of atmospheric neutrinos.” In: *Phys. Rev. Lett.* 81 (1998), pp. 1562–1567. DOI: 10.1103/PhysRevLett.81.1562. arXiv: hep-ex/9807003 [hep-ex].

[14] Q. R. Ahmad et al. “Direct evidence for neutrino flavor transformation from neutral current interactions in the Sudbury Neutrino Observatory.” In: *Phys. Rev. Lett.* 89 (2002), p. 011301. DOI: 10.1103/PhysRevLett.89.011301. arXiv: nucl-ex/0204008 [nucl-ex].

[15] Frank T. Avignone III, Steven R. Elliott, and Jonathan Engel. “Double Beta Decay, Majorana Neutrinos, and Neutrino Mass.” In: *Rev. Mod. Phys.* 80 (2008), pp. 481–516. DOI: 10.1103/RevModPhys.80.481. arXiv: 0708.1033 [nucl-ex].

[16] Werner Maneschg. “Review of neutrinoless double beta decay experiments: Present status and near future.” In: *Nucl. Part. Phys. Proc.* 260 (2015), pp. 188–193. DOI: 10.1016/j.nuclphysbps.2015.02.039.

[17] J. Schechter and J. W. F. Valle. “Neutrinoless Double beta Decay in SU(2) x U(1) Theories.” In: *Phys. Rev.* D25 (1982). [,289(1981)], p. 2951. DOI: 10.1103/PhysRevD.25.2951.

[18] Sacha Davidson, Enrico Nardi, and Yosef Nir. “Leptogenesis.” In: *Phys. Rept.* 466 (2008), pp. 105–177. DOI: 10.1016/j.physrep.2008.06.002. arXiv: 0802.2962 [hep-ph].

[19] Marco Drewes and Shintaro Eijima. “Neutrinoless double β decay and low scale leptogenesis.” In: *Phys. Lett.* B763 (2016), pp. 72–79. DOI: 10.1016/j.physletb.2016.09.054. arXiv: 1606.06221 [hep-ph].

[20] C. Patrignani and Particle Data Group. “Review of Particle Physics.” In: *Chinese Physics C* 40.10 (2016), p. 100001. URL: http://stacks.iop.org/1674-1137/40/i=10/a=100001.

[21] A. P. Meshik et al. “Weak decay of ^{130}Ba and ^{132}Ba : Geochemical measurements.” In: *Phys. Rev. C* 64 (3 Aug. 2001), p. 035205. DOI: 10.1103/PhysRevC.64.035205. URL: http://link.aps.org/doi/10.1103/PhysRevC.64.035205.

[22] Yu. M. Gavrilyuk et al. “Indications of $2\nu2K$ capture in ^{78}Kr.” In: *Phys. Rev. C* 87 (3 Mar. 2013), p. 035501. DOI: 10.1103/PhysRevC.87.035501. URL: http://link.aps.org/doi/10.1103/PhysRevC.87.035501.

[23] S. S. Ratkevich et al. “Comparative study of the double K-shell-vacancy production in single- and double-electron capture decay.” In: *Phys. Rev.* C96.6 (2017), p. 065502. DOI: 10.1103/PhysRevC.96.065502. arXiv: 1707.07171 [nucl-ex].

[24] S. Singh et al. “Nuclear deformation and the two neutrino double-beta decay in Xe-124,126, Te-128,130, -132 and Nd-150 isotopes.” In: *Eur. Phys. J. A* 33 (2007), pp. 375–388. DOI: 10.1140/epja/i2007-10481-7.

[25] Jouni Suhonen. “Double beta decays of ^{124}Xe investigated in the QRPA framework.” In: *J. Phys. G* 40 (2013), p. 075102. DOI: 10.1088/0954-3899/40/7/075102.

[26] M. Aunola and J. Suhonen. “Systematic study of beta and double beta decay to excited final states.” In: *Nucl. Phys. A* 602 (1996), pp. 133–166. DOI: 10.1016/0375-9474(96)00087-5.

[27] Pekka Pirinen and Jouni Suhonen. “Systematic approach to beta and 2vbetabeta decays of mass A=100–136 nuclei.” In: *Phys. Rev.* C91.5 (2015), p. 054309. DOI: 10.1103/PhysRevC.91.054309.

[28] Jonathan Engel and Javier Menéndez. “Status and Future of Nuclear Matrix Elements for Neutrinoless Double-Beta Decay: A Review.” In: *Rept. Prog. Phys.* 80.4 (2017), p. 046301. DOI: 10.1088/1361-6633/aa5bc5. arXiv: 1610.06548 [nucl-th].

[29] Jay N. Marx and David R. Nygren. “The Time Projection Chamber.” In: *Phys. Today* 31N10 (1978), pp. 46–53. DOI: 10.1063/1.2994775.

[30] C. Rubbia. “The Liquid Argon Time Projection Chamber: A New Concept for Neutrino Detectors.” In: (1977).

[31] H. J. Hilke. “Time projection chambers.” In: *Rept. Prog. Phys.* 73 (2010), p. 116201. DOI: 10.1088/0034-4885/73/11/116201.

[32] Matteo Agostini, Giovanni Benato, and Jason Detwiler. “Discovery probability of next-generation neutrinoless double-beta decay experiments.” In: *Phys. Rev.* D96.5 (2017), p. 053001. DOI: 10.1103/PhysRevD.96.053001. arXiv: 1705.02996 [hep-ex].

[33] P. Agnes et al. “First Results from the DarkSide-50 Dark Matter Experiment at Laboratori Nazionali del Gran Sasso.” In: *Phys. Lett.* B743 (2015), pp. 456–466. DOI: 10.1016/j.physletb.2015.03.012. arXiv: 1410.0653 [astro-ph.CO].

[34] P. -A. Amaudruz et al. “First results from the DEAP-3600 dark matter search with argon at SNOLAB.” In: (2017). arXiv: 1707.08042 [astro-ph.CO].

[35] M. G. Boulay and A. Hime. “Technique for direct detection of weakly interacting massive particles using scintillation time discrimination in liquid argon.” In: *Astropart. Phys.* 25 (2006), pp. 179–182. DOI: 10.1016/j.astropartphys.2005.12.009.

[36] K. Ueshima et al. “Scintillation-only Based Pulse Shape Discrimination for Nuclear and Electron Recoils in Liquid Xenon.” In: *Nucl. Instrum. Meth.* A659 (2011), pp. 161–168. DOI: 10.1016/j.nima.2011.09.011. arXiv: 1106.2209 [physics.ins-det].

[37] J. Thomas and D. A. Imel. “Recombination of electron-ion pairs in liquid argon and liquid xenon.” In: *Phys. Rev.* A36 (1987), pp. 614–616. DOI: 10.1103/PhysRevA.36.614.

[38] T. Doke et al. “Let Dependence of Scintillation Yields in Liquid Argon.” In: *Nucl. Instrum. Meth.* A269 (1988), pp. 291–296. DOI: 10.1016/0168-9002(88)90892-3.

[39] E. Aprile et al. “Dark Matter Results from 225 Live Days of XENON100 Data.” In: *Phys. Rev. Lett.* 109 (2012), p. 181301. DOI: 10.1103/PhysRevLett.109.181301.

[40] E. Aprile et al. “Physics reach of the XENON1T dark matter experiment.” In: *JCAP* 1604.04 (2016), p. 027. DOI: 10.1088/1475-7516/2016/04/027.

[41] Emily Grace and James A. Nikkel. “Index of refraction, Rayleigh scattering length, and Sellmeier coefficients in solid and liquid argon and xenon.” In: *Nucl. Instrum. Meth.* A867 (2017), pp. 204–208. DOI: 10.1016/j.nima.2017.06.031. arXiv: 1502.04213 [physics.ins-det].

[42] Jingqiang Ye. “in preparation.” PhD thesis. USA: University of California, San Diego, exp. 2020.

[43] Hamamatsu Photonics K.K. *Photomultiplier Tubes*. 2007. URL: http://www.hamamatsu.com/resources/pdf/etd/PMT_handbook_v3aE.pdf (visited on 04/28/2018).

[44] Alexander Kish. “Dark Matter Search with the XENON100 Experiment.” PhD thesis. Switzerland: Universitaet Zuerich, 2011.

[45] E. Aprile and T. Doke. “Liquid Xenon Detectors for Particle Physics and Astrophysics.” In: *Rev. Mod. Phys.* 82 (2010), pp. 2053–2097. DOI: 10.1103/RevModPhys.82.2053. arXiv: 0910.4956 [physics.ins-det].

[46] Carl Eric Dahl. “The physics of background discrimination in liquid xenon, and first results from Xenon10 in the hunt for WIMP dark matter.” PhD thesis. Princeton U., 2009. URL: https://www.princeton.edu/physics/graduate-program/theses/theses-from-2009/E.Dahlthesis.pdf.

[47] M. Szydagis et al. “NEST: A Comprehensive Model for Scintillation Yield in Liquid Xenon.” In: *JINST* 6 (2011), P10002. DOI: 10.1088/1748-0221/6/10/P10002.

[48] E. Aprile et al. “Observation of Anti-correlation between Scintillation and Ionization for MeV Gamma-Rays in Liquid Xenon.” In: *Phys. Rev.* B76 (2007), p. 014115. DOI: 10.1103/PhysRevB.76.014115. arXiv: 0704.1118 [astro-ph].

[49] Akira Hitachi et al. “Effect of ionization density on the time dependence of luminescence from liquid argon and xenon.” In: *Phys. Rev.* B27 (1983), pp. 5279–5285. DOI: 10.1103/PhysRevB.27.5279.

[50] D. -M. Mei et al. “A Model of Nuclear Recoil Scintillation Efficiency in Noble Liquids.” In: *Astropart. Phys.* 30 (2008), pp. 12–17. DOI: 10.1016/j.astropartphys.2008.06.001. arXiv: 0712.2470 [nucl-ex].

[51] D. S. Akerib et al. “Signal yields, energy resolution, and recombination fluctuations in liquid xenon.” In: *Phys. Rev.* D95.1 (2017), p. 012008. DOI: 10.1103/PhysRevD.95.012008. arXiv: 1610.02076 [physics.ins-det].

[52] M. Auger et al. “Search for Neutrinoless Double-Beta Decay in ^{136}Xe with EXO-200.” In: *Phys. Rev. Lett.* 109 (2012), p. 032505. DOI: 10.1103/PhysRevLett.109.032505. arXiv: 1205.5608 [hep-ex].

[53] Christian Wittweg. “XENON100 Dark Matter Search with the PAX Raw Data Processor for XENON1T.” MA thesis. Germany: Westfaelische Wilhelms-Universitaet, 2016.

[54] E. Conti et al. “Correlated fluctuations between luminescence and ionization in liquid xenon.” In: *Phys. Rev. B* 68 (5 Aug. 2003), p. 054201. DOI: 10.1103/PhysRevB.68.054201. URL: https://link.aps.org/doi/10.1103/PhysRevB.68.054201.

[55] Tadayoshi Doke et al. “Absolute Scintillation Yields in Liquid Argon and Xenon for Various Particles.” In: *Japanese Journal of Applied Physics* 41.3R (2002), p. 1538. URL: http://stacks.iop.org/1347-4065/41/i=3R/a=1538.

[56] E. Aprile et al. “Signal Yields of keV Electronic Recoils and Their Discrimination from Nuclear Recoils in Liquid Xenon.” In: (2017). arXiv: 1709.10149 [astro-ph.IM].

[57] E. Aprile et al. “The XENON100 Dark Matter Experiment.” In: *Astropart. Phys.* 35 (2012), pp. 573–590. DOI: 10.1016/j.astropartphys.2012.01.003.

[58] E. Aprile et al. “Response of the XENON100 Dark Matter Detector to Nuclear Recoils.” In: *Phys. Rev.* D88 (2013), p. 012006. DOI: 10.1103/PhysRevD.88.012006. arXiv: 1304.1427 [astro-ph.IM].

[59] Brian Lenardo et al. “A Global Analysis of Light and Charge Yields in Liquid Xenon.” In: *IEEE Trans. Nucl. Sci.* 62.6 (2015), pp. 3387–3396. DOI: 10.1109/TNS.2015.2481322. arXiv: 1412.4417 [astro-ph.IM].

[60] M. Szydagis et al. “NEST: A Comprehensive Model for Scintillation Yield in Liquid Xenon.” In: *JINST* 6 (2011), P10002. DOI: 10.1088/1748-0221/6/10/P10002. arXiv: 1106.1613 [physics.ins-det].

[61] Lawrence M. Widrow, Brent Pym, and John Dubinski. “Dynamical Blueprints for Galaxies.” In: *Astrophys. J.* 679 (2008), pp. 1239–1259. DOI: 10.1086/587636. arXiv: 0801.3414 [astro-ph].

[62] Christopher McCabe. “The Astrophysical Uncertainties Of Dark Matter Direct Detection Experiments.” In: *Phys. Rev.* D82 (2010), p. 023530. DOI: 10.1103/PhysRevD.82.023530. arXiv: 1005.0579 [hep-ph].

[63] J. D. Lewin and P. F. Smith. “Review of mathematics, numerical factors, and corrections for dark matter experiments based on elastic nuclear recoil.” In: *Astropart. Phys.* 6 (1996), pp. 87–112. DOI: 10.1016/S0927-6505(96)00047-3.

[64] Martin C. Smith et al. “The RAVE Survey: Constraining the Local Galactic Escape Speed.” In: *Mon. Not. Roy. Astron. Soc.* 379 (2007), pp. 755–772. DOI: 10.1111/j.1365-2966.2007.11964.x. arXiv: astro-ph/0611671 [astro-ph].

[65] Jelle Aalbers. “Dark Matter Search with XENON1T.” PhD thesis. Netherlands: Universiteit van Amsterdam, 2018.

[66] Anne M Green. “Astrophysical uncertainties on the local dark matter distribution and direct detection experiments.” In: *J. Phys.* G44.8 (2017), p. 084001. DOI: 10.1088/1361-6471/aa7819. arXiv: 1703.10102 [astro-ph.CO].

[67] J. Engel, S. Pittel, and P. Vogel. “Nuclear physics of dark matter detection.” In: *Int. J. Mod. Phys.* E1 (1992), pp. 1–37. DOI: 10.1142/S0218301392000023.

[68] E. Aprile et al. “Limits on spin-dependent WIMP-nucleon cross sections from 225 live days of XENON100 data.” In: *Phys. Rev. Lett.* 111.2 (2013), p. 021301. DOI: 10.1103/PhysRevLett.111.021301.

[69] D. S. Akerib et al. “Limits on Spin-Dependent WIMP-Nucleon Cross Section Obtained from the Complete LUX Exposure.” In: *Phys. Rev. Lett.* 118 (25 June 2017), p. 251302. DOI: 10.1103/PhysRevLett.118.251302. URL: https://link.aps.org/doi/10.1103/PhysRevLett.118.251302.

[70] K. Schneck et al. “Dark matter effective field theory scattering in direct detection experiments.” In: *Phys. Rev.* D91.9 (2015), p. 092004. DOI: 10.1103/PhysRevD.91.092004. arXiv: 1503.03379 [astro-ph.CO].

[71] E. Aprile et al. “Effective field theory search for high-energy nuclear recoils using the XENON100 dark matter detector.” In: *Phys. Rev.* D96.4 (2017), p. 042004. DOI: 10.1103/PhysRevD.96.042004. arXiv: 1705.02614 [astro-ph.CO].

[72] Martin Hoferichter, Philipp Klos, and Achim Schwenk. “Chiral power counting of one- and two-body currents in direct detection of dark matter.” In: *Phys. Lett.* B746 (2015), pp. 410–416. DOI: 10.1016/j.physletb.2015.05.041. arXiv: 1503.04811 [hep-ph].

[73] R. Machleidt and D. R. Entem. “Chiral effective field theory and nuclear forces.” In: *Phys. Rept.* 503 (2011), pp. 1–75. DOI: 10.1016/j.physrep.2011.02.001. arXiv: 1105.2919 [nucl-th].

[74] XENON collaboration et al. “in preparation.” In: (exp. 2018).

[75] Meng Wang et al. “The AME2016 atomic mass evaluation (II). Tables, graphs and references.” In: *Chin. Phys.* C41.3 (2017), p. 030003. DOI: 10.1088/1674-1137/41/3/030003.

[76] M. Goeppert-Mayer. “Double Beta-Disintegration.” In: *Phys. Rev.* 48 (6 Sept. 1935), pp. 512–516. DOI: 10.1103/PhysRev.48.512. URL: https://link.aps.org/doi/10.1103/PhysRev.48.512.

[77] S. R. Elliott, A. A. Hahn, and M. K. Moe. “Direct evidence for two-neutrino double-beta decay in ^{82}Se.” In: *Phys. Rev. Lett.* 59 (18 Nov. 1987), pp. 2020–2023. DOI: 10.1103/PhysRevLett.59.2020. URL: https://link.aps.org/doi/10.1103/PhysRevLett.59.2020.

[78] Ruben Saakyan. “Two-Neutrino Double-Beta Decay.” In: *Annual Review of Nuclear and Particle Science* 63.1 (2013), pp. 503–529. DOI: 10.1146/annurev-nucl-102711-094904. eprint: https://doi.org/10.1146/annurev-nucl-102711-094904. URL: https://doi.org/10.1146/annurev-nucl-102711-094904.

[79] W. H. Furry. “On transition probabilities in double beta-disintegration.” In: *Phys. Rev.* 56 (1939), pp. 1184–1193. DOI: 10.1103/PhysRev.56.1184.

[80] Stefano Dell’Oro et al. “Neutrinoless double beta decay: 2015 review.” In: *Adv. High Energy Phys.* 2016 (2016), p. 2162659. DOI: 10.1155/2016/2162659. arXiv: 1601.07512 [hep-ph].

[81] D. A. Nesterenko et al. “Double-beta transformations in isobaric triplets with mass numbers A=124, 130, and 136.” In: *Phys. Rev. C* 86 (2012), p. 044313. DOI: 10.1103/PhysRevC.86.044313.

[82] Jouni T. Suhonen. “Value of the Axial-Vector Coupling Strength in beta and double beta Decays: A Review.” In: *Front.in Phys.* 5 (2017), p. 55. DOI: 10.3389/fphy.2017.00055. arXiv: 1712.01565 [nucl-th].

[83] M. Hirsch et al. “Nuclear structure calculations of beta+ beta+, beta+ / EC and EC / EC decay matrix elements.” In: *Z. Phys. A* 347 (1994), pp. 151–160. DOI: 10.1007/BF01292371.

[84] O. A. Rumyantsev and M. H. Urin. “The Strength of the analog and Gamow-Teller giant resonances and hindrance of the 2 neutrino Beta Beta: Decay rate.” In: *Phys. Lett. B* 443 (1998), pp. 51–57. DOI: 10.1016/S0370-2693(98)01291-X.

[85] A. Shukla, P. K. Raina, and P. K. Rath. “Study of two neutrino + beta+ / beta+ EC / ECEC decay of Xe-124,126 and Ba-130,132 for 0+ —> 0+ transition in PHFB model.” In: *J. Phys. G* 33 (2007), pp. 549–563. DOI: 10.1088/0954-3899/34/3/013.

[86] XMASS Collaboration. “Improved search for two-neutrino double electron capture on 124Xe and 126Xe using particle identification in XMASS-I.” In: *Progress of Theoretical and Experimental Physics* 2018.5 (2018), p. 053D03. DOI: 10.1093/ptep/pty053. eprint: /oup/backfile/content_public/journal/ptep/2018/5/10.1093_ptep_pty053/3/pty053.pdf. URL: http://dx.doi.org/10.1093/ptep/pty053.

[87] J. Kotila and F. Iachello. “Phase space factors for $\beta^+\beta^+$ decay and competing modes of double-β decay.” In: *Phys. Rev.* C87.2 (2013), p. 024313. DOI: 10.1103/PhysRevC.87.024313. arXiv: 1303.4124 [nucl-th].

[88] Masaru Doi and Tsuneyuki Kotani. “Neutrino emitting modes of double beta decay.” In: *Prog. Theor. Phys.* 87 (1992), pp. 1207–1232. DOI: 10.1143/PTP.87.1207.

[89] J. Kotila, J. Barea, and F. Iachello. “Neutrinoless double-electron capture.” In: *Phys. Rev. C* 89.6 (2014), p. 064319. DOI: 10.1103/PhysRevC.89.064319.

[90] J. Bernabeu, A. De Rujula, and C. Jarlskog. “Neutrinoless Double Electron Capture as a Tool to Measure the ν_e Mass.” In: *Nucl. Phys. B* 223 (1983), pp. 15–28. DOI: 10.1016/0550-3213(83)90089-5.

[91] M. I. Krivoruchenko et al. “Resonance enhancement of neutrinoless double electron capture.” In: *Nucl. Phys. A* 859 (2011), pp. 140–171. DOI: 10.1016/j.nuclphysa.2011.04.009.

[92] D. Frekers et al. “Double-electron capture of Se-74 and the search for neutrinoless decay.” In: *Nucl. Phys.* A860 (2011), pp. 1–7. DOI: 10.1016/j.nuclphysa.2011.05.002.

[93] P. P. Povinec, D. Frekers, and F. Simkovic. “Recent searches for double-electron capture of nuclei to excited states.” In: *AIP Conf. Proc.* 1686 (2015), p. 020018. DOI: 10.1063/1.4934907.

[94] E. Aprile et al. “The XENON dark matter search experiment.” In: *New Astron. Rev.* 49 (2005), pp. 289–295. DOI: 10.1016/j.newar.2005.01.035.

[95] E. Aprile et al. “Design and Performance of the XENON10 Dark Matter Experiment.” In: *Astropart. Phys.* 34 (2011), pp. 679–698. DOI: 10.1016/j.astropartphys.2011.01.006. arXiv: 1001.2834 [astro-ph.IM].

[96] E. Aprile et al. “The XENON1T Dark Matter Experiment.” In: *Eur. Phys. J.* C77.12 (2017), p. 881. DOI: 10.1140/epjc/s10052-017-5326-3. arXiv: 1708.07051 [astro-ph.IM].

[97] M Ambrosio et al. “Vertical muon intensity measured with MACRO at the Gran Sasso laboratory.” In: *Phys. Rev. D* 52 (7 Oct. 1995), pp. 3793–3802. DOI: 10.1103/PhysRevD.52.3793. URL: https://link.aps.org/doi/10.1103/PhysRevD.52.3793.

[98] M. Aglietta and others. “Neutrino-induced and atmospheric single-muon fluxes measured over five decades of intensity by LVD at Gran Sasso Laboratory.” In: *Astroparticle Physics* 3.4 (1995), pp. 311–320. ISSN: 0927-6505. DOI: https://doi.org/10.1016/0927-6505(95)00012-6. URL: http://www.sciencedirect.com/science/article/pii/0927650595000126.

[99] J. Bieringer et al. “Trace analysis of aerosol bound particulates and noble gases at the BfS in Germany.” In: *Applied Radiation and Isotopes* 67.5 (2009). 5th International Conference on Radionuclide Metrology - Low-Level Radioactivity Measurement Techniques ICRM-LLRMT’08, pp. 672–677. ISSN: 0969-8043. DOI: https://doi.org/10.1016/j.apradiso.2009.01.008. URL: http://www.sciencedirect.com/science/article/pii/S096980430900013X.

[100] E. Aprile et al. “Intrinsic backgrounds from Rn and Kr in the XENON100 experiment.” In: *Eur. Phys. J.* C78.2 (2018), p. 132. DOI: 10.1140/epjc/s10052-018-5565-y. arXiv: 1708.03617 [astro-ph.IM].

[101] E. Aprile et al. “The neutron background of the XENON100 dark matter search experiment.” In: *J. Phys.* G40 (2013), p. 115201. DOI: 10.1088/0954-3899/40/11/115201. arXiv: 1306.2303 [astro-ph.IM].

[102] E. Aprile et al. “Analysis of the XENON100 Dark Matter Search Data.” In: *Astropart. Phys.* 54 (2014), pp. 11–24. DOI: 10.1016/j.astropartphys.2013.10.002.

[103] E. Aprile et al. “Conceptual design and simulation of a water Cherenkov muon veto for the XENON1T experiment.” In: *JINST* 9 (2014), P11006. DOI: 10.1088/1748-0221/9/11/P11006. arXiv: 1406.2374 [astro-ph.IM].

[104] E. Aprile et al. “Lowering the radioactivity of the photomultiplier tubes for the XENON1T dark matter experiment.” In: *Eur. Phys. J.* C75.11 (2015), p. 546. DOI: 10.1140/epjc/s10052-015-3657-5. arXiv: 1503.07698 [astro-ph.IM].

[105] K. Lung et al. “Characterization of the Hamamatsu R11410-10 3-Inch Photomultiplier Tube for Liquid Xenon Dark Matter Direct Detection Experiments.” In: *Nucl. Instrum. Meth.* A696 (2012), pp. 32–39. DOI: 10.1016/j.nima.2012.08.052. arXiv: 1202.2628 [physics.ins-det].

[106] P. Barrow et al. “Qualification Tests of the R11410-21 Photomultiplier Tubes for the XENON1T Detector.” In: *JINST* 12.01 (2017), P01024. DOI: 10.1088/1748-0221/12/01/P01024. arXiv: 1609.01654 [astro-ph.IM].

[107] L. Baudis et al. “Performance of the Hamamatsu R11410 Photomultiplier Tube in cryogenic Xenon Environments.” In: *JINST* 8 (2013), P04026. DOI: 10.1088/1748-0221/8/04/P04026. arXiv: 1303.0226 [astro-ph.IM].

[108] Zach Greene. “in preparation.” PhD thesis. United States of America: Columbia University, New York, exp. 2019.

[109] E. Aprile et al. “Removing krypton from xenon by cryogenic distillation to the ppq level.” In: *Eur. Phys. J.* C77.5 (2017), p. 275. DOI: 10.1140/epjc/s10052-017-4757-1. arXiv: 1612.04284 [physics.ins-det].

[110] Michael Murra. “in preparation.” PhD thesis. Germany: Westfaelische Wilhelms-Universitaet, exp. 2018.

[111] Sebastian Lindemann and Hardy Simgen. “Krypton assay in xenon at the ppq level using a gas chromatographic system and mass spectrometer.” In: *Eur. Phys. J.* C74 (2014), p. 2746. DOI: 10.1140/epjc/s10052-014-2746-1. arXiv: 1308.4806 [physics.ins-det].

[112] Alexander Fieguth. “Investigations of impurities in xenon gas with a cold-trap-enhanced quadrupole mass spectrometer.” MA thesis. Germany: Westfaelische Wilhelms-Universitaet, 2014.

[113] E. Aprile et al. “Online^{222} Rn removal by cryogenic distillation in the XENON100 experiment.” In: *Eur. Phys. J.* C77.6 (2017), p. 358. DOI: 10.1140/epjc/s10052-017-4902-x. arXiv: 1702.06942 [physics.ins-det].

[114] E. Aprile et al. “Material radioassay and selection for the XENON1T dark matter experiment.” In: *Eur. Phys. J.* C77.12 (2017), p. 890. DOI: 10.1140/epjc/s10052-017-5329-0. arXiv: 1705.01828 [physics.ins-det].

[115] E. Aprile et al. “First Dark Matter Search Results from the XENON1T Experiment.” In: *Phys. Rev. Lett.* 119.18 (2017), p. 181301. DOI: 10.1103/PhysRevLett.119.181301. arXiv: 1705.06655 [astro-ph.CO].

[116] S. Rosendahl et al. “Determination of the separation efficiencies of a single-stage cryogenic distillation setup to remove krypton out of xenon by using a 83mKr tracer method.” In: *Rev. Sci. Instrum.* 86.11 (2015), p. 115104. DOI: 10.1063/1.4934978.

[117] Stephan Rosendahl. “Gas purification of the XENON dark matter search.” PhD thesis. Germany: Westfaelische Wilhelms-Universitaet, 2015.

[118] V. Hannen et al. “Limits on the release of Rb isotopes from a zeolite based 83mKr calibration source for the XENON project.” In: *JINST* 6 (2011), P10013. DOI: 10.1088/1748-0221/6/10/P10013. arXiv: 1109.4270 [astro-ph.IM].

[119] E. Aprile et al. “Results from a Calibration of XENON100 Using a Source of Dissolved Radon-220.” In: *Phys. Rev.* D95.7 (2017), p. 072008. DOI: 10.1103/PhysRevD.95.072008. arXiv: 1611.03585 [physics.ins-det].

[120] R. F. Lang et al. “Characterization of a deuterium–deuterium plasma fusion neutron generator.” In: *Nucl. Instrum. Meth.* A879 (2018), pp. 31–38. DOI: 10.1016/j.nima.2017.10.001. arXiv: 1705.04741 [physics.ins-det].

[121] Jelle Aalbers and Christopher Tunnell. *The pax data processor v6.4.2*. 2017. URL: https://zenodo.org/record/546239#.WsNRVda-lhE (visited on 04/07/2018).

[122] J. Billard, L. Strigari, and E. Figueroa-Feliciano. “Implication of neutrino backgrounds on the reach of next generation dark matter direct detection experiments.” In: *Phys. Rev.* D89.2 (2014), p. 023524. DOI: 10.1103/PhysRevD.89.023524. arXiv: 1307.5458 [hep-ph].

[123] XENON collaboration. *Technical Design Report XENONnT*. Technical Design Report. LNGS, Italy, 2018.

[124] Ethan Brown et al. “Magnetically-coupled piston pump for high-purity gas applications.” In: (2018). arXiv: 1803.08498 [physics.ins-det].

[125] B. J. Mount et al. “LUX-ZEPLIN (LZ) Technical Design Report.” In: (2017). arXiv: 1703.09144 [physics.ins-det].

[126] DARWIN collaboration. “DARWIN: towards the ultimate dark matter detector.” In: *JCAP* 1611.11 (2016), p. 017. DOI: 10.1088/1475-7516/2016/11/017. arXiv: 1606.07001 [astro-ph.IM].

[127] A. Fieguth et al. “Discriminating WIMP-nucleus response functions in present and future XENON-like direct detection experiments.” In: *Phys. Rev.* D97 (2018), p. 103532. DOI: 10.1103/PhysRevD.97.103532. arXiv: 1802.04294 [hep-ph].

[128] E. Aprile et al. “Dark Matter Search Results from a One Tonne×Year Exposure of XENON1T.” In: (2018). arXiv: 1805.12562 [astro-ph.CO].

[129] D. Akimov et al. “Observation of Coherent Elastic Neutrino-Nucleus Scattering.” In: *Science* 357.6356 (2017), pp. 1123–1126. DOI: 10.1126/science.aao0990. arXiv: 1708.01294 [nucl-ex].

[130] Glen Cowan et al. “Asymptotic formulae for likelihood-based tests of new physics.” In: *Eur. Phys. J.* C71 (2011). [Erratum: Eur. Phys. J.C73,2501(2013)], p. 1554. DOI: 10.1140/epjc/s10052-011-1554-0,10.1140/epjc/s10052-013-2501-z. arXiv: 1007.1727 [physics.data-an].

[131] E. Aprile et al. “Likelihood Approach to the First Dark Matter Results from XENON100.” In: *Phys. Rev.* D84 (2011), p. 052003. DOI: 10.1103/PhysRevD.84.052003. arXiv: 1103.0303 [hep-ex].

[132] Gary J. Feldman and Robert D. Cousins. “A Unified approach to the classical statistical analysis of small signals.” In: *Phys. Rev. D* 57 (1998), pp. 3873–3889. DOI: 10.1103/PhysRevD.57.3873.

[133] Knut Mora. “in preparation.” PhD thesis. Sweden: Stockholms universitet, exp. 2019.

[134] D. S. Akerib et al. “Results from a search for dark matter in the complete LUX exposure.” In: *Phys. Rev. Lett.* 118.2 (2017), p. 021303. DOI: 10.1103/PhysRevLett.118.021303. arXiv: 1608.07648 [astro-ph.CO].

[135] Richard H. Helm. “Inelastic and Elastic Scattering of 187-Mev Electrons from Selected Even-Even Nuclei.” In: *Phys. Rev.* 104 (1956), pp. 1466–1475. DOI: 10.1103/PhysRev.104.1466.

[136] Clifford Cheung et al. “Prospects and Blind Spots for Neutralino Dark Matter.” In: *JHEP* 05 (2013), p. 100. DOI: 10.1007/JHEP05(2013)100. arXiv: 1211.4873 [hep-ph].

[137] Peisi Huang and Carlos E. M. Wagner. “Blind Spots for neutralino Dark Matter in the MSSM with an intermediate m_A.” In: *Phys. Rev.* D90.1 (2014), p. 015018. DOI: 10.1103/PhysRevD.90.015018. arXiv: 1404.0392 [hep-ph].

[138] Andreas Crivellin et al. “Light stops, blind spots, and isospin violation in the MSSM.” In: *JHEP* 07 (2015), p. 129. DOI: 10.1007/JHEP07(2015)129. arXiv: 1503.03478 [hep-ph].

[139] JiJi Fan, Matthew Reece, and Lian-Tao Wang. “Non-relativistic effective theory of dark matter direct detection.” In: *JCAP* 1011 (2010), p. 042. DOI: 10.1088/1475-7516/2010/11/042. arXiv: 1008.1591 [hep-ph].

[140] A. Liam Fitzpatrick et al. “The Effective Field Theory of Dark Matter Direct Detection.” In: *JCAP* 1302 (2013), p. 004. DOI: 10.1088/1475-7516/2013/02/004. arXiv: 1203.3542 [hep-ph].

[141] Nikhil Anand, A. Liam Fitzpatrick, and W. C. Haxton. “Weakly interacting massive particle-nucleus elastic scattering response.” In: *Phys. Rev.* C89.6 (2014), p. 065501. DOI: 10.1103/PhysRevC.89.065501. arXiv: 1308.6288 [hep-ph].

[142] L. Vietze et al. “Nuclear structure aspects of spin-independent WIMP scattering off xenon.” In: *Phys. Rev.* D91.4 (2015), p. 043520. DOI: 10.1103/PhysRevD.91.043520. arXiv: 1412.6091 [nucl-th].

[143] G. Co’ et al. “Nuclear proton and neutron distributions in the detection of weak interacting massive particles.” In: *JCAP* 1211 (2012), p. 010. DOI: 10.1088/1475-7516/2012/11/010. arXiv: 1211.1787 [nucl-th].

[144] D. G. Cerdeno et al. “Nuclear uncertainties in the spin-dependent structure functions for direct dark matter detection.” In: *Phys. Rev.* D87.2 (2013), p. 023512. DOI: 10.1103/PhysRevD.87.023512. arXiv: 1208.6426 [hep-ph].

[145] Rene Brun. *ROOT - reference guide*. 1994. URL: https://root.cern.ch/doc/master/classTH2.html (visited on 06/23/2018).

[146] E. Aprile et al. “XENON100 Dark Matter Results from a Combination of 477 Live Days.” In: *Phys. Rev.* D94.12 (2016), p. 122001. DOI: 10.1103/PhysRevD.94.122001. arXiv: 1609.06154 [astro-ph.CO].

[147] P. Klos et al. “Large-scale nuclear structure calculations for spin-dependent WIMP scattering with chiral effective field theory currents.” In: *Phys. Rev.* D88.8 (2013). [Erratum: Phys. Rev.D89,no.2,029901(2014)], p. 083516. DOI: 10.1103/PhysRevD.89.029901,10.1103/PhysRevD.88.083516. arXiv: 1304.7684 [nucl-th].

[148] Ruben Saakyan. “Two-Neutrino Double-Beta Decay.” In: *Ann. Rev. Nucl. Part. Sci.* 63 (2013), pp. 503–529. DOI: 10.1146/annurev-nucl-102711-094904.

[149] N. Ackerman et al. “Observation of Two-Neutrino Double-Beta Decay in ^{136}Xe with EXO-200.” In: *Phys. Rev. Lett.* 107 (2011), p. 212501. DOI: 10.1103/PhysRevLett.107.212501. arXiv: 1108.4193 [nucl-ex].

[150] A. Gando et al. “Measurement of the double-beta decay half-life of ^{136}Xe with the KamLAND-Zen experiment.” In: *Phys. Rev.* C85 (2012), p. 045504. DOI: 10.1103/PhysRevC.85.045504. arXiv: 1201.4664 [hep-ex].

[151] M. Pujol et al. “Xenon in Archean barite: Weak decay of ^{130}Ba, mass-dependent isotopic fractionation and implication for barite formation.” In: *Geochim. Cosmochim. Acta* 73 (Nov. 2009), pp. 6834–6846. DOI: 10.1016/j.gca.2009.08.002.

[152] Yu. M. Gavrilyuk et al. “Search for $2K(2\nu)$-capture of ^{124}Xe.” In: *Phys. Part. Nucl.* 48.1 (2017), pp. 38–41. DOI: 10.1134/S1063779616060083. arXiv: 1507.04520 [nucl-ex].

[153] Masaru Doi and Tsuneyuki Kotani. “Neutrinoless modes of double beta decay.” In: *Prog. Theor. Phys.* 89 (1993), pp. 139–160. DOI: 10.1143/PTP.89.139.

[154] D.E. Cullen. *Program RELAX: A code designed to calculate atomic relaxation spectra of x-rays and electrons*. Tech. rep. UCRL-ID–110438. CA (United States): Lawrence Livermore National Laboratory.

[155] NIST. *X-Ray Mass Attenuation Coefficient*. 2018. URL: https://physics.nist.gov/PhysRefData/XrayMassCoef/ElemTab/z54.html (visited on 02/19/2018).

[156] E. Aprile et al. “Search for two-neutrino double electron capture of ^{124}Xe with XENON100.” In: *Phys. Rev.* C95.2 (2017), p. 024605. DOI: 10.1103/PhysRevC.95.024605. arXiv: 1609.03354 [nucl-ex].

[157] XENON collaboration. “in preparation.” In: (exp. 2018).

[158] D. -M. Mei et al. “Measuring Double-Electron Capture with Liquid Xenon Experiments.” In: *Phys. Rev. C* 89.1 (2014), p. 014608. DOI: 10.1103/PhysRevC.89.014608.

[159] S. Valkiers et al. “A primary xenon isotopic gas standard with SI traceable values for isotopic composition and molar mass.” In: *International Journal of Mass Spectrometry and Ion Processes* 173.1 (1998), pp. 55–63. ISSN: 0168-1176. DOI: https://doi.org/10.1016/S0168-1176(97)00274-7. URL: http://%20sciencedirect.com/science/article/pii/S0168117697002747.

[160] Rene Brun. *ROOT - reference guide*. 1999. URL: https://root.cern.ch/doc/master/classTGraphAsymmErrors.html (visited on 03/25/2018).

[161] Allen Caldwell, Daniel Kollar, and Kevin Kroninger. “BAT: The Bayesian Analysis Toolkit.” In: *Comput. Phys. Commun.* 180 (2009), pp. 2197–2209. DOI: 10.1016/j.cpc.2009.06.026.

[162] Adrian E. Raftery Robert E. Kass. “Bayes Factors.” In: *Journal of the American Statistical Association* 90.430 (1995), pp. 773–795.

[163] F. Beaujean et al. “p-values for model evaluation.” In: *Phys. Rev. D* 83 (1 Jan. 2011), p. 012004. DOI: 10.1103/PhysRevD.83.012004. URL: http://link.aps.org/doi/10.1103/PhysRevD.83.012004.

[164] Adrian Bevan. *ROOT - reference guide*. 2001. URL: https://root.cern.ch/doc/master/classTFeldmanCousins.html (visited on 03/25/2018).

[165] Christian Wittweg. “in preparation.” PhD thesis. Germany: Westfaelische Wilhelms-Universitaet, exp. 2020.

[166] NIST. *Thermophysical Properties of Fluid Systems*. 2018. URL: https://webbook.nist.gov/chemistry/fluid/ (visited on 07/12/2018).

[167] Valdimir Tretyak. *DECAY0 event generator for initial kinematics of particles in α,β and 2β-decays year = 2015*. URL: https://agenda.infn.it/getFile.py/access?resId=0&materialId=slides&confId=9358 (visited on 06/28/2018).

[168] S. Agostinelli et al. “GEANT4: A Simulation toolkit.” In: *Nucl. Instrum. Meth.* A506 (2003), pp. 250–303. DOI: 10.1016/S0168-9002(03)01368-8.

[169] John N. Bahcall, Aldo M. Serenelli, and Sarbani Basu. “New solar opacities, abundances, helioseismology, and neutrino fluxes.” In: *Astrophys. J.* 621 (2005), pp. L85–L88. DOI: 10.1086/428929. arXiv: astro-ph/0412440 [astro-ph].

[170] Jiunn-Wei Chen et al. “Low-energy electronic recoil in xenon detectors by solar neutrinos.” In: *Phys. Lett.* B774 (2017), pp. 656–661. DOI: 10.1016/j.physletb.2017.10.029. arXiv: 1610.04177 [hep-ex].

[171] Yu. Khazov, A. Rodionov, and F. G. Kondev. “Nuclear Data Sheets for A = 133.” In: *Nucl. Data Sheets* 112 (2011), pp. 855–1113. DOI: 10.1016/j.nds.2011.03.001.

[172] F. James and M. Roos. “Minuit: A System for Function Minimization and Analysis of the Parameter Errors and Correlations.” In: *Comput. Phys. Commun.* 10 (1975), pp. 343–367. DOI: 10.1016/0010-4655(75)90039-9.

[173] Piti Ongmongkolkul (@piti118) et al. *iminuit - A Python interface to MINUIT*. [Online; accessed 2018.06.29]. 2012–. URL: https://github.com/iminuit/iminuit.

[174] Fabio Valerio Massoli. “The XENON1T experiment: Monte Carlo background estimation and sensitivity curves study.” PhD thesis. Italy: Universita di Bologna, 2015.

[175] J. Katakura. “Nuclear Data Sheets for A = 125.” In: *Nucl. Data Sheets* 112 (2011), pp. 495–705. DOI: 10.1016/j.nds.2011.02.001.

[176] J. H. Hubbell et al. “A Review, Bibliography, and Tabulation of K, L, and Higher Atomic Shell X-Ray Fluorescence Yields.” In: *Journal of Physical and Chemical Reference Data* 23.2 (Mar. 1994), pp. 339–364. DOI: 10.1063/1.555955. URL: https://doi.org/10.1063%2F1.555955.

[177] NIST. *X-Ray Transition Energies Database*. 2018. URL: http://physics.nist.gov/XrayTrans (visited on 07/01/2018).

[178] A. Rindi et al. “UNDERGROUND NEUTRON FLUX MEASUREMENT.” In: *Nucl. Instrum. Meth.* A272 (1988), p. 871. DOI: 10.1016/0168-9002(88)90772-3.

[179] P. Belli et al. “Deep Underground Neutron Flux Measurement With Large Bf-3 Counters.” In: *Nuovo Cim.* A101 (1989), pp. 959–966. DOI: 10.1007/BF02800162.

[180] Z. Debicki et al. “Thermal neutrons at Gran Sasso.” In: *Nucl. Phys. Proc. Suppl.* 196 (2009), pp. 429–432. DOI: 10.1016/j.nuclphysbps.2009.09.084.

[181] Andreas Best et al. “Low energy neutron background in deep underground laboratories.” In: *Nucl. Instrum. Meth.* A812 (2016), pp. 1–6. DOI: 10.1016/j.nima.2015.12.034. arXiv: 1509.00770 [physics.ins-det].

[182] H. Wulandari et al. “Neutron flux underground revisited.” In: *Astropart. Phys.* 22 (2004), pp. 313–322. DOI: 10.1016/j.astropartphys.2004.07.005. arXiv: hep-ex/0312050 [hep-ex].

[183] Xiangyi Cui et al. “Dark Matter Results From 54-Ton-Day Exposure of PandaX-II Experiment.” In: *Phys. Rev. Lett.* 119.18 (2017), p. 181302. DOI: 10.1103/PhysRevLett.119.181302. arXiv: 1708.06917 [astro-ph.CO].

[184] E. Bagnaschi et al. “Likelihood Analysis of the pMSSM11 in Light of LHC 13-TeV Data.” In: *Eur. Phys. J.* C78.3 (2018), p. 256. DOI: 10.1140/epjc/s10052-018-5697-0. arXiv: 1710.11091 [hep-ph].

[185] Z. Sujkowski and S. Wycech. “Neutrinoless double electron capture: A Tool to search for Majorana neutrinos.” In: *Phys. Rev. C* 70 (2004), p. 052501. DOI: 10.1103/PhysRevC.70.052501.

Danksagung

Prof. Dr. Gernot Münster erklärte kürzlich in einer Ehrenrede, dass Physik eine große Gemeinsamkeit mit Brot aufweist: Irgendwann wird es hart.
Mein wesentlich beschränkterer Einblick in die Materie bestätigt das in vollem Umfang. Aus diesem Grund kann man es nicht alleine bewältigen und auch diese Arbeit ist nur durch die Hilfe vieler verschiedener Menschen ermöglicht worden. Auf diesem Wege versuche ich meinen Dank für all die Unterstützung, die ich bekommen habe, mit Worten auszurdrücken. Das kann natürlich nicht komplett gelingen und so entschuldige ich mich für jeden der hier namentlich vergessen wurde!
Mein erster, aber auch mein größter Dank geht an Prof. Dr. Christian Weinheimer. Von einer unerschöpflichen Förderung, die mir eine Entwicklung ermöglicht hat, die ich selbst am wenigsten für möglich gehalten habe, bis hin zur unerschöpflichen physikalischen Hilfe für wahrlich jedes Problem. All das ist mit einem einfachen Danke kaum abzutun. Ob für die Motivation in schwierigen Momenenten, die vor allem durch vorbildhaftes eigenes Einbringen in jedes Problem gefördert wurde, oder für den politischen Schutzschild, wenn ich mal wieder mit der Brechstange mein Glück probiert habe, aber auch für die moralische Integrität mit der jeder Konflikt angegangen wurde, möchte ich mich zutiefst bedanken.
Prof. Dr. Dieter Frekers möchte ich danken, dafür dass er die Zweitkorrektur dieser Arbeit übernommen hat, aber auch dafür, dass er mich an vielen Abenden und Wochenenden erinnert hat, doch endlich mal zu gehen.
Prof. Dr. Michael Klasen möchte ich für die Betreuung im Rahmen des Graduiertenkollegs danken.
Danke auch an alle, die einen so reibungslosen Ablauf im Institut für Kernphysik garantieren. Ein spezielles Dankeschön an Michaela Erdmann, Petra Voß und Uta Mayer für all die Hilfe bei den vielen Nebentätigkeiten, die im Rahmen einer Promotion so anfallen.
Für die unfassbar lockere und angenehme Atmosphäre kann ich mich bei allen Mitgliedern der AG Weinheimer bedanken, die hier in meinen 7 Jahren mitgewirkt haben. Zahllose Tage und Abende habe ich in Heiterkeit hier verbracht. Danke dafür an Jan, Mariia, Olli, Daniel, Simon, StephanD, ChristianE, Hans-Werner, Axel, Nicho, Maik, Philipp, Rudolf, AlexF der Zweite, Volker,
Mein nächster Dank geht direkt an die XENON Gruppe in Münster. Viele lustige und produktive Momente werden mir tief im Gedächtnis bleiben. Danke Denny, Kevin, Henning, Sergej, StephanR, MichaelM, MichaelW, Lutz, Miguel, ChristianWi, ChristianH.
Im Rahmen der großen XENON-Familie möchte ich der gesamten Kollaboration danken für die viele freundliche und forderende Zusammenarbeit. Danke an alle, die ich mit zahllosen Fragen bombadiert habe, vor allem an Constanze, Stefan Edelweiss Bruenner, Natascha, Teresa, Qing, Jelle, Sander, Fei, Fabio, Knut und Rafael. Es hat mir immer viel Spaß gemacht mit euch zusammen zu arbeiten. Danke an Moritz für die lehrreiche Zusammenarbeit im Rahmen meiner ersten Publikation mit XENON100. Danke auch an Achim, Martin, Philipp und Javier, die mir mein Theorieprojekt zur großen Freude gemacht haben und die ein schier unendliches Wissen bereitstellen konnten.
Im speziellen möchte ich mich auch bei Ludwig dafür bedanken, dass ich ihm beibringen durfte wie man lebt als ich in Heidelberg gastiert habe, aber vor allem für die grenzenlose Hilfsbereitschaft was jegliches Physikwissen betraf. Ach, und danke dafür, dass du mal ein bisschen Action wolltest bei deinem Shifturlaub! Einen Orangensaft auf dich!
Wenn es um Physik geht, kann ich nicht drumherum Nils ein ebenso großes Danke auszusprechen. Man, hab ich viel in diesem Kaffeeraumbüro an späten Abenden und Wochenenden gelernt.
Ein ähnlich hilfreichen Fundus an Wissen durfte ich bei Lutz jederzeit anzapfen, wenn es auch nur im entferntesten um Computer ging.

Für viele sinnvolle Korrekturen zu dieser Arbeit danke ich auch ausgiebig Nils, Miguel, Olli, Lutz,Michael, Martin und Javier.
Für all den herrlichen Unfug und sinnlosen Spaß während des Studiums und vor allem während der Promotion möchte ich mich auch explizit nochmal bei Nils, Christopher, Serge, Sammy, Michael und Olli bedanken.
Michael und Olli, haben wir es doch tatsächlich geschafft, das durchzuziehen. Danke, dass ihr euch damals auch für den 3. Versuch entschieden habt.
An Sam geht nochmal ein riesiger Dank in vielen Formen. Seien es die unzähligen gemeinsamen Stunden an Arbeit, die wir in die Suche dieses Zerfalls gesteckt haben, die viele Physik an die wir uns gewagt haben oder die viele Statistik, die uns schier in den Wahnsinn gerieben hat, sei es das Korrekturlesen dieses gesamten Werkes mit einer Akribie, die ihresgleichen sucht, oder sei es der unnachahmliche Humor den du dein Eigen nennst, der in so einigen harten Momenten das Blatt gewendet hat. Ohne all das, wäre diese Arbeit so garantiert nicht enstanden, which is why I say thanks!
Meinen Freunden, vor allem meinen Mitbewohnern aus der gesamten Zeit, möchte ich danken, dass sie mir die Zeit jenseits der Physik mehr als vergoldet haben, aber auch, dass man mich speziell in den letzten Monaten ertragen hat. Ganz explizit muss ich hier Paul hervorheben. Was waren die gesamten 10 Jahre in Münster eine rasante Fahrt an deiner Seite!
Meiner gesamten Familie möchte ich hier auch nochmal für all die Unterstützung danken.
Zum Schluss möchte ich Nina danke sagen: Danke für wirklich jede Facette deines unbezahlbaren Charakters. Auf ins Abenteuer!

Appendix A

Report on the RGA studies

The report given below was attached to one of the PhD reports necessary for the Research Training Group (RTG, GRK 2149) and has not been altered.

A.1 Introduction

When starting my RTG membership I realized that my chosen project for the PhD thesis, the experimental search for the double electron capture in XENON data and the additional theory project part, the investigation of the impact of different form factors within our dark matter search, will not involve any hardware oriented work. Therefore, in order to keep the spectrum of skills I want to develop as broad as possible, I joined the effort of testing the radon distillation at the XENON100 experiment and the final development of the krypton distillation column for the XENON1T experiment (both part of PhD thesis of Michael Murra). Additionally, after consulting my two supervisors, I started to pursue a follow-up of my master thesis work, which was permitted as long as my main topics were not put aside by this effort.
This hardware oriented project was about a residual gas analyzer (RGA) system for the XENON1T experiment, where the final sensitivity for the detection of krypton in xenon was shown to be 67 parts per trillion (ppt) within my master thesis. Since this was not the desirable value, as for XENON1T measurements at the sub-ppt level would be required, I noted some possible improvements within the thesis. These improvements where tested within the first year of my RTG membership and will be presented here. In order to be able to improve the system, various hardware parts of the experiment had to be changed at the test facility in the Muenster laboratory. In Figure 2 the changes with respect to the previous set-up are marked in red. For further clarity two subsystems will be described in more detail, namely the recuperation cold trap (Re-CT) and the additional second cooling stage including a cold-head (CH).

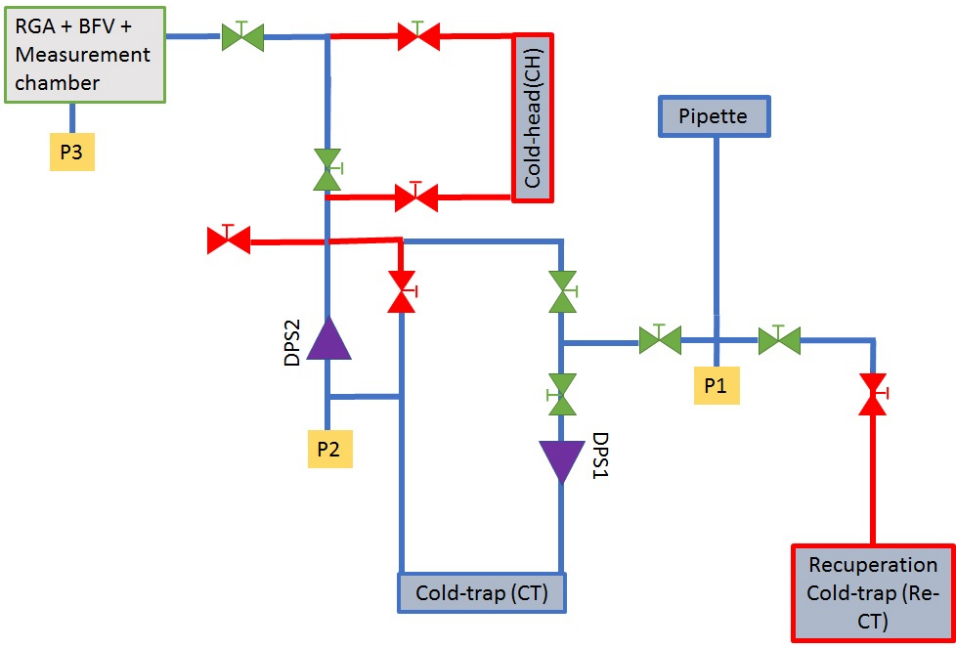

Figure A.1.: Sketch of the RGA-setup. Changes from the ideas presented here are indicated in red.

A.1.1 Investigation on gas dynamics and more with the Re-CT

During the operation of the system within my master thesis and beforehand the actual behavior in terms of krypton freezing within the cold trap (CT) remained unclear. In order to test, if and how much krypton is trapped within the xenon ice in the cold trap, we added a second cold trap, which could be immersed in liquid nitrogen simultaneously. The idea behind this was to make a measurement as usual and then afterwards heat the original cold trap, freezing the evaporating gas in the cold Re-CT. Therefore, another valve had been added to the system in order to shut off the turbo molecular pump from the cold trap. By measuring now afterwards the xenon gas from the Re-CT, we could check if the krypton concentration changed due to the first freeze-out. The result was, that with each recuperation the krypton signal was reduced by around 60% in the remaining gas, while nearly 100% of the xenon gas was re-used. While the first fact was not expected, the second adds an advantage to the method. Now any measurement consumes basically no xenon gas anymore, which reduces the cost to operate the system significantly. Furthermore, the recuperation technique has been proved to produce very clean samples, if repeated frequently. This samples can be used to cross-check sensitivity signals but also in order to establish a new krypton doping method directly at the setup, which has been done for the CH tests mentioned in the next subsection.

A.1.2 Improving the sensitivity using an additional cold head(CH)

The tests with the Re-CT enabled a new method, which could be able to enhance the sensitivity. Therefore, a second system has been added with the main component being a cold head (CH), which can operate at temperatures as low as 30 K. Various methods utilizing the new two-stage cooling have been tested, where only the most promising will be discussed here.
The main idea behind this was, that we first send the gas through the first cold trap, building a krypton enriched gas phase above it. Additionally, we open to the CH, who freezes the gas-phase further down to total pressures less then 10^{-7}mbar, which is four orders of magnitude lower than at liquid nitrogen temperature. This way we accumulate for a fixed amount of time krypton enriched gas at the CH. In the second step we then close the valves to the cold trap and open the CH chamber to the RGA measurement chamber. By turning the cold head off, it slowly warms up releasing the adsorbents on its surface. As krypton is lighter than xenon, it is expected to enter the main chamber before the xenon evaporates, which can be monitored by the pressure within the chamber. This allows for a better sensitivity, since the main chamber is not flooded with xenon as in the classical measurement. The sensitivity of this measurement procedure has been tested with artificially doped samples down to sub-ppt samples and have been compared with krypton-free samples produced with the Re-CT method described above. A clear different behavior can be seen for the krypton containing samples when one compares figure 3 with figure 4. So this method seem to allow for measuring krypton at lower levels than before.

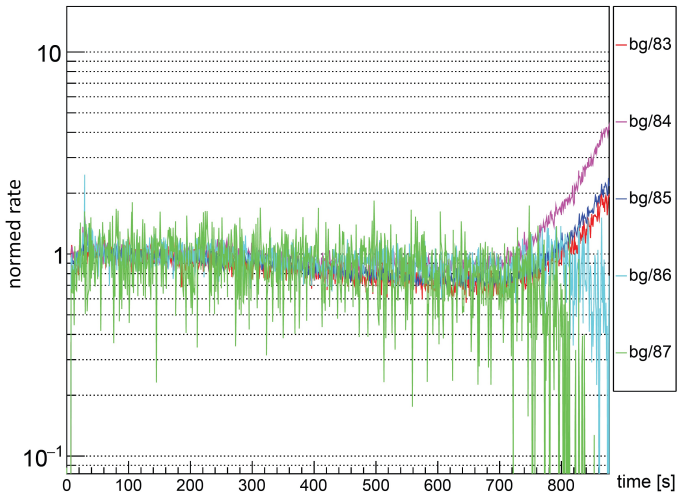

Figure A.2.: Measurement of a krypton-free sample. Normed rate vs time, which is related to the temperature at the CH. The most important isotopes Krypton-84 (pink) and Krypton-86(light blue) behave not in the same way. Moreover, most of the time they show the same behavior as less present isotopes or background measurements (e.g., mass-87 (green)).

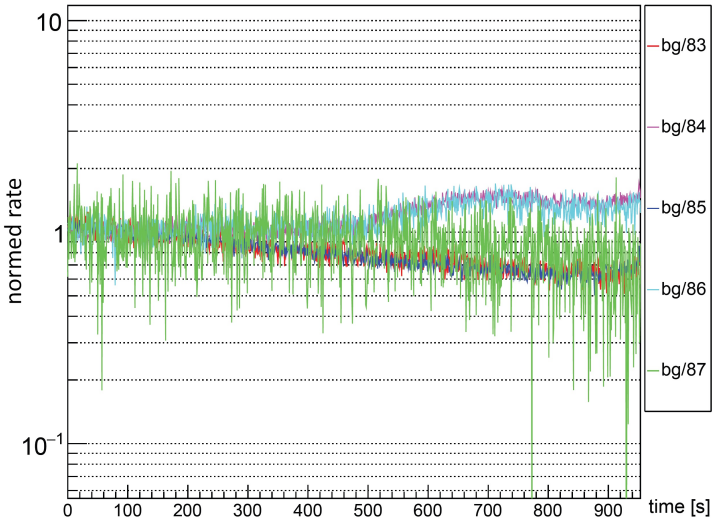

Figure A.3.: Measurement of a sample with about 0.180 ppt krypton content Here one sees that starting at about 300 seconds, the two prominent krypton isotopes (Krypton-84 and Krypton-86) show an increasing intensity, while all others drop. This is an indication that a measurable amount of krypton was present on the cold head.

Summary

The changes made within my PhD thesis improved the setup significantly. While beforehand the xenon was only once used, it can now be reused completely. The dynamic behavior of the system can now be studied by using the Re-CT and clean doping samples can be produced on-site. Additionally, the final goal, a sensitivity enhancement, seems to be accomplished by the added second cooling stage. However, due to the strong focus within the thesis on analysis for the XENON1T experiment, the quantification and reproducibility check as well as further improvements could not be pursued anymore. This leaves space for further research either by myself in the future or other students.

Appendix B

Support material for discrimination study

B.1 Signal models for the tested non-standard underlying nuclear form factors

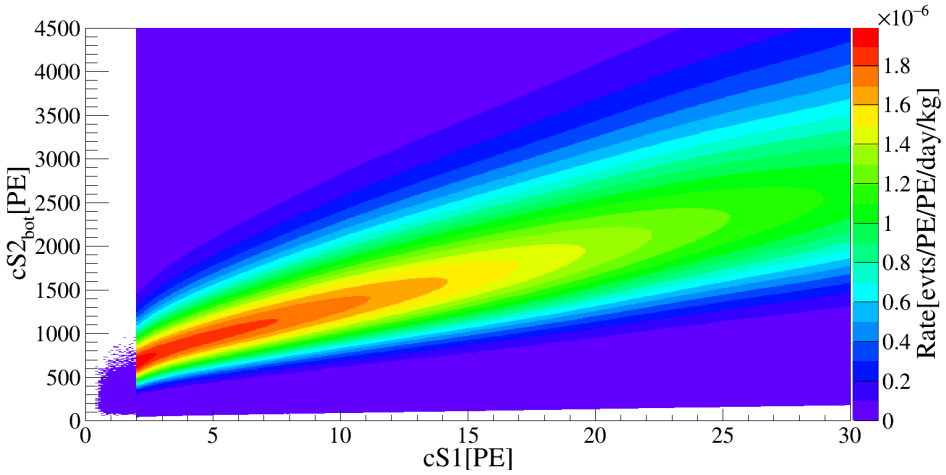

Figure B.1.: Input background model for the MC as given from XENON100 run 10. This model includes ER and NR according to the background model in run10 in XENON100.

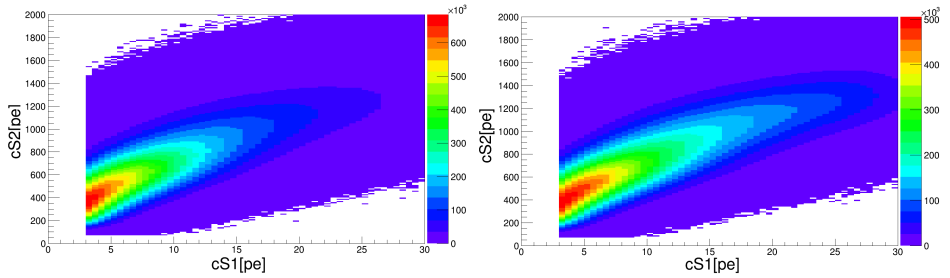

Figure B.2.: Signal models of non-standard interaction channels Left: Signal model for $|\mathcal{F}_{-}^{M}|^2$. Right: Signal model for $|\mathcal{F}_{\pi}|^2$.

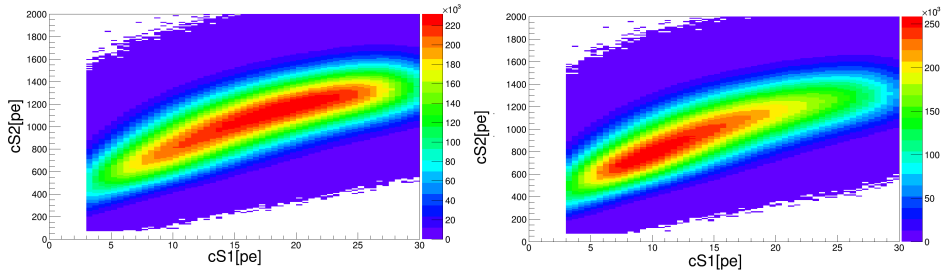

Figure B.3.: Signal models of non-standard interaction channels Left: Signal model for $q^4/m_{nn}^4|\mathcal{F}_{+}^{M}|^2$. Right: Signal model for $q^4/m_{nn}^4|\mathcal{F}_{-}^{M}|^2$.

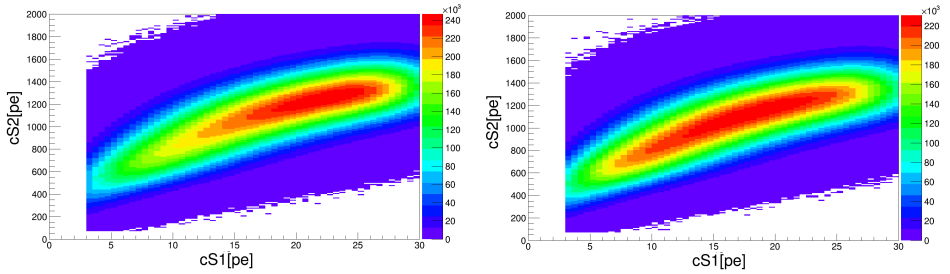

Figure B.4.: Signal models of non-standard interaction channels Left: Signal model for $q^4/4m_{nn}^4|\mathcal{F}_{+}^{\Phi''}|^2$. Right: Signal model for $q^4/4m_{nn}^4|\mathcal{F}_{-}^{\Phi''}|^2$.

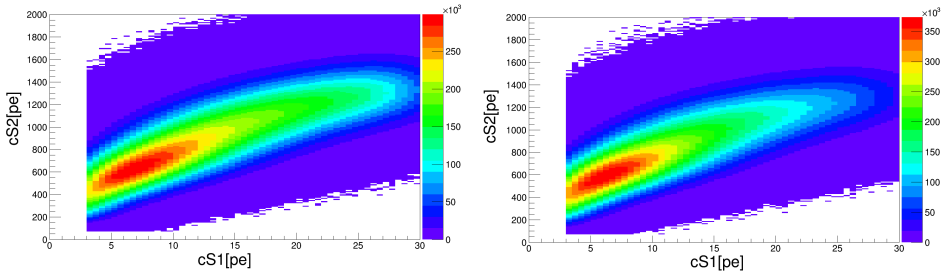

Figure B.5.: Signal models of non-standard interaction channels Left: Signal model for $q^2/4m_{\chi}^2|\mathcal{F}_{+}^{M}|^2$. Right: Signal model for $q^2/4m_{\chi}^2|\mathcal{F}_{-}^{M}|^2$.

B.2 Discrimination power of background versus non-standard nuclear form factors.

Below the tables for the discrimination power of the respective non-standard interaction mechanism from a background-only null hypothesis are shown.

Table B.1.: Discrimination power with respect to background-only (in %) of the XENON1T settings after $1.0\,\mathrm{t\,yr}$ of exposure.

m_χ	100 GeV		1 TeV	
$\sigma_{nn}\,[\mathrm{cm}^2]$	10^{-46}	10^{-47}	10^{-45}	10^{-46}
$\lvert\mathcal{F}_-^M\rvert^2$	55	31	60	33
$q^2/4m_\chi^2\lvert\mathcal{F}_+^M\rvert^2$	100	21	100	25
$q^2/m_\chi^2\lvert\mathcal{F}_-^M\rvert^2$	99	24	100	27
$q^4/m_{nn}^4\lvert\mathcal{F}_+^M\rvert^2$	99	19	100	22
$q^4/m_{nn}^4\lvert\mathcal{F}_-^M\rvert^2$	100	20	100	22
$\lvert\mathcal{F}_\pi\rvert^2$	71	38	62	42
$q^4/4m_{nn}^4\lvert\mathcal{F}_+^{\Phi''}\rvert^2$	99	19	100	22
$q^4/4m_{nn}^4\lvert\mathcal{F}_-^{\Phi''}\rvert^2$	99	19	100	21

Table B.2.: Discrimination power with respect to background-only (in %) of a XENONnT-like experiment after $30\,\mathrm{t\,yr}$ of exposure.

m_χ	100 GeV			1 TeV		
$\sigma_{nn}\,[\mathrm{cm}^2]$	10^{-46}	10^{-47}	10^{-48}	10^{-45}	10^{-46}	10^{-47}
$\lvert\mathcal{F}_-^M\rvert^2$	100	97	20	100	99	21
$q^2/4m_\chi^2\lvert\mathcal{F}_+^M\rvert^2$	100	87	31	100	94	34
$q^2/4m_\chi^2\lvert\mathcal{F}_-^M\rvert^2$	100	84	16	100	96	17
$q^4/m_{nn}^4\lvert\mathcal{F}_+^M\rvert^2$	100	79	14	100	90	15
$q^4/m_{nn}^4\lvert\mathcal{F}_-^M\rvert^2$	100	81	15	100	90	16
$\lvert\mathcal{F}_\pi\rvert^2$	100	56	23	100	61	26
$q^4/4m_{nn}^4\lvert\mathcal{F}_+^{\Phi''}\rvert^2$	100	77	14	100	92	16
$q^4/4m_{nn}^4\lvert\mathcal{F}_-^{\Phi''}\rvert^2$	99	79	15	100	90	16

Table B.3.: Discrimination power with respect to background-only(in %) of a DARWIN-like experiment after $200\,\mathrm{t\,yr}$ of exposure.

m_χ	$100\,\mathrm{GeV}$			$1\,\mathrm{TeV}$		
$\sigma_{nn}\,[\mathrm{cm}^2]$	10^{-46}	10^{-47}	10^{-48}	10^{-45}	10^{-46}	10^{-47}
$\lvert\mathcal{F}_-^M\rvert^2$	100	100	69	100	100	75
$q^2/4m_\chi^2\lvert\mathcal{F}_+^M\rvert^2$	100	100	48	100	100	57
$q^2/4m{\chi}^2\lvert\mathcal{F}_-^M\rvert^2$	100	100	55	100	100	62
$q^4/m_{nn}^4\lvert\mathcal{F}_+^M\rvert^2$	100	99	40	100	100	50
$q^4/m_{nn}^4\lvert\mathcal{F}_-^M\rvert^2$	100	98	41	100	100	51
$\lvert\mathcal{F}_\pi\rvert^2$	100	100	56	100	100	67
$q^4/4m_{nn}^4\lvert\mathcal{F}_+^{\Phi''}\rvert^2$	100	100	58	100	100	69
$q^4/4m_{nn}^4\lvert\mathcal{F}_-^{\Phi''}\rvert^2$	100	99	40	100	100	51

Appendix C

First observation of double electron capture

C.1 Sideband fit results

Table C.1.: Sideband fit results for the Xe-125 extraction. Matching was performed in two volumes simultaneously.

Parameter	Fit result
M_{inner}	1.00 ± 0.01
M_{outer}	1.00 ± 0.01
κ_{inner}	0.85 ± 0.20
κ_{outer}	0.34 ± 0.30
Co-60	$3 \cdot 10^{-8} \pm 1 \cdot 10^{-1}$
K-40	$5 \cdot 10^{-6} \pm 3 \cdot 10^{-2}$
U-238	$3 \cdot 10^{-3} \pm 1 \cdot 10^{-1}$
Ra-226	$4 \cdot 10^{-6} \pm 4 \cdot 10^{-2}$
Th-232	131.3 ± 25.7
Th-228	-1.3 ± 13.1
Xe-125	$(-3.20 \pm 0.16) \cdot 10^{-2}$
Xe-133	$(4.7 \pm 1.2) \cdot 10^{-2}$
Pb-214	8.5 ± 0.3
Kr-85	7.1 ± 1.0
Solar ν	1.06 ± 0.20
Xe-136	0.99 ± 0.04
$N_{\text{Kr-83m}}$	$(4.47 \pm 0.05) \cdot 10^{-2}$
$\mu_{\text{Kr-83m}}$	41.48 ± 0.02
$\sigma_{\text{Kr-83m}}$	2.33 ± 0.02
$N_{\text{Kr-83m-miss}}$	$(6.6 \pm 1.1) \cdot 10^{-5}$
$\mu_{\text{Kr-83m-miss}}$	32.8 ± 0.3
$\sigma_{\text{Kr-83m-miss}}$	1.8 ± 0.4
$N_{\text{Xe-131m}}$	$(5.03 \pm 0.06) \cdot 10^{-2}$
$\mu_{\text{Xe-131m}}$	164.76 ± 0.04
$\sigma_{\text{Xe-131m}}$	4.45 ± 0.04
$N_{\text{Xe-129m}}$	$(3.12 \pm 0.07) \cdot 10^{-2}$
$\mu_{\text{Xe-129m}}$	236.82 ± 0.08
$\sigma_{\text{Xe-129m}}$	5.43 ± 0.07

C.2 Sanity checks of the double electron capture signal

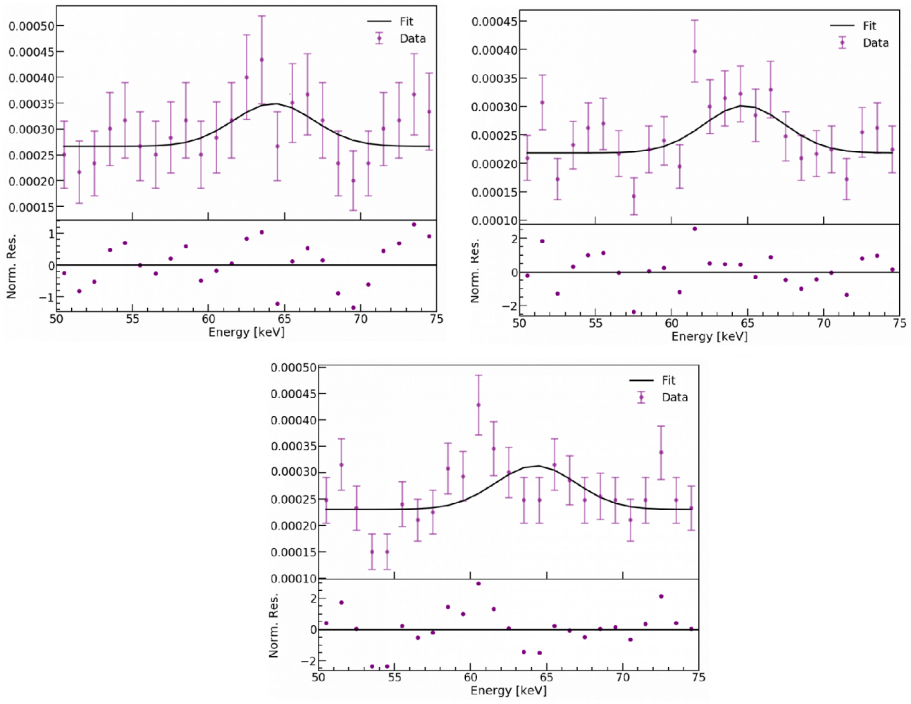

Figure C.1.: Binned temporal analysis of the XENON1T data. The three time bins were simultaneously fitted using a constrained Gaussian with a background constant. The latter was allowed to vary while the Gaussian was shared among the three. The reduced χ^2 is at 1.1 with 71 degrees of freedom. The fit yields $(178 \pm 37)\,\mathrm{events}$, which is in agreement with the final result. However, we do not use any background model here except the flat constant which changes over time. The time bins chosen are: Upper left: 39.1 days. Upper right: 88.6 days. Bottom middle: 88.9 days.

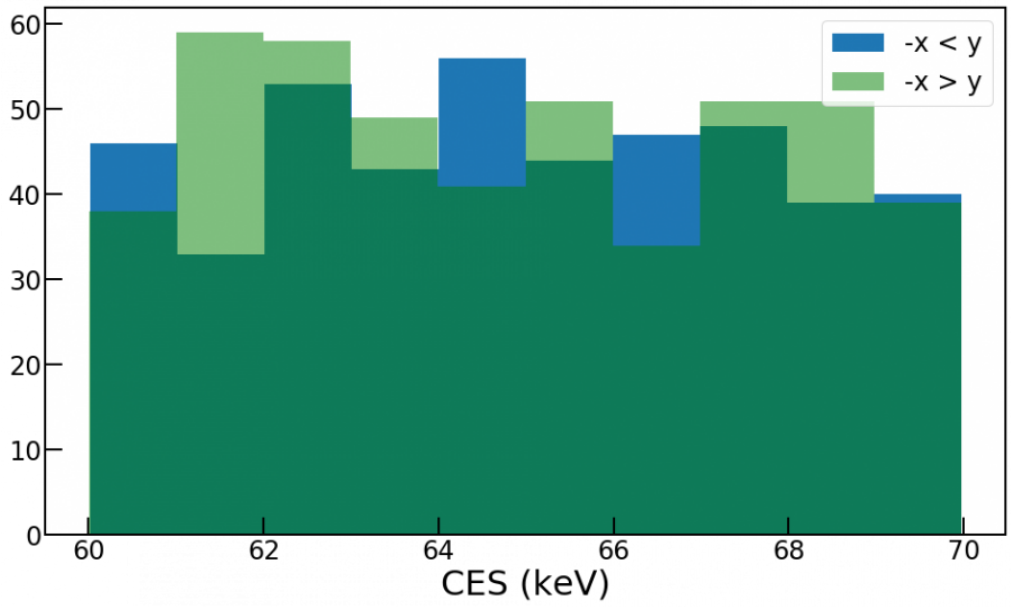

Figure C.2.: Energy spectrum of the spatial halves of the detector. The detector was divided at $-x = y$ and both halves are indicated by green and blue. No particular energy dependency within the region of interest is found.

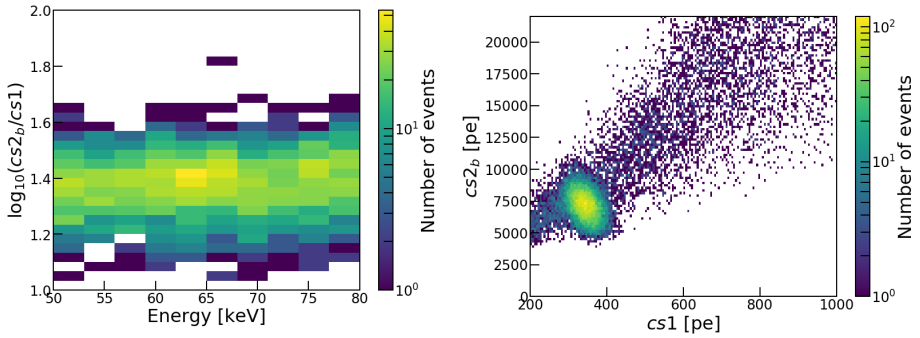

Figure C.3.: Region of interest in discrimination space Left: The discrimination space ($\log_{10}$(cS2b/cS1)) is shown as a function of the energy. All events are valid ER events and the mean of the band is represented well. Right: $cS2b$ as a function of $cS1$ is shown. The large structure around 400 pe in $cS1$ belongs to ^{83m}Kr. The statistics for the double electron capture is too small to form a visible ellipse.

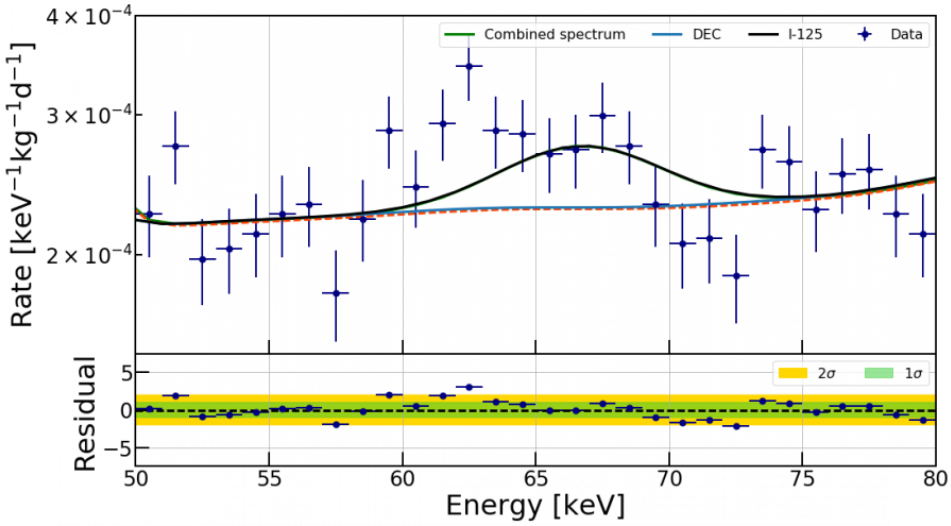

Figure C.4.: Pure iodine signal fit to the unblinded data. The Gaussian at the double electron capture region has been set to 0 and the iodine signal was allowed to fit freely. The best-fit is shown as a comparison versus the background-only scenario. The χ^2 detoriates by 14 within the $\sim 20\,\mathrm{keV}$ window, which clearly points (next to the visible mis-fit) to the fact that iodine cannot account for the signal. This was also proven with the dedicated neutron activation studies.

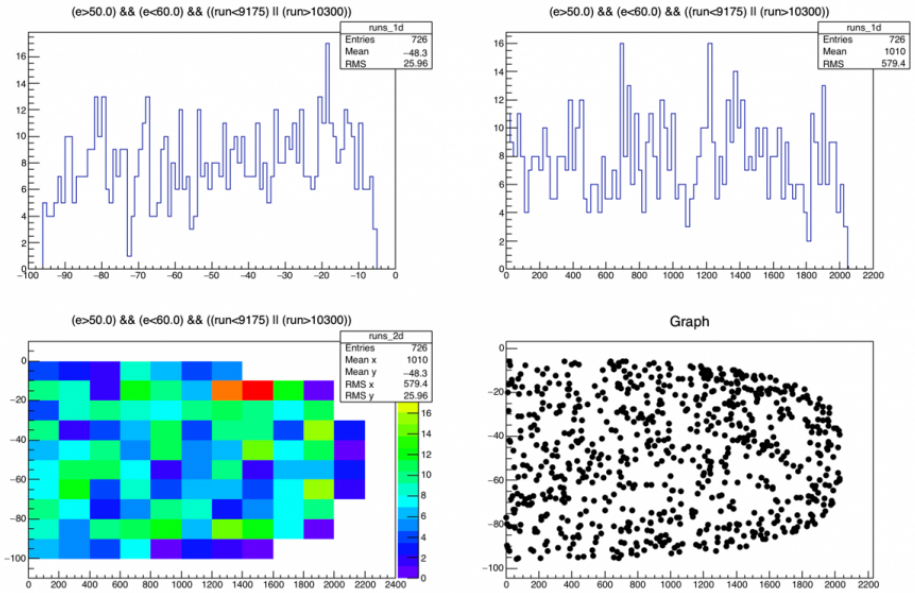

Figure C.5.: Spatial distribution of events with an energy between $50\,\mathrm{keV}$ to $60\,\mathrm{keV}$ Figure by C.Weinheimer.

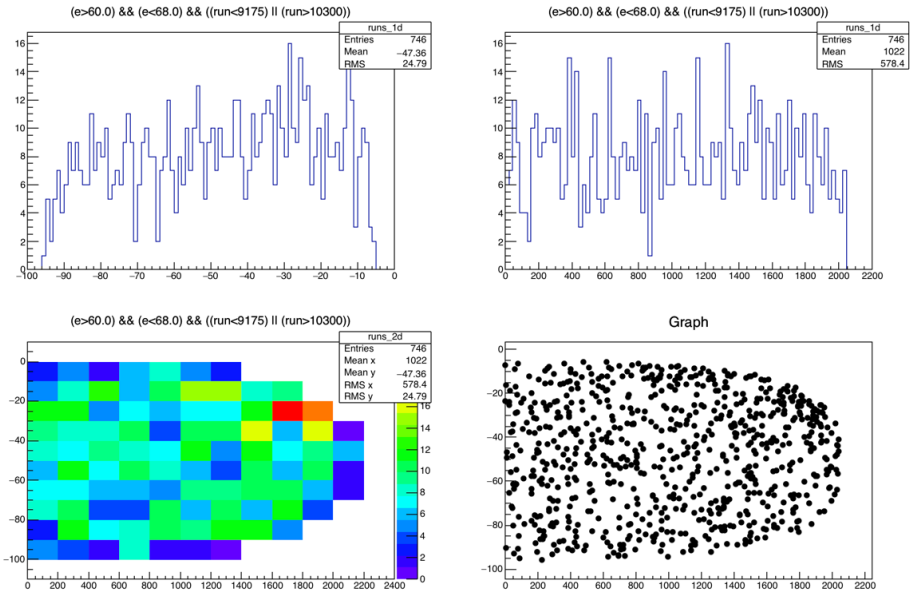

Figure C.6.: Spatial distribution of events with an energy between $60\,\mathrm{keV}$ to $68\,\mathrm{keV}$ Figure by C.Weinheimer.

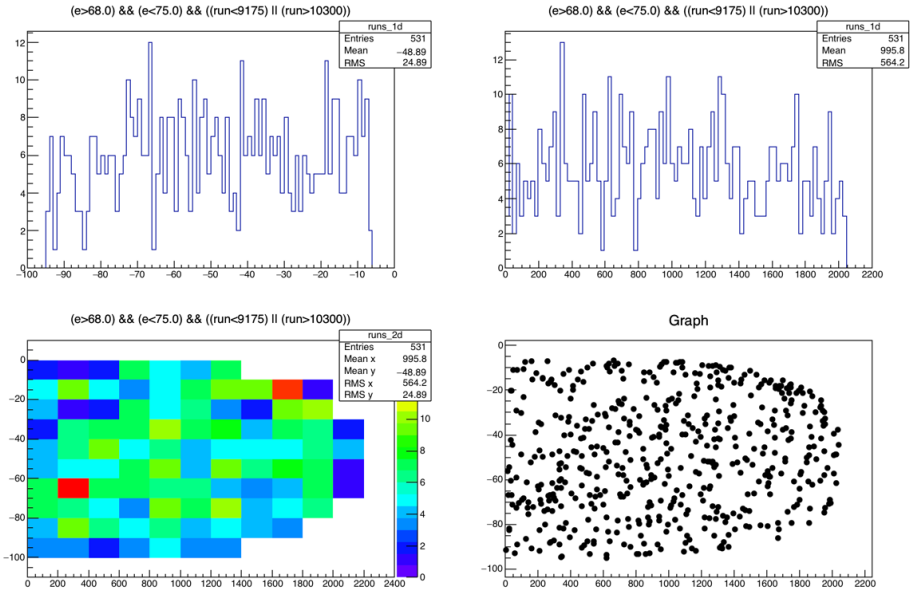

Figure C.7.: Spatial distribution of events with an energy between $68\,\mathrm{keV}$ to $75\,\mathrm{keV}$ Figure by C.Weinheimer.